5-2007

Equal-Channel-Angular Processing (ECAP) of Materials: Experiment and Theory

Grigoreta Mihaela Stoica
University of Tennessee - Knoxville

To the Graduate Council:

I am submitting herewith a dissertation written by Grigoreta Mihaela Stoica entitled "Equal-Channel-Angular Processing (ECAP) of Materials: Experiment and Theory." I have examined the final electronic copy of this dissertation for form and content and recommend that it be accepted in partial fulfillment of the requirements for the degree of Doctor of Philosophy, with a major in Materials Science and Engineering.

Peter K. Liaw, Major Professor

We have read this dissertation and recommend its acceptance:

Joseph E. Spruiell, Hahn Choo, John D. Landes

Accepted for the Council:
Dixie L. Thompson

Vice Provost and Dean of the Graduate School

(Original signatures are on file with official student records.)

To the Graduate Council:

I am submitting herewith a dissertation written by Grigoreta Mihaela Stoica entitled ″Equal-Channel-Angular Processing (ECAP) of Materials: Experiment and Theory.″ I have examined the final electronic copy of this dissertation for form and content, and recommend that it be accepted in partial fulfillment of the requirements for the degree of Doctor of Philosophy, with a major in Materials Science and Engineering.

Peter K. Liaw

_____

Major Professor

We have read this dissertation
and recommend its acceptance:

Joseph E. Spruiell

_____

Hahn Choo

_____

John D. Landes

_____

Accepted for the Council

Carolyn Hodges

_____

Dean of the Graduate School

(Original signatures are on file with official student records.)

Equal-Channel-Angular Processing

(ECAP)

of Materials: Experiment and Theory

A Dissertation

Presented for the

Doctor of Philosophy

Degree

The University of Tennessee, Knoxville

Grigoreta Mihaela Stoica

May 2007

This work is dedicated

To my husband, who gave me everything: love, children, and permanent support;

To my children, who are my pride;

To my Romanian and American friends, who really care about me, and are so patient and kind;

To my entire family, who is the reason for everything that happens to me.

ACKNOWLEDGEMENTS

I am the most grateful to the committee members: *Prof. Peter K. Liaw, Prof. Joseph E. Spruiell, Prof. Hahn Choo, and Prof. John D. Landes,* for their agreement to be part of the present research effort. *Prof. Raymond A. Buchanan*, in your memory, we work hard to continue your and Prof. P. K. Liaw′s initiative in the field of the severe plastic deformation of metals. Foremost, I express to you, *Prof. Liaw,* my thanks for the constant support, the tremendous energy, and excellent guidance in my graduate career and beyond the school borders. My sincere gratitudes for the remarkable lectures, discussions, and advices are directed to *Prof. Joseph E. Spruiell*. To *Prof. Hahn Choo and Prof. John D. Landes I* address my special thanks for their interest in my project, and for their kind suggestions and support. I had a fruitful learning experience working together with *Dr. Lijia Chen*. I thank you, *Jerry-Liang Wu,* for your dedication and passion; you are an admirable colleague and a perseverant researcher. Thank you, *HH-Hao Hsiang Liao* for sharing your enthusiasm for the ECAP project. Here is the place to thank my lab mates, *Dr. George-Gongyao Wang, Mr. Robert Mc Daniels, Ms. Mary Qiao, and Ms. Carol Winn* for our work together. I thank you, *Dr. Yandong Wang and Dr. Victor-Guojiang Fan* for the interesting discussions and help. I'm happy to say a word of gratitude to *Lanlan Huang*, to *Prof. B. Huang* and *Dr. Y. Liu* for the tremendous help and interest in the ECAP project. I owe my special appreciations to Dr. *Louis-Yulin Lu and Julia Sun, to Dr. Hongbo Tian and Jing He, to Dr. Bing Yang, to Fengxiao Liu, to Dr. Mark Morrison and Dr. Bill Peters, to Ms. Brandice Green, Dr. Rejanah Steward and Ms. Sujing Xie.* Thank you for being such good friends and partners for work and discussions.

Routinely, a miracle happened when entering the mechanical shop, lead by Mr. Douglas E. Fielden. Special thanks to you, Prof. Fielden, and to your team, *Mr. Larry A. Smith and Mr. Dan Hackworth* for your permanent help, innovative ideas, and professionalism. And thank you, *Mr. Gregory L. Jones, Mr. Michael R. Neal, and Mr. Stephen A. Stiner* for your constant help. This is an opportunity for me to thank the staff of the Materials Science and Engineering Department at UT, wonderfully represented by *Ms. Carla Lawrence, Ms. Sandy P. Maples, Ms. Roberta L. Campbell, Ms. Carolyn S. Nelson, Ms. Patricia A. Houser, Mr. W. Frank Holiway, and Mr. Randall D. Stooksbury.* All of them consistently help me on everyday basis. I have a heart-felt admiration for *Prof. George Pharr,* a perfect teacher and educator. All of the above are again so many reasons to always remember the days we worked together at UT.

Thank you, *Dr. Andrew E. Payzant,* for your competent help and cooperation, including the provision of kind comments and suggestions during our work on Mg textures. The collaboration with *Dr. Cam Hubbard, Dr. Roberta Peascoe, Dr. Thomas Watkins, Dr. Claudia J. Rawn, and Dr. Laura Riester* at HTML-ORNL was essential for the present work. I am very grateful to you all. Many thanks are addressed to *Dr. Sean R. Agnew* for the extensive and passionate collaboration on the ECAP project. I'm very thankful to *Prof. Terrence G. Langdon,* who produced the first ECAP billet I ever saw. Thank you, *Dr. Cheng Xu,* for providing the ECAP-ed billets for our research on Al-alloys. I thank you, *Dr. Don A. Carpenter and Dr. Sven Vogel*, for the delicate orientation-imaging microscopy and neutron measurements performed on our Mg-samples.

I would like to express my special thanks and appreciations for the financial support from (1) the University of Tennessee Scholarly Activities Research Incentive Fund (SARIF) with *Dr. K. Walker* as the Program Director; (2) the Southeastern Universities Research Association (SURA) with *Dr. T. E. Hutchinson and Dr. G. Gruzalski* as the Program Coordinators; (3) National Science Foundation - Combined Research-Curriculum Development Program (CRCD), under EEC-9527527, with *Ms. M. Poats* as the Program Director; (4) National Science Foundation - Integrative Graduate Education and Research Training Program (IGERT), under DGE-9987548, with *Dr. C. J. Van Hartesveldt, Dr. D. Dutta, Dr. W. Jennings, Dr. L. Goldberg, and Dr. L. Clesceri* as the Program Directors, and (5) National Science Foundation - International Materials Institutes (IMI) Program, under DMR-0231320 with *Dr. C. Huber* as the Program Director, and support from the Assistant Secretary for the Energy Efficiency and Renewable Energy, Office of FreedomCAR and Vehicle Technologies, as part of the Material Science and Technology User Program, Oak Ridge National Laboratory, managed by UT-Battelle, LLC, for the U.S. Department of Energy under contract number DE-AC05-00OR22725, and the NSF at the University of Southern California, under Grant DMR-02343331. The use of the Advanced Photon Source was supported by the U. S. Department of Energy, Office of Science, Office of Basic Energy Sciences, under Contract No. DE-AC02-06CH11357. We address special thanks to the Centroid Corporation of Howard, Pennsylvania, for the donated software on the Computerized Numerical Controlled (CNC) milling machine functioning at UT, which was essential in solving the difficulty and accuracy requirements for the sample preparation.

ABSTRACT

Equal Channel-Angular Processing (ECAP), as a severe plastic deformation of metals and composites, is analyzed both theoretically - to describe the ECAP macromechanics - and experimentally - to obtain ultrafine-grained materials with new thermo-mechanical properties - with a focus on hexagonal-closed-packed (HCP) structures such as Mg alloys. Due to their obvious similarity to ECAP, the slip-line–field theories developed for orthogonal cutting are applied to the ECAP deformation for predicting the shear-strain spatial heterogeneities. A theoretical model for predicting the plastic-deformation zone in an ECAP-ed billet with a free surface is provided, and is validated experimentally. A shear-strain-mapping procedure was developed by decomposing the large deformation process into fine steps, and, by analyzing the partially-deformed billets, the strain maps captured the spatio-temporal evolutions of the ECAP-induced plastic shear strains. This approach was later generalized for studying the local behavior of different material parameters, such as textures (texture mapping).

The mechanical testing of the as-received and ECAP-deformed Mg-alloys (ZK60 and AZ31) was performed in monotonic and cyclic tests, for three loading orientations. The ECAP-ed samples demonstrate: (a) a good grain refinement from 50 - 70 μm down to 2.5 - 7 μm), (b) a superplastic ZK60 alloy, with an elongation to failure of 371 % at 350^0C and the strain rate of 10^{-2} s^{-1}, and (c) a longer fatigue life for the AZ31 alloy, relative to the as-received material.

The starting and ECAP-deformed materials were characterized by optical microscopy, X-ray diffraction using both soft and hard X-rays, and neutron diffraction. The grain sizes,

the textures, the coherent-domain sizes, the elastic microstrains, and the dislocation densities were determined for the samples deformed by rolling, extrusion, and ECAP. The synchrotron radiation measurements allowed monitoring the lattice rotation induced by the ECAP deformation in Mg alloys. The grain-orientation dependent deformation is studied relative to the deformation history, and its influence on the mechanical behavior is analyzed relative to the twinning contribution.

The results of the present work constitute a valuable benchmark for the understanding and modeling of the deformation mechanisms, such as the dislocations slip, twinning, recovery, or recrystallization in HCP structures.

Table of Contents

Chapter /Section	Description	Page
1	**INTRODUCTION**	**1**
2	**ECAP MACROMECHANICS**	**13**
2.1	Die Design and Processing Parameters	13
2.2	Plastic-Deformation Zone (PDZ) in ECAP: Theoretical Modeling	17
2.3	Plastic-Deformation Zone (PDZ) in ECAP: Experiment	41
3	**CHARACTERIZATION TECHNIQUES**	**47**
3.1	Microscopy	47
3.2	Diffraction Techniques	51
3.3	Mechanical Testing under Monotonic and Cyclic Loadings	69
4	**ECAP APPLIED TO Mg-ALLOYS**	**70**
4.1	Grain Refinement During ECAP	70
4.2	Orientation Effects on Mechanical Properties	78
4.3	Deformation Textures in Mg-Alloys	90
4.4	Mapping the Texture Evolution in ECAP	104
5	**SUMMARY**	**115**
6	**CONCLUSIONS**	**130**
7	**FUTURE WORK**	**134**
	REFERENCES	**136**
	APPENDIX: Tables and Figures	**151**
	VITA	**251**

LIST OF TABLES

Table	Description	Page
1	ECAP parameters used to obtain UFG materials.	152
2	Microstructures and mechanical properties obtained on pure metals, Cu, Al, Ti, and W using the ECAP technology.	159
3	Microstructures and mechanical properties obtained on Al alloys using the ECAP technology.	160
4	Microstructures and mechanical properties obtained on Mg alloys using the ECAP technology.	161
5	Microstructures and mechanical properties obtained on Cu, Zn, Fe and Ti Alloys using the ECAP technology.	162
6	The compositions and mechanical properties of the as-received Al- and Mg-alloys; ρ - density, E -Young modulus, ν - Poisson ratio, $\sigma_{0.2}$ and Y - tensile and yield strengths, ε - elongation, H - hardness, G - shear modulus, σ_f - fatigue strength.	163
7	The apparent-shear strain, γ_T, and equivalent strain, ε_{eq}, as derived from the models predicting the plastic-deformation zone (PDZ) in ECAP (from Ref. 65).	164
8	The apparent-equivalent strain, P_r, describing the degree of redundancy for the routes, A, B_A, B_C, and C, in multipass ECAP; n - integer, N - number of passes.	165
9	The four emission lines, $\lambda_1, \lambda_2, \lambda_3$, and λ_4 and their widths and weights used to determine the instrumental resolution [108].	165
10	The slip systems, dislocations types, and contrast parameters for Mg [119].	166
11	The fatigue-strength exponent, b, and the fatigue-strength coefficient, σ_f', determined from the low-cycle fatigue of the Mg alloys, AZ31 (hot rolled) and ZK60 (hot extruded), and tested in the CC - and TT - loading directions.	167
12	The fatigue-strength exponent, b, and the fatigue-strength coefficient, σ_f', for the Mg alloy, AZ31, before and after ECAP, 1, 2, and 8 passes, routes A and B.	167
13	The low energy XRD results from the whole-pattern fitting of the profiles obtained for the AZ31 compressed samples for different loading directions: FF, CC, and TT, which are normal to the flow,	168

cross, and top planes, respectively, and at different testing temperatures; D_V - the volume-averaged coherent-domain size; a, a + c, and c - percentage of the dislocation debris corresponding to the three orientations of the Burgers vectors; ρ - dislocation density.

LIST OF FIGURES

Figure	Figure Caption	Page
1	In the ECAP technique, the billet is passing through the two channel die (in this case, a 90^0 die). The coarse-grained billet is plastically deformed by a simple shear at the shearing plane, ABCD, and, at the exiting channel, the UFG material is obtained; XD, TD, and ND are the pressing, transverse, and normal directions.	163
2	The ECAP configurations: (a) a sharp corner between the two channels at $\Phi = 90^0$, and with a single shear-plane, ABCD, and (b) a round corner between the channels at 120^0, and with the angular span, 2Ψ, encompassing the roundness of the outer corner. The shearing plane, OO′, is at the intersection of the channels.	163
3	The ECAP straining routes: route A with no rotation between passes; route B_A with alternate rotation of 90^0; and route B_C with consecutive rotation of 90^0, and route C with a rotation of 180^0 of the billet between passes.	164
4	A split ECAP-die with sharp-corner; the sliding floor reduces the friction billet-die, and is the second channel of the die.	165
5	Lateral view of the ECAP setup, including the pressing machine, ECAP die, and a frame for the back-pressure.	165
6	(a) The components of the modified sharp-corner ECAP die: upper and lower assemblies, and the sliding floor; (b) assembled die.	166
7	The components of the symmetric ECAP die designed to process two billets at once; the billets are square-shaped, and the size can vary from 9.5 × 9.5 to 25 × 25 mm, with the length of 102 mm. The die allows for flexible angles between the two channels ranging from 90º to 120º, and the die-billet interface has a minimal friction, i.e., the two billets move together with the holder.	167
8	Assembly of the symmetric ECAP die, including the main body with the guiding and filling plates mounted to form the first and second channel of the die, and the holder for the two billets. The billet size can vary from 9.5 × 9.5 to 25 × 25 mm, with the length of 102 mm.	168
9	The components of the sharp-corner ECAP die.	169
10	A sharp-corner ECAP die with a sliding floor in the second channel, and moving together with the billet during the processing. The billet size is 12.5 × 12.5 × 102 mm.	170
11	A round-corner ECAP die with the angular span, $2\Psi = 60^0$, which is	170

the roundness of the outer corner of the die.

12 The ECAP sharp-corner die mounted on the hydraulic pressing machine, Interlaken - 200 kip. 171

13 Partially-deformed billets during ECAP: (a, b, and c) billets processed in a sharp-corner die, and (d and e) billets processed in a round-corner die. Prior ECAP, the billets were split in two parts, scribed with a network of 1 × 1 mm, and processed at room temperature, with a pressing speed of 0.5 mm/sec. 172

14 Partially-deformed billets in a round-corner ECAP die at high temperature. The split billets of (a and b) the 6061 Al alloy, and Mg alloys, (c) ZK60 and (d) AZ31B, were scribed with a network of 1 × 1 mm, and were processed at temperature, T = 250^0C, with a pressing speed of 0.5 mm/sec. 173

15 Geometrical parameters in the case of (a) the orthogonal-cutting deformation, and (b) ECAP deformation; OO′ is the shear plane, T is the working piece thickness, t is the chip thickness, v_0 and v are the velocities before and after the deformation, respectively. 174

16 The ECAP-die configurations with the two channels at the angle, $2\Phi = 120^0$, and with: (a) sharp corner, and (b) round corner. The unit element, abcd, is moving from the first into the second channel, and is transformed into a′b′c′d′ after the deformation. The PDZ extension is inside AOB, and encompasses the angular span, 2Ψ. Inside AOB (right insert), the two orthogonal slip-line families are represented, and AO and BO are the two rigid-plastic boundaries (reproduced from Ref. 78). 175

17 Four ECAP models for the plastic-deformation zone (PDZ) shape and size: (a) single-shear plane, AO: SP-PDZ model; (b) shearing fan, AOB: Ψ-PDZ model; (c) shearing plane, MO, and splitting, MAB: partial-split, PS-PDZ model; and (d) shearing fan, MON, and splitting, AMNB: full-split, FS-PDZ model (reproduced from Ref. 65). 176

18 The finite-element modeling (FEM) predicting the shear-strain nonuniformity across the billet (when moving from the top position, O, to the bottom position, B′) in ECAP. Different angular spans of a round-corner die, with the two channels at 90^0, are considered (reproduced from Ref. 93 and modified). 177

19 Partial-split model, PS-PDZ [79], for the ECAP plastic deformation, in a 90^0 die, including the straight rigid-plastic boundary (RPB), QM, two curved RPBs, MA and MB, a free-surface, AB, and the variable angles, δ and χ, when moving the point, P, on curved RPBs. The right 178

insertion shows the velocity components.

20 Comparison of the calculated equivalent-strains as a function of the relative position across the billet (the top of the billet toward the bottom) for different PDZ models in ECAP (die with $2\Phi = 90^0$): the single-plane model (SP-PDZ), the shearing-fan model (ψ-PDZ), the partial-split model (PS-PDZ), and the full-split model (FS-PDZ), for two shearing fans of 20^0 and 40^0 (from Refs. 2, 78 , 79, and 81). 179

21 The apparent equivalent strain, $\varepsilon_a = P_r \times \varepsilon_{eq}$, describing the degree of redundancy for each route in ECAP. 180

22 The shear-strain mapping and the calculated flow-lines grids for the billet of pure Cu deformed in one pass of ECAP using (a) a sharp-corner die, and (b) a round-corner die. The ECAP-ed billets are shown above the maps. 181

23 The **s**hear-strain distributions for the sharp-corner die: a comparison between the experiment and theory shows a good agreement for Al and Cu billets, but for the Pb billet there is a significant instability near the bottom of the billet. 182

24 The **s**hear-strain distributions for the round-corner die**:** the apparent shear strain values, γ_T, as a function of the position across the billet for Al, Cu, and Pb billets shows a significant decrease towards the bottom of the die. 182

25 Sample preparation for the microstructural characterizations. The three surfaces of observation are flow plane (F) with normal TD, top plane (T) with normal ND, and cross plane (C) with normal XD. The XD is the extrusion/rolling direction, and CC, TT, and FF are the designations of the three orientations for machining the samples. 183

26 Optical micrographs of the as-received alloys: (a) AZ31-H24 (hot-rolled), flow plane, and (b) ZK60-T5 (hot-extruded), flow, top, and cross planes. 183

27 Schematic of the electron-backscattered diffraction (EBSD) used in orientation-imaging microscopy (OIM). 184

28 The grain-boundaries distribution obtained from the orientation-imaging microscopy (OIM) measurements on the ZK60 samples in the as-received condition; the blue color shows the low-angle grain boundaries (LAGBs), and the black color, the high-angle grain boundaries (HAGBs). 184

29 The whole-pattern fitting of the θ - 2θ scan with low-energy (LE) XRD obtained for the instrumental profile using a Si standard; the theoretical predictions (the red line) are in a good agreement with the 185

experimental data (the open dots).

30 The diffraction contrast parameters, q_1 and q_2, calculated for the edge dislocations in Mg using the data from the Ref. 119. 185

31 In the low-energy (LE) XRD measurements for obtaining the pole figures, the sample is rotated with an angle, φ, and tilted with an angle, χ, varying from 0^0 to 75^0: (a) the 3-D arrangement; (b) the measured diffracted intensities, projected in one plane, cover 75^0, and the remaining 15^0 are calculated to obtain the full pole figure; (c) the horizontal section through the arrangement. 186

32 The low-energy (LE) XRD pole-figures of the as-received samples: (a) AZ31-H24 (hot rolled), and (b) ZK60-T5 (hot extruded), for three surfaces of observations, flow (F), top (T), and cross (C) planes, and for the reflection planes, (10.0) and (00.2). 187

33 The inverse pole-figures (IPFs) calculated from the LE-XRD data obtained for the ZK 60-T5 (hot extrusion) sample observed on flow, top, and cross planes: (a) as-received, and (b) after compression CC (with the loading direction parallel to the extrusion direction). The XD, ND, and TD are the directions normal to the cross, top, and flow planes, respectively. 188

34 (a) In the high-energy (HE) XRD (synchrotron radiation) measurements in transmission geometry, the scattered radiation is detected by an image-plate (detector) as a diffraction-ring pattern; the diffraction angle is 2θ, and the rotation angle, φ; (b) The in-plane pole distribution (IPPD) covers a section of ~ 1^0, with the orientations almost perpendicular to the beam direction (equivalent to a tilting angle, $\chi \sim 90^0$). 189

35 The diffraction-rings pattern recorded in the high-energy (HE) XRD experiment for the Mg alloy, AZ31-H24 (rolled): (a) as-received, (b) annealed at 350^0C for 1h, and (c) ECAP at 250^0C, 2 passes, route B_C. On the lower row, d, e, and f, are shown the 2-D rectangular maps of the three unfolded diffraction rings (from a total of 22 rings shown in a, b, and c), corresponding to the reflection planes (10.0), (00.2), and (10.1). 190

36 The diffraction-ring pattern recorded in the high-energy (HE) XRD experiment for the Mg alloy, ZK60-T5 (hot extruded): (a) as-received, (b) annealed at 350^0C for 1h, and (c) ECAP at 260^0C, 2 passes, route A. On the lower row, d, e, and f, are the 2D-rectangular maps for the three out of 22 rings in a, b, and c captured by the measurements. 191

37 The diffraction-ring patterns for three peaks recorded in the HE-XRD experiment for the ZK60 samples compressed along the extrusion direction (ZK-CC) at (a) room temperature (RT), (b) 150^0C, and (c) 192

350^0C. The corresponding representation of the in-plane pole distributions (IPPDs) is shown for the reflection planes (10.0), (00.2), and (10.1), for (d) RT, (e) 150^0C, and (f) 350^0C.

38 The high-energy (HE) XRD intensities, integrated over the rotation angle, φ, and represented versus 2θ for the reflections (10.0), (00.2), and (10.1) obtained for the Mg alloy, AZ31, observed on the top surface: (a) as-received (hot-rolled), and (b) after ECAP, 1 pass. 193

39 The 3D representation (for three planes of observations) of the in-plane pole distributions (IPPDs) in polar plots of the two Mg alloys characterized using the high-energy (HE) XRD technique: (a) AZ31-H24 (hot rolled), as-received, and (b) ZK60-T5 (hot extruded), as-received. 194

40 In neutron diffraction measurements (HIPPO, Los Alamos), the detectors are placed at 20^0, 40^0, 90^0, and 150^0 to record the intensities; (b) The coverage of the projected in one plane intensities are discs, corresponding to the four detector positions. 195

41 The PFs for six reflection planes obtained from the neutron diffraction on the ZK60 sample in the as-received condition (hot extruded). 195

42 Comparison of the prismatic PFs obtained on an as-received ZK60 sample, cross plane: (a) from the low-energy (LE) XRD, and (b) from the orientation-imaging microscopy (OIM) measurements. 196

43 The grain-size refinement (flow plane) for the ZK60 alloy before and after the ECAP deformation: (a) as-received, (b) ECAP, 4 passes, route A (4A), (c) ECAP - 4B, and (d) ECAP - 4C. 197

44 Optical micrographs of the ZK60-T5 alloy after the ECAP deformation for (a) 4 passes, route C, and (b) ECAP, 8 passes, route C; XD - pressing direction. 198

45 The effect of the ECAP temperature on grain refinement in the Mg alloy, AZ31B, after ECAP: (a) at 300^0C, 1 pass, (b) at 300^0C, 8 passes, route A, and (c) at 200^0C, 2 passes, route B_C. 199

46 The ECAP deformation homogeneity observed on the micrographs on flow (F), top (T), and cross (C) planes of the AZ31B, after ECAP at 200^0C, 2 passes, route B_C. 200

47 Grain refinement after the ECAP deformation of Mg alloys, AZ31 and ZK60. The AZ31 alloy was ECAP-deformed at two different temperatures. 200

48 The grain size and the grain-boundary distributions obtained from the OIM measurements for the ZK60-T5 alloy: (a) as-received, and (b) ECAP, 8 passes, route A. At the right, the basic stereographic 201

triangles show the color code representing the lattice orientation of the observation planes, before (C plane) and after ECAP (T plane), respectively.

49 The grain-boundary-misorientation distributions obtained from the OIM data for the ZK60-T5: (a) as–received and (b) ECAP, 8 passes, route A. 202

50 Experimental results of the hardness versus the grain size for the AZ31B alloy in the as-received condition and ECAP-deformed in 1, 2, and 8 passes with backpressure; the comparison with the Hall-Petch relationship (red line) shows the grain-refinement efficiency during ECAP. The two sets of data (in black and blue) represent the values measured on the cross and top planes, respectively. 203

51 The orientation dependence of the stress-strain curves for the (a) AZ31B samples, and (b) ZK60 samples tested in compression at room temperature for three orthogonal loading directions: FF, TT, and CC. 204

52 The true stress-strain curves obtained from the compressive testing at different temperatures of the AZ31B-H24 rolled alloy for the CC-, TT-, and FF-loadings, respectively. 205

53 The true stress-strain curves obtained from the compressive testing at different temperatures of the ZK60-T5 extruded alloy for the CC-, TT-, and FF-loadings, respectively. 206

54 The hardening rate versus the plastic strain resulted from the compression at different temperatures of the AZ31 alloy (a) for the CC loading, and (b) for the TT loading. 207

55 The hardening rate versus the plastic strain resulted from the compression at different temperatures of the ZK60 alloy (a) for the CC loading, and (b) for the TT loading. 208

56 Stress amplitude versus cycles to failure of the AZ31B alloy samples for the CC-loading (along the rolling direction) and for the TT-loading (perpendicular to the rolling direction). 209

57 Total strain versus reversals to failure for two loading directions applied to the ZK60-T5 alloy samples during low-cycle fatigue: CC-loading, along the extrusion direction, and TT-loading, perpendicular to the extrusion direction. 210

58 True stress-strain curves of the ZK60 samples, deformed by ECAP for 1, 2, 4, and 8 passes, route A, and tested in tension with the strain rate of 5×10^{-3} s^{-1} at (a) room temperature (RT), and (b) 350^0C. 211

59 The normalized stress of ZK60, tested in tensile, (a) versus strain rate, at testing temperature, T = 350^0C, and (b) versus test temperatures for 212

the samples before and after ECAP, 4 passes, route A; (c) the strain-rate sensitivity versus number of ECAP passes of the ZK60 alloy tested in tension at 350^0C.

60 The elongations obtained from the tensile testing of AZ31B and ZK60 alloys at different temperatures, before and after ECAP for 1, 2, 4, and 8 passes, route A: (a) AZ31 and (b) ZK60. 213

61 Superplastic behavior of the ZK60 deformed in ECAP for 4 passes, and tested in tension at different temperatures, and for different ECAP routes (A, B, and C). 214

62 The stress amplitude versus cycles-to-failure resulted from the fatigue testing of ECAP-ed AZ31 (routes A and B_C) for 1 pass, 2 passes, 8 passes without back-pressure (8B), and 8 passes with back-pressure (8BB). During fatigue, three loading directions were used: (a) CC loading, along the pressing direction, and (b and c) TT and FF loadings, perpendicular to the pressing direction. 215

63 The twin formation in the hexagonal-closed packed (HCP) structure of Mg: (a) the HCP structure of Mg before twinning, with the lattice constants a = b, and c, where $\frac{c}{a} = 1.624 < \sqrt{3}$; (b) the HCP structure after twinning (the twin is represented with red lines); (c) the tensile twin formation after a compressive loading perpendicular to the c-axis. The shear strain, γ, due to twinning is $\gamma = \frac{c}{a\sqrt{3}} - \frac{a\sqrt{3}}{c}$. 216

64 The characterizations of the two Mg alloys in the as-received condition, for three surfaces of observations, F - flow, T - top, and C - cross planes, and for two reflections planes, (10.0) and (00.2): (a) the high-energy (HE) XRD in-plane pole distributions (IPPDs) of the hot-rolled AZ31 alloy, (b) the HE-XRD IPPDs of the hot-extruded ZK60 alloy; (c) the neutron-diffraction pole figures of the ZK60 alloy, cross plane. 217

65 The low-energy (LE) XRD pole-figures of the ZK60-T5 samples after uniaxial compression at room temperature along the CC axis. The (10.0) reflection is shown for the three planes of observations (F - flow, T - top, and C - cross), where XD, ND, and TD are the pressing, normal, and transverse directions, respectively. The mother grains are designed with *M*, and the daughter grains with *D*. 218

66 The low-energy (LE) XRD pole-figures of the ZK60-T5 samples after uniaxial compression at room temperature along the CC axis. The (00.2) reflection is shown for the three planes of observations (F - flow, T - top, and C - cross), where XD, ND, and TD are the pressing, normal, and transverse directions, respectively. The mother grains are designed with *M*, and the daughter grains with *D*. 219

67	The low-energy (LE) XRD pole-figures of the ZK60-T5 samples after uniaxial compression at room temperature along the TT axis. The (10.0) reflection is shown for the three planes of observations (F - flow, T - top, and C - cross), where XD, ND, and TD are the pressing, normal, and transverse directions, respectively. The mother grains are designed with *M*, and the daughter grains with *D*.	220
68	The low-energy (LE) XRD pole-figures of the ZK60-T5 samples after uniaxial compression at room temperature along the TT axis. The (00.2) reflection is shown for the three planes of observations (F - flow, T - top, and C - cross), where XD, ND, and TD are the pressing, normal, and transverse directions, respectively. The mother grains are designed with *M*, and the daughter grains with *D*.	221
69	The neutron diffraction PFs for the reflection planes, (10.0) and (00.2), of the ZK60 samples, (a) as-received, and after the compression tests at room temperature: (b) CC-loading, 5% strain, (c) CC-loading, 11% strain, and (d) TT-loading, 25% strain.c	222
70	The neutron diffraction PFs for the reflection planes, (10.0) and (00.2), of the ZK60 samples, (a) as-received, and after the compression tests at room temperature: (b) CC-loading, 5% strain, (c) CC-loading, 11% strain, and (d) TT-loading, 25% strain.	223
71	The HE-XRD IPPDs of the basal poles, (00.2), of the AZ31 samples tested in compression, CC, TT, and FF, at different temperatures, and on three planes of observations: the flow plane (F), with the normal, TD, the top plane (T), with the normal, ND, and the cross plane (C), with the normal, XD.	224
72	The HE-XRD IPPDs of the prismatic poles, (10.0), of the ZK60 samples tested in compression, CC and TT, at different temperatures, and on three planes of observations: the flow plane (F), with the normal, TD, the top plane (T), with the normal, ND, and the cross plane (C), with the normal, XD.	225
73	The HE-XRD IPPDs of the basal poles, (00.2), of the ZK60 samples tested in compression, CC and TT, at different temperatures, and on three planes of observations: the flow plane (F), with the normal, TD, the top plane (T), with the normal, ND, and the cross plane (C), with the normal, XD.	226
74	The twinning mechanism during the plastic deformation in uniaxial compression of the ZK60 alloy for two loading directions: (a) compression CC, along the extrusion direction, and (b) compression TT, perpendicular to the extrusion direction. The mother texture, M, becomes daughter, D, after the compression test.	227

75	Texture development with the number of ECAP passes for the ZK60 samples: (a) as-received, (b) ECAP, 1 pass, c) ECAP, 4 passes, route A, and (d) ECAP, 8 passes, route A.	228
76	Comparison of the PFs for the ZK60-T5 deformed in ECAP for 8 passes, route A: (a) low-energy (LE) XRD and (b) orientation-imaging microscopy (OIM) for three reflections planes, (10.0), (00.2), and (10.1).	229
77	The LE- XRD PFs of the ZK60-T5 (hot extrusion): (a) as-received, (b) ECAP- 4A, (c) ECAP-4B, and (d) ECAP-4C; XD, ND, and TD - pressing, normal, and transverse directions.	230
78	The low-energy (LE) XRD PFs of the AZ31-H24 (hot rolling), before and after one pass of ECAP, observed on three surfaces, flow, top, and cross planes, for three reflection planes, (10.0), (00.2), and (10.1).	231
79	The texture evolution with the strain intensity obtained from the low-energy (LE) XRD PFs for the prismatic and basal poles, for the AZ31B samples: (a) as-received, (b) 1 pass, (c) 2 passes, route B_C, and (d) 8 passes, route B_C with back-pressure. The experimental (I) and full PFs (II) are shown for each case.	232
80	The high-energy (HE) XRD in-plane pole distributions (IPPDs) for the three reflection planes (10.0), (00.2), and (10.1) of the ZK60 samples observed on flow and top planes, before and after ECAP, 1 pass.	233
81	The theoretical modeling (red lines) are in good agreement with the experimental (open dots) LE-XRD profiles measured for the ZK60 alloy; the partial θ - 2θ scans show the maxima at <20.0>, <11.2>, and <20.1> for the (a) ZK60, as-received, and (b) ZK60, after compression CC.	234
82	The XRD profile (red lines) obtained from the whole-pattern fitting are in good agreement with the experimental (open dots) profile measured for the ZK60 alloy after one pass of ECAP at 260^0C; the partial θ - 2θ scan show the maxima at <20.0>, <11.2>, and <20.1>.	235
83	The partially-ECAP-ed billet of the Mg alloy, ZK60, with the flow lines network of the stream and cross lines (1 × 1 mm), and the locations (a through g) for the pole-figure mapping. The billet was deformed in a round-corner die, with the angular span of its roundness of $2\psi = 60^0$. The intersection between the channels is OO′.	236
84	The two-mirror parts of the partially ECAP-deformed ZK60 billet cut in horizontal and vertical bars (1.25 mm each) for the high-energy (HE) XRD mapping. The horizontal bars allow the measurements of the cross-undeformed and top-deformed planes, when rotated 90^0, and	236

the vertical bars allow the measurements of the top-undeformed and cross-deformed planes, when rotated 90^0.

85 The low-energy (LE) XRD texture mapping of the ZK60 partially-deformed billet, ZK-CC-T, during the ECAP in one pass, at the locations defined in Figure 83: (a, b, and c) before ECAP, (d) at the intersection between the two channels, and (e and g) after ECAP. The shear-strain values, γ, were determined experimentally, and are taken from Ref. 65. 237

86a The HE-XRD IPPD mapping at the locations a through g (see Fig. 83) for the central stream line of the partially-deformed ZK60, ZK-CC-T, for three reflections, (10.0), (00.2), and (10.1), and on the flow plane of observations. The directions (defined in Fig. 25) before ECAP are XD, ND, and TD; the directions in the first channel are marked with ′, and in the second channel with ″. 238

86b The HE-XRD IPPD mapping at the locations a through g (see Fig. 83) for the central stream line of the partially-deformed ZK60, ZK-CC-T, for three reflections, (10.0), (00.2), and (10.1), and on the cross undeformed (a, b, and c) and top deformed (e, f, and g) planes of observations. The directions (defined in Fig. 25) before ECAP are XD, ND, and TD; the directions in the first channel are marked with ′, and in the second channel with ″. 239

86c The HE-XRD IPPD mapping at the locations a through g (see Fig. 83) for the central stream line of the partially-deformed ZK60, ZK-CC-T, for three reflections, (10.0), (00.2), and (10.1), and on the top undeformed (a, b, and c) and cross deformed (e, f, and g) planes of observations. The directions (defined in Fig. 25) before ECAP are XD, ND, and TD; the directions in the first channel are marked with ′, and in the second channel with ″. 240

87a The HE-XRD IPPD mapping at the locations a through g (see Fig. 83) for the central stream line of the partially-deformed ZK60, ZK-CC-F-F, for three reflections, (10.0), (00.2), and (10.1), and on the flow (undeformed and deformed) plane of observations. The directions (defined in Fig. 25) are XD, ND, and TD before ECAP; the directions in the first channel are marked with ′, and in the second channel with ″. 241

87b	The HE-XRD IPPD mapping at the locations a through g (see Fig. 83) for the central stream line of the partially-deformed ZK60, ZK-CC-F-H (H - the horizontal bars), for three reflections, (10.0), (00.2), and (10.1), recorded on the cross undeformed (a, b, and c) and top deformed (e, f, and g) planes of observations. The directions (defined in Fig. 25) are XD, ND, and TD before ECAP; the directions in the first channel are marked with ′, and in the second channel with ″.	242
87c	The HE-XRD IPPD mapping at the locations a through g (see Fig. 83) for the central stream line of the partially-deformed ZK60, ZK-CC-F-V (V - the vertical bars), for three reflections, (10.0), (00.2), and (10.1), and on the top undeformed (a, b, and c) and cross deformed (e, f, and g) planes of observations. The directions (defined in Fig. 25) are XD, ND, and TD before ECAP; the directions in the first channel are marked with′, and in the second channel with ″.	243
88a	The HE-XRD IPPD mapping at the locations a through g (see Fig. 83) for the central stream line of the partially-deformed ZK60, ZK-FF-T-F, for three reflections, (10.0), (00.2), and (10.1), and flow (undeformed and deformed) plane of observations. The directions (defined in Fig. 25) are XD, ND, and TD before ECAP; the directions in the first channel are marked with ′, and in the second channel with ″.	244
88b	The HE-XRD IPPD mapping at the locations a through g (see Fig. 83) for the central stream line of the partially-deformed ZK60, ZK-FF-T-H (H - horizontal bars), for three reflections, (10.0), (00.2), and (10.1), and on the cross undeformed (a, b, and c) and top deformed (e, f, and g) planes of observations. The directions (defined in Fig. 25) are XD, ND, and TD before ECAP; the directions in the first channel are marked with ′, and in the second channel with ″.	245
88c	(c) The HE-XRD IPPD mapping at the locations a through g (see Fig. 83) for the central stream line of the partially-deformed ZK60, ZK-CC-F, for three reflections, (10.0), (00.1), and (10.1), and on the top undeformed (a, b, and c) and cross deformed (e, f, and g) planes of observations. The directions (defined in Fig. 25) before ECAP are XD, ND, and TD; the directions in the first channel are marked with ′, and in the second channel with ″.	246
89	The HE-XRD IPPD mapping at the locations a through f (see Fig. 83) for the central stream line of the partially-deformed AZ31, AZ-CC-T-F, for three reflections, (10.0), (00.2), and (10.1), recorded on the flow (undeformed and deformed) plane of observations. The directions (defined in Fig. 25) are XD, ND, and TD before ECAP; the directions in the first channel are marked with ′, and in the second channel with″.	247

90 The HE-XRD IPPD mapping, following the central stream line (the locations a through g in Fig. 83) of the partially-deformed billet of AZ31, AZ-CC-T, on the flow plane, for three reflections, (10.0), (00.2), and (10.1). The billet was deformed in ECAP at 250^0, 2 passes, route B_C. The directions (defined in Fig. 25) are XD, ND, and TD before ECAP; the directions in the first channel are marked with ′, and in the second channel with ″. 248

91 The experimental lattice rotation as a function of the position on the billet (the locations a through g in Fig. 83) resulted from the HE-XRD IPPD data on the partially-ECAP-deformed ZK60 billets, ZK-CC-T and ZK-CC-F. The three texture components, C-01, C-02, and C-03 are shown for both billets, and the rigid-body rotation is given for comparison. The lattice rotations versus time are shown for the three cases: the c-axis parallel to the pressing direction, XD′, and perpendicular to the pressing directions, TD′ and ND′. 249

92 The temporal evolution of the lattice spin resulted from the HE-XRD measurements on the partially-ECAP-deformed ZK60 billets, ZK-CC-T and ZK-CC-F. The three texture components, C-01, C-02, and C-03, are produced during the ECAP deformation of the Mg alloy, ZK60, and the rigid-body spin is shown for comparison. The lattice spin versus time is shown for the three cases: the c-axis parallel to the pressing direction, XD′, and perpendicular to the pressing directions, TD′ and ND′. 250

Motto: Nature reveals herself slowly, teasing us with little glimpses of her beauty.

1. INTRODUCTION

Little is known about the human being. Altogether, humans want to fly and discover the universe. For this purpose they need materials science. A droplet of this science will be included in the present study. The questions to be answered are: (1) How to obtain ultrafine-grained (UFG) metals and composites, which are stronger, more ductile, with a longer fatigue life than their coarse counterparts? (2) How the materials deform under a severe plastic deformation, such as equal-channel-angular processing (ECAP)? (3) How to predict the plastic-deformation zone (PDZ) shape and size in ECAP? (4) How to interpret the response of the UFG materials to mechanical testing? (5) How the rolling, extrusion, or ECAP deformation textures influence the mechanical properties of the hexagonal-closed packed (HCP) structures, such as Mg-alloys? (6) How the nondestructive evaluations through X-ray or neutron-diffraction studies can help the understanding of the deformation mechanisms in ECAP? To accomplish these goals, experimental and theoretical studies were performed, knowing that the fundamental progress is just the reinterpretation of the basic ideas, and that the purpose of the models is not to fit the data but to sharpen the questions.

Different ECAP dies (solid versus split die, sharp-corner versus round-corner die) were designed and built. Various metals were deformed by ECAP at room and high temperatures, and the billets of pure metals (Cu, Al, and Pb), Al alloys (6061 Al matrix

and 6061 Al composite) and Mg-alloys (AZ31 and ZK60) were processed in both sharp-corner die and round-corner die.

Advanced characterization methods were used to assess the complex structures and novel thermo-mechanical properties of the alloys deformed in ECAP. The relationship among the processing, microstructures, and mechanical properties is studied on Mg-alloys, before and after the ECAP deformation. A double-feedback scheme is used for the experimental-theoretical validations, in order to optimize and implement the ECAP technology for producing materials with good mechanical properties, and to contribute to an in-depth understanding of the deformation mechanisms during the processing, or during the monotonic and cyclic loadings of the studied materials.

Equal-Channel-Angular Processing - Background. In the metal-forming industry, the processes, such as the rolling, drawing, or extrusion, can induce a plastic deformation into a workpiece, resulting in the grain refinement or the increased strength of materials, usually with a loss of ductility. However, these effects are collateral for the metal-forming processes. Purposely, by increasing the amount of the plastic deformation to produce UFG metals and composites, a great impact on the mechanical properties is expected. Two methods of the severe plastic deformation (SPD), equal-channel-angular processing (ECAP) [1-6], and high-pressure torsion (HPT) [7, 8], have the potential to improve both the strength and ductility. The main inconvenience of the HPT method is that it can deform small samples (12 mm × 20 mm × 1 mm) [7], while the ECAP deformation can produce large bulk nonporous billets (e.g., 55 mm in diameter and 100 mm in length) [9]. Very high strains without a geometrical change can be attained in

ECAP, because the billet can be pressed several times through a die with two intersecting channels of an equal cross-section. Therefore, engineering applications will benefit from the ECAP-deformed materials. Moreover, ECAP could replace extrusions or other steps prior to the forging operations, at lower costs. The ECAP technology is already successfully used for refining grains of many metallic alloys and composites down to 100 nm or less.

A successful ECAP deformation can be attained by controlling the influence of the processing parameters (die geometry, temperature, routes, induced strain, deformation rate, and back-pressure), and of the initial material properties (the composition, phase, yield stress, grain size, texture, etc.).

Segal and collaborators [1-6] first developed the ECAP technique as a method of materials processing by the severe-plastic deformation. These papers, including a US patent [3], define the ECAP technology as a deformation process by a simple shear, which produces a considerable grain refinement.

In the ECAP technique (Fig. 1),* a well-lubricated billet enters a vertical channel, and is pressed with a force, P, characteristic of the material, into a second channel with the same cross section, and usually at 90^0 relative to the first channel (called in the following 90^0-ECAP die). The coarse-grained billet is plastically deformed by the simple shear (the shearing plane formed by ABCD), and the UFG material is obtained at the exiting channel.

---

*Note: All tables and figures are located in the Appendix.

Two ECAP-die configurations are represented in Figure 2: a) the ECAP configuration with a sharp-corner die and the two channels at an angle, $\Phi = 90^0$, and with a single-shear plane, ABCD, and (b) the ECAP configuration with a round-corner die and the two channels at 120^0, and with the angular span, 2Ψ, which represents the plastic deformation zone (PDZ) extension, symmetrically placed relative to the intersection of the two ECAP channels. A large amount of strain can be induced by processing the same billet for a repetitive number of passes. The different routes or straining paths used in ECAP are shown in Figure 3: route A: no rotation; route B_A: alternate rotation of 90^0, and route B_C: consecutive rotation of 90^0; and route C: rotation of 180^0 of the billet between passes. The processing conditions during ECAP of different metals and composites are given in Table 1. The temperature during ECAP is ranging from room temperature to ~$1,000^0$C for hard-to-deform material such as Ti-6Al-4V [10]. The rate of the deformation varies from 0.5 to 25 mm/s, and different routes, A, B, and C are used.

Different classes of materials have been studied using the ECAP technology. Some novel properties (the grain size, ECAP specific microstructures, or mechanical properties) of the pure metals (such as Cu, Al, Ti, and W) [11-19], deformed by ECAP are presented in Table 2, for the Al alloys and composites [9, 20-34], in Table 3, for the Mg alloys [21,29,35-41] in Table 4, and for the Cu-, Fe-, Zn-, Ti alloys [42-48], in Table 5. The general trend for most of the materials is that ECAP resulted in a significant grain refinement, increased the ductility or even superplastic behavior, and/or to increased fracture toughness and hardness.

The most amazing combination of the strength and ductility was obtained for pure Cu deformed in 16 passes of ECAP [14]. However, the fatigue behavior of the UFG-Cu [12] subjected to low-cycle fatigue (strain control) showed a shorter life than coarse-grained (CG) materials, and a significant softening. Room-temperature strengthening was obtained on pure Ti [15]. Pure Al**,** ECAP-ed at room temperature [14], exhibits uniform equiaxed grains, and increased yield strength (YS).

The results on ***Al alloys*** and *composite*, presented in the Table 3, demonstrate that, after ECAP, these alloys present a Hall-Petch strengthening, but the ductility and toughness remain unchanged. A room-temperature strengthening was obtained on the 5056 Al-alloy [20-22], but the high-cycle fatigue testing of the UFG 5056 Al-alloy [20] exhibits a modest enhancement (10^7 as compared to 10^6 before ECAP) of the fatigue performance. An increased fatigue life in the low-cycle regime was observed on this material, and it is believed to be due to a higher resistance to the crack nucleation of UFG materials having a greater yield stress. The surface of the 5056 Al alloy subjected to the cyclic plastic deformation has slips at 45^0 to the loading axis, similar to the results of the ECAP-ed Cu [8]. An elongation of 1,900% (at 3.3 x 10^{-2} /s) for Zn-22Al after ECAP [15] was obtained. The addition of scandium in an ECAP-deformed Al-3%Mg alloy [23, 26, 32, 33] yielded an elongation of 2,280% at 400^0C and strain rate of 3.3 $\times 10^{-2}$ s^{-1}. This result was obtained because the requirement for achieving the superplasticity was met: a small grain size was retained through the presence of Al_3Sc precipitates at temperatures up to 477^0C.

Some properties of ***Mg alloys*** tested after ECAP [35-41] are presented in the Table 4. The grain-size evolution as a function of the number of ECAP passes shows a better stability when the ECAP temperature is lower and is combined with the back-pressure, as shown for the AZ31-alloy [49]. Comparing the extrusion with ECAP, it can be noted that a better elongation to failure after ECAP, ε = 371% [38, 50], was observed as compared to the extrusion (ε =220%) [39]. The values of the strain-rate sensitivity, m = 0.4, for ECAP [34], and m = 0.2, for the extrusion [35] suggest different deformation mechanisms for the two processes. The latest result of the superplastic behavior of the Mg alloy, ZK60 [51], gives an elongation of 1,400% after tensile testing of the cast/homogenized/ECAP-ed ZK60 alloy at 220^0C, and at the strain rate of 3×10^{-3}/s. The billets were processed using the back-pressure during ECAP, and a bimodal microstructure was detected. It has to be pointed out that for the same alloy, but with a rolling step before ECAP, the elongation, in the same testing conditions, dropped to 480%.

Some results on other materials, such as ***Cu*** [42, 43]**,** ***Fe*** [45, 46]**,** ***Zn*** [44]**,** ***Al-2%Fe*** [48]**,** ***and Ti alloys*** [47, 48]**,** are shown in the Table 5. An elongation of 900% (400^0C and 10^{-4} s^{-1}) was obtained for the Cu-Zn-Sn alloy subjected to ECAP [42]. An increased yield stress of 910 MPa, as compared to 600 MPa for the undeformed materials, was obtained for TiNi intermetallic samples. This fact confirms the great potential of the ECAP technology in processing hard-to-deform materials with better thermo-mechanical properties.

In addition to the grain refinement, ECAP may induce some other changes in the microstructure, such as the increase or decrease in the root-mean-squared (r.m.s) elastic microstrain and effective-domain size, as well as the development of crystallographic textures. X-ray diffraction profiles [52] and pole-figure measurements have been successfully used to study the microstructural evolutions of some ECAP-deformed materials. Investigations of the ECAP textures showed specific preferential orientations, for different crystallographic structures, including the face-centered-cubic (FCC) copper [12, 53], body-centered-cubic (BCC) iron [54], or hexagonal-close-packed (HCP) magnesium [29].

To conclude the benefits of the ECAP technology, it has to be pointed out that: (a) a significant grain refinement is obtained for most of the materials, (b) better strength and/or better ductility are obtained in UFG-ECAP-ed materials; (c) the superplastic behavior at low temperatures and high strain rates is met for a large class of materials, (d) in the ECAP structures, the combination of the small grains with a high-density of dislocations can yield the simultaneous increase of both the strength and ductility.

Critical Issues. The main effect of the ECAP on microstructures is the grain-size refinement. The dislocation-mediated plasticity has been successful in explaining the mechanical properties of polycrystalline aggregates with coarse and fine grain sizes down to the UFG level having the grain size, d, in the range from 100 to 1,000 nm. Unless the grain-size distribution is inhomogeneous or bimodal, the hardness, the yield stress, and the strength of the materials with the same composition but different grain sizes will be inversely proportional to the square root of the grain size, according to the Hall-Petch

relationship. For nano-grained materials (d < 100 nm), the mechanisms of the plastic deformation become more complex, and many efforts are concentrated now on understanding the mechanical behaviors in this range of grain sizes. Given the greater number of the grain boundaries (GBs), the restrictions on the dislocations generation and their movement are higher. Therefore, features, such as small grains, uniformly distributed or not, with different sizes and morphologies, highly-distorted GBs and crystal lattices, the high density of defects, will trigger different deformation mechanisms in comparison with the coarse-grained materials [55-58]. The GBs are certainly more involved in the plastic deformation either as sources of dislocations or partial dislocations, or for providing sites for slip and grain rotation, which are enhanced by the increased atomic activity in GBs [57, 58]. As a result, the Hall-Petch relationship ceases to work, and the expected increase of strength in nanomaterials is steadily diminished. An inverse Hall-Petch behavior was observed at very small nano-grain sizes (< 10 nm) [56]. Moreover, the UFG materials have lower activation energies for the grain growth. Therefore, they grow faster. Usually, ECAP is performed at high temperatures in order to prevent billet cracking, and, consequently, a continuous dynamic recrystallization (CDR) is accompanying the deformation mechanisms in ECAP.

As pointed out by Segal, the inventor of ECAP, a simple shear seems to dominate the macromechanical-deformation mode of ECAP [2, 4]. For a sharp-corner die, Segal's model defines a simple-shear plane, where most of the plastic deformation takes place. ECAP assimilates to orthogonal cutting, which also shows the shear-plane localized deformation [59]. From this point of view, the ECAP can be assigned as a cutting

process constrained by the channel walls. The macromechanics of the chip deformation during cutting was extensively studied, based on the slip-line-field (SLF) theory [60-64]. However, the macromechanics of the plastic deformation associated with ECAP uses rough approximations, including the difficulty to predict the shear-strain heterogeneities. The SLF models for the plastic-deformation zone (PDZ) developed for ECAP [6] include stress singularities and a limited range of validity. Therefore, further studies to establish the modeling relations with the die design, and friction conditions are needed, in order to predict the PDZ and the induced shear-strain in ECAP. The shape of PDZ in a steady-state deformation regime does not follow a close contact between the billet and the die. There are two PDZ configurations often observed experimentally, which involve either the formation of a ″dead metal″ zone at the outer corner of the die, or the existence of a free surface in the same zone [65]. These circumstances have to be investigated in more detail, as well as the resulting inhomogeneities of the induced strain. Moreover, the theoretical predictions of the PDZ shape and size during the ECAP deformation, as well as the induced shear-strain have to be validated experimentally on partially-deformed specimens. The analysis of scribed samples allows the mapping of the plastic strain in partially-deformed specimens for cutting, extrusion, and ECAP [55,66-68]. Additionally, a comprehensive mapping of the material parameters, such as the grain size, grain-boundary state, microhardness, elastic microstrain, and texture, can be conducted. By decomposing the large deformation process into fine steps, a spatial-temporal evolution of the mapped material parameter can be obtained. Although the mapping of the induced plastic strain cannot be continued in the multipass ECAP, the one-pass data can be used to predict the deformation for different straining paths. An equivalent strain [69] has to

be defined in a consistent way in order to characterize the multi-pass ECAP deformation, and to be related to the material behaviors.

In the present study, efforts will be concentrated on the specific deformation behaviors of the hexagonal-crystallographic structures of a Mg-based alloy. The deformation of the hexagonal-closed packed (HCP) polycrystalline materials became, recently, an important field of both the experimental and theoretical research, due to the contribution of deformation by twinning, which shows a significant change in the crystallographic texture even at small levels of the plastic deformation [70]. Therefore, the characteristic changes of the texture can be used as an indicator for the twinning mechanism of deformation, and a different behavior is expected in severe-plastic-deformation conditions, such as ECAP. The analysis of the mutual influence between the ECAP deformation and textures is expected to provide the valuable information for the general understanding of the plastic deformation of the HCP structures, and for designing the optimal deformation paths to fabricate UFG materials.

The objectives of the present work: (a) Theoretical and experimental studies of the ECAP macromechanics; (b) Fabrication of the UFG Al- and Mg-alloys, using ECAP deformation at room and high temperatures ; (c) Assessment of the ECAP straining paths (or routes) and cumulative strains (or numbers of passes) effects on microstructural parameters, such as the grain size, preferential crystallographic orientations (or textures), or elastic microstrains; (d) Investigations of the mutual interactions of crystallographic textures and ECAP deformation mechanisms in the HCP structures of Mg alloys; (e) Studies of the mechanical behavior (strength, ductility, fatigue, and/or superplasticity) of

the ECAP-ed Al- and Mg-alloys at room and high temperatures using monotonic (tensile/compressive) and cyclic loading (fatigue), and relating the novel properties to the ECAP-deformed microstructures.

Contributions [29,37,49,50,65,77,78,79,112,148,151,154]. Although ECAP has been a well-researched topic in materials science over the last decade, the macromechanical description of the plastic deformation associated with this process uses rough approximations, including the ability to predict the spatial shear-strain heterogeneities. The SLF theories developed for cutting, due to their obvious similarity to ECAP, are expected to impact the general understanding in this field. New insights are most likely to emerge from a careful analysis of the SLF theory designed to describe the steady-state ECAP deformation with an analogy to orthogonal cutting. *A theoretical model for the plastic-deformation zone (PDZ) in an ECAP-ed billet with a free surface* is provided. The model predicts the shear-stain nonhomogeneity across the ECAP-deformed billet. The deformation gradient was used to describe the ECAP severe plastic deformation, and the theoretical shear-strain values, derived from four PDZ models, were compared to the experimental data obtained on partially-deformed specimens. The range of the validity of each model is discussed. *The mapping of the plastic strain* in partially-deformed specimens, together with a comprehensive mapping of material parameters, such as the grain size, microhardness, elastic microstrain, and texture, constitutes a new approach for understanding the details of the ECAP deformation mechanisms *by decomposing the large deformation process into fine steps*. First results of the *lattice rotation during ECAP of Mg alloys are reported.* Knowing the lattice rotation, the plastic spin can be

further deduced, and can be applied to describe the evolution of the anisotropic yield function.

Recently, the deformation of polycrystalline materials with hexagonal structures became an important field of both experimental and theoretical research, due to their special deformation features, which show a significant change in the crystallographic texture even at small levels of the plastic deformation. The studies of the close relationship between the crystallographic textures and the deformation mechanisms in ECAP, including the dislocation slip, twinning, and/or recovery/recrystallization, showed that they reciprocally influence each other, and, consequently, determine the mechanical behavior of the wrought materials [148,151]. It was established that the tension-compression asymmetry of the studied Mg alloys, AZ31 and ZK60, is due to the twinning activity, and is orientation dependent. The evidence of *the deformation by twinning under compression and in early stage of the ECAP deformation of Mg alloys is provided* [151]. The XRD peak-broadening analyses of compressed samples at different temperatures, allowed obtaining *the volume-averaged coherent domain sizes, the elastic microstrain* evolutions*, the dislocations density, ρ,* and the percentage of the dislocation debris contributing to the deformation for the <a>, <a + c>, and <c>-types of dislocations, corresponding to the three orientations of the Burgers vectors. Grain-orientation effects were found to influence the fatigue behavior of the Mg alloys. In this regard, for tailoring the mechanical properties, specific *textures prior ECAP*, as well as, the most efficient *processing path* for the ECAP deformation have to be considered.

2. ECAP MACROMECHANICS

2.1 Die Design and Processing Parameters

In designing the ECAP equipment, some important factors are to be considered: (a) assure an uniform plastic deformation, given the fact that in ECAP, large bulk billets can be processed; (b) attain the efficiency of the process, i.e., an efficient grain refinement; (c) control the plastic-deformation zone (PDZ), shape and size depending on the die configuration; (d) enable the die ability to process the billet by repetitive pressing, because a multipass ECAP induces, on one hand, a large amount of strains, and on the other hand, results in the microstructure stability. The encountered difficulties, while using the ECAP technology, are related to the hardening/softening behavior specific to the material, to the shear localization, or other factors resulting in the strain nonuniformity and microstructural instability. The friction, the back-pressure, and the material constitutive behavior determine the shape and stability of the plastic zone located at the intersection of the two channels. Generally, the billet does not fill the outer die corner, and a strong inhomogeneity of the plastic flow appears at the outer corner of the die. However, by reducing the friction, increasing the back-pressure, and choosing the appropriate strain rate/temperature conditions, the inhomogeneity of the induced shear strain can be corrected.

Die design. The ECAP-die design and the fabrication of the lab-scale ECAP for processing metals and composites at room and high temperatures were pursued to minimize the induced-strain inhomogeneities in the bulk of the billet and the shear

localization. The dies were designed to be mounted on the pressing equipment (Interlaken-200 kip), which has the loading capacities ranging from 1,000 to 2,500 kN (or even more for harder materials), a remote control, a data acquisition system, a dedicated software, and is able to provide a controlled pressing speed of the billets through the die.

Different die configurations have been designed and built, and few schematics are given in Figures 4 to 8. The most successful construction solution for the sharp-corner die is based on the design from Figure 6. The analysis of certain similarities between the ECAP and orthogonal cutting suggested a new design, which is at the development stage: *the symmetric ECAP die.* This die is under construction, and few schematics are presented in Figures 7 and 8. The components of the symmetric die are presented in Figure 7: the main body, the guiding and filler plates for the two billets holder, and the cutting plates. The die is designed to be mounted on the Interlaken pressing machine, and is moving up with a constant pressing speed. The filler plates hold the two billets, the guiding plates, and the cutting tool through the dowel pins. The guiding plates are in contact with the two billets, forming two lateral walls of the entrance channel and two top walls of the exiting channel. The plunger is mounted on the upper grip that is pushing the billets holder. The cutting plates**,** which are at the same time the bottom of the exiting channel, constrain the billets to enter the second channel at an angle, which can be varied from 90^0 to 120^0 relative to the first channel. During the processing, the holder for the two billets is pushed by the upper plunger, and slides through the guiding plates and the cutting tool, while the bottom grip is moving up together with the ECAP die. The locations for the cartridges, necessary for the processing at high temperatures (25^0C and

400^0C) are also included in the die design. The assembly of the symmetric ECAP-die is presented in Figure 8, and the main characteristics are: (i) the die is able to process two billets at once, and the symmetry in positioning the two billets is assuring a uniform distribution of the load during the deformation, (ii) the die allows for flexible angles between the two channels ranging from 90º to 120º, (iii) the die can process billets with the square profile varying from 9.5 × 9.5 to 18 × 18 mm, and with the length of 102 mm, (iv) the die contains few interchangeable parts allowing for a very good flexibility in changing the billet shape, size, and the angle between the two channels (90^0 to 120^0), and (v) the processing can be performed at room and high temperatures up to 400^0C.

The sharp-corner die, built from special steel for tools, is presented in the Figures 9 (the parts of the die) and 10 (the assembly of the die). The die has two modules allowing an easy removal of the billet after the processing, and a sliding floor, moving together with the billet in the second channel of the die, which minimizes the friction between the die walls and the billet. The die was designed to be mounted on the hydraulic pressing machine, Interlaken-220kip, available at UT. The die has the following characteristics: (i) is composed of a number of parts, with the two channels intersecting at 90º, containing a sharp-outer corner and a sliding floor in the second channel; (ii) can process a billet with the size of 12.7 × 12.7 × 102 mm; (iii) is functioning at temperatures up to 400 ºC; (iv) the load applied to press the billet inside the die can be varied, but cannot be greater than 1.5 tons/cm^2; and (v) the pressing speed is kept constant during the deformation; usually, a pressing speed of 0.5 mm/s was used.

In collaboration with the Central South University, Changsha, Hunan [71] *a round-corner die* was built (Fig. 11). The die characteristics are: (i) it is a solid die, with the two channels intersecting at 90º; the die has a roundness at the outer corner, with an angular span of 60º; (ii) the die can process a billet with the size of 9.5 × 9.5 × 51 mm, and (iii) the die is capable of functioning at temperatures up to 400 ºC. Similar to the sharp-corner die, the load is limited at a maximum value of 1.5 tons/cm^2, and the pressing speed of 0.5 mm/s is used.

The ECAP equipment setup represented in Figure 12 shows the sharp-corner die mounted on the hydraulic pressing machine, the data-acquisition system, the remote control, and the billet, which is pressed by a plunger from the first into the second channel of the die. A careful alignment before processing is required, and for the processing at high temperatures it is necessary to stabilize the temperature of the die for 20 - 30 minutes.

By adjusting the processing conditions, such as the temperature, billet configuration, pressing route, etc., a refined, stable and uniform grain structure of the material will be obtained. If the die configuration and loading conditions allow, it is desirable that the ECAP temperature does not surpass 0.5 of the melting temperature, T_m, and it has to be as low as possible in order to avoid the recrystallization, or even the grain growth.

Pure metals, including Al and Cu, can be processed at room temperature, due to their good ductility. For alloys, the ECAP deformation needs to be performed at high temperatures (90ºC to 600ºC), because the lower flow stress of a material at elevated

temperatures permits larger strain rates to be achieved, and, consequently, a lower power and shorter processing time.

Using both configurations, sharp-corner and round-corner ECAP dies, the billets of pure metals (Pb, Al, and Cu) and of Al- and Mg-alloys (6061 Al, AZ31B, and ZK60) were scribed and partially-deformed at room temperature (see Fig. 13) and at 250^0C (see Fig. 14), respectively. These billets were used for studying the deformation behavior of these materials during ECAP, including the mapping of the shear strain and of the texture for billets cut with different orientations relative to the working direction. Fully-processed billets were also produced in one and two passes of ECAP, and further used for mechanical testing.

2.2 Plastic-Deformation Zone (PDZ) in ECAP: Theoretical Modeling

Reviewing the latest results for the strain induced during ECAP, one can find two ways for the macroscopic strain calculations: the SLF theory [1-5] and finite-element modeling (FEM) [72-76]. The strain and strain-rate are deduced using both the SLF theory and FEM, but the results show deviations from the real-materials behavior due to the ideal cases considered and approximations, such as the rigid body, perfect-plastic material, or friction conditions. Predicting the microstructural changes during ECAP requires reliable macroscopic strain and strain-rate data. This fact is consequential for comparing the ECAP deformation with other processes. Therefore, the starting point of the ECAP deformation analysis will be the theoretical modeling of the plastic deformation in ECAP. Although ECAP has been a well-researched topic in the materials science over the last

decade, the macromechanical description of the plastic deformation associated with this process uses rough approximations, or has no ability to predict the spatial shear-strain heterogeneities. The present analysis, based on the SLF theory, is designed to describe the steady-state ECAP deformation with an analogy to orthogonal cutting (Section 2.2.1).

Four models for predicting the PDZ in ECAP have been developed [2, 4, 65, 77-82]: (a) the single-plane (SP-PDZ) model for a sharp-corner die configuration; (b) the ψ-PDZ, or a round-corner fan model, (c) the partial-split PDZ (PS-PDZ) model, and (d) the full-split PDZ (FS-PDZ) model. These models will be described in the following, and will be compared to the experimental observations on partially-ECAP-deformed specimens (Section 2.2.2).

2.2.1 ECAP Similarities with Orthogonal Cutting

The ECAP technology, as well as orthogonal cutting, involves high strain rates, when hardening has a limited influence on the plastic flow, and the perfectly plastic flow assumption provides a good approximation [62]. Given these conditions, the slip-line plane-strain approach can be used to study the steady-state pattern of the flow in the shear-deformation zone.

The SLF theory has been successful in describing the plastic deformation for ideally-chosen conditions, such as under plane strain and at a constant speed [61]. In the rigid-plastic approach (RPA), the material is moving as a rigid body except a plastic-deformation zone (PDZ), where the material can be considered as an incompressible fluid. The PDZ borders (or RPBs) are fully determined by the yield strength of the material

(usually the von Misses criterion). Then, the material is considered as perfectly rigid outside the PDZ, and perfectly plastic inside the PDZ.

Since the material could be considered as incompressible, the state of stress at each point is a pure-shear stress, τ, superimposed on a hydrostatic pressure, P. The two directions of the maximum shear stress are inclined at 45^0 relative to the principal stresses. The directions of the maximum shear stress coincide with those of the maximum shear strain-rate. Inside the PDZ, *"the two orthogonal families of curves, whose directions at every point coincide with those of the maximum shear rate, are named slip lines"* [61]. The two families of the slip lines will define a pair of right-handed axes at each point, including the greatest principal stresses in the first and third quadrants. If neglecting the friction, the SLF inside the PDZ should be surrounded by the slip lines or by a free surface. Thus, the RPB determines the SLF, and, in a steady flow case, the velocity component normal to the RPB must be compatible with the rigid motion outside the zone. On the other hand, the slip lines should intersect the free surface under an angle of 45^0 due to the circumstance that the principal stress perpendicular to the free surface needs to be zero.

The SLF concept was applied to describe many 2-D steady deformation processes, such as drawing and rolling. Each particular problem was solved by choosing intuitively a slip-line field, and was validated by the experiment. Among the metalworking processes, the most striking similarities with ECAP belong to the orthogonal cutting (Fig. 15a). In this process, a chip of metal is removed by a wedge-shaped tool, which is constrained to travel parallel to the surface at a chosen depth and at a right angle to the cutting edge. A first approximate model following the SLF approach is assuming [72] that the

deformation takes place on a single-shear plane. For a given tool angle relative to the working piece surface, the inclination angle, α (relative to the piece surface), determines the ratio of the chip thickness, *t*, to the depth of the cut, *T*. Let β denote the angle between the shear plane and the tool surface and, consequently, the tool angle is $\pi-\alpha-\beta$. If the elastic deformation is ignored, the chip ratio, t/T, is inversely related to the velocity ratio, v_0/v, due to the volume conservation, and can be written as follows:

$$\frac{t}{T}=\frac{\sin\beta}{\sin\alpha}=\frac{v_0}{v}. \tag{1}$$

The velocity, v_0, before the deformation becomes v after the deformation. Then, the tangential component of the velocity is discontinuous across the shear plane, and, from Figure 15a, the total shear-strain for cutting, γ_c, is: $\gamma_c=\frac{\Delta v}{v_n}$, where Δv is the velocity variation: $\Delta v=v_0\cos\alpha+v\cos\beta$, and v_n is the normal component of the velocity: $v_n=v_0\sin\alpha=v\sin\beta$. This value must be regarded as the limit of a narrow transition region in which the rate of the shear strain along the shear-plane direction is very large.

The material deformation when crossing the discontinuity boundary can be described using *the deformation-gradient matrix, F* [83]. If the shear plane, OO′, is chosen as a reference coordinate system, with the *x*-axis perpendicular to the shear plane, and the *y*-axis along the plane (Fig. 17b), the matrix, F_c, correlates the incremental coordinates, (*dx*, *dy*), of a material point before the deformation, with the new coordinates, (*dx′*, *dy′*), after the deformation: $\begin{bmatrix}dx'\\dy'\end{bmatrix}=F_c\times\begin{bmatrix}dx\\dy\end{bmatrix}$.

It follows that for cutting, the deformation-gradient matrix, F_c, and the shear strain, γ_c, will be:

$$F_c = \begin{bmatrix} 1 & 0 \\ \gamma_c & 1 \end{bmatrix}; \qquad \gamma_c = \cot\alpha + \cot\beta. \tag{2}$$

Following the same approach, the ideal ECAP deformation using a die with a sharp-outer corner can be considered as having the PDZ reduced to a single plane [1, 2], i.e., the shear plane, OO′, (Fig. 15b). Compared to the orthogonal cutting, the ECAP case is even simpler because the shear-plane position is fixed and should not be considered as a free parameter of the model. It follows then:

$$\alpha = \beta = \Phi;\ v = v_0;\ F_s = \begin{bmatrix} 1 & 0 \\ \gamma_0 & 1 \end{bmatrix} \tag{3}$$

where F_s is the deformation-gradient matrix for a sharp-corner ECAP die, and γ_0 is the shear strain. Then, Eq. (2) becomes:

$$\gamma_0 = 2\cot\Phi \tag{4}$$

as was deduced by Segal et al. [1, 2] for the shear strain, induced by a sharp-corner die in one pass of deformation.

A distinct point for the symmetrical shear-plane location in the ECAP case is that the alternate simple-shear direction, corresponding to the deformation decomposition, lies along the exiting direction due to the fulfillment of Eq. (4). This is why the simple shear

can be also considered in the exiting channel coordinate system [81] (the *x*-axis along the pressing direction), and the deformation-gradient matrix, F_p, becomes [78]:

$$F_p = \begin{bmatrix} 1 & \gamma_0 \\ 0 & 1 \end{bmatrix} . \tag{5}$$

In conclusion, the simple-shear plane concept, developed by Segal et al. [1, 2] for a sharp-corner die, is described by F_s, when the shear direction is along the shear plane. The concept for a round-corner die of Iwahashi et al. [81] is described by F_p, when the shear direction is along the pressing direction. These two concepts are simply two cases corresponding to the ECAP-deformation decomposition in two directions. Therefore, it can be observed that in the ECAP, the angle, between the main pure-shear direction and the exiting channel direction, is $\Phi/2$, as was derived before by Xia and Wang [84].

2.2.2 Four Models to Predict the Plastic-Deformation Zone (PDZ) in ECAP

For studying the plastic deformation in a two-dimensional (2-D) approximation, a die with a sharp-outer corner, O′ (Fig. 16a), and a die with a round-outer corner (Fig. 16b), are considered [78, 79]. In the former die-configuration, the plastic-deformation zone (PDZ) is formed by a single plane (OO′ in Fig. 16a) at the intersection between the two channels of the die. In the later case, the roundness at the outer corner of the die (arc AB) is encompassing an angular span, 2Ψ. The points, A and B, are at the intersection between the two channels, and the circle centered at the inner corner, O. The angle, 2Ψ, may vary between $0^0 \leq 2\Psi \leq 90^0 - \Phi$, but has an arbitrary value in Fig. 15b. A central span, AOB, is defining the PDZ for the round-corner die, and the planes, OA and OB in

Fig. 16b, are the rigid plastic boundaries (RPBs). At RPBs, the deformation process has discontinuities, i.e., a change of the flow-line direction occurs.

The models assuming different shapes for the PDZ [6, 79-81], as shown in Figure 17, are mainly based on the experimental evidence of a significant roundness of the billet at the outer corner of the die [79], or the intentional design of the ECAP die with a round-outer corner [81]. From these models, the shear strain and equivalent strain in ECAP can be calculated. Each model assumes more or less ideal conditions for the plastic deformation during ECAP, and, therefore, has a limited range of validity. The real friction conditions or the material-specific behavior (hardening/softening) will be the main factors for the deviations from the theoretical predictions.

The models available in literature to predict the PDZ in ECAP: the single-shear plane (AO) model, or the SP-PDZ [Fig. 17, the shearing-fan model or Ψ-PDZ (AOB in Fig. 17b), the partial-split model or PS-PDZ (the shearing plane, MO, and splitting, MAB in Fig. 17c), and the full-split model or FS-PDZ (the shearing fan, MON, and splitting, AMNB in Fig. 17d) will be described in the following.

a) Single-plane PDZ, SP-PDZ model. [1-4] Among the first attempts to apply the SLF theory to the orthogonal cutting and ECAP deformations were the shear-plane models proposed by Merchant [59] and by Segal et al. [2, 4], respectively. Segal's model reduces the PDZ to a single plane (SP), defining a straight rigid-plastic boundary (RPB), which separates two zones of a rigid body movement. In this SP-PDZ model, a discontinuity in the velocity direction at RPB is induced, and a simple-shear deformation

along RPB occurs. Given the condition of a very large strain induced in ECAP, the deformation-gradient matrix [78, 79] was used to describe the momentary state of a unit element during the deformation. A total apparent shear, γ_T, is defined in Eq. (4) for the SP-PDZ model [2]. The model has a limited range of validity, and it can be shown that the SP-PZD model is not a stable solution except in the frictionless 90^0 case.

b) Shearing fan, Ψ–PDZ model [81]. A round-corner fan model (Ψ-PDZ model) [81] allows the PDZ to extend over the whole angular range, 2Ψ, corresponding to the roundness of the billet (Fig. 17b). The material deformation starts with a simple shear upon entering RPB, and continues with an incremental simple shear, tangential to the circular slip lines centered at the inner corner of the die. Finally, another simple shear, along the exiting RPB, occurs. This model predicts a constant deformation gradient across the billet, similar to the SP-PDZ model. In both cases, the total deformation of the unit material element can be represented as an apparent simple shear along the exiting channel axis. But this representation doesn't take into account the deformation history. It is shown that the SP-PDZ model can be adjusted for describing the friction influence through the formation of a ″dead-metal″ zone, but is not valid for the formation of a free surface, which was often noticed at the outer corner of the die.

Before presenting the other two models, which are introducing curved RPBs for the PDZ to describe the ECAP deformation macromechanics, it is necessary to analyze the equivalent strain evaluations, and some experimental and FEM results.

c) Equivalent strain in ECAP. The state of stresses inside the PDZ belongs to a yield locus. The most often employed criterion is the von Misses yield locus for isotropic materials:

$$\frac{1}{2}\left(\sigma_{xx}-\sigma_{yy}\right)^2+\frac{1}{2}\left(\sigma_{yy}-\sigma_{zz}\right)^2+\frac{1}{2}\left(\sigma_{zz}-\sigma_{xx}\right)^2+3\sigma_{xy}^2+3\sigma_{yz}^2+3\sigma_{zx}^2=Y^2 \tag{6}$$

where σ_{ij}, with $i,j \in \{x,y,z\}$ are the components of the stress tensor, and Y is the yield stress in the uniaxial tension or compression. With the above definition of the yield locus, an equivalent stress, σ_{eq}, can be defined, since the material behavior in different loading conditions depends only on the following state average [14]:

$$\sigma_{eq}=\sqrt{\frac{1}{2}\left[\left(\sigma_{xx}-\sigma_{yy}\right)^2+\left(\sigma_{yy}-\sigma_{zz}\right)^2+\left(\sigma_{zz}-\sigma_{xx}\right)^2\right]+3\left[\sigma_{xy}^2+\sigma_{yz}^2+\sigma_{zx}^2\right]} \tag{7}$$

For isotropic materials, a set of equations relate the components of the strain increment tensor to those of the stress tensor [85]:

$$\begin{aligned}
d\varepsilon_{xx}&=\left[\sigma_{xx}-\frac{1}{2}\left(\sigma_{yy}+\sigma_{zz}\right)\right]d\lambda; \quad d\varepsilon_{xy}=\frac{3}{2}\sigma_{xy}d\lambda;\\
d\varepsilon_{yy}&=\left[\sigma_{yy}-\frac{1}{2}\left(\sigma_{zz}+\sigma_{xx}\right)\right]d\lambda; \quad d\varepsilon_{yz}=\frac{3}{2}\sigma_{yz}d\lambda;\\
d\varepsilon_{zz}&=\left[\sigma_{zz}-\frac{1}{2}\left(\sigma_{xx}+\sigma_{yy}\right)\right]d\lambda; \quad d\varepsilon_{zx}=\frac{3}{2}\sigma_{zx}d\lambda.
\end{aligned} \tag{8}$$

The increment, $d\lambda$, depends on the shape of the hardness state of the material, and shows an unbounded increase when considering perfect plastic materials, but even so, the

proportionality, prescribed by Eqs. (8), among the different strain components ($d\varepsilon_{xx}$, $d\varepsilon_{yy}$, $d\varepsilon_{zz}$, etc.) must be always satisfied. Consequently, the work increment, *dW*, for any state of stresses can be described as a product of the equivalent strain and a corresponding equivalent strain increment [85]:

$$dW = \sigma_{xx}d\varepsilon_{xx} + \sigma_{yy}d\varepsilon_{yy} + \sigma_{zz}d\varepsilon_{zz} + 2\sigma_{xy}d\varepsilon_{xy} + 2\sigma_{yz}d\varepsilon_{yz} + 2\sigma_{zx}d\varepsilon_{zx} = \left(\sigma_{eq}\right)^2 d\lambda = \sigma_{eq}d\varepsilon_{eq} \quad (9)$$

$$d\varepsilon_{eq} = \sqrt{\frac{2}{9}\left[\left(d\varepsilon_{xx} - d\varepsilon_{yy}\right)^2 + \left(d\varepsilon_{yy} - d\varepsilon_{zz}\right)^2 + \left(d\varepsilon_{zz} - d\varepsilon_{xx}\right)^2\right] + \frac{4}{3}\left[d\varepsilon_{xy}^2 + d\varepsilon_{yz}^2 + d\varepsilon_{zx}^2\right]}. \quad (10)$$

For conditions of proportional straining, in which the ratio between the components of the strain increment tensor remains fixed during the deformation process, the differential signs may be eliminated in Eq. (10), and a total equivalent strain can be defined using the same expression. For the non-proportional straining, the total equivalent strain can be obtained only by integrating the equivalent strain increment over the strain path characterizing the specific deformation process.

The equivalent-strain evaluations for one pass and multipass ECAP deformation [1, 2, 87] need to be systemized and redefined to some extent. To accomplish this task, the strain tensor needs to be defined for large deformations starting from the deformation-gradient matrix, F. The symmetric stretch tensor, *U*, should be defined first as follows [72]:

$$U^2 = F^T \times F \quad (11)$$

where F and F^T are the deformation-gradient matrix, and the transposed matrix, respectively. Then, the strain tensor can be defined in many ways. An usual approach corresponds to the one-dimensional (1-D) engineering strain (Green strain) [83]:

$$E = \frac{1}{2}\left(U^2 - I\right). \tag{12}$$

Using Eq. (2) or (5), $U^2 = \begin{bmatrix} 1 & \gamma \\ \gamma & 1+\gamma^2 \end{bmatrix}$ is obtained, and replacing the terms in Eq. (12), the strain tensor, E, results in:

$$E = \begin{bmatrix} 0 & \frac{\gamma_0}{2} \\ \frac{\gamma_0}{2} & \frac{\gamma_0^2}{2} \end{bmatrix}. \tag{13}$$

The incremental strain tensor will retain only the non-diagonal terms: $d\varepsilon_{xy} = \frac{d\gamma}{2}$. Assuming a proportional-shearing process, the equivalent engineering-strain, ε_{eq}^{eng}, can be calculated by combining Eqs. (5) and (11):

$$\varepsilon_{eq}^{eng} = \frac{2}{\sqrt{3}}\cot\Phi. \tag{14}$$

Then, using the strain tensor defined in Eq. (12), the equivalent engineering-strain induced in one pass of the ECAP deformation (Eq. 14), previously deduced by Segal et al. [1, 2], is obtained.

An alternate expression for the equivalent strain [83] is using another definition for the strain tensor (Hencky strain):

$$E = \ln U \tag{15}$$

i.e., the tensor, U, is reduced to the principal axes. The eigenvalues, λ, of the matrix, U, are calculated from $|U^2 - \lambda^2 I| = 0$, and, then, the strain, $\varepsilon = ln\ \lambda$, is obtained. Assuming a proportional straining during the ECAP deformation, the strain components will be: $\varepsilon_{xx} = \varepsilon$, $\varepsilon_{yy} = -\varepsilon$, $\varepsilon_{zz} = \varepsilon_{xy} = \varepsilon_{yz} = \varepsilon_{zx} = 0$, and replacing these values in Eq. (10), the equivalent true-strain, ε_{eq}^{true}, becomes:

$$\varepsilon_{eq}^{true} = \frac{2}{\sqrt{3}} \ln\left(\frac{1+\cos\Phi}{\sin\Phi}\right). \tag{16}$$

Equation (16) was also deduced by Xia and Wang [84] using the principal-strain concept. Then, the total equivalent strains calculated from the Equations (14) and (16) can be defined as the engineering and true equivalent strains, respectively, if the deformation is a simple shear along the intersection plane between the two channels of the ECAP die. In the following, these issues and the accuracy of this approach are discussed.

d) Explanations for the SP-PDZ and Ψ–PDZ models. The results for the Ψ–PDZ model, which include some original findings, will be discussed in the following.

In a round-corner ECAP die (Fig. 16b), the PDZ is replacing the single-shear plane, OO′, defined in Figure 16a for a sharp-corner die. The simplest way to account for a spatially-extended PDZ and for a billet roundness at the outer-corner of the die is to introduce two

straight RPBs [77, 81], (AO and BO in Fig. 16b), and, then, the PDZ size/shape will be AOB. In this geometry, any slip line from the corresponding slip-line family is also straight, and the slip lines belonging to the orthogonal family are concentric circular arcs (see the right insert in Fig. 16b). A natural choice for the center of those circular slip lines could be the inner corner of the die, O. The roundness of the outer free surface of the billet could be an element of the die design or could be a billet deformation effect. In this simple model, the angular span, 2Ψ, is symmetric relative to the line, OO′. The total shear strain, γ_T, corresponding to this PDZ shape in a round-corner die, was estimated first by Iwahashi et al. [81], and the formula:

$$\gamma_T = 2\cot(\Phi + \Psi) + \frac{2\Psi}{\sin(\Phi + \Psi)} \tag{17}$$

was almost unanimously accepted as a basic guide mark in the ECAP literature. However, Eq. (17) was deduced by considering that the velocity of a material point changes its direction, but preserves its size when crossing the RPB. Using a rigorous analysis, this assumption demands the existence of a tensile strain, when entering RPB, and a compressive strain for exiting from RPB [79]. This is not in agreement with the SLF theory, which always stipulates for the conservation of the material-specific volume [61], during the plastic deformation, and, as a consequence, the conservation of the normal to the RPB velocity component.

When crossing RPB at the entrance in PDZ, the material is subjected to a large simple-shear deformation similar to that described by Eq. (4). In this particular case: $\alpha = \Phi + \Psi$

and $\beta = 90^0$, then $\gamma = \cot(\Phi + \Psi)$. The problem arises when the deformation is described in the coordinate reference having one axis along the tangent to the circular slip lines (tangent to the arc AB family in Fig. 17b). In these coordinates, the deformation is no more a simple shear, and the deformation-gradient matrix, F_{P1}, when crossing the RPB, becomes:

$$F_{P1} = \begin{bmatrix} \sin(\Phi + \Psi) & \gamma \sin(\Phi + \Psi) \\ 0 & 1/\sin(\Phi + \Psi) \end{bmatrix}. \tag{18}$$

The deformation inside the PDZ can be described using the following deformation-gradient matrix [78]:

$$F_{P2} = \begin{bmatrix} 1 & 2\Psi \\ 0 & 1 \end{bmatrix} \tag{19}$$

and the deformation for exiting from RPB can be described in a similar way as for the entrance in RPB:

$$F_{P3} = \begin{bmatrix} 1/\sin(\Phi + \Psi) & \gamma \sin(\Phi + \Psi) \\ 0 & \sin(\Phi + \Psi) \end{bmatrix}. \tag{20}$$

It can be observed that comparing with the results from Ref. [78], only the matrix, F_{P2}, has the same expression as Eq. (19) [78], while F_{P1} and F_{P3} change when the condition for the volume conservation from Eq. (1) is applied. The total deformation-gradient matrix, F_T, becomes:

$$F_T = \begin{bmatrix} 1 & 2\gamma + 2\Psi / \sin^2(\Phi + \Psi) \\ 0 & 1 \end{bmatrix}. \tag{21}$$

This result is formally equivalent to a simple shear along the exiting-channel direction as obtained by Iwahashi et al. [81], but the total shear is different from Eq. (17):

$$\gamma_T = 2\cot(\Phi+\Psi)+\frac{2\Psi}{\sin^2(\Phi+\Psi)}. \tag{22}$$

The difference is a consequence of the conservation of the velocity component normal to RPB. However, Eq. (22) can be used only for determining the total deformation of the material element. For the equivalent-strain evaluation, each deformation step is considered separately: crossing RPB at the entrance in PDZ, passing through PDZ and crossing RPB at the exit from PDZ (Fig. 17b). Equations (12) and (15) for the equivalent engineering- and true-strains, respectively, become:

$$\varepsilon_{eq}^{eng} = \frac{2}{\sqrt{3}}\left[\cot(\Phi+\Psi)+\Psi\right] \tag{23}$$

$$\boldsymbol{\varepsilon_{eq}^{true}} = \frac{2}{\sqrt{3}}\left[\ln\left(\frac{1+\cos(\Phi+\Psi)}{\sin(\Phi+\Psi)}\right)+\ln\left(\sqrt{1+\Psi^2}+\Psi\right)\right]. \tag{24}$$

Another equation, proposed by Goforth et al. [86] for the total shear strain:

$$\gamma_T^{eq} = 2\cot\left(\Phi+\Psi\right)+2\Psi \tag{25}$$

should be considered as an ″equivalent″ shear, as it can be used for determining the equivalent strain in ECAP from the previously accepted expression:

$$\varepsilon_{eq}^{eng} = \frac{\gamma_T^{eq}}{\sqrt{3}} \ . \tag{26}$$

However, the two estimations deduced from Eqs. (17) and (25) differ by an amount of less than 5% [87].

e) Theory-experiment disagreement in ECAP. The deformation mechanics was studied by physical modeling on transparent ECAP dies using plasticine billets [88, 89]. In order to reveal the plastic deformation, striped two-color plasticine structures were used [89]. In these experiments, the shear-strain value, γ_T, relative to the exit-channel direction was directly determined from the strip-inclination angle, θ_s:

$$\gamma_T = \cot \theta_s \tag{27}$$

The measured θ_s-values at the center of the billet match well with the theoretical values given by Eq. (4), while the θ_s-values, away from the center, differ substantially from the predicted values, and show wavy strips [89]. If friction is involved in the deformation process, these deviations evidence the development of a complex strain state at the periphery of the billet. The total strain is reduced when moving from the center of the billet to the periphery. The main source of this effect was considered to be the friction between the billet and the die walls. Nevertheless, the uniform deformation does not take place for a round-outer corner die configuration even under ideal frictionless conditions [89]. The plasticine strips broaden while passing around the round corner, and then become compressed while exiting from the PDZ. In the second channel, the strips reach a characteristic curved shape [89]: without friction, forward curved strips, and with friction, backward-curved strips are formed.

The studies of the ECAP flow lines using markers on real materials show a similar inhomogeneous deformation across the billet. The usual procedure [1, 5, 90, 91] is to split along the billet in two parts, and scribe or point the grid on the interior surface. For example, the experiment on a 1100 Al alloy with a painted grid pattern has documented the formation of a free curved surface on the outer sharp corner of the die, causing a non-uniform deformation occupying 15% from the billet area [80]. Similar testing was done on Cu [1], Fe [91], and Ti [92].

FEM has been used for more comprehensive evaluations [73, 74, 90]. The first goal of these simulations was to investigate the effect of the die geometry on the strain evolution during ECAP. A surprising result was obtained by comparing the sharp and round corners [93]. In a sharp-corner die, the PDZ is localized in a thin band along the main shear plane, OO′ (Fig. 16a). In a round-corner die (Fig. 16b), the PDZ may have the AOB shape encompassing an angular span, 2Ψ, which characterizes the roundness of the outer corner [81, 78]. It is shown in the Figure 18 (reproduced from Ref. [94]) that the ECAP-induced strain diminishes when moving across the billet (from points O to B′). The zone with a lower strain extends on almost 40% of the thickness of the billet, and this amount decreases, if the angular span, 2Ψ, is decreasing [93]. The extended PDZ has already been considered by the SLF theory (see the insert in Fig. 16b), but the nonuniformity of the effective plastic strain, as obtained from the FEM [93], has not been predicted yet.

During the last few years, ECAP studies emphasized the detailed effects of the material constitutive behavior on the metal flow through the die [73, 74, 94]. The strain-

hardening behavior significantly increases the outer-corner gap (the material doesn't fill the outer corner of a sharp-corner die), and a large value of Ψ may form. Here, 2Ψ is the angular span of the billet roundness at the outer-corner, when deformed in a sharp-corner die. Both the experimental results and the FEM simulations exhibited a quite large value for the angular span, Ψ. For example, $2\Psi \sim 22^0$ in a quasi-perfect plastic material (6061Al), and $2\Psi \sim 51^0$ in a strain-hardened material (1100 Al) [73].

As a conclusion, both the experimental and FEM results have documented the presence of a certain roundness of the billet at the outer corner of the die (even for a sharp-corner die), and a significant inhomogeneity of the induced strain was obtained (see Fig. 18, reproduced and modified after Ref.[93]). These features have to be taken into account, while modeling the ECAP deformation. A refining of the SLF modeling will be presented in the following.

f) *Partial-Split, PS-PDZ, model.* An alternative way to allow a free round-surface involves the splitting of the straight RPB, corresponding to the SP-PDZ model, into two curved RPBs [6, 65, 77, 79]. The partial-split, PS-PDZ [65, 79] and full split, FS-PDZ [6], models were proposed, and they are represented schematically in Figures 17c and 17d, respectively. The velocity-boundary conditions at a curved RPB require a rigid rotation, which, eventually, could correspond to the rotation around the inner corner of the die. On the other hand, the two RPBs should intercept the circular boundary of the billet just at extremities, and at an angle of 45^o. These conditions fully determine the curvature of the RPBs and the angular range of the splitting, 2Ψ. A more detailed description of the PS-PDZ model for an ECAP-die having $2\Phi = 90^o$ is represented in

Figure 19. The angular range of the splitting, viewed from the rotation center, Q, should be 30^o. The location of the material unit element across the billet imposes the deformation mode that the unit element experiences. If the flow line intercepts the single straight RPB, MQ, the deformation corresponds to a simple shear as in the case of a SP-PDZ model. If the flow line intercepts the curved RPB, the material is subjected to a simple shear along the tangent to the entering RPB, MA, rotates as a rigid body until it reaches the second RPB, MB, and, while crossing this exiting RPB, another simple shear occurs. The total amount of the shear is determined by the local discontinuity in the velocity direction (see the right insert in Fig. 19), which can be represented as a function of angles, $\alpha = \Phi + \chi$ and $\beta = \chi - \delta$. The angles, δ and χ, are both functions of the coordinate across the billet.

The shearing process corresponds to the previously analyzed case of the orthogonal cutting (Fig. 15a), and Eqs. (1) and (2) are applicable when $\alpha = \Phi + \chi \; and \; \beta = \chi - \delta$, where χ and δ are the variable angles shown in Figure 19. Then, the total shear strain, γ, induced into the material after passing through the two circular RPBs, MA and MB, will depend on the transversal coordinate across the billet in a complex way:

$$\gamma = 2 \times \left[cot(\Phi + \chi) + tan(\chi - \delta) \right]. \qquad (28)$$

Using Eqs. (28) and (26), the reduction of the shear strain along the TQ direction (see Fig. 20) was calculated for a 90^0-ECAP die ($2\Phi = 90^0$). Figure 20 shows the equivalent strain calculated for each model as a function of the relative position, x/t*, where t* is the coordinate of the rotation center, Q, along the TQ direction. This reduction of the shear

strain, when moving from points, Q to T, at the periphery of the billet, is quite similar to the FEM (Fig. 18) results.

g) Full-Split Model. The PS-PDZ model could be considered too restrictive, as the angular span of the round corner is always a fixed amount from the inter-channel angle, 2Φ. A simple-shearing fan model does not describe correctly the case of the outer-round corner die. Segal [6] proposed a mixed model with a full-split PDZ, FS-PDZ model (Fig. 17d). The model contains a more elaborated slip-line field, combining the fan concept with the idea of the rigid-rotation zone near the outer-round corner. The slip-line field spanned from the inner toward the outer corner (MON span) with the opening, 2φ, and this field continues with two circular shearing surfaces, AM and BN, including the round-outer corner. Starting from the arc, MN, to the billet-die curved boundary, AB, the material describes a rigid rotation around O between two circular RPBs, MA and NB. The rigid-rotation zone extends the angular span of the PDZ to the nominal value, 2Ψ. The relation between the model span angle, ϕ, and the nominal value, Ψ, is controlled by the resolved-shear stress at the billet-die interface. It can be seen that $\phi = \Psi$ when the frictional-shear stress equalizes the shear-flow stress, and the model reduces to the shearing fan model.

Combining the results of the two models, Ψ-PDZ and PS-PDZ, the apparent shear, γ_T, for the FS-PDZ model was calculated. The total-shear strain, γ_{T1}, for the elements traveling through the rigid-rotation zone (as for the partial-split model) is:

$$\gamma_{T1} = 2 \times \left[\cot\left(\Phi + \varphi + \chi\right) + \tan\left(\chi - \delta\right) \right] \tag{29}$$

The total shear strain, γ_{T2}, for the elements traveling through the fan, MON (as for the round-corner shearing-fan model) is:

$$\gamma_{T2} = 2\cot\left(\Phi + \varphi\right) + \frac{2\varphi}{\sin^2\left(\Phi + \varphi\right)} \tag{30}$$

An abrupt decrease of the shear-strain value takes place when crossing the fan boundary, MN. The value of the jump is:

$$\Delta\gamma = 2\varphi / \sin^2\left(\Phi + \varphi\right) \tag{31}$$

This feature is illustrated in Figure 20. If the flow lines intercept the fan zone, the deformation starts with a simple shear upon entering RPB, at MO, and continues with an incremental simple shear, tangential to the circular slip lines centered at the inner corner of the die. Finally, another simple shear along the exiting RPB, at NO, occurs. The total apparent shear is given by an equation similar to that presented for the shearing-fan model. If the flow line intercepts the curved RPBs, the material, which is subjected to a simple shear along the tangent to the entering RPB, MA, rotates as a rigid body until it reaches the second RPB, NB, and, while crossing this exiting RPB, another simple shear occurs. In this case, the total-apparent shear is given by an equation similar to the equation for the partial-split-shearing model.

Both the experimental and FEM results have documented the presence of a certain roundness of the billet at the outer corner of the die (even for a sharp-corner die), and a significant inhomogeneity of the induced strain was obtained. These features have to be

taken into account, while modeling the ECAP deformation. The PS-PDZ and FS-PDZ models could predict this nonuniformity of deformation.

This kind of approach can potentially explain the observed total shear variation across the billet, and was refined by including a spatial extension of the split-shear zone. Recently, the analytical modeling of the material flow in the PDZ has received a new impetus mainly related to predicting the ECAP influence on textures [82, 95-98].

An analytical model, based on the assumption of a smooth deformation of the unit element, with no discontinuities at RPBs, is another way to model the plastic deformation during ECAP. Such a model could provide reasonable values for the strain rate, in accordance with the FEM simulations. The flow lines may not have a circular shape, rather a variable curvature. The extended PDZ is defined, similarly to the round-corner configuration, for the maximal value of the angular span, $2\Psi = 90^0 - 2\Phi$, but the amplitude of deformation is controlled by imposing a nonlinear variation of the flow-line curvature. The flow-line configuration determines the velocity-gradient field and the strain-rate tensor, as was recently shown for a similar model by Toth [97]. Then, this approach can be implemented in material-properties simulations, as the crystallographic-texture evolution during ECAP.

2.2.3 Multi-pass ECAP

The apparent shear strain, as determined from the SLF theory or experimentally is not suitable to characterize the one-pass ECAP deformation into a sequence with multiple deformations steps. It is necessary to define a parameter proportional to the plastic work

per volume. Using the von Mises yield locus for the isotropic materials, the equivalent strain increment, $d\varepsilon_{eq}$, was defined [85] as in Eq. (10). Integrating along the deformation path, the accumulated equivalent-strain, ε_{eq}, induced in one pass of ECAP is obtained. As was pointed out previously [79], there are two different ways to derive the strain tensor from the deformation-gradient matrix, and they correspond to the classical definitions of the engineering and true strains. Although the equivalent strain based on the von Mises yield locus has broad applications, it is strictly valid only for the isotropic materials and at the beginning of the deformation. Even in the isotropic case, the polycrystalline materials could have a different yield locus, and Eq. (10) should be correspondingly adjusted. In face-centered cubic (FCC) metals, the Taylor model of the plastic deformation predicts the relation between the yield stress, in different loading conditions, and the critical resolved-shear stress, τ_c, characterizing the slip in the grains taken as single crystals. For a material with randomly oriented grains, subjected to uniaxial tensile loading [99], the calculated yield stress is $Y = 3.06 \times \tau_c$. Applying the same approach for the shear loading until the yielding point, τ_y, the following result is obtained: $\tau_y = 1.56 \times \tau_c$. Therefore, the definition of the incremental strain gives:

$$d\varepsilon_{eq} = \frac{dW}{Y} = \frac{\tau_y \times d\gamma}{3.06 \times \tau_c} = \frac{d\gamma}{1.97}. \tag{32}$$

The coefficient, 1.97, is close to the value, 2, corresponding to the Tresca yield locus, and different from the $\sqrt{3}$ value predicted by the von Mises approach.

The plastic anisotropy is due, usually, to the preferential grain orientation, or texture. Moreover, on the top of the starting texture, the ECAP deformation generates another specific texture. Then, the equivalent-strain concept, even using more refined shapes for the yield locus, is not able to capture the changes in material properties for a multi-pass ECAP. It seems to be more adequate to define an incremental equivalent shear strain as:

$$d\gamma_{eq} = \frac{dW}{\tau_c} = \bar{M} \times d\gamma, \tag{33}$$

where $\bar{M}$ is the average Taylor factor for shear loading, which contains the texture influence and could also incorporate the hardening and strain-rate sensitivity.

The processing route (or strain path) is also an important ECAP parameter because it determines in a great deal the structural homogeneity and the average shapes of the individual grains [100-102]. Route A (no rotation), route B_A or B_C (alternate or consecutive 90° rotation), and route C (180° rotation) are the strain paths used in ECAP (see Fig. 3). For the multi-pass ECAP, the cumulative equivalent-strain, ε_c, induced into a material is usually calculated by multiplying the one-pass equivalent strain, ε_{eq}, with the number of passes, N: $\varepsilon_c = N \times \varepsilon_{eq}$. This estimate is only a rough approximation, and a better description must contain the degree of redundancy of each route. A way to determine the apparent strain, ε_a, induced in a multi-pass ECAP should contain the rising trend of ε_a, if the route A or B_c is used, and the oscillatory trend of ε_a, if the route B_a or C is applied, as delineated in Figure 21. In practice, the deformation of the unit material element shows a different pattern for each route [100-102]. The apparent equivalent-

strain, ε_a, can be determined using a multiplying factor, P_r, different for each route: $\varepsilon_c = P_r \times \varepsilon_{eq}$. The values of the factor, P_r, as a function of N (see Table 8) show that the degree of redundancy is increasing from the route A toward the route C, while the routes, B_C and C, are restoring periodically the material element initial shape. For a FCC structure, with a constant critical resolved shear stress, a grain-refinement modeling [103] predicts the diminishing route efficiency with the increase of the redundancy. However, there are experimental evidences that the route, B_C, is more effective in producing equiaxed-refined microstructures. To explain this behavior, few models [100-103] have been developed. Therefore, finding the optimal multi-pass ECAP route is still under study, questioning the involvement of the material specific properties. The route efficiency and the degree of redundancy determine mainly the grain refinement [100-102]. But the specific microstructures created by each route are more complex [104], because of the inter-crossing of the strain path with other materials characteristics, such as textures.

2.3 Plastic-Deformation Zone (PDZ) in ECAP: Experiment

The models for the PDZ in ECAP, described in the previous section, can be compared with the experimental results on partially-deformed billets. In order to assess experimentally the plastic deformation during ECAP, the billets are cut in two parts, and the cut surfaces are scribed with a grid to form a network of two perpendicular families of lines. The process is stopped before passing the whole billet through the ECAP die, i.e., a portion of the billet remains undeformed, so that the distortion of the linear network can be measured before and after the ECAP deformation.

In order to determine the shear-strain spatial distributions, lubricated scribed billets of pure Pb, pure Cu, and pure Al were subjected to ECAP using both sharp-corner and round-corner dies mounted in an Interlaken (100 tons) hydraulic-pressing system. Each billet was split in two halves prior to pressing, and the inside surface of one half was scribed with a network of two sets of perpendicular lines with a lateral separation of 1 mm. Billets having sizes of 12.7 × 12.7 × 50 mm were processed for a single pass through the sharp-corner die at room temperature using a pressing speed of 0.5 mm s^{-1} (Fig. 13). Billets with a size of 9.5 × 9.5 × 50 mm were also processed under the same conditions with a round-corner die (the angular fan was $2\Psi = 60°$), and are shown in Figure 14. The digital pictures of the deformed samples were used to read the coordinates of the various grid points at the intersections between the stream lines (along the pressing direction) and the cross lines, which lay perpendicular to the stream lines before the deformation. Because the readings and the digital data may be affected by errors, a B-spline smoothing is performed for each line, based on the fact that the B-spline functions are interpolation polynomials of the third order, and can ensure the continuity up to the second-order derivative. The corrected grid points are obtained by intersecting the two families of the smoothed curves, and the solutions derive simultaneously from an iterative approach by minimizing the distances between the points on different types of curves. This method allows the extraction of all components of the deformation-gradient matrix, and assesses the ECAP-induced plastic deformation of pure metals and alloys.

The corrected grid points were obtained by intersecting the two families of the smoothed curves, and the solutions were obtained simultaneously from an iterative approach by minimizing the distances between the points on different types of curves. After determining the new grid, and knowing the local equations of the curves crossing a certain point, the increments were evaluated along each family of curves, where the S_X, S_Y pair relates to the stream lines, and the C_X, C_Y pair to the cross lines. If X and Y are the coordinates in the initial frame, the rotation angle, α, of the stream-line direction is given by $\tan\alpha = \frac{S_Y}{S_X}\frac{\Delta X_0}{\Delta Y_0}$, where ΔX_0 and ΔY_0 are the undeformed dimensions of the unit element. Since the angle between the channels in the die is 90°, the angle, α, increases during the deformation from 0° to ~ 90°. The transient value of the shear strain was calculated in each node from the relationship:

$$\gamma_T = \frac{\left(\frac{\Delta Y_0}{\Delta X_0}\right)C_X S_X + \left(\frac{\Delta X_0}{\Delta Y_0}\right)C_Y S_Y}{\sqrt{(C_Y S_X - C_Y S_X)\left[\left(\frac{\Delta Y_0}{\Delta X_0}\right)S_X^2 + \left(\frac{\Delta X_0}{\Delta Y_0}\right)S_Y^2\right]}}. \qquad (34)$$

Equation (34) includes the normalization of the strain-gradient matrix required by the volume conservation due to material incompressibility.

Figure 22 shows the shear-strain maps and the refined flow-lines grid for the Cu deformed at room temperature in two dies configurations: (a) in a sharp-corner and (b) in a round-corner die. The digital pictures of the partially-deformed billets were used to calculate the flow-lines grids, based on the previously described procedure for the

reading and smoothing of the data points at the intersection of the two families of lines, stream lines and cross lines. It is apparent that these maps exhibit different shear-strain distributions. Thus, for the sharp-corner die, a higher shear strain is introduced, compared to the round-corner case, and the PDZ is concentrated around a plane at the intersection of the channels as in the SP-PDZ model. By contrast, for the round-corner die, the PDZ shape is not well defined, and a higher shear strain is introduced near the top of the billet along the inner wall of the die. Although the transient values of the shear component from the strain-deformation gradient, as well as its diagonal components, may be used to study the strain-rate evolution, the discussion here will be restricted to the spatial variations of the total shear strain, averaged for each individual stream line, where α reaches 90°.

Both Cu and Al show the formation of a small gap at the outer corner of the sharp-corner die (see Figs. 13b and 13c, respectively), i.e., the billets don't fill the outer corner. The billets roundness is close to the intersection plane between the two channels, with an angular span, 2ψ, similar to the constrained deformation in a round-corner die, except the fact that the rounded-outer surface of the billet is a free surface, which is not in the friction condition with the die walls. This behavior requires a lower shear strain near the bottom of the billet. The experimental shear-strain variations across the Cu and Al billets deformed in the sharp-corner die are compared in Figure 23 with the theoretical values calculated for the SP-PDZ and PS-PDZ models. For the PS-PDZ model, the full opening of the split zone was considered to be 30°, and the center of the rotation was taken in the middle of the billet. These characteristics were selected because they roughly match a

visual inspection of the billets. The angular span of the free surface viewed from the inner corner corresponds to about 15°, and the radius of curvature is less than the distance to the inner corner. However, the free surface shows a marked asymmetry, which is not taken into account in the PS-PDZ model.

A different behavior was observed for the deformed Pb sample in a sharp-corner die: the material fills the corner but the stream-line near the outer corner is rounded. Thus, a ″dead-metal″ zone is formed in this region, and an extended shearing fan is present. The measured shearing fan is $2\Psi = 40°$, and it is apparent from the Figure 23 that the shear strain predicted by the Ψ-PDZ model provides a good representation of the experimental results in the bulk. The sharp increase in the experimental shear strain near the bottom of the billet is related to the enhanced frictional effect occurring between the ″dead-metal″ and the flowing material.

For a billet deformed in a round-corner die (see Fig. 22b), it is clear that the PDZ is extended. Thus, the shear-strain map for Cu shows a gradual increase of strain in contrast with the map for the sharp corner. This behavior is expected and provides a good fit according to the Ψ-PDZ predictions. An unexpected feature is the significant decrease in the values of the shear strain when approaching the lower surface of the billet as shown in Figure 24.

It may be concluded that the FS-PDZ model for the round-corner die, which assumes two deformation modes (as the PS-PDZ model for the sharp-corner die), is meant to predict the decrease of the ECAP-induced shear strain in the vicinity of the outer corner of the

die. A shearing fan of 60° in the FS-PDZ model provides a good estimate of the strain at the inner edge, but in practice there is a gradual decrease in the strain before reaching the middle part of the billet, whereas the FS-PDZ model confines the free-rotation zone to a thin layer close to the outer surface (i.e., a layer representing ~ 20% of the billet thickness). Thus, an explanation of the variation of the shear strain in a round-corner die remains a challenge for the further analytical modeling.

3. CHARACTERIZATION TECHNIQUES

The microstructures of the as-received and ECAP-deformed samples have been characterized using the optical microscopy (OM), scanning-electron microscopy (SEM), electron-backscattered diffraction (EDBS), with the orientation-imaging microscopy (OIM) analyses, transmission-electron microscopy (TEM), X-ray diffraction (XRD), and neutron diffraction. The mechanical properties were characterized using the monotonic and cyclic loadings of the undeformed and ECAP-ed alloys. These techniques and some examples obtained on Mg alloys will be presented in the following.

3.1 Microscopy

Optical microscopy (OM) and *scanning-electron microscopy (SEM)* are extensively used for the measurements of the grain-size distributions, defects identifications, surface morphologies, or local compositions. Nowadays, the measurements of the grain size are carried out with the aid of computerized image analyzers. Various parameters describing the grain size are interdependent [105]. The *mean-intercept length, E*(*l*), is measured by counting the intersection points of the test lines with the grain boundaries (GBs), revealed on a section of the polycrystalline material. Parallel lines on a random section can be used for equiaxed grains. For an anisotropic grain structure, the lines should be randomly oriented in space, and, consequently, the test lines on a section will have irregular shapes.

In the present study, the alloys were characterized before and after ECAP, using mainly the metallography, given the fact that the grain refinement provided grain sizes of approx.

2 - 3 μm. These values were determined with a good accuracy from the OM measurements using the planimetric American Society for Testing and Materials (ASTM) procedure, E112-96, Standard Test Methods for Determining Average Grain Size [106], and averaging the values measured on a circular grid for a minimum of five fields.

Grain refinement during the ECAP deformation. Metallography was extensively used to determine the grain sizes of the as-received, ECAP-deformed, and mechanically-tested alloys. The samples for the structural characterizations were cut on three orthogonal directions (Fig. 25) relative to the rolling or extrusion directions, easily recognizable on the wrought Mg alloys, AZ31 (hot rolled) and ZK60 (hot extruded), used in the present study. The rolled plate, AZ31-H24, has the nominal composition in the weight percent of 96Mg-1Zn-3Al, and the extruded plate, ZK60-T5, has the nominal composition in the weight percent of 93.05Mg-5.5Zn-0.45Zr. The H24-temper signifies a solid-solution hardened alloy, and partially-annealed at 330^0C, 1 hr. The T5-temper is an artificially-aged alloy (solution-treated at 535^0C for 2 hrs, quenched in hot water, and aged at 185^0C for 24 hrs). The three orthogonal sample orientations: CC, TT, and FF, shown in Figure 25, are denominated after the normal to the cross (C), top (T), and flow (F) planes, respectively. The AZ31B samples were etched in an acetal-picric solution (4.2 g picric acid, 10 ml acetic acid, 70 ml ethanol, and 10 ml water) for about 5 seconds, and the ZK60 samples were etched in 3 g picric acid, 20 ml acetic acid, 50 ml ethanol, and 20 ml water). The OM characterization results of the as-received and ECAP-deformed alloys will be presented in the Section 4.1. As an example, the micrographs obtained for the as-received samples of AZ31 and ZK60, are presented in Figure 26. The rolled sample of

AZ31 has the average grain size of 50 μm, with similar morphologies on the three planes of observations (Fig. 26a). The extruded ZK60 sample has two grain-size components: larger grains of 50 - 100 μm, and smaller grains with the size less than 10 – 15 μm. From the three-dimensional micrograph in Figure 26b, it is noted that the grain sizes and shapes are comparable among the three planes of observations, flow (F), top (T), and cross (C) planes.

Computer-aided electron-backscattered diffraction (EBSD) method, based on the Kikuchi pattern interpretation, has been implemented along with the SEM techniques [107]. The schematic of the EBSD method is presented in Figure 27. The incident electron beam from SEM strikes the specimen mounted in a special EBSD holder so that the specimen surface is inclined at a steep angle (~ 70 degrees). A diffraction pattern is formed on a phosphor screen, and a low-light camera is used to capture the pattern to be analyzed using the *orientation-imaging-microscopy* (OIM) software. The pattern is named a *back-scattering Kikuchi pattern,* and consists of intersecting light and dark bands. The width and intensity of the bands are related to the crystallographic arrangement of atoms, particularly to the lattice orientation relative to a laboratory reference frame. If the electron beam is incident within a region of the specimen corresponding to a single grain, and the crystal symmetry is already known, then the *Euler angles* between the crystal frame and the sample frame (φ_1, Φ, φ_2) can be determined by a fitting procedure within an angular accuracy of approximately two degrees. The images are obtained by progressively displacing the electron beam over a pre-selected area on the sample surface in a raster pattern. The coordinates of the scanned locations and the Euler angles are

stored, and the software allows computing the *orientation-grain map*, the pole figures representing the preferred grain orientation (*texture*), and the *disorientation-distribution histogram*. The number of the disorientations in a data set should exceed 10^3 to minimize the errors. The EBSD analysis with the OIM software is the most powerful method to characterize the microstructure of metallic materials. The method becomes impractical only in areas with a severe lattice curvature or on a grain boundary where two overlapping patterns are produced simultaneously. The spatial resolution is usually 100 nm on the surface and 20 nm in depth with a W filament, and, for a field-emission source, the surface resolution is 50 nm.

The OIM measurements of the ZK60 alloy, before and after the ECAP deformation, were performed at ORNL/Y12, and are reported in Reference 50. The OIM data were carried out using a TSL/EDAX system with a 1612 Digiview camera in a SEM, LEO Stereoscan 440, with a W filament. The specimens were mounted on a 70° pre-tilted sample holder. A 30 kV beam potential (with 50 – 200 nA) was chosen because the alloy tended to form a surface-oxidation film, and because the SPD material produced poor quality EBSD patterns. Polishing samples for the OIM observations was carried out with mineral oil and alumina powder, with the final polishing step using 0.05 μm powders for 15 hours. The samples were, then, argon-ion-beam milled at 4kV in an electron spectroscopy for the chemical-analysis (ESCA) instrument until all surface oxygen and carbon had been removed. At that point, each sample was expeditiously transferred to the SEM chamber under the dry alcohol to avoid the re-oxidation of the surface. An inverse PF map, image quality (IQ) map, and PF images were collected from the OIM analyses. After the OIM

analyses were completed, each sample was oriented normal to the beam for the EDS analyses and the backscattered-electron (BSE) imaging. The energy dispersive X-ray (EDS) system consists of an Oxford light-element detector controlled by an Intelligent Correlation Agent (INCA) system, a flexible framework for the automated testing of the grid areas.

The typical OIM pattern for the ZK60 alloy, as-received sample, from Figure 30 confirmed the OM results, and exhibit a bimodal microstructure with the coarse grains surrounded by fine recrystallized grains. In addition to the OM results, the OIM analyses provided the grain-boundaries distribution, and, as in Figure 28, the blue color shows the low-angle grain boundaries (LAGBs), and the black color, the high-angle grain boundaries (HAGBs). The GBs evolution during ECAP will be discussed in Section 4.1. The EDS analysis of the same as-received sample showed two phases: a solid-solution matrix phase containing 6 - 7 atomic % Zn, and a precipitate phase containing Zn (more then 7 atomic %) and Zr. A small number of Zn_2Zr_3 inclusions and a small amount of fluorine evenly distributed were detected.

3.2 Diffraction Techniques

Diffraction methods using neutral particles, namely *X-ray or neutron diffraction*, are another way to probe the material microstructure. The classical procedures and instruments allow measuring some statistical average over a macroscopic part of the sample, and the novel methods under development at synchrotron radiation sources can provide grain-by-grain measurements with a better accuracy than EBSD.

The diffraction techniques have been extensively used in the present study to characterize the Mg alloys, before and after the ECAP deformation, by determining non-destructively the coherent-domain size, the elastic microstrain, and the preferential-crystallographic orientation (or texture). In material processing, the phase structure is usually well known, and the diffraction analysis focuses on revealing the differences between the measured and the ideal diffraction pattern. This fact often involves a laborious data processing in order to obtain the information about the *size distribution* of the grains and their *texture*, and also about the *lattice-defect substructure*. The primary data extracted from a diffraction pattern are the *peak positions*, *integral intensities*, or other peak-shape parameters, such as *full-width-at-half maximum* (FWHM) or *integral breadths*, and the data analyses can encompass various approaches.

Coherent-domain size and elastic microstrain. The XRD pattern of the $\theta - 2\theta$ scans contains the information about the grain substructure, and the peak-broadening profile is usually interpreted in terms of the coherent-domain size, d_X, and elastic microstrain non-uniformity, e_m, or root-mean-squared (r.m.s.) elastic microstrain. There are two common approaches to extract the crystallite size and strain associated with lattice defects from the powder-diffraction data by *line-broadening analysis* (LBA). One method is based on the integral breadth of the diffraction lines, and gives the volume-averaged apparent dimension in the direction normal to the reflecting planes (domain size), D_V. The other method is based on the Fourier analysis of the line profile and gives the area-averaged apparent dimension (column length) in the direction normal to the reflecting plane, D_A. These two crystallite-size dimensions are called "apparent" because they only relate to

the real average crystallite dimension. In fact, always the diffraction crystallite-size average is smaller than the grain size estimated from the microscopic observations.

3.2.1 Instrumental Profile

The line broadening of a diffraction peak in a XRD spectrum contains mainly two components: the instrumental profile and the sample profile. For the laboratory X-ray diffractometer, the instrumental profile consists of two components: the broadening due to the characteristic line emission and the broadening due to the geometry.

The X-ray K_α-characteristic profile, following the Holtzer et al. approach [108], contains four-emission lines (see Table 9), accounting for the simultaneous multielectronic transitions in the atom. These four emission lines, $K\alpha_{11}$, $K\alpha_{12}$, $K\alpha_{21}$, and $K\alpha_{22}$, contribute to the broadening of a diffraction peak with four Lorentz distributions. The Lorentz FWHM, Γ_L, of each component-line depends on the angle, θ, as follows:

$$\Gamma_L = \frac{360}{\pi}\frac{\Delta\lambda}{\lambda}\tan\theta, \tag{35}$$

The ratio, $\frac{\Delta\lambda}{\lambda}$, for each emission line of wavelength, λ, and the width, $\Delta\lambda$, as well as, the averaged values for λ and their relative intensities are given in Table 9 for the most used radiation of CuK_α. The geometry of the experimental arrangement contributes to the peak broadening with a Gaussian, with the FWHM, Γ_G, depending on the diffraction angle, θ, and following the empirical equation:

$$\Gamma_G^2 = w + v\tan\theta + u\tan^2\theta\,, \tag{36}$$

where u, v, and w are the empirical parameters to be determined from the instrument calibration. Consequently, each component of the instrumental profile is a convolution of Lorentz and Gauss distributions, i.e., it is a Voigt function, V (z):

$$V(z) = \int_{-\infty}^{\infty} G(x)L(z-x)dx \tag{37}$$

Calculating the Voigt function involves numerical problems. Therefore, a simple analytical approximation [109] will be a pseudo-Voigt function, P_i, defined as:

$$P_i(\Gamma_L,\Gamma_G) = \frac{2\eta}{\pi\,\Gamma}\frac{1}{1+\left(\frac{2\Delta\theta}{\Gamma}\right)^2} + \frac{2(1-\eta)}{\Gamma}\sqrt{\frac{\ln 2}{\pi}}e^{-\ln 2\left(\frac{2\Delta\theta}{\Gamma}\right)^2}\,, \tag{38}$$

where:

$$\eta = 1.36603\frac{\Gamma_L}{\Gamma} - 0.47719\left(\frac{\Gamma_L}{\Gamma}\right)^2 + 0.11116\left(\frac{\Gamma_L}{\Gamma}\right)^2; \tag{39}$$

$$\Gamma = (\Gamma_G^5 + 2.69269\Gamma_G^4\Gamma_L + 2.42843\,\Gamma_G^3\Gamma_L^2 + 4.47163\Gamma_G^2\Gamma_L^3 + 0.07842\Gamma_G\Gamma_L^4 + \Gamma_L^5)^{\frac{1}{5}}\,. \tag{40}$$

Following this procedure, the XRD spectrum of a Si standard was used to calibrate the instrument profile, as shown in Figure 29. The resulted instrument-profile parameters, u, v, and w, are: u = -0.00052, v = 0.000959, and w = 0.000996.

3.2.2 XRD Peak-Broadening Analysis

Two methods, used for the X-ray line-broadening analyses (PBA), the Williamson-Hall [WH] [110] and the whole-pattern fitting (WPF) [112], will be described in the following.

The PBA through *the WH method* [110] assumes that the integral breadth, β, of a diffraction-line broadening induced by the sample is defined as:

$$\beta = \frac{\cos\theta}{\lambda} \frac{\int I(2\theta)\, d(2\theta)}{I_{\max}}. \tag{41}$$

Its dependence of sinθ corresponds to a straight line:

$$\beta = \beta_{grain} + \beta_{strain} = \frac{1}{d_x} + 2e_m \frac{2\sin\theta}{\lambda}. \tag{42}$$

The initial coordinate gives the values of the grain size, $d_{x,}$ and the slope of the curve, β(s), gives the elastic microstrain, $e_{m,}$ based on the fact that, if viewed in the reciprocal space, the crystallite size is diffraction-order independent, while the lattice distortion is diffraction-order dependent. The integral-breadth method provides the volume-averaged apparent dimension of the crystallites, as well as the microstrain, in the direction normal to the reflecting planes. This method can be applied only on peak profiles corrected for the instrument contribution.

Alternatively, the microstructure of the polycrystalline materials can be studied by the *whole-pattern fitting (WPF) method.* To model the influence of the grain size, which is

rather the size of a coherent domain with the same lattice orientation and relatively low concentration of defects, the gamma distribution, f(R), for the grain-radii was considered:

$$f(R) = \frac{\left(\frac{1}{c}\right)^{\frac{1}{c}}}{\bar{R}\,\Gamma\left(\frac{1}{c}\right)}\left(\frac{R}{\bar{R}}\right)^{\frac{1}{c}-1} e^{-\frac{R}{C\bar{R}}}, \tag{43}$$

where R is the radius of a random spherical grain, $\bar{R}$ is the average radius of the grains, and $c = \frac{\sigma_R^2}{\bar{R}^2}$ is the ratio between the dispersion, σ_R^2, and $\bar{R}$. Using the gamma distribution from Eq. (43), the volume-averaged apparent domain size, D_V, as well as area-average domain size, D_A, can be evaluated as follow [113]:

$$D_V = \frac{3}{2}\bar{R}\,(1+3c); \tag{44}$$

$$D_A = \frac{4}{3}\bar{R}\,(1+2c). \tag{45}$$

The grain-size induced line profile, corresponding to the f(R) distribution from Eq. (43), can be approximated with a pseudo-Voigt as follows [113]:

$$P_s(s) = \eta_s L(\Gamma_{LS}, s) + (1-\eta_s) G(\Gamma_{GS}, s), \tag{46}$$

where:

$$\eta_s = 1 - 0.407597e^{-7.752c} + 0.336093e^{-0.633744c}; \tag{47}$$

$$\Gamma_{Ls} = \frac{a_1}{4\pi \overline{R}}; \tag{48}$$

$$\Gamma_{Gs} = \frac{\sqrt{\pi \ln 2}}{4\pi \overline{R}} \left(\frac{1-\eta_s}{\frac{3}{8}(1+3c) - \frac{\eta_s}{a_1}} \right); \tag{49}$$

and

$$a_1 = 4.98231e^{-27.1875c} + 1.75734e^{-4.86798c} + 1.38542e^{-0.736325c}. \tag{50}$$

Assuming that the microstrain-broadening component is Voigt distributed with the two FWHM-s, Γ_{Lm} and Γ_{Gm}, the sample-broadening profile, $P_{sm}(s)$, resulting from the convolution of the size broadening with the microstrain broadening, can be represented as a sum of two Voigt functions:

$$P_{sm}(s) = \eta_s \, V\left(\Gamma_{Ls} + \Gamma_{Lm}, \Gamma_{Gm}\right) + (1-\eta_s) \, V\left(\Gamma_{Lm}, \sqrt{\Gamma_{Gs}^2 + \Gamma_{Gm}^2}\right). \tag{51}$$

The Γ_{Lm} and Γ_{Gm} are proportional to tanθ. The microstrain contribution to the integral breadth could be approximated by the equation:

$$\beta_m = \frac{\pi}{2} \Gamma_m \left[\eta_m + (1-\eta_m)\sqrt{\pi \ln 2}\right] \tag{52}$$

with η_m and Γ_m being the pseudo-Voigt parameters calculated from Γ_{Lm} and Γ_{Gm} using Eqs. (39) and (40). Finally, the convolution of the sample broadening with the instrumental broadening gives a summation of eight Voigt functions, and each of the

Voigt function was approximated by a pseudo-Voigt following the same approach as in Eqs. (39) and (40). The whole-diffraction pattern was fitted with a sum of diffraction lines and a background contribution by using the least-square method.

3.2.3 Lattice Defects and Microstrain Anisotropy

The lattice defects are visible in diffraction due to the elastic strain field produced into the ordered lattice around. The strain field decays as $1/r^2$ (r is the distance from the defect to the point for measuring the strain) around point defects, as 1/r around linear defects (dislocations), and is space independent for plane defects. As a result of the reciprocity between the crystal and reciprocal space, the point defects have diffraction effects far from the peak position, and it is difficult to be observed in powder-diffraction measurements. The plane defects, the most common being the GBs, induce line shifts in the diffraction pattern. The average shift results from the Type-I residual stress always present inside the nonhomogenous or multi-phase materials. The orientation-dependent shift is produced by Type II inter-granular stress originating from the elastic anisotropy in connection with the texture constraints. Both types of stresses induce a constant strain across a single crystal block considered as diffraction source. The early models considered the spatial fluctuations of this inter-granular stress as the origin of strain broadening.

Much progress has been made in the last several years by considering the dislocation influence (Type-III intra-granular stress) on the strain broadening. The FEM-calculated slip-system strength correlates with the strain broadening [114], suggesting that the intra-

granular immobile dislocations structure is mainly responsible for the strain broadening. The sensitivity of diffraction to the dislocation-strain field is modulated by the relative orientation of the diffraction vector with respect to the dislocation-line orientation and the displacement vector (Burgers vector). This problem was first solved by Wilkens [115] for randomly-distributed screw dislocations using an analytical equation for the strain Fourier coefficients and an average contrast factor. Later, this approach was extended to all types of dislocations, including the elastic anisotropy of the material (see, for example, Ref.[116]).

The simplest way to separate the size and strain contributions to broadening is to use the Williamson-Hall plot as in Eq. (42). In the case of the strain caused by dislocations, the second term becomes [117]:

$$e_m = \left(\frac{\pi A b^2}{2} \right)^{\frac{1}{2}} \rho^{\frac{1}{2}} \overline{C}^{\frac{1}{2}} \tag{53}$$

ρ - the density of dislocations with a random location, b - the Burgers vector, C - the contrast factor of the dislocations relative to a certain diffraction plane, and A is a parameter determined by the effective outer cutoff radius of dislocations. Therefore, the proper scaling factor for β in Eq. (42) is $\frac{2\sin\theta}{\lambda} C^{\frac{1}{2}}$.

The contrast factor obeys certain crystallographic symmetry rules. For the cubic symmetry, a quasi-linear dependence of a unique fourth-order invariant in *hkl* indices, H_{hkl}, is expected [118]:

$$C_{hkl} = C_0\left(1 - qH_{hkl}^2\right);\ H_{hkl}^2 = \frac{h^2k^2 + k^2l^2 + l^2h^2}{\left(h^2 + k^2 + l^2\right)^2}\ . \tag{54}$$

The slope value, q, depends on the dislocation type. Therefore, the microstrain anisotropy can be used [118] to assess the dislocation character (*screw* or *edge*).

For the hexagonal symmetry, there are two fourth-order invariants in *hkl* indices to be considered. However, the crystallographic anisotropy of the contrast factor can be reduced to a parabolic dependence of a unique parameter, x, as follows [119]:

$$C_{hkl} = C_{hk0}\left(1 + q_1x + q_2x^2\right)\ ;\ x = \frac{2}{3}l^2\left[\frac{4}{3}\left(h^2 + l^2 + hk\right) + \left(\frac{a}{c}\right)^2 l^2\right]^{-1} \tag{55}$$

The slip systems in hexagonal crystals and the contrast parameters for Mg reported by Dragomir and Ungar [119] are included in Table 10.

As only the immobile dislocations contribute to the diffraction contrast, and the screw dislocations are less prone to be pinned, a major contribution from the screw dislocations is not expected. But even considering the edge dislocations only, it will be not possible to decide the dislocation-type distribution from the two measurable quantities, q_1 and q_2. Analyzing the distribution of the (q_1, q_2) - pairs (see Fig. 29), it can be concluded, qualitatively, that the <*a*> dislocations (corresponding to the orientation <a> of their Burgers vector) prevail when q_1 is negative and q_2 small; the <*c* + *a*> dislocations prevail when q_1 is positive and q_2 negative; and the <*c*> dislocations prevail when both q_1 and q_2 are positive. In fact, for the *a*-type dislocations, the (*hk0*) diffraction lines are the broadest,

whereas the (00l) lines are the broadest for <*c*> and <*c* + *a*> edge dislocations. Surprisingly, the (203) line is the broadest for the screw dislocations.

To simplify the problem, the peak broadening due to the dislocation debris was considered first as proportional to the contrast averaged over the weighting factors, p_i, of the dislocations type, *i*:

$$\beta_{dis}^2(hkl) \propto \sum_i p_i C_i = \sum_i p_i C_i(hk0)\,(1 + q_{1i}x + q_{2i}x^2) \tag{56}$$

Therefore, the experimental data for q_1 and q_2 can be represented by averaging over all possible orientations of edge dislocations:

$$q_j^{\exp} = \sum_{i=1}^{8} p_i C_i(hk0) q_{ji} \;/\; \sum_{i=1}^{8} p_i C_i(hk0) \;\; ; \;\; \sum_{i=1}^{8} p_i = 1. \tag{57}$$

Random sequences of p_j values were generated, and the resulting q_j values were compared with the experimental data in order to determine a set of approximate solutions of Eq. (57). The eight p_i values were reduced to three f_j values corresponding to each Burgers-vector type: < *a* >, < *a* + *c* >, and < *c* >. The averaged values of f_j, compatible with the experimental data, can be used to calculate the most probable values of the concentration, h_j, of the type *j* dislocations:

$$h_j = \frac{f_j b_k^2 b_l^2}{f_1 b_2^2 b_3^2 + f_2 b_3^2 b_1^2 + f_3 b_1^2 b_2^2} \;\; ; \;\; k \neq l \neq j \tag{58}$$

Knowing the h_j values corresponding to a particular sample, it is possible to extract the total density of dislocations, ρ, by using the following equation:

$$\beta_{dis}{}^{2}(hk0) = \rho \sum_{j=1}^{3} h_j b_j^2 C_j \left(hk0\right). \tag{59}$$

Although the h_j values are generally not precise, the ρ value is pretty stable and its accuracy is less than 10%.

3.2.4 XRD Profile Measurements

The LE-XRD profiles (θ – 2θ scans) were recorded at University of Tennessee using a Philips diffractometer, Cu-Kα radiation, 45K × 40 mA, and a line focus of 1 mm × 10 mm. For the incident beam, a fixed divergence slit of 1^0, a 0.04 rads soller slit, and a mask of 10 mm height are used. For small samples, the mask was replaced with a cross-slit stage, with the possibility to vary the beam size horizontally and vertically; usually, a window of 1.5 × 1.5 mm in size was used. For the diffracted beam, a receiving slit of 0.2 mm in height, and an antiscatter slit of 1^0 were used. The LE-XRD profiles of the Mg alloys, before and after the deformation, were analyzed using the whole-pattern-fitting (WPF) method, and the instrumental profile was determined with a Si standard. The WPF in Figure 29 is shown to fit well the experimental data. The XRD profiles analyses will be presented in the Section 4.3, in connection to the texture evolution and the mechanisms of deformation after ECAP and mechanical testing at different temperatures.

3.2.5 Preferential-Crystallographic Orientation or Texture

The variation of the integral intensity of the diffraction peaks is mainly related with the preferential orientation of the grains, namely the crystallographic texture. Thus, the texture measurements are designed to determine the intensity variation of a certain

diffraction peak, indexed $\boldsymbol{h}$ = (h,k,l), as a function of the measurement direction ($\boldsymbol{y}$) relative to the sample-reference frame. After corrections and normalizations, the probability maps, $P(\boldsymbol{h},\boldsymbol{y})$, or *pole figures (PFs)* can be constructed to describe the distribution of different crystal directions in the sample space. While the PFs are obtained by keeping the crystal direction constant, the *inverse-pole figures (IPFs)* can display the texture by keeping the sample orientation constant, and the crystal direction is varied, thus, mapping a particular sample direction in the crystal space. With the X-ray laboratory instruments, the incomplete PFs can be recorded, because the low-energy X-rays (8KeV for CuK_{α}) show a small penetration inside the material, and the measurement becomes difficult at a small incidence angle, corresponding to a tilt angle greater than 75^0. This impediment can be overcome by using the neutron diffraction or synchrotron radiation (SR) with high-energy X-rays (80 - 100 keV). The time-of-flight (TOF) neutron diffraction allows the measurement of a large number of peaks and orientations simultaneously. Therefore, the neutron-texture measurements are realized without rotating the sample or by accomplishing a small number of rotations. The SR sources produce very high intensity beams of high energy, and a sample of millimeter thickness can be measured in transmission in seconds. Using 2-D detectors, a large number of Debye rings can be recorded simultaneously, thus reducing the number of necessary sample rotations. In all variants, the PFs contain some partial data about the *orientation-distribution function* (ODF), which is directly determined in the EBSD method. Two circumstances contribute to this behavior: first, the ODF is defined in 3-D, and the PFs in 2-D will result from the integration of all crystal orientations with a particular direction fixed; secondly, because of the crystal symmetry, each measured *hkl* corresponds to many

equivalent directions in the crystal frame. Two approaches are extensively used to find the ODF from at least three PFs: a *harmonic method* based on the series-expansion approximation of the ODF, and a purely algebraic *vector method*. The algorithm of obtaining the ODF from a set of PFs consists of finding the vectors, which connect each cell from the orientation space to the cells of the various PFs. The commercial codes, such as the Preferred-Orientation Package, Los Alamos (popLA) [120] and Beartex [121], are available for the texture analyzes from the PFs measured data.

Texture measurements using the low-energy (LE) XRD. The crystallographic textures of the studied materials were determined by the laboratory X-ray diffraction or low-energy (LE) XRD, and the schematic of the measurements is shown in Figure 31. The PFs of the {10.0}, {00.2}, and {10.1} reflections and on three planes of observations, F, T, and C planes, were measured at ORNL using a Scintag XDS2000 diffractometer, with Cr Kα radiation, a 2 mm-diameter incident beam collimator, and a four-axis polycrystal-texture-stress (PTS) goniometer. The PFs were collected for the sample tilts ranging from $\chi = 0^o$ to 75^o, with a step of 5^o, and for the sample rotations ranging from $\varphi = 0^o$ to 355^o, at the rate of 100^o/min. The LE-XRD PFs were analyzed using popLA software [120], including the PFs extrapolation for the tilting angle, $\chi > 75^o$. As an exemplification, the LE-XRD PFs of the starting materials of two Mg alloys, AZ31-H24 (hot-rolled) and ZK60-T5 (hot-extruded), obtained for three surfaces of observations, flow, top, and cross planes, and for three reflections, (10.0), (00.2), and (10.1), are represented in Figure 32. The PFs captured the typical textures for rolling and extrusion processes, respectively. This somewhat redundant procedure of measuring on three surfaces of the sample

confirmed that the textures reflect the bulk response of the samples. The IPFs were calculated using popLA for the three planes, and, as can be seen in Figure 33, they are similar on any observed surface, i.e., the measurements reflect the texture of the bulk. Comparing the as-received and compressed samples from the Figures 33a and 33b, a drastic change of the texture is observed following the compression. The as-received IPFs show a main texture component, with a prismatic pole aligned along the extrusion direction, XD (on the cross plane observed), and a basal pole preferentially oriented along the TD and ND (on the flow and top planes, respectively). The in-detail analyses of the deformation textures of the two alloys, AZ31 and ZK60, will be given in Section 4.3.

Diffraction data obtained using the high-energy (HE) XRD synchrotron radiation.

For the present study, the synchrotron-radiation (SR), or high-energy XRD (HE-XRD) method was used for measuring the part of the texture, which was not captured by the classical LE-XRD measurements. In the schematic of the HE-XRD setup from the Figure 34, are represented the sample and the detector (an image plate) placed at the diffraction angle, 2θ, and the rotation angle is defined as φ. The SR in the transmission scheme produces on the image plate the Debye-Scherrer rings originating from the through-thickness volume of each sample (in our case, a 1.25 mm thick sample was used for the measurements). Therefore, the XRD intensities will reflect those orientations of the grains, with a given crystallographic direction, and oriented almost perpendicular to the beam direction, as the diffraction angles are small due to the short wavelength of the

SR used. Then, the HE-XRD technique allows for the in-plane pole distribution (IPPD) measurement, equivalent to the LE-XRD measurement, for a tilting angle, $\chi \sim 90^{o}$.

The high-energy SR at the Advanced Photon Source (APS), Argonne National Laboratory, at the X-ray Operations and Research Beamline 11-ID-C, was used to obtain the diffraction rings for 22 peaks from the Mg spectra. The monochromatic beam, with a radiation wavelength of 0.108004 Å, has a cross section of 0.3 × 0.3 mm. The scattered radiation was collected on an image plate (MAR 345). The diffraction-ring radius is determined by the diffraction angle, 2θ, and each point along the circle corresponds to a particular rotation angle, φ, around the beam axis, which is perpendicular to the sample surface in a regular transmission setup. The measurement direction, i.e., the normal to the diffracting crystallographic plane, divides in half the angle between the diffraction direction and the reversed beam direction. Therefore, it does not lie in the sample surface plane, but raises out-of-plane under a θ angle. As the 2θ - angles for the first three analyzed rings have small values, the out-of-plane component will be neglected in the following, and the measurement directions will be considered as being contained in the plane perpendicular to the incoming beam, i.e., parallel to the sample surface. Consequently, the integral-intensity distribution along each diffraction ring is a direct representation of the IPPD.

Although the HE-XRD measurements provide the information on about 16 different directions in the reciprocal space, only three reflection planes, {10.0}, {00.2}, and {10.1}, were selected for the texture analysis. The beam center, detector location, and angular positioning were determined using silicon and CeO_2 calibration-powder samples. The

diffraction rings were visualized with the Fit2D code [122]. The ″Powder Diffraction-2D″ interface of the Fit2D code, provided the *2D-circular maps*, as exemplified for the AZ31 and ZK60 samples, in the as-received, annealed and ECAP conditions, respectively (see Figs 35a, 35b, and 35c, and Figs. 36a, 36b, and 36c). For both cases, below the circular maps, the *2D-rectangular maps*, in the 2θ - φ coordinates, are represented for only three out-of-22 diffraction rings (see Figs. 35d, 35e, and 35f and Figs. 36d, 36e, and 36f). With the goal to evaluate the texture evolution from the IPPDs, each diffraction line was separately integrated over the 2θ coordinate for each φ value. In order to visualize the domain-size effect, the resolution in φ was kept at 0.2^0, an unusual value for a texture measurement. This choice allows visualizing the coarse crystallized patterns, such as in Figures 35b and 35e, for the annealed samples of AZ31 alloy. The integrated intensities as a function of the φ angle were represented as *IPPDs in polar plots* (see Fig. 37). The example from the Figure 37, represents the 2D-rectangular maps (see Figs. 37a, 37b, and 37c) and the corresponding IPPDs for the three reflection planes, (10.0), (00.1), and (10.1), obtained for the ZK60 samples after compression at room temperature (Fig. 37d), at 150^0C (Fig. 37e), and at 350^0C (Fig. 37f). The texture evolution and the orientation effects studied for the AZ31 and ZK60 compressed samples at different temperatures will be described in Section 4.2.

The high-spatial resolution of this technique and the 3-D data recording allowed assessing the texture evolution and identifying different deformation mechanisms. The intensities integrated over φ, and represented versus 2θ calculated from the HE-XRD data are exemplified in Figure 38, where the comparison of the AZ31, as-received and ECAP-

1 pass, is showing the drastic intensity change of the (00.2) reflection. Finally, for the ease of the data interpretation, the *IPPDs* were represented in *3-D plots,* corresponding to the flow, top, and cross planes of observations, as shown in Figure 39 for the two as-received alloys, AZ31 and ZK60.

The neutron diffraction was used as complementary to the LE-XRD technique to study the preferential orientation of the grains in the bulk of the sample. The time-of-flight neutron diffraction allows the measurement of a large number of peaks and orientations simultaneously, with no need to rotate the sample. The measured data are slightly affected by the absorption. The neutron diffraction has modest expectations in the area of the high spatial-resolution determinations, but the penetrability of neutrons through thick samples make this method applicable for the nondestructive accurate texture, size, and strain measurements in the bulk of he material. Both high-energy SR and neutron diffraction are prone to be used for in-situ parametric experiments of material processing or testing.

The neutron PFs were obtained using the high-pressure preferred orientation (HIPPO) [123] neutron diffractometer at the Los Alamos Neutron Science Center (LANSCE). A large neutron-beam size of 5 mm in diameter, with the incident flight path of 8 m, and a ^{3}He detector system of rings placed around the incident direction at 10^{0}, 20^{0}, 40^{0}, 90^{0}, and 150^{0} diffraction angles, constituted the experimental setup, as schematically drawn in Figure 40. The neutron PFs were collected from a bulk of 7.5 × 7.5 × 7.5 mm, representing the size of each sample. The PFs data are further analyzed with a full-pattern method (Rietveld analyses) [124]. From the example in Figure 41, the neutron

PFs for the ZK60 alloy, as-received, are recalculated from the ODF for six crystallographic directions, and show a similar prismatic pole along the extrusion direction, confirming the LE-XRD measurements (see Fig. 32b).

3.3 Mechanical Testing under Monotonic and Cyclic Loadings

Tensile and compressive tests, as well as cyclic loading, are used to evaluate the strength, ductility, and fatigue life of the ECAP-deformed materials. The uniaxial tensile/compressive tests in the temperature range from 25^0C to 350^0C, and the strain rates ranging from 10^{-4} to 10^{-2} s^{-1}, and stress and strain-controlled fatigue experiments were done along three orientation of the samples, CC, TT, and FF, corresponding to the cross (XD), top (ND), and flow (TD) directions, respectively, as drawn in Figure 25. The tensile samples were flat bars, with a gage length of 12.7 mm, and the cross section of 2.1 × 2.8 mm. The samples for compression tests were cubes of the size of 7.5 mm, and the samples for the fatigue tests were round-shaped with thread, with the diameter at the ″one point″ gage of 3.175 mm, and a total length of 17.5 mm. The mechanical tests were performed at constant speed of the crosshead using a servo-hydraulic machine, MTS-810 (Material Test System, Model 810), equipped with a controller and data-acquisition system. The displacement was measured using a miniature extensometer. The fatigue tests were conducted at room and high temperatures, under both load control and strain control. The load controlled tests were performed at a frequency of 10 Hz, and a stress ratio of R = –1, where $R = \sigma_{min.} / \sigma_{max.}$; $\sigma_{min.}$ and $\sigma_{max.}$ are the applied minimum and maximum stresses, respectively. The testing conditions for the strain-controlled tests were: straining in the range of 0.2 and 1.5 %, at a frequency of 0.5 Hz.

4. ECAP APPLIED TO MG ALLOYS

4.1 Grain Refinement during ECAP

Background. The microstructure evolution of the ECAP materials is intensively studied, and different concepts were developed. It has already been accepted that for the ultrafine-grained (UFG) materials, the main element of the deformation microstructure is the grain boundary (GB). Hughes and Hansen [104] give a more elaborated model for the grain refinement during extrusion. It seems that a gradual conversion of the incidental-dislocation boundaries (IDBs) into high-angle-grain boundaries (HAGBs) takes place when the grain-size refinement occurs. It is considered [104] that the microstructural features defined as *geometrical-necessary boundaries* (GNBs), which are glide-induced lattice rotations associated with the HAGBs, and IDBs, associated with low-angle GBs (LAGBs), have a separate role in the deformation strengthening of the material. It is believed that LAGBs can cause dislocation strengthening, while HAGBs will contribute to GB strengthening. The distribution of the deformation structure, volume fraction, morphology, orientation, and dislocation density will have a significant influence on material strengthening, and also could be the parameters affecting the flow stress anisotropy. Thus, the main microstructural parameters to be designed could be the grain-size and the amount of HAGBs. The grain-size refinement is responsible for the material strengthening as predicted by the Hall-Peach relation. On the other hand, the increase of the amount of HAGBs can improve the ductility by enhancing the GB sliding (GBS) mode during the material deformation up to a superplastic behavior at lower temperatures and higher strain rates.

The multipass ECAP, together with different strain paths (or routes), can induce large accumulated strains in the material, and different shear systems may be developed, resulting in various microstructures, including a substantial grain refinement. The research efforts are directed in establishing a rule for the route efficiency, relative to the grain refinement and processing conditions. The results on pure Al (99.99%) [125], using an ECAP die with $2\Phi = 90^0$ and $2\Psi = 20^0$, conclude that the effectiveness of the ECAP routes in producing equiaxed fine grains lies in the sequence: $B_C > C > A = B_A$. At the die angle, $2\Phi = 120^0$, the route A is the most effective in refining the grains of Al-3%Mg alloy, and the sequence is $A > B_C = B_A > C$ [126]. A tentative explanation of these contradictory behaviors, considers that the deformation textures reorients the slip plane between the shear direction and the grain-elongation direction. This assumption, may agrees well with the face-centered-cubic (FCC) metals, but may not agree with the results of the body-centered-cubic (BCC) metals, indicating a different deformation mechanism for FCC and BCC metals, respectively. Another work [24] reconsiders the grain-refinement efficiency by comparing the microstructures obtained on commercial-pure Al, AA1050 (55.5%), with two different dies ($2\phi = 90^0, 2\Psi = 20^0$ and $2\phi = 120^0, 2\Psi = 0^0$) using the route C. After enforcing a cumulative strain of ~ 4, the microstructure developed by both dies has similar characteristics, banded structures and equiaxed grains (subgrains). But at a cumulative strain of ~ 8, the 120^0 - die produces mainly banded structure, and the 90^0-die mainly equiaxed grains. The fraction of the HAGBs reaches a level of 38% for both types of die. Thus, compared at the same level

of strain and on the same material, the influence of the die angle is reduced to the change in the microstructure morphology rather then to the grain-refinement efficiency.

The grain-refinement efficiency is strongly related with the metal purity. The pure Al (99.99%) [125] or even 99.9% [126] demonstrates the refinement saturation near 1 μm. The EBSD measurements [127] on pure Al as a function of number of passes show a gradual decrease of the grain-size until 4 passes, and a decrease in aspect ratio from 3 to 1.5. The amount of HAGBs is also increasing up to 40%. Further pressing over 4 passes, produced no change in the grain-size and the aspect ratio, while the misorientation continues to increase, and LAGBs are transformed in HAGBs. The saturation of the grain-size refinement, observed experimentally in pure Al, is a result of the balance between the deformation and the dynamic recrystallization (DRX) process.

The presence of impurities can trigger this balance, and considerable finer grain-size (0.35 μm) is obtainable in commercially pure Al (99.5%) [128, 129]. The equiaxed grains show three types of boundaries, observed using TEM: *polygonized-dislocation walls (PDWs),* which consist from perfect lattice-dislocations, *partially-transformed boundaries (PTBs*), and GBs. The PDWs have grain-to-grain misorientation $< 1^0$, while the misorientation of PTBs lies in the range of about $1 - 5^0$. It was observed that for low strains of $\Delta\varepsilon^T_{eq} \sim 2$ (2 passes), a conventional structure of PDWs is prevalent, and some PTBs and GBs may appear. For medium strains of $\Delta\varepsilon^T_{eq} \sim 4$ (4 passes), the PDWs transform into PTBs, and the PTBs into GBs. And finally, for high strains of $\Delta\varepsilon^T_{eq} \sim 8$ (8 passes), most boundaries are HAGBs, with a misorientation $> 10^0$.

For metallic alloys, the ECAP technology shows a great flexibility in designing various microstructures. The presence of the dispersed phases in the starting material has an important influence on the properties and stability of the final product. The fine precipitates are prone to be dissolved as the result of ECAP deformation even at room temperature. As an example, in Al-1.7Cu alloy containing θ′- precipitates, the ECAP deformation initiates the precipitate fragmentation, and, eventually, the phase dissolution to form a supersaturated solid-solution. This fact was proved by TEM [130], and can explain why the ECAP of some aging-strengthened Al-alloys show a little or no enhancement of the material strength [26].

The ECAP generated microstructures are usually highly unstable with temperature due to the dramatic decrease of the recrystallization temperature. Then, prior-ECAP, stable precipitates are effective pinning sites for the dislocation movement, and can enhance considerable the thermal stability of the fine-grained material after ECAP. An outstanding result was obtained for the Al-3%Mg alloy containing 0.2% scandium [130]. The ECAP-ed alloys had a superplastic behavior at relatively low temperatures (400^0C) and high strain-rates ($3.3 \times 10^{-3}s^{-1}$). The optimum superplastic ductility is achieved after 8 ECAP passes, route B_C. The grain-size reduction from 200 μm to 0.2 μm is accompanied by a homogeneous array of grains with HAGBs. These HAGBs are a prerequisite for the superplasticity based predominantly on the GBS mechanism. The stability of the UFG at high temperatures is attributed to the presence of a dispersion of very fine coherent Al_3Sc precipitates, which are known to be stable up to temperatures close to the melting point of the material.

Metallography of the undeformed and ECAP deformed, AZ31 and ZK60, alloys. The grain-size and the morphology of the grains for three surfaces of observations for the Mg alloys in the as-received conditions have been presented in the Section 3.1, Figure 26. From the optical micrographs in Figure 26, it can be seen that the AZ31B alloy has an average grain size of 50 μm, uniformly distributed, and the ZK60 samples, shown on the three orthogonal surfaces, flow, top, and cross sections, revealed a heterogeneous microstructure, with some larger grains (ranging from 50 to 100 μm) surrounded by fine grains of less than 10 μm. After 1 pass of ECAP deformation, the microstructures of both alloys remained largely heterogeneous. Further pressing, up to 4 passes, revealed a significant grain refinement for the ZK 60 alloy [29]. The differences between the grain sizes for the samples processed with routes 4A, $4B_C$, or 4C were not significant, and the top plane had the most uniform distribution among the observed planes of the sample. In Figure 43, the grain sizes of the as-received and ECAP deformed ZK60 via three routes, A, B_C, and C, are compared for the flow plane of observation. The coarse-grains shape remain elongated in the pressing direction for route 4A, while for routes, 4B and 4C, it becomes more equiaxed (Fig. 43). The coarse-grains size decreased down to 15 - 50 μm, and they were surrounded by the fine grains structure of 2.5 μm. Further ECAP straining of the ZK60 samples up to 8 passes conducted to more elongated coarse-grains component of the microstructure, while the small grains component is no longer refined (see Fig. 44b).

A different behavior was observed from the metallographic observations of the AZ31B, before and after ECAP, as shown in Figures 45a, 45b, and 45c. Processing at 300^0C

resulted in a poor grain refinement of only 17 μm after 8 passes of ECAP (Fig. 45b), while ECAP at 200^0C with the back-pressure leads to a grain size of 2.5 μm after 8 passes, route B_C (Fig. 45c). The grain refinement is significant after only one or two passes of ECAP, and the subsequent passes don't change the grain size too much. This effect is evidenced in the Figure 46 for the AZ31 alloy, after 2 passes, route $B_{C,}$ where the three planes of observations, flow, top and cross planes, show similar grain sizes of ~ 2.5 μm and similar morphologies of the grains. The overall grain-size refinement with the number of ECAP passes for the two alloys, AZ31 and ZK60, is represented in Figure 47. The grain-refinement efficiency during ECAP is different for the two alloys, and the main influencing factor is the processing temperature. The grain size after ECAP has changed for both alloys, AZ31 and ZK60, from 50 μm down to 2 - 5 μm. It can be seen in Figure 47 that the bimodal grain-size distribution of the ZK60 was preserved after ECAP, with the large-grains component refined from 50 – 100 μm down to an average of 30 μm, and the small-grains component was refined during ECAP from ~ 10 μm down to an average grain size of 3 μm, but grains of 7 μm are also present.

The metallographic results were confirmed by the OIM measurements of the same ZK60 samples, before (Figs. 48a) and after ECAP (Fig. 48b). The bimodal-grain distribution is preserved for the ECAP-ed ZK60 alloy, with an effective grain refinement. The GB misorientation distributions, obtained from the OIM data, for the starting material and the ECAP-ed sample for 8 passes via route A were compared in Figures 49a and 49b, respectively. The comparison indicates a reduction in the number of low-angle grain boundaries (LAGBs), i.e., angles less than 15^0, relative to the number of high-angle grain

boundaries (HAGBs) as a result of the ECAP deformation. Therefore, by increasing the amount of straining, a transition from LAGBs to HAGBs occurs, conducting to a more stable microstructure. On the contrary, after one ECAP pass, the material was so severely deformed that only an occasional and diffuse EBSD pattern could be obtained, denoting an unstable microstructure, with a large LAGBs/HAGBs ratio.

Strength. A higher yield value for an UFG material is reflected in the Hall-Petch relationship: smaller grains will conduct to higher yield. In the UFG materials, GBs have an additional effect on the deformation behavior, and act as barriers to the movement of dislocations. The Hall-Petch relationship describes the strengthening of metals and composites, when the grain size decreases:

$$\sigma_y = \sigma_0 + \frac{k_{HP}}{\sqrt{D}} \tag{62}$$

where σ_y is the yield stress, σ_0 is the frictional stress reflecting the resistance of the material to the motion of gliding dislocations (or internal back-stress), and k_{HP} is the Hall-Petch slope, which is considered to be a measure of the resistance of the GBs to slip transfer (or hardening contribution of GBs). In conventional coarse–grained materials, k_{HP} is positive at room temperature. The mechanism behind this behavior involves the generation of dislocations at the Frank-Read sources inside the grain, and the dislocations pile-up at the GBs. There is a limit of the applicability of the Hall-Petch relation, if the grain size is comparable to dislocation loops, usually tens of nanometers. When transiting from the coarse grains to UFG (100 – 1,000 nm), the deformation modes preponderance change gradually, and the work hardening or shear localization effects will reflect the

dislocations dynamics. One can retrieve in the UFG pure metals mechanisms of deformation, such as: (i) the hardening effect, associated with the increase of the density of the dislocations debris inside the grains, or, macroscopically, hardening reflects the critical-resolved shear-stress (CRSS) evolution corresponding to each deformation mode present in the sample: slip, twinning and, eventually, the interaction between the two; (ii) the strengthening effect associated with the grain fragmentation, which increases the density of GBs, therefore more barriers for dislocation movements (Hall-Petch effect discussed earlier); or (iii) the specific texture formation, which modifies the distribution of the crystallographic orientations of the grains. More contributions should be taken into account in the case of the *UFG alloys*: (iv) the solid-solution strengthening; or (v) the precipitate/dispersoids strengthening through aging. Each of the above contributions to the plastic deformation of the material can vary significantly depending on the processing sequence and the chemical composition. Therefore, besides the Hall-Petch strengthening, other factors, such as: the grain morphology (shape and size), specific textures, precipitate dissolution, and/or defect density, are to be analyzed in order to determine their influence on the thermo-mechanical behavior of the studied materials.

Hall-Petch relationship applied to Mg alloys. The measurements of the Vickers microhardness, H_v, were done on the F and C planes of the as-received and ECAP-deformed samples [49] using a Buehler Micromet®-2100 microhardness tester equipped with a diamond pyramidal indenter. For each data point, a load of 300 gf was applied for 15 s. Ten separate hardness measurements were recorded at randomly selected points for each sample and, then, averaged to obtain H_v. The microhardness measurements of the AZ31B alloy, as-received and ECAP-deformed in 1, 2, and 8 passes are represented in

Figure 50. The microhardnesses have similar values on both flow and cross planes, although the hardness on the flow plane is somewhat higher than that on the cross plane [49]. In Figure 50, the comparison of the microhardness values with the Hall-Petch relationship (red line) shows an increasing hardness when the grain size decreases, i.e., after ECAP, a grain-size strengthening predicted by the Hall-Petch relationship is observed. There is a large hardness jump from the as-received to 1-pass sample. Further pressing only results in a slight hardness increase. The as-received sample has the lowest hardness due to the coarse-grain microstructure, and after one pass, the hardness is increased by 36% on the flow plane because of the formation of the ultra-fine microstructure with only a few coarse grains, but further pressing to $2B_C$ passes only increases the hardness by 5%. The hardness remains unchanged up to $8B_C$ passes, because by increasing the strain intensity, the grain sizes do not change significantly.

4.2 Orientation Effects on Mechanical Properties

Extensive works are available in literature regarding the mechanical response under monotonic or cyclic loading of the ECAP-deformed metals and composites. It is expected that the strength, ductility, and/or superplastic behavior of the ECAP-deformed materials will be greater than for the starting material. There are already recognized some specific mechanisms acting in UFG-ECAP materials: (i) a bimodal grain-size resulted from material preparation shown to improve both strength and ductility as compared to the coarse counterparts; (ii) a bimodal grain-size resulted from deformation, such as stress-induced in-situ grain growth or dynamic recrystallization; (iii) a twinning mechanism shown to have an important contribution when an inhomogeneous

microstructure results after ECAP, e.g., the nanoscale twins could produce both high strength and uniform ductility; and (iv) a low-temperature ECAP deformation, which results in an increased strain hardening.

Recent studies of the twinning mechanism during monotonic loading [131-134] or cyclic loading [135-138] evidenced the tension/compression asymmetry, the hardening evolution, and the twinning-untwinning phenomena produced by compression and subsequent tension. The rolled Zr was tested in compression for different loading directions at -198^{0}C, and the texture was shown to evolve due to the slip and twinning mechanisms [139]. A composite-grain model was developed and introduced in the Visco-Plastic-Self Consistent (VPSC) model [140] to describe the twinning contribution to the deformation.

Therefore, by studying the orientation effects in Mg alloys, the combination of the deformation modes in the presence of a strong initial texture can be quantified and used to control the material response during mechanical testing. The influence of the textures on monotonic behavior was extensively studied, while for the cyclic studies of the ECAP-ed materials only few data are available. Moreover, the mechanical properties combined with the texture information can help optimize the texture requirements prior to ECAP, as well as the processing path. Hence, in the following, the mechanical response will be analyzed in view of the grain refinement, texture evolution, and the interplay of different mechanisms of deformation during ECAP and mechanical testing under monotonic and cyclic loadings.

4.2.1 The Mechanical Tests in Compression and Fatigue of the As-received Materials

Compression tests of both alloys, AZ31B and ZK60, were performed for three orientations, CC, TT, and FF. The testing temperatures were RT, 150^0C, 250^0C, and 350^0C. The compression tests at RT and 150^0C were conducted until failure, whereas during the tests at 250^0C and 350^0C, the failure was not reached, and the displacement-controlled deformation was limited to about 50 - 60% of the engineering strain. The stresses versus plastic strains curves for both alloys, obtained at room temperature, with straining at a rate of 5×10^{-3} s^{-1}, are presented in Figures 51a and 51b, respectively. The AZ31 alloy, compressed along the TT direction, displays a higher yield stress and lower ductility than the tests performed along the CC and FF directions, for which the results are quite similar. The stress-strain behavior of the alloys is represented in Figure 52 (AZ31) and Figure 53 (ZK60), for the compressive tests at room temperature, 150^0C, 250^0C, and 350^0C. A gradual decrease of the strength accompanied by a ductility increase can be observed for both alloys when the temperature rises up to 350^0C. Moreover, the differences between the TT loading and CC or FF loadings reside in the hardening-rate dependences on the induced plastic strain, ε_p, which are represented in Figures 54 and 55. For the TT loading, the hardening rate, defined as the flow-stress variation over the strain variation, $d\sigma/d\varepsilon_p$, is decreasing steadily during the deformation (Fig. 54b), as expected for the deformations caused by the dislocation-slip mechanism. On the contrary, for the CC loading direction, after a short initial decreasing stage, the hardening rate gradually increases with the enforced plastic deformation, and starts to decrease only in a late stage (Fig. 54a). This unusual behavior is believed to be the footprint of the twinning mechanism. In the early

stage of deformation, the twinning mechanism dominates the slip and reduces the hardening rate. The increase of the hardening rate comes with the gradual exhaustion of the twinning mechanism, which promotes an increased slip contribution. These two different hardening behaviors are common for the tests at room temperature, 150^0C, and 250^0C. The data collected at 350^0C show a dramatic reduction of the hardening rate, but the TT and CC/FF loadings give still different results.

The twining-like behavior is clearly visible in the AZ31 specimens loaded along the CC and FF directions from room temperature up to 350^0C. These specimens are rather brittle, with a better ductility when loaded along the FF direction. The TT-loaded samples show the temperature dependence, typical of a strain-stress curve, with a significant increase in the ductility when the temperature exceeds 150^0C. From the stress-strain curves of the ZK60 samples, CC, TT, and FF compressed at different temperatures (Fig. 53), it can be observed that the behavior of the FF-loaded samples is roughly similar with the AZ31 specimens FF compressed. At 350^0C for all loading directions, the ultimate stress of the ZK60 specimens is drastically diminished, and the ductility is improved up to 30 - 40% of the true strain. Meanwhile, the CC-loaded ZK60 samples show a twining-like behavior from room temperature up to 350^0C. However, the twining contribution seems to be reduced in the ZK60 specimens loaded along the TT direction.

Fatigue tests of both alloys, AZ31B and ZK60, were done for the samples loaded in the CC- and TT-directions. The stress amplitude versus cycles-to-failure for the two loading directions applied to the AZ31 samples is shown in Figure 56. The applied stress amplitudes during the fatigue tests were above the endurance limit, thus, the cycles-to-

failure are usually less than ~ 10^5 cycles. The S-N curves are sharply distinct for the two orientations, CC or TT. Higher stress amplitude is noticed for the CC-samples as compared to the TT-samples, where a sharper slope evidences a shorter fatigue life for this orientation. This trend seems to be the result of the grain-preferential orientation, relative to the cycling-loading direction.

The S-N curves, or the stress amplitude, $\Delta\sigma/2$, versus the number of reversals to failure, $2N_f$, can be expressed in terms of the Basquin equation [141]:

$$\frac{\Delta\sigma}{2} = \sigma_f^{'} \left(2N_f\right)^b \tag{63}$$

which provides two parameters for characterizing the fatigue life: σ_f' - the fatigue-strength coefficient, and b - the fatigue-strength exponent. The values estimated from the log-log experimental plots for both alloys are presented in Table 11. It can be seen that for the as-received material, both fatigue-strength parameters are more than twice greater for the TT-cut as compared to the CC-cut. As the value of b, rather then σ_f', determines the material endurance, the CC-cut, due to its enhanced ductility, exhibits a better fatigue life span than the TT cut, which can be considered as a brittle material.

In Figure 57, the total strain versus reversals to failure, for two loading directions, CC and TT, applied to the ZK60 samples, shows a much smaller difference between the CC- and TT-samples than for the AZ31 alloy.

The fatigue tests of the ZK60 alloy were performed under a total strain-controlled mode at room temperature. A triangular waveform with the total-strain amplitudes ranging

from 0.5% to 1.5% was applied in all fatigue tests. Fatigue experiments were run to the failure or separation of the specimens. The number of cycles-to-failure or separation was taken as the fatigue life, N_f. The total-strain amplitude, $\Delta\varepsilon_t/2$, was decomposed into the elastic, $\Delta\varepsilon_e/2$ and plastic, $\Delta\varepsilon_p/2$, components using the half-life hysteresis loops data, and represented in Figures 57a and 57b for the CC-loading and TT-loading, respectively. The elastic-strain amplitude can be related to the stress amplitude using the equation [141]:

$$\Delta\varepsilon_e/2 = E\cdot(\Delta\sigma/2) \tag{64}$$

where E is the Young's modulus, and $\Delta\sigma/2$ is the cyclic-stress amplitude, which is determined by the Basquin Eq. (63). The empirical Coffin-Manson law is relating the strain-fatigue life to the plastic-strain amplitude, $\Delta\varepsilon_p/2$, and can be expressed as [140]:

$$\Delta\varepsilon_p/2 = \varepsilon'_f(2N_f)^c \tag{65}$$

where ε'_f is the fatigue-ductility coefficient, and c is the fatigue-ductility exponent. The strain-amplitudes dependences of the number of reversals, as in Figures 57a and 57b, show a marked difference in the fatigue behavior of the CC and TT samples. Combining the two equations, the fatigue life under a given total-strain amplitude can be expressed as following:

$$\Delta\varepsilon_t/2 == \varepsilon'_f(2N_f)^c + \frac{\sigma'_f}{E}(2N_f)^b \tag{66}$$

These results will be further analyzed in correlation to the grain size and crystallographic texture.

4.2.2 Ductility and Fatigue after ECAP

Strain-rate sensitivity. It is known that the general flow curve for a given material depends on the temperature, T, and on the strain rate, $\dot{\varepsilon}$. This dependence varies with the material structure: BCC are more sensitive to T and strain rate than FCC. To define the overall response of the material, a relation between the dependence of the true stress and strain, strain rate, and temperature has to be found. Similar to the Hollomon relationship of the strain hardening, $\sigma = K \times \varepsilon^n$ (where n is the strain-hardening coefficient, and K is a material constant), the relation to include the strain-rate sensitivity factor, m, will be: $\sigma = K \times \dot{\varepsilon}^m$, where σ is the true stress, K is a material constant, and $\dot{\varepsilon}$ is the strain rate. Therefore, the strain-rate sensitivity, m, can be deduced from: $m = \frac{\partial \ln \sigma}{\partial \ln \dot{\varepsilon}}$. For the coarse-grained materials, the m values lie in the range $0.02 < m < 0.2$, while in UFG, a superplastic deformation behavior with $m \sim 0.5$ is to be expected. The superplastic behavior is linked mostly to the grain-boundary sliding (GBS), grain rotation, grain boundary migration, and/or bimodal grain size distribution [142-144]. It was found experimentally that the rate of flows in the superplasticity varies inversely with the grain size raised to a power of ~2. It was obtained, also, that the superplastic regime is displaced to faster strain rates when the grain size is reduced. The constitutive equation to describe the superplasticity can be expressed by [145]:

$$\dot{\varepsilon} = A \frac{D_0 G b}{KT} \left(\frac{b}{D} \right)^p \left(\frac{\sigma - \sigma_0}{G} \right)^n \exp\left(-\frac{Q}{RT} \right) \tag{67}$$

where $\dot{\varepsilon}$ - strain rate, A - constant, D_0 – the pre-exponential factor of diffusion, σ - stress, σ_0 - threshold stress, G - shear modulus, n - stress exponent, D - grain size, b - Burgers vector, p – the grain-size exponent, R - gas constant, T – the absolute temperature, and Q – the activation energy, which is dependent on the rate-controlling process. The three variables of n, p, and Q are often used to identify the deformation mechanism. Equation (67) was found to apply to Mg alloys [11]. For the AZ31 annealed alloy n = 3, p = 0, i.e., the deformation is independent of the grain size, and the activation energy is similar to that of the Al diffusion in Mg (Q_s = 143 kJ/mol). This means that for the coarse-grained alloy, the deformation mechanism is, probably, the glide of dislocations in grains. For the ECAP-ed AZ31, n = 2, p = 3, and the activation energy was 96 KJ/mol (as compared with 127 kJ/mol for the as-annealed samples), which is close to the value of the activation energy for the grain-boundary diffusion in Mg (Q_{GB} = 92 kJ/mol). These results suggest that the dominant deformation mechanism in the UFG-Mg alloy is, probably, that of the GBS accommodated by slip controlled by the GB diffusion [11]. For the AZ61 alloy, the activation energy was 143 kJ/mol, close to the value for the lattice diffusion in Mg (Q_L = 135 kJ/mol), then the dominant deformation mechanism is GBS accommodated by the slip controlled by the lattice diffusion [11].

Ductility. Tensile testing of the Mg alloys, ZK60 and AZ31B, at temperatures ranging from room temperature to 450^0C, showed [37, 50] that after ECAP, the yield and the UTS decreased at the expenses of the ductility, which was improved 2 - 3 times for the ZK60, but not significant for the AZ31B alloy. The tensile testing results of ZK60 for different number of ECAP passes are shown in Figure 58a for the testing at room temperature, and in Figure 58b for the testing at 350^0C. Few observations can be made: (i) the ductility of

ZK60 improved after first pass of ECAP, when tested in tension at room and high temperatures; (ii) two passes and more continued to improve the ductility based on the conversion of the LAGBs into HAGBs, and the increased amount of HAGBs enhances the GBS mode of deformation; (iii) at room temperature, even the grain size decreased, the yield stress drops with the number of ECAP passes; the effect could be due to the reduction of the precipitate strengthening at the high ECAP temperature of 260^0C, as compared to the T5 aging at 177^0C; (iv) the strain hardening and ultimate tensile strength are almost not changed after ECAP; and (v) at high temperatures, the initial flow stress hardens rapidly, while for the ECAP-ed samples it drops, and, with increasing the strain, a quasi-steady state behavior with a wavy shape of the flow denotes that the dynamic recovery/recrystallization process occurs. After tensile testing at 350^0C, as in Figure 58b, the ductility is improved after 1, 2, 4, and 8 passes of ECAP, route A. At the beginning of the deformation, the as-received samples harden abruptly, and afterwards the flow stress decreases, and the strain is limited to a value of ~ 5%. The stress-strain curves of all ZK60 ECAP-ed samples demonstrate an almost constant increase of the ductility, which reaches values of 70 - 90 %.

The normalized stress, calculated as a ratio between the ultimate-tensile true stress, σ_{UTS}, and the shear modulus, G (the value of G is taken from Ref. [40]), is represented in Figures 59a and 59b, versus the strain rate and test temperature, respectively [50]. The activation energy, calculated from the stress data versus temperature (Figure 59b), at the strain rate of 5×10^{-3} s^{-1}, has the value of 80 kJ/mol for the ECAP-4A. This value suggests that the main ECAP deformation mechanism in the ZK60 alloy is the GBS

accommodated by slip controlled by GB diffusion, as shown for the AZ91 Mg alloy [21] (with the activation energy of 95 kJ/mol). The strain-rate sensitivity at 350^0C seems to be in the range of m = 0.3 - 0.5 regardless of the processing history (see Fig. 59c), i.e., the ECAP deformed samples via route A, B, or C give similar results, independent of the straining path, when tested at 350^0C.

In Figure 60, the elongation-to-failure versus ECAP strain intensity (1, 2, 4, and 8 passes, route A) is represented for the AZ31 and ZK60 samples (gage length of 25.4 mm), tested in tension at room temperature and at high temperatures, with a strain rate of 5×10^{-3} s^{-1}. It can be observed that at room temperature, an improved ductility trend starts right after one pass of ECAP, but the differences are not significant if the deformation continues up to 8 passes. At high temperatures, the ductility is clearly increased as compared to the as-received samples. After ECAP, 2 passes, route A, the elongation increases by ~ 2 times, and it maintains approximately the same value until 8 passes. Furthermore, at 450^0C and strain rate of 5×10^{-3} s^{-1}, the elongation-to-failure of the ECAP-ed samples reaches the value of 155%, which corresponds to ~ 3 times of that of the as-received ZK60 alloy.

Various strain paths were analyzed, and, as shown in Figure 61 (for the tensile samples with the gage length of 12.7 mm), a ductility of 371% was obtained after the ECAP deformation in 4 passes via route A, a 335% value for the deformation in 4 passes via route C, and a value of 325% for ECAP, 4 passes, route B_C, when ZK60 was tested in tension at 350^0C, and the strain rate of 10^{-2} s^{-1}. Therefore, the elongation shows no clear dependence on the strain path.

Cyclic fatigue. The samples geometry for fatigue was round and tapered at both ends, with a diameter of 3.175 mm and a total length of 17.5 mm. The samples were cut from the as-received plate and the ECAP-deformed billets along two different directions, CC and TT: CC - parallel to the extrusion/pressing direction and normal to the C plane, and TT - normal to the T plane. The fatigue tests were conducted at room temperature, under a load control, at a frequency of 10 Hz and a stress ratio of R = –1, where $R = \sigma_{min.} / \sigma_{max.}$; $\sigma_{min.}$ and $\sigma_{max.}$ are the applied minimum and maximum stresses, respectively. The stress amplitudes versus cycles-to-failure of ECAP-ed AZ31 are represented in Figure 62, for the three loading directions, CC, TT, and FF. After one and two passes of ECAP deformation, there is a steady decrease in the fatigue-strength coefficient with the number of passes, but the absolute values of the fatigue-strength exponent are reduced in a higher degree, resulting in a significant improvement of the fatigue endurance. Moreover, the improvement of the fatigue life due to the ECAP prior to the cyclic loading is more pronounced in the specimens loaded along the TT-direction, rather than CC. As was mentioned before, the as-received material has a hard orientation with the load applied along the TT-direction, for both compression and tension. The change in the texture induced by the ECAP is improving the ductility, as a smaller amount of grains are oriented with the *c*-axis along the loading direction. The case of the CC-loading is quite different. For the as-received samples, the CC-orientation is soft in compression, due to the contribution of twinning to the plastic deformation [135]. However, this orientation is still hard in tension, and a significant increase in tensile ductility is expected when the basal fiber orientation goes out of the plane perpendicular to the loading direction. The enhancement of the tensile ductility with the number of ECAP passes (up to 4 passes) for

the samples loaded in the CC-direction was reported recently [147], and our fatigue results seem to follow the same trend.

A further pressing from the $2B_C$ to $8B_C$ passes results in a different fatigue behavior. In both CC and TT cases, the fatigue curves corresponding to the specimens tested after $8B_C$ passes of ECAP are obviously distinct from the other cases. The CC-loaded samples are showing a decrease in ductility due to the fact that the fatigue-strength exponent, b, increases (see Table 12). In the TT-loaded samples the ductility reaches a value compatible with the CC loading after one pass of ECAP, but it is accompanied by a much smaller strength. A significant decrease in tensile ductility of the CC-loaded samples, between 4 and 8 passes of ECAP, was also reported in Reference 147. The ductility evolution with the level of the plastic strain enforced by ECAP, i.e. the number of passes, can be linked with the texture evolution. This trend could be the case with our measurements, but a quantitative evaluation is beyond the scope of this work. Even if we explain qualitatively the change in the ductility by the texture evolution, it is still not clear why the fatigue strength in the TT direction after $8B_C$ passes of ECAP is diminished if compared with a CC-oriented sample after one pass, which has the same ductility. It will be shown below that the processing in $8B_C$ passes using the back-pressure improves the fatigue strength. Figure 62 exhibits the fatigue improvement of the $8B_C$ passes samples loaded along the TT direction using a back-pressure. For the $8B_C$ samples without the back-pressure, the fatigue lives are shorter than those of the $2B_C$ passes specimen for stress amplitude greater then 140 MPa. Due to the application of the back-pressure, the fatigue lives are improved greatly, and also longer than those of the $2B_C$ passes samples (Fig. 62). However, the enhancement in the strength induced by the back-

pressure is accompanied by a loss in the ductility, visible from the slope of fitted lines (see also Table 12), which suggest that beside the microstructure improvement a texture difference can be also involved in changing the fatigue behavior of the $8B_C$ specimens.

4.3 Deformation Textures in Mg-Alloys

Studies of the deformation textures, developed by a simple shear during ECAP, showed specific preferential orientations, for different crystallographic structures including the face-centered-cubic (FCC) copper [82, 148-153]. It was found that the ECAP textures have characteristic features, if compared to the typical rolling or drawing (pure shear), or torsion (simple shear) textures. The cursory analysis for cubic materials suggests that a texture similar to rolling will develop when using route A, and an extrusion-type texture when using route B. The texture was found [153] to depend, as well, on the ECAP-die angle.

4.3.1 Rolling and Extrusion Textures in Mg alloys

In polycrystalline materials with a hexagonal structure, the texture is more influential in determining the mechanical properties. This trend is due to the limited number of slip systems available for accommodating the plastic deformation, and other mechanisms of deformation, such as twinning, become more probable. Classical forming processes, including extrusion or rolling, produce strong textures, which enforce an unusual anisotropy of the mechanical properties. For pure Mg and Mg-alloys, the rolling texture exhibits a strong preferential grain orientation with the <00.1> basal poles parallel to the normal direction, whereas an hydrostatically-extruded bar shows a fiber texture with <10.0> prismatic poles parallel to the extrusion direction [149]. Starting a subsequent

process step with such highly anisotropic materials would be a risky endeavor without understanding the mechanisms of deformation. The deformation of Mg and Mg-alloys involves crystallographic <a> slip along three $\langle 11\bar{2}0 \rangle$ type directions on one basal-plane (0001), three $\{10\bar{1}0\}$ prismatic-planes, and six $\{10\bar{1}1\}$ pyramidal planes, as well as twinning on pyramidal $\{10\bar{1}2\}$ planes along $\langle \bar{1}011 \rangle$ [70]. As for magnesium with c/a = 1.624 < $3^{1/2}$, the twinning will lengthen the grain along the original basal direction (tensile twin, see Fig. 63). Therefore, the twining will operate efficiently in compression on those grains oriented with the basal pole almost perpendicular to the pressing direction.

The effect of twinning during compression at room and high temperatures of 150^0C, 250^0C, and 350^0C will be analyzed for two starting textures, rolling (AZ31) and extrusion (ZK60), in order to explain the mechanical responses of these two Mg alloys. The established specific mechanisms of the plastic deformation will constitute the database for studying and understanding the ECAP textures.

The techniques used to characterize the textures were low-energy (LE) XRD, high-energy (HE) XRD (synchrotron radiation), and neutron diffraction, which were described in the Section 3.2. The deformation textures by the rolling and extrusion, as measured by the LE-XRD technique, have been presented in Figures 32a and 32b for the AZ31 and ZK60 alloy, respectively. The most important distinction between the two modes of deformation is that the rolled AZ31 exhibits a basal fiber along the ND direction, which is the normal to the rolling direction (see the (00.2) PF in Fig. 32a on the top, T, plane), and a prismatic fiber for the extruded ZK60 along the extrusion direction, XD, (see the

(10.0) PF in Fig. 32b on the cross, C, plane). As the LE-XRD probes only a superficial layer of the sample, the PF's on three orthogonal planes, F, T, and C were recorded. The fiber along the XD direction is not directly accessible in the experimental PF's on the top and flow planes, but the patterns extrapolated with the popLA software (for tilting angles larger than 75^0) confirm the existence of this texture feature, i.e., the right and left spots of the <10.0> PF's measured on the T and F planes. Thus, by combining the three PF's, it is possible to identify the texture features which correspond to the bulk of the material, as they should be observed on all three surfaces accounting for the coordinate system change. This is why a three-dimensional (3D) representation of the PF's in Figures 32a and 32b was preferred.

The same samples, taken from the starting materials, were characterized by the HE-XRD (Fig. 64a and 64b) and neutron diffraction (Fig. 64c) techniques. In the neutron diffraction measurements, the texture information is averaged over the whole-sample volume, and clearly represents the bulk. The corresponding PF's calculated for the neutron diffraction on the C plane and for two reflections, (10.0) and (00.2), of the as-received ZK60 are presented in Figure 64c. The comparison of the (10.0) PF from Figure 64c with the same X-ray pattern from Figure 64b, plane T, confirms the existence of the <10.0> fiber texture oriented along the XD direction. This fiber is rather inhomogeneous, as the distribution of the basal poles in the C plane is not homogeneous. The basal poles are more likely to align close to the normal directions, ND and TD, (see Fig. 32b, T and F planes) corresponding to the top and flow planes, respectively. Beside the main <10.0> fiber, a basal preferential orientation can be observed as a central spot in the LE-XRD

<00.1> PF on the C plane (Fig. 32b). This feature is not confirmed by the corresponding neutron PF from Figure 64c, and is probably due to a surface artifact.

The characterizations of the as-received samples, AZ31 and ZK60, using the synchrotron radiation, provided the HE-XRD IPPDs represented in Figures 64a and 64b, respectively, for the three surfaces of observations, F, T, and C, and for two reflections planes (10.0) and (00.2). For the ZK60 samples, the HE-XRD (Fig. 64b) and LE-XRD (Fig. 32b) results are similar and confirm each other, but some details can be discussed. The samples have a medium grain size, as the angular dependences are relatively smooth. As seen in the optical micrograph from the Figure 26b, the bimodal grain size indicates that a grain substructure may be present, and it is detected by this high-resolution technique. From the IPPDs in Figure 64b, it results that the prismatic fiber component, <10.0>, parallel to the XD axis, confines the basal poles close to the C plane. The basal pole from the IPPD in Figure 64b, is seen as spreading in the F plane about the ND axis with $\pm 20^0$ out-of-plane**,** and less then 10^0 in the T plane (about the TD axis).

4.3.2 Texture Evolution during Uniaxial Compression of Mg Alloys

The tension/compression asymmetry, as shown in Section 4.2.1, was explained by the involvement of the twinning mechanism during monotonic loading [131-134]. The rolled Zr was tested in compression for different loading directions at -198^0C, and the texture was shown to evolve due to the slip and twinning mechanisms [138]. A composite-grain model was developed and introduced in the Visco-Plastic-Self Consistent (VPSC) model [139] to describe the twinning contribution to the deformation.

To elucidate the deformation modes under compression of Mg alloys, the unixaxial compression was performed at room and high temperatures, and the texture evolution, characterized using LE-XRD, HE-XRD, and neutron diffraction, will be described in the following.

Uniaxial compression at RT. The LE-XRD PFs of the ZK60 samples, compressed at RT and loaded CC and TT, are represented in Figures 65 to 68. During the CC-compression up to 5% of the engineering strain, the main texture component seen in the as-received specimen (the <10.0> pole on the C plane in Fig. 65a) is transformed into a strong fiber texture (the daughter component on the C plane in Fig. 65b), with the basal pole aligned parallel to XD, evidencing the twinning effect. Due to the twinning mechanism, the basal poles tend to reorient against the CC direction, inducing a material hardening, as indicated in the hardening-rate curve from Figure 55a. The texture transformation is not complete, the initial texture components being easily recognizable (see on the C plane the remaining mother <10.0> in Fig. 65b). After the TT-compression (perpendicular to the extrusion direction), the effect of twinning is less evident as seen in Figure 67 for the (10.0) reflection, and in Figure 68 for the (00.2) reflection. However, the basal poles, initially aligned along the TD direction (the F and T planes in Fig. 68a), reorient at $\pm 30^0$ against the loading direction, ND (the T plane in Fig. 68b) forming the daughter-grain component of the texture. As the basal poles belonging to the daughter-grain population are not perfectly aligned along the loading direction (Fig. 68b, T plane), the hardening rate shown in Figure 55b is almost constant with the imposed plastic strain, and is not increasing significantly as in the CC-loading case (Fig. 55a).

In addition to the LE-XRD measurements, the neutron-diffraction of the CC- and TT-compressed ZK60 samples helped to quantify the twinning fraction for different levels of straining. For example, the PFs of the CC compressed samples, strained at 5% and 11%, respectively, show that at 5% straining (Fig. 69b), the mother texture persists in the (00.2) PF, and the daughter texture is formed as a <00.1> fiber parallel to the XD-direction, while at 11% straining (Fig. 69c), only the daughter texture is visible, in accordance with the HE-XRD results of the same sample, ZK-CC-RT, in Figure 73. The ZK-TT sample after 25% compression (Fig.69c) exhibits the transformation of the basal poles of the starting material, lying along the ND and TD axis, into four basal components deviated from the ND-direction (the top plane observed in Fig. 68c), in accordance with the LE-XRD measurements from the Figure 68b.

The AZ31 samples, compressed along CC, TT, and FF directions (AZ-CC-RT, AZ-TT-RT, and AZ-FF-RT), were characterized using the HE-XRD technique, and the IPPDs were taken from three planes of observations, F, T, and C, and represented in 3-D plots for only two (out of 21 peaks measured) reflection planes, (10.0) in Figure 70, and (00.2) in Figure 71. Comparing the IPPDs of the as-received and after the CC-compression at RT, in both figures, it can be seen that the material has much smaller grains than before the compression. The twinning activity during the CC-compression of the AZ31B alloy is evidenced by comparing, for example, the basal poles, before and after the deformation by compression. The basal poles after compression align near the XD-axis (see AZ-CC-RT and AZ-CC-350^{0}C), as compared to the as-received sample (Fig. 71), which show a preferential orientation of the <00.1> pole along the ND axis. This result clearly

indicates a twinning mechanism, where the initial basal-fiber texture (mother), parallel to the ND-axis, was transformed during the CC-compression into a basal-daughter fiber texture, parallel to the XD-axis, i.e., along the loading direction. Thus, the grains oriented with their crystallographic axis perpendicular to the loading direction will completely reorient during compression along the loading direction, CC.

The HE-XRD IPPDs of the ZK60 samples, CC-compressed at RT with a strain rate of 5×10^{-3} s^{-1} are represented for the reflection (10.0) in Figure 72, and for the reflection (00.2) in Figure 73. A broad <00.1> basal fiber along the XD-axis is observed, in accordance with the LE-XRD and neutron-diffraction results (Figs. 66b and 66c). More details are provided by the IPPDs of the same sample, where, as seen in Figure 73, the angular spread of the basal pole pointing toward the XD-axis is 40 - 50^0, in both T and F planes, being rather asymmetric in the F plane. Some grains are still having the basal pole oriented perpendicular to the XD-axis, almost parallel to the ND-axis, and, probably, it is what it has been left from the initial texture.

While the effect of the CC compression can be rationalized as a texture transformation from a prismatic fiber along XD (Fig. 72, as-rec.) to a basal fiber about the same direction (Fig. 73, the planes, F and T, of the ZK-CC-RT sample; see also Fig. 74a for the schematic of the twinning of the CC samples), in the case of the TT compression, the texture change exhibits a much more complex behavior. A part of the initial prismatic fiber (Fig. 72, as-rec.), i.e., the grains with the basal pole aligned close to the ND direction (Fig. 73, as-rec.) is preserved. A new prismatic fiber of daughter grains appears along the TD direction, as seen in Figure 72, the sample, ZK-TT-RT. For this kind of

grains, the basal poles of the same sample in Figure 73 are aligned at $\pm 30^0$ relative to the ND normal, in the F plane (see Fig. 74b for the schematic of twinning of the TT samples).

Uniaxial compression at high temperatures. The study of the textures, resulted after the CC, TT, and FF compression of the AZ31 alloy at higher temperatures (150^0C, 250^0C, and 350^0C), showed no significant changes up to 250^0C, and, this is why, only the RT and 350^0C are represented in Figures 70 and 71. After the CC-compression at 350^0C, as it can be seen in Figure 70 (the sample, AZ-CC-350^0C), the IPPDs structure displays multiple sharp peaks, suggesting that the grains are growing during the test, and large recrystallized grains are formed during the plastic deformation in compression at 350^0C. Moreover, the IPPDs of the sample, AZ-CC-350^0C, in Figure 71, exhibits a splitting of the basal fiber, parallel to the XD-axis, in two components at $\pm 30^0$ relative to the CC loading. The TT-loading of the AZ31 samples, at RT and up to 350^0C, keeps the basal pole parallel to the ND-axis, just like in the as-received material (Fig. 71), and, similarly, the <10.0>, lying in the T-plane (Fig. 70), is also preserved. The only difference is that the grains are smaller as compared to the as-received samples, which yield to the conclusion that the plastic deformation during the TT-loading enforces the grain refinement and very little changes in the texture. In the case of the AZ-FF samples (Fig. 71), the compression resulted in a basal fiber reorientation from the ND-axis to the TD-axis (compression direction), which is essentially the same behavior as for the CC-compressed samples, but no temperature dependence was noticed.

The HE-XRD IPPDs of the ZK60 samples, CC- and TT-compressed at high temperatures, are shown for the (10.0) reflection in Figure 72, and for the (00.2) reflection in Figure 73.

The ZK-CC samples display a well-defined basal fiber along the XD-axis, much sharper than that observed in the sample processed at RT. Beside this texture component induced by twinning, the basal pole in the C-plane (Fig. 73) is what is left from the initial texture, and amounts ~ 5 to 15 percent from the total grains, depending on the testing temperature, and, probably, of the value of the plastic strain.

The compression TT of the ZK60 samples at high temperatures produced a change in texture similar to the RT compression (Fig. 73, ZK-TT samples). However, by increasing the testing temperature, a sharpening of the basal-pole distribution around the ND-axis (Fig. 73), as well as the homogenization of the prismatic-pole distribution in the T plane (Fig. 72) is noticed. Therefore, whereas the deformation texture after the TT compression at RT should be attributed to a sum of two prismatic fibers (Fig. 72), the texture resulting from the compression at 350^0C can be considered as a basal fiber along the ND direction, i.e., along the TT loading. This complex behavior after the TT compression of the ZK60 alloy was not yet predicted by the theoretical models. It is possible that the dynamics of the available slip systems is different for the TT compressed ZK60, and the role of the < c + a > dislocations is diminished, as will be analyzed in the Section 4.4.

4.3.3 Texture Evolution during ECAP Deformation of Mg Alloys

The analyses of the texture evolution during the uniaxial compression of Mg alloys, as discussed in the Section 4.3.2, showed that the twinning mechanism can induce major changes in the texture, if the initial texture contains a significant fraction of the grains

oriented with their c-axis nearly perpendicular to the compression direction. The questions we want to answer will be: (i) to identify the specific textures formed during ECAP deformation, depending on the initial texture, on the strain intensity, and on the processing routes, and (ii) to track the possible twinning contributions in a severe deformation mode, such as ECAP.

Some experimental results concerning the texture generated after multipass ECAP of ZK60 have been reported [50,114,148,154], as well as, polycrystal-plasticity simulations to discriminate the relative activities of the different deformation mechanisms [148].

The stability of the texture component <00.1>, parallel to TD after one pass of ECAP was interrogated in [50]. However, further processing of the ZK60 samples in ECAP via route A, gradually suppressed the <00.1> preferential orientation (see Fig. 75). The resulting basal fiber is oriented almost parallel to the ND, and slightly rotated counterclockwise (CCW) around TD. This is not a simple stable texture feature, as found in a monotonic-straining process, because the ECAP deformation enforces a rigid-body rotation. Thus, during each pass, the grains rotate in a consistent way, generating a similar texture at the end of the processing step. The basal fiber in Figure 75, parallel to ND, was obtained by the extrapolation of the data recorded on the F plane. Therefore, a detailed analysis was not possible. Subsequent measurements, using LE-XRD and OIM techniques (see Fig.76) on the T plane of a specimen representative for the ECAP after 8A passes show a split in the basal fiber (Fig. 76a, LE-XRD PFs). This texture feature reproduces the OIM result on the same sample, which exhibits two distinct preferential orientations (Fig. 76b, OIM PFs): one aligned fairly close along the top-plane direction,

ND, and another at ~ 45^0 away from this direction. Based upon the OIM data set, the grains that were less deformed had the <00.1> poles split away from ND, and the more severely deformed grains had the poles near <1.02>, aligned with ND. However, the poor statistics of the OIM data could not provide the texture components with certainty.

The PFs of the ZK60 deformed in ECAP using different routes (A, B_C, and C), 4 passes, are represented in Figure 77. Whereas the routes, A and C, give similar results, the route B demonstrates a different behavior. An intense basal fiber, oriented parallel to TD can be seen in Figure 77c for the route 4B. As the billet is rotated 90^0 around its axis (XD), before each pass, it is possible to consider this texture component as remnant from the previous step. The degree of redundancy in the case of the route B_c (a consecutive rotation of 90^0 between the passes) demonstrated in Figure 21 is the leading factor for this behavior. Thus, the two basal fibers seem to persist along a B processing path of ZK60, at least for relatively small number of passes. The OIM of the LAGBs and HAGBs distributions (Fig. 49) of the ZK60 ECAP-ed in 8 passes, route A, resulted in only a 20% increase of the HAGBs as compared to the as-received sample, and this is why it is reasonable to believe that after 4 passes little change in texture can be expected.

The ECAP of Mg alloy, AZ31, produced a different texture evolution. After one pass, the initial basal fiber parallel to ND rotates CCW around the TD axis with a significant amount (Fig. 78). The split in the final fiber is also evident. The lattice rotation during ECAP seems to differ significantly as opposed to ZK60, which evidenced a rigid-body rotation. The plastic spin becomes important, and is not restricted in the F plane when route B is used. The PFs showing the progressive texture evolution along route B, with

back-pressure are represented in Figure 79, before and after the popLA extrapolation to full PFs. The PFs were recorded in the F plane, and clearly demonstrate how the fiber axis is moving out-of plane. The texture is strengthened during ECAP, contrary to believe that ECAP weakens the texture.

The evolution of the ECAP textures of the ZK60 and AZ31 alloys can be understood by considering only the slip, as a main plastic deformation mechanism. As shown from the VPSC modeling by Agnew et al. [148], the <a> dislocations - basal and prismatic slip - is mainly responsible for the texture evolution and plastic deformation. An important amount of the deformation is also produced by the < c + a > dislocations pyramidal slip, which can explain the splitting of the fiber texture in both alloys. No significant traces of twinning were detected. However, a detailed study of one pass of ECAP, which will be presented in the next section, was able to reveal the contribution of twinning during the early stage of ECAP deformation, when the material is under the constrain by the die walls compression, and the shearing process has not started yet, i.e., a stationary regime was not reached. Figure 80 includes the IPPDs obtained from the HE-XRD on the ZK60, as-received sample and at a location close to the entrance in the first channel of the partially-deformed billet. Given the fact that this location is away from the intersection between the two channels, and, therefore, away from the PDZ, the billet was subjected to a hydrostatic pressure only at the ECAP temperature of 250^0C. The corresponding IPPDs exhibit a new texture component developed in the billet, with the basal pole <00.1> oriented along the pressing direction. This preferential orientation is clearly produced by

twinning the grains, which had the basal pole oriented almost perpendicular to the pressing direction.

4.3.4 Elastic Microstrain and Coherent-Domain Size from the XRD Profiles

The XRD pattern of the $\theta - 2\theta$ scans contains the information about the grain substructure, and the peak-broadening profile is usually interpreted in terms of the coherent-domain size, d_X, and elastic microstrain non-uniformity, e_m, or root-mean-squared (r.m.s.) elastic microstrain. As was already shown in the Section 3.2.2, there are two common approaches to extract the crystallite size and strain associated with lattice defects from the powder-diffraction data by *line-broadening analysis* (LBA): Williamson-Hall [110] evaluating the coherent-domain size and elastic microstrain based on the integral breadth of the diffraction lines, or the other method, Warren-Averbach [111] based on the Fourier analysis of the line profiles.

Dislocations can produce a line-broadening anisotropy [116], because they are lattice anisotropic defects, which give an anisotropic contrast in diffraction. To account for this anisotropy, the classical models of WH and WA are modified [117] by replacing the modulus of the diffraction vector, g, with $g \times C^{1/2}$, where C is the average contrast factor. Therefore, the peak-broadening analyses enable the determination of the coherent-domain size, the elastic microstrain, and the structure of the dislocations, including the dislocation density and their character, edge or screw, or a combination between the two. From the $\theta - 2\theta$ spectra measured on three planes of observations, flow, top, and cross, for the as-received alloys, AZ31 and ZK60, and for the compressed and ECAP-deformed

samples, only three directions were selected to illustrate the peak-broadening changes, i.e., the maxima at <20.0>, <11.2>, and <20.1> for each case (see Figs. 81 and 82).

The whole-pattern fitting (WPF) method used for the peak-broadening analyses of samples, before and after plastic deformation during compression and ECAP was described earlier in the Section 3.2. The $\theta - 2\theta$ scans have been obtained, similar to the pole figures, on three surfaces of observations, flow (F), top (T), and cross (C). In Figure 81, a large peak broadening is observed for the compressed ZK60 sample, as compared to the as-received condition. Surprisingly, the ECAP-ed samples do not show a broadening effect relative to the as-received samples, which can be due to the severe plastic deformation in ECAP, they show even a peak sharpening in the flow direction (Fig. 82). For this direction, the elastic microstrain was reduced to 10^{-4}, suggesting that a dynamic recovery/ recrystallization process was activated during the ECAP at 260 ^{0}C.

From the LE-XRD profiles analyses, the volume-averaged coherent-domain size, D_V, the percentage of the <a>, <a + c>, and <c> dislocation debris, corresponding to the three orientations of the Burgers vectors, and the dislocations density, ρ, were calculated, and presented in the Table 13 for the AZ31 alloy. The intensities ratio, $I_{00.2}/I_{10.0}$, is also shown for comparison. From the Table 13, is can be seen that in the AZ31 alloy, compressed at RT, the contribution of the <a> dislocations decreased. Therefore, the components, <c> and <c + a>, become active during the deformation. At high temperatures, the weight percentage of the <a> dislocations is increasing to the initial value. Thus, the recovery/recrystallization processes came into play. The total density of the dislocations

increased during the deformation, and decreased when the material was tested at 350^0C, supporting well this assumption.

4.4 Mapping the Texture Evolution in ECAP

Two Mg alloys, AZ31B (hot-rolled), and ZK60-T5 (hot-extruded) were subjected to severe plastic deformation by ECAP, using a die with 90^0 between the two channels. All billets were deformed at the ECAP temperature of 250^0 C (with a pre-ECAP heating for 30 min), and the processing rate of 0.5 mm/sec. In order to assess the different deformation mechanisms activity, the texture evolution during ECAP was mapped on partially-deformed samples, using both LE-XRD and HE-XRD techniques. The mapping procedure allowed obtaining the pole-figures (PFs) for the undeformed and deformed areas of each billet, at approx. 20 - 60 locations, with different shear-strain values, determined experimentally on the same billets. The basal, prismatic and pyramidal poles were mapped on three orthogonal surfaces of each billet, and for billets cut along (named CC-billets) and perpendicular (named FF-billets) to the rolling/extrusion directions.

Background. For understanding the details of the ECAP deformation mechanisms, a texture-mapping procedure was applied by *decomposing the large ECAP-deformation into fine steps* to capture, in a spatial-temporal manner, the texture evolution of the partially-deformed billets (PDB) during ECAP. The texture mapping provided the first evidence of the *lattice rotation during ECAP of Mg alloys.* In contrast with uniaxial tensile or compression straining, the simple-shear deformation in ECAP implies a rigid-body rotation, similar to the deformation by torsion [155]. In this case, the initial texture

and work hardening are two effects which influence the directional properties of a single-phase alloy, and were shown to contribute to compression (or lengthening) at room temperature, or tension (or shortening) at high temperatures [156] along the torsion axis. The texture was observed to tilt in the sense opposite to the shear (at small strains), or parallel to the shear at large strains [157]. In the ECAP mapping case, given the fact that during the steady deformation process was suddenly stopped, different points on the texture maps will correspond to different deformation times, the rotation of the material element (rigid body), the plastic rotation, and the lattice rotation are to be considered in the texture evolution. The rigid-body spin, $\dot{\beta}$, (the rotation rate of the material element in laboratory coordinates) is defined [155] as the difference between the velocity gradient, $\dot{d}$, and the principal axes of the strain rate, $\dot{\varepsilon}$, in laboratory coordinates:

$$\dot{\beta} = \dot{d} - \dot{\varepsilon} \tag{68}$$

Note that the material flow lines are parallel to the principal axes of the strain rate, $\dot{\varepsilon}$. The rigid-body spin decomposes into the lattice rotation, $\dot{\Omega}$, (the rotation of the lattice with respect to the laboratory coordinates), and the plastic spin, $\dot{\omega}$ (the rotation rate of the material element with respect to the crystal-lattice coordinates):

$$\dot{\beta} = \dot{\omega} + \dot{\Omega}. \tag{69}$$

If $\dot{g}$ is the velocity gradient of the material with respect to the lattice, the plastic spin, $\dot{\omega}$, will be defined as:

$$\dot{\omega} = \dot{g} - \dot{\varepsilon} \tag{70}$$

The plastic spin was shown [155] to solve the unrealistic response of the materials to the severe plastic deformation by a simple shear, and plays a role in materials where the plastic anisotropy was induced by deformation. The crystallographic textures promote such anisotropies. In the present texture-mapping procedure, the experimental macroscopic-deformation gradient was obtained from the distortion of the scribed network of the partially-deformed billet [65,78,112], while the lattice rotation was determined from the incremental texture evolution along a flow line.

The texture evolution during ECAP can impact the mechanical behavior of the materials. Some experimental results concerning the texture generated after multipass ECAP of ZK60 have been reported [50,148], as well as, polycrystal-plasticity simulations designed to discriminate the relative activities of different deformation mechanisms [148]. The present mapping procedure allowed identifying the texture changes not only at the beginning and the end of deformation; the measurements captured, in a spatio-temporal manner, the texture evolution of the partially ECAP-deformed billets. When mapping the ECAP texture, the amount of the shear-strain at each sampling point of the ECAP-ed specimen was known from the experiment on scribed billets, and calculated, based on the slip-line theory [61], by using a reported method [65].

Samples preparation. The samples for this study were cut from the rolled plate of the Mg-alloy, AZ31-H24, with the nominal composition in weight percent (wt%) of 96Mg-1Zn-3Al, and from the extruded plate of ZK60-T5, with the nominal composition of 94Mg-5.5Zn-0.45Zr. The H24-temper signifies a strain hardened and annealed alloy, and T5-temper an artificially-aged alloy (solution treatment at 535^0C for 2 hrs, quenching in

hot water, and aging at 185^0C for 24 hrs). The billets for the ECAP deformation and characterizations were cut in two different directions, along (named CC-billets) and perpendicular (named FF-billets) to the rolling/extrusion directions, and, therefore, during ECAP, the billets were pressed along the CC- and FF- directions, respectively. The three directions in the sample coordinates were assigned as shown in Figure 25: the direction, XD, parallel to the rolling/ extrusion/pressing direction and normal to the cross plane, C; the direction, TD, normal to the flow plane, F, and the direction, ND, normal to the top plane, T.

The 9.5 × 9.5 × 51 mm billets for the ECAP deformation were split in two parts, and scribed with a 1 x 1 mm grid in order to visualize the macroscopic deformation pattern (see Ref. 151 for details). The processing die has two channels at 90^0 with an outer-corner roundness of 30^0. For both alloys, the ECAP temperature was 250^0C, and the pressing speed was 0.5 mm/sec. The process was suddenly stopped and the two L-shaped parts of the billet were quickly removed from the die. The partially-deformed billets (PDBs) were later examined for determining the grid deformation (stream lines and transversal lines, see Fig. 83), as well as the local preferential orientation of the grains. It is important to mention that the billets were ECAP-ed in two conditions: in the first case, the billet was introduced in the die in such a manner that the top plane (after rolling or extrusion) becomes flow plane in ECAP, and in the second case, the initial flow plane remains flow plane in ECAP.

In order to collect the information from all three surfaces of each PDB, the billets were cut in small bars of 1.25 × 1.25 mm cross section. The bars cut horizontally (Fig. 84a)

were rotated 90^0 in order to be used for recording the IPPDs of the undeformed C_0-plane, which is becoming after ECAP the final T_1-plane (top). Similarly, the bars cut vertically (Fig. 84b) were rotated 90^0 and used to record the IPPDs for the undeformed T_0-plane, which is becoming after ECAP the C_1-plane (cross). The IPPDs measurements were performed for approx. 50 locations to cover the whole undeformed and deformed areas. The LE-XRD technique was used only for the locations from the central part of the billet (″a″ through ″g″ as in Fig. 83), and the corresponding transient shear-strain values, γ, determined experimentally [65] are: 0.2 (a), 0.5 (b), 1.1 (c), 1.35 (d), and 1.4 (e), 1.5 (f), and 1.55 (g).

Results. The textures of the *as-received* materials were investigated from the XRD-PFs, taken from three orthogonal planes of the samples, and completed to full PFs using the popLA software [120]. This somewhat redundant procedure confirmed that the medium-energy XRD data reflect the bulk response of the samples. In Figures 32a and 32b, the initial textures of the rolled AZ31B and the extruded ZK60 samples are presented in a 3-D plot of the LE-XRD PFs for the three surfaces of observations**,** and for the three reflection planes, {10.0}, {00.2}, and {10.1}. The grains of the as-received AZ31 are preferentially oriented with the basal pole, <00.1>, perpendicular to the rolling direction, along the ND axis (on the top plane observed). Meanwhile, the PFs of the as-received ZK60 alloy show a main texture component, with a prismatic pole aligned along the extrusion direction, XD (on the cross plane observed). The basal pole was oriented perpendicularly to the XD, preferentially along the TD (on the flow plane observed) rather than along the ND.

The HE-XRD IPPDs for three planes observations of the same samples (Fig. 39) in the as-received condition confirmed the LE-XRD results, but some details can be discussed. The AZ31 samples show large variations of the pole intensities, indicating the presence of recrystallized grains after hot rolling, while the IPPDs of the as-received ZK60 exhibit a medium grain size for this sample. A fiber component, <10.0>, which contains 60% of the grains with the basal pole, <00.1>, is spreading over ± 30^0 toward the ND axis. On the other hand, the <10.0> pole was pointing toward the XD axis, and had two components: one component was spanned over 20^0, and was lying in the T plane, and the other component was spanned over 10^0, and was lying in the F plane. Some of the grains, with the basal pole oriented along the ND axis, and with the <10.0> pole along TD, were not included in the main texture (<10.0> parallel to XD).

In Figure 85, the LE-XRD PFs collected on the ECAP flow plane illustrate the texture evolution along the central stream line for a ZK60 billet, ZK-CC-T. As the observation point enters the PDZ, the measured PFs gradually change following the increase of the induced shear strain. Two main features were observed: the texture rotation and the texture sharpening and fragmentation, which start inside the PDZ and develop until the end of the deformation. The later was associated with a possible recrystallization during ECAP at high temperature of 260^0C, based on the observed microstrain relaxation from the XRD profiles [151]. A texture rotation was identified around the TD direction (the normal to flow plane) of ECAP. However, the most representative grain orientations correspond to the basal and prismatic poles almost aligned within the flow plane. This region of orientations cannot be accessed with the LE-XRD.

The data presented in Figure 85 include the PFs extrapolation toward the equatorial circle, i.e., the completion of the experimental PFs for tilting angles, $\chi > 75^0$, using popLA software. This operation is highly unstable when the symmetry of the texture in the sample space is not known, as it seems to be the case. It is more attractive to investigate the preferential orientation in the flow plane by HE-XRD, with the limitation that the observed region reduces to a circle in the orientation space of a particular direction in the crystal reciprocal space. Therefore, the data obtained on the flow plane were consolidated by measuring the IPPDs from the top and cross planes. This procedure means that the investigated zone of the unit sphere of directions includes three full principal circles normal to each other. The main characteristics of the texture rotation can be consistently evaluated, although the data are inadequate for the calculation of the orientation distribution function (ODF), and, therefore, for the normalization of the IPPD.

The polar plots of the IPPDs obtained for the partially-deformed ZK60 sample, ZK-CC-T, on all three planes (F, C, and T) for the central stream-line are presented in Figures 86a, 86b and 86c, using a logarithmic scale for the intensity representation. The initial texture had the pyramidal fiber oriented along the initial pressing direction of ECAP, <10.0> || XD. The preferential orientation of the prismatic pole along the XD can be observed in both <10.0> IPPDs along TD′ and ND′ (Fig. 86a, <10.0>, the locations a through g), which contain the XD axis. These two IPPDs show secondary peaks located at $\pm 30^0$ and $\pm 60^0$ relative to the XD. The intensities of these maxima correlate with the preferential orientation of the basal poles, which are mainly contained in the cross plane. Their distribution can be observed in the <00.1> IPPD recorded on the C′ plane, showing a

preferential orientation in ± 30^0 range relative to the ECAP ND. On the other hand, the <00.1> IPPDs recorded on the T′ plane (Fig. 86c) show a broader distribution about the TD as compared to the <00.1> IPPD on the F′ plane (Fig. 86a) about the ND. Taking into account this circumstance, the prismatic fiber can be decomposed in two virtual components: the strongest prismatic component, C-01, containing ~ 4/5 of grains (calculated from the ratio between the intensities), with the basal poles oriented close to the ND of ECAP in a ± 30^0 range toward the TD (Fig. 86b, <00.1>), and only few degrees toward the XD (Fig. 86a, <00.1>); the weakest prismatic component, C-02, containing about 1/5 of the grains, with the <00.1> direction included in a 30^0 cone around the TD. These two components transform differently during the ECAP deformation. However, a common characteristic seems to be the texture rotation around the TD of ECAP. The total rotation of the texture corresponding to the C-01 component amounts to about 90^0, and includes both basal and prismatic poles, whereas the C-02 component shows a total rotation of about 60^0 around the TD. In the last case, only the prismatic-poles rotation is visible on <10.0> IPPD, as the basal poles are too close to the TD.

Another billet of ZK60, ZK-CC-F, was ECAP-ed by maintaining its orientation as in the original extrusion process. In this case, the initial texture was rotated with 90^0 around the XD relative to the previous case. The two texture components mentioned before, C-01 and C-02, are present in the IPPDs, but they switched places (see Figs. 87a, 87b and 87c) as compared to the ZK-CC-T billet. The texture rotation retains the same characteristics: the C-02 component, which has the basal poles along the ND, when passing through the

plastic zone is rotating 90^0, whereas the C-01 rotates only about 60^0. The C-01 component initially displays an anisotropic broadening around the TD (initially significantly broaden toward the ND), the basal poles rotation manifests through a steady broadening of the <00.1>distribution near TD measured on the T′ plane (see Fig. 87c).

A new texture component (C-03), inexistent in the original as-received material, seems to be generated during the first stage of ECAP, before the material is reaching the plastic zone (Figs. 86c and 87c, i.e., the T′ plane observed at the locations a, b, and c). This component can be assigned as a basal fiber aligned along XD. It can be seen in the mentioned figures that starting from the location d up to g, the C-03 component decreases. The presence of this component is more evident in the billet, ZK-CC-F, but some traces are also visible on the billet, ZK-CC-T (the T′ plane observed). It is believed that the C-03 component was produced by twining during the compression of the billet in the first stage of ECAP. In the plastic zone, the grains belonging to the C-03 rotate about TD with less then 60^0.

A third ZK60 billet, ZK-FF-T, was cut with its axis along the TD in the initial extrusion framework (FF cut). The initial T stands for the top plane, i.e., when introduced in the die channel, the as-received top plane is becoming flow plane in ECAP. In this case, the initial prismatic fiber was aligned with the ND of ECAP and, therefore, the C-01 component was aligned with XD of ECAP (see Fig. 88). The C-02 component has the same orientation as that for the billet, ZK-CC-T, and behaves similarly except the total rotation angle, which is rather closer to 30^0. The C-01 component also shows a reduced total rotation, below the value obtained for C-03, which might be similar. The

broadening of the <00.1> preferential orientation on the F′ plane during the ECAP is also a specific feature.

The AZ31 billets, AZ-CC-T and AZ-FF-T, were cut along XD (CC cut) or TD (FF cut) in the framework of rolling, and the ND was aligned with TD of ECAP. Therefore, the rolling basal fiber (C-04) lies along TD. Unfortunately, these IPPDs have noisy intensities due to the coarse grain-size of this alloy, and it is more difficult to visualize the preferential orientations. In the Figures 89 and 90, the IPPDs of the AZ31 billet, AZ-CC-T are shown for one and two passes of ECAP, route B_C (Figs. 90 and 91), and for all measured locations, the large grains are visible. For this case, a much lower resolution could be used (in the present IPPDs, the angular step for integrating the intensity was 0.2^0). The ECAP deformation induces some grain fragmentation, as the number of the spots is increasing (up to an order of magnitude for the {00.2} reflection), but the refinement is not so significant to smoothen the IPPDs, which suggests that the recovery and/or recrystallization accompanies the fragmentation. As for ZK60, the early stage of deformation involves some twinning, and the characteristic C-03 component is clearly visible in the FF-cut billet. The total rotation of the C-03 texture component matches the total rotation observed in ZK60. The rotation of the main texture component, C-04, is hard to analyze, as the direction of the fiber remains unchanged during the plastic deformation, and the distribution of the prismatic poles does not show enough features to allow the visualization of the texture rotation.

As the basal fiber C-04 remains almost unchanged after one pass ECAP, it is of essence to follow the ECAP effect on a billet subjected to a 2B partial processing. In this case,

the billet was rotated with 90^0 around the XD axis, i.e., the fiber was aligned along ND. The texture transformation was recorded on the F′ plane only (see Fig. 90), but it is clear that the fiber rotation roughly reproduced the rotation of the C-01 component aligned along ND, similar to the ZK60 sample.

5. SUMMARY

5.1 ECAP Macromechanics

The ECAP-die design in Figure 6 was chosen as a successful construction solution in building at UT the sharp-corner die (Figs. 9 to 12), able to process billets size of 12.5 × 12.5 × 100 mm. A round-corner die, working as the later with a hydraulic pressing machine at UT, was the result of the collaboration between UT and the Central South University, Changsha, Hunan [71], and is able to process billets of 9.5 × 9.5 × 100 mm. The ECAP equipment was used to process scribed billets at room (pure Pb, pure Cu, and commercial-pure Al) and higher temperature of T = 250^0C (6061Al, AZ31, and ZK60) for the shear-strain mapping and texture mapping. The billets processed at UT in one and two passes using the round-corner die were characterized in tensile tests, which gave similar results (the increased ductility by 2 - 3 times as compared to the starting material) as the billets (22 × 22 × 114 mm) processed at the Idaho National Laboratory (INL) using an ECAP die with a sharp corner.

The simple shear seems to dominate the macromechanical-deformation mode in ECAP. For a sharp-corner die, Segal's model defines a simple-shear plane, where most of the plastic deformation takes place. ECAP assimilates to orthogonal cutting, which also shows the shear-plane localized deformation. From this point of view, the ECAP can be assigned as a cutting process constrained by the channel walls. The macromecanics of the chip deformation during cutting was extensively studied, based on the slip-line-field (SLF) theory. However, the macromechanics of the plastic deformation associated with

ECAP uses rough approximations, including the difficulty to predict the shear-strain heterogeneities. The SLF models for the plastic-deformation zone (PDZ) developed for ECAP include stress singularities and a limited range of validity. Therefore, the present study initiated the modeling of the ECAP deformation for predicting the PDZ shape and the induced shear-strain in each pass.

The shape of the PDZ in a steady-state deformation regime does not follow a close contact between the billet and the die. There are two PDZ configurations often observed experimentally, which involve either the formation of a ″dead metal″ zone at the outer corner of the die, or the existence of a free surface in the same zone. These circumstances have been investigated in detail, and a model for predicting the induced strain inhomogeneities in ECAP was developed.

The theoretical predictions of the PDZ shape and size during the ECAP deformation, as well as the induced shear-strain have been validated experimentally on partially-deformed specimens. The analysis of the scribed samples after processing allowed mapping of the plastic strain in partially-deformed specimens. Although the mapping of the induced plastic strain cannot be continued in the multipass ECAP, the one-pass data can be used to predict the deformation for different straining paths. An equivalent strain was defined in a consistent way in order to characterize the multi-pass deformation, and the response of the materials to such a severe plastic deformation as ECAP.

5.2 *Characterization Techniques*

A variety of characterization methods have been used to assess the complex structures and novel thermo-mechanical properties of the alloys deformed in ECAP, including mechanical testing in monotonic and cyclic loadings, and structural characterizations, with an emphasis on nondestructive characterizations using the LE and HE-XRD techniques. The relationship among the processing, the microstructure, and the mechanical properties was studied on Mg-alloys, before and after the ECAP deformation. The experimental-theoretical validations have been cconducted in order to optimize and implement the ECAP technology for producing materials with good mechanical properties, and to contribute to an in depth understanding of the deformation mechanisms during the processing, or during the monotonic and cyclic loadings of the studied materials.

The characterization methods allowed determining, on one hand, the mechanical properties, such as the ductility, strength, or the fatigue life, and, on the other hand, the structural properties, such as the grain sizes, the coherent-domain sizes, the elastic microstrains, the dislocation densities, and textures of the as-received and ECAP deformed Mg alloys, AZ31 and ZK60.

The OM, SEM, and OIM techniques were used to determine the grain size, the grains morphology, the fracture modes for the samples tested in tensile and fatigue, the low-angle grain boundaries (LAGBs) and high-angle grain boundaries (HAGBs) distributions, and the OIM microtextures.

5.3 Grain Refinement in ECAP

The most important result of the plastic deformation by ECAP was grain refinement. Different straining paths were used: routes A, B, and C, and the microscopy observations showed similar morphologies of the grains, with more elongated grains after route A, and more equiaxed grains after route B. An average grain size of 2.5 μm was reached after only 2 passes of ECAP for both alloys, AZ31 and ZK60, and further pressing up to 8 passes was not refining the grains, and contributed rather to the transformation of the LAGB into HAGBs. For the ZK60 samples observed with OIM, the ECAP-ed samples deformed in 8 passes, route A, the percentage of the HAGBs increased from 45% in the as-received to the 65% in the ECAP-8A), leading to a more stable microstucture after ECAP.

5.4 Mechanical Properties after ECAP

Various strain paths were analyzed, and, as shown in Figure 62, a ductility of 371% was obtained after ECAP, 4 passes, route A, when ZK60 was tested in tension at 350^0C, and the strain rate of 10^{-2} s^{-1}. This extended ductility in the warm tensile experiment (T = 0.68 T_m) was associated with a large strain-rate sensitivity (m = 0.3 - 0.4), and an increased number of HAGBs, in the presence of a dual grain-size distributions. The grain-boundary sliding mechanism of deformation, accommodated by slip controlled by grain-boundary diffusion, could have the main contribution for the plastic strain at the loading temperature of 350^0C. The grain size refinement is expected to enhance the GBS mechanism, over the normal twinning-slip mechanism, up to the onset of the

superplasticity. In these conditions, the GBS mechanism of deformation, accommodated by slip controlled by GB diffusion, could have the main contribution for the plastic strain accommodation and dislocation movement. The activation energy, calculated from the stress data versus temperature, at the strain rate of 5×10^{-3} s^{-1}, has the value of 80 kJ/mol for the ECAP-4A.

As shown in the Section 4.2, the strengthening of the ZK60 alloy is not improved after 8 passes of ECAP, and, it is believed that the controlling mechanism is the precipitate dissolution (formed prior ECAP in the T5 treatment) during the high temperature ECAP.

5.5 Orientation Effects on Mechanical Properties

Two Mg alloys, AZ31 and ZK60, with the starting rolling and extrusion textures, respectively, were tested in uniaxial compression and cyclic fatigue for different orientations of the samples, CC samples cut along the working direction, and TT and FF samples cut perpendicular to the working direction. The deformation textures by rolling, studied with the LE-XRD and HE-XRD techniques for the Mg alloy, AZ31B-H24, and measured on three surfaces, F, T, and C, are characterized by a basal pole, <00.1> (Fig. 32a), preferentially-oriented perpendicular to the rolling direction. The HE-XRD PFs confirmed this initial texture (Fig. 39), and evidenced the large recrystallized grains (probably larger than 10 μm) formed during the hot-rolling process. For the AZ31 it is clear from the metallography (Fig. 26) that the grains are not subdivided, they are rather recrystallized during the hot-working process.

In the AZ31 samples, CC compressed, the initial <00.1> fiber along the TT axis reorients completely along the CC axis. This reorientation effect is the result of a twinning mechanism, produced by the one-step rotation of a ″mother grain″ toward the closest to the loading axis <10.0> direction. Therefore, the resulting daughter texture spread around the fiber axis on the TD-XD plane amounts about 30^0 (Fig. 70, AZ-CC), as, initially, the <10.0> pole was randomly distributed in a ± 30^0 range against the CC axis.

Although the full strain induced by twinning corresponds to a small part of the total strain, as this process controls the early stage of the deformation, the twinned ″daughter″ texture determines the mechanical behavior during compression in a late stage of the deformation. The twinning is also, probably, responsible for a grain-refinement effect, which was clearly evidenced during the compression at room temperature and beyond, up to 250^0C. At 350^0C, a recrystallization process competes with the other modes of deformation, producing a significant change of the texture, by splitting the ″daughter″ texture and conducting to the grains growth (Fig. 71, AZ-CC-350^0C).

In contrast with this behavior, when the AZ31 alloy is loaded along the TT axis (Figs. 70 and 71, AZ-TT), the preferential orientation of the grains prevents the twinning to occur, and the initial texture is preserved during compression for the whole range of testing temperatures from 25^0C to 350^0C.

The deformation textures by extrusion were captured using the LE-XRD, HE-XRD, and neutron diffraction techniques, and the prismatic fiber, <10.0>, aligned along the extrusion direction, XD, is confirmed as being characteristic for the ZK60 texture (Figs.

64a-b and 64b-b). Other components of the texture, not accessible for the LE-XRD measurements (Fig. 64a-b, <10.0> poles observed as left and right spots in the F and T planes), have been correctly extrapolated with popLA software. The neutron diffraction of the extrusion texture was able to detect the inhomogeneity of the prismatic fiber in the C plane, as in Figure 64b-c, which shows that the basal poles tend to align close to the normal directions, ND and TD. This trend is questioning the popLA extrapolation of the LE-XRD PF from Figure 64a-b, reflection (00.2) on the C plane, which shows a larger spread of the basal poles orientations than the neutrons and the HE-XRD measurements.

Due to the twinning mechanism, a partial or total transformation (depending on the strain level) of the existent prismatic fiber along the extrusion direction, XD, into a basal fiber along the same direction results when the ZK60 alloy is loaded along the CC axis. However, the CC compression of this alloy produced a marked difference in the behavior between the room-temperature and higher-temperatures experiments. After the CC compression at room temperature, the final texture roughly reproduces the twinning ″daughter″-broad texture (Fig. 73, ZK-CC-RT), as was observed for the rolled AZ31 alloy (Fig. 71, AZ-CC-RT). At temperatures ranging from 150^0C to 350^0C, the resulting <00.1> fiber, parallel to XD, is significantly sharpened (Fig. 73, ZK-CC). This circumstance suggests that the slip mechanism, accompanying twinning at high temperatures, is different in the ZK60 alloy as compared to the AZ31 alloy.

When ZK60 is loaded along the TT direction, only the grains with the <00.1> axis close to the TD direction (Fig. 73, ZK60, as-rec.) are prone for twinning. Therefore, the <00.1> directions close to the ND axis, as a part of the initial <10.0> fiber, parallel to CC,

are preserved during the TT compression. The resulting texture of the twinned grains shows a characteristic double-peak pattern (Figs. 68b, T plane, 68c, and 72, ZK-TT-RT). For the grains undergoing twinning during the TT compression, a <10.0> direction of each grain is initially oriented close to the XD axis (Fig. 72, ZK-as-rec.), and the corresponding <00.1> direction lies in the neighborhood of the TD axis (Fig. 73, ZK-as-rec.). Consequently, another <10.0> direction, will be located at about 30^0 relative to the ND axis, almost in the XD-ND plane (Fig. 72, ZK-as-rec, F plane). Due to twinning, during the TT compression, the <00.1> pole, belonging to the ″mother grains,″ roughly ″replaces″ the <10.0> pole. As a result, the <00.1> ″daughter grains″ will be oriented on either side of the ND axis, in the XD-ND plane, 60^0 apart (Figs. 68b, 68c, and 73, ZK-TT-RT). This split was evident for the TT samples, compressed at room temperature (Fig. 72, ZK-TT-RT) and at 150^0C (Fig. 72, ZK-TT-150^0C). For the ZK-TT samples, a texture-sharpening tendency, with the increase of the compression temperature (Fig. 72, ZK-TT, plane C), occurs similarly with the ZK-CC samples. As a result, at 250^0C and 350^0C, the original and the twinned textures are merging, and generate a unique basal fiber, parallel to the ND axis (Fig. 73, ZK-TT, F plane).

The preferential orientations of the grains in the rolled Mg alloy, AZ31, and in the extruded alloy, ZK60, are shown to affect the mechanical behavior of these hexagonal-closed packed (HCP) structures. The uniaxial compression for three orthogonal loading directions, CC, TT, and FF produced drastic changes in the textures when the initial texture was oriented with the c-axis of the hexagonal lattice cell, perpendicular to the loading direction. Different deformation mechanisms are identified during uniaxial

compression, such as twinning, crystallographic slip, and recrystallization processes. Moreover, in the same condition of straining, the two alloys have different behavior, leading to the conclusion that different deformation modes are active, such as twinning combined with a specific to each alloy slip system. Twinning process controls the early stage of the deformation, and the twinned ″daughter″ texture determines the mechanical behavior during compression in a late stage of the deformation. The twinning is also, probably, responsible for a grain-refinement effect, which was evident in the AZ31 alloy, containing initially recrystallized grains. The competing deformation mechanism by crystallographic slip is shaping the texture during the hardening stage in both alloys, AZ31 and ZK60. In this regard, the texture features, as well as their hardening figures, are more stable in the initially hot-rolled AZ31 samples. The complex behavior during the TT compression is subject to further experimental and theoretical studies.

The hardening behavior during the uniaxial compression is closely related to the texture evolution during this plastic deformation of the Mg alloys, AZ31 and ZK60. In the early stage of the deformation, the sharp decrease of the hardening rate can be related to the dramatic change in the texture induced by twinning. Hence, the twinning mechanism proves to be responsible for the initial relative softening of the material, when the starting texture contains an appreciable amount of grains with an orientation favorable for twinning. During the compression, the grains reorient with the basal pole close to the compressive loading direction via a twinning mechanism, until the exhaustion of the twinning activity. When the straining contribution provided by twins is ceased, a strengthening effect results in a significant increase of the hardening rate (Figs. 54a and

55a). This effect can be observed for the whole temperature range from RT up to 350^0C, but is less pronounced when the temperature is moving toward the higher levels. In the temperature range of RT to 350^0C, the twinning deformation is always present in compression, if enough grains, prone for twinning, are present in the initial texture.

The deformation textures in ECAP were studied for the Mg alloys, AZ31 and ZK60, deformed in 1, 2, 4, and 8 passes using routes A, B, and C. Should be noted that the deformation of Mg and Mg-alloys at low temperatures involves crystallographic <a> slip along three $\langle 11\bar{2}0\rangle$ type directions on one basal-plane (0001), three $\{10\bar{1}0\}$ prismatic-planes, and six $\{10\bar{1}1\}$ pyramidal planes, as well as twinning on pyramidal $\{10\bar{1}2\}$ planes along $\langle\bar{1}011\rangle$. The results obtained from the present study of Mg alloys showed that a new texture component may form in the early stage of the ECAP deformation, which is generated by the twinning under the compressive loading of the billet in the first channel of the die (see Fig. 80). In a late stage of ECAP deformation, a recrystallization process competes with the deformation, changing the texture (Fig. 85) and relaxing the elastic microstrain (see Fig. 82 as compared to the as-received material in Fig. 81a). Moreover, by the newly developed mapping procedure, three distinct behaviors of the texture spin are observed during ECAP (see Figs. 85 to 89), depending on the billet orientation (CC or FF billets) relative to the pressing direction, and these behaviors are similar for both studied Mg-alloys. The main difference noticed for the AZ31 billets, was the presence of the recrystallized grains at the beginning of deformation.

The results of the texture mapping constitute: (1) a database for the further modeling of the deformation textures in HCP materials, (2) a clear evidence of the presence of twinning in early stage of the ECAP deformation at high temperatures, and (3) a bench-mark to control the mechanical properties of the Mg-alloys by manipulating the texture.

The formation of the dual-basal texture, tilted about the ND, was observed after the first ECAP pass. This texture component was preserved from one pass to another, and, in the case of route B, is accompanied by a component along the TD. The texture evolution from one to 8 passes reflects the changes in deformation mechanisms contributions, including twinning, dislocation slip, GBS, and/or the dynamic recovery/CDRX processes.

5.6 XRD Peak-Broadening Analyses

The XRD profiles measurements of the Mg samples, before and after the plastic deformation in compression, fatigue or ECAP, were conducted using the LE-XRD and HE-XRD techniques, in reflection and transmission geometries, respectively. The $\theta - 2\theta$ scans have been obtained, similar to the pole figures, on three surfaces of observations, flow (F), top (T), and cross (C). Based on the peak-broadening analyses of the data, the grain size, coherent-domain size, elastic microstrain, dislocation density, and the type of dislocations corresponding to their Burgers vectors and to the active slip systems have been determined.

The whole-pattern fitting (WPF) method was used for the peak-broadening analyses, with a Si standard for the instrumental profile. The method is shown to give a good agreement with the measurements, and the elastic microstrain results have been correlated to the

pole-figures findings regarding the presence of a recrystallization process during ECAP. The XRD peak-broadening analyzes indicate the decrease in the coherent-domain size as well as the reduction in the internal elastic strain after ECAP. The r.m.s. elastic microstrain was reduced by 8 passes, route A of ECAP from 8×10^{-3} to 1×10^{-4}. This behavior was interpreted as a dynamic-recrystallization process. As for the coherent-domain size, the WPF resulted in some ambiguities, and the comparison between the LE-XRD and HE-XRD data is in progress.

From the LE-XRD profiles analyses obtained for the AZ31 alloy, before and after the uniaxial compression at RT, it was found that the contribution of the <a> dislocations decreased as compared to the starting material. Therefore, the components, <c> and <c +a >, become active during the deformation. At high temperatures, the weight percentage of the <a> dislocations is increasing to the initial value. Thus, the recovery/recrystallization processes came into play. The total density of the dislocations increased during the deformation, and decreased when the material was tested at 350^0C, supporting well this assumption.

5.7 Mapping the Texture Evolution in ECAP

The spatial-temporal texture changes during ECAP were accurately determined by mapping the texture along a flow line in a partially-deformed billet, using both the LE-XRD and HE-XRD techniques. By mapping the texture evolution for three planes of observations, quantitative results were obtained for the texture rotation corresponding to the texture components.

The present mapping procedure allowed identification of the texture components, described in a spatio-temporal manner. The rigid-body spin, determined experimentally from the shear-strain mapping, together with the lattice spin, determined from the HE-XRD measurements, were used to obtain the net plastic spin of the texture in ECAP-ed Mg alloys. The rigid-body spin was determined from the stream lines corresponding to each particular location. The experimental lattice rotation (Fig. 91) was shown to evolve during the deformation, and three situations are encountered: (i) the <00.1> spin of the basal component parallel to T′; (ii) the <00.1> spin of the basal component parallel to C′, and (iii) the <10.0> spin of the basal component parallel to F′. These three cases correspond actually to the rotation of the c-axis, when c-axis is, at the beginning of the deformation, along ND and XD directions, and to the case when the a-axis rotates, and when the c-axis is parallel to the TD (at the beginning and the end of deformation, doesn't matter, because it is not rotating).

The texture response to the plastic deformation can be rationalized as originating from the lattice rotations of individual grains. The lattice rotation shows a marked grain-orientation dependence, which was evidenced by observing the average rotation of different initial texture components. Three crystallographic orientations were selected to illustrate the grain-orientation dependence: <00.1> parallel to T′, <00.1> parallel to C′, and <00.1> parallel to F′. Due to the fact that the ECAP deformation is macroscopically confined in the flow plane, the grains rotate around the flow axis, F′. Therefore, the lattice rotation was derived from the rotation of the texture maxima in both <00.1> and <10.0> IPPDs for the first two cases, and only from the <10.0> IPPD, corresponding to

the <00.1> parallel to F′ case. The experimental results from HE-XRD of the cumulative lattice rotation versus the position in the billet are presented in Figure 91, for the partially- ECAP-ed billets, ZK-CC-T and ZK-CC-F, deformed along the CC direction and rotated or not with 90^0 to reveal the T of F plane, respectively, for scribing the billet. The rigid-body rotation, determined from the stream-lines corresponding to each particular location, is shown in Figure 91 for comparison.

The total lattice rotation (Fig. 91) is shown to evolve during the deformation, and three situations are encountered when: (1) the <00.1> rotation of the basal component is parallel to ND′; (b) the <00.1> rotation of the basal component is parallel to XD′ and (c) the <10.0> rotation of the basal component is parallel to TD′. These three cases correspond actually to the rotation of the c-axis, when c-axis is, at the beginning of the deformation, along ND and XD directions, and to the case when the a-axis rotates, when the c-axis is parallel to the TD (at the beginning and end of deformation, it doesn't matter, because it is not rotating). The cumulative data from Figure 91 can be used to derive the instantaneous rotation as presented in Figure 92 for the dependence of the lattice spin versus time. As the results for the <00.1> // XD′ and <00.1> // TD′ are consistent for both investigated samples, in Figure 92, the averaged values for these two initial orientations are represented. The <00.1> // ND′ case shows different rotations in different samples: (i) the lattice rotation follows closely the rigid-body rotation, whereas, (ii) in another situation, the lattice rotation slows down in the late stage of the ECAP deformation. Beside the experimental errors, this difference in behavior can be linked to the texture spread in the initial state.

The XRD techniques, LE and HE, were successfully used to map the texture evolution during one pass of the ECAP plastic deformation for the locations on the partially-deformed billets, before reaching the plastic-deformation zone (PDZ), passing through the PDZ, and after the deformation. The in detail analyses of the in-plane pole distributions (IPPDs) allowed determining the texture components, as well as, the lattice rotations during ECAP, which correspond to the basal-pole orientation of the grains. The lattice rotations correlate with the macroscopic deformation maps, determined on the same samples, allowing the evaluation of the local rigid-body rotation of the material element. Thus, it is possible to determine directly from the experiment the plastic spin in ECAP for specific grain orientations. Such experimental results are not available for the hexagonal-closed packed structures as Mg alloys, and can be further used for modeling the textures evolution in ECAP.

6. CONCLUSIONS

1. The ECAP macromechanics assimilates to orthogonal cutting, which also shows the shear-plane localized deformation, and can be assigned as a cutting process constrained by the channel walls. The macromechanics of the chip deformation during cutting was extensively studied, based on the slip-line-field (SLF) theory. The SLF models for the plastic-deformation zone (PDZ) developed for ECAP include stress singularities and a limited range of validity. There are two PDZ configurations often observed experimentally, which involve either the formation of a ″dead metal″ zone at the outer corner of the die, or the existence of a free surface in the same zone. These circumstances have been investigated in the present work in more detail, as well as the resulting inhomogeneities of the induced strain. A partial-split PDZ model was proposed to explain the induced shear-strain inhomoneneity across the billet. The large plastic deformation formalism was used in defining the shear strain and the equivalent strain in ECAP for the main SLF models, correcting some ambiguities from the literature. Our analytical approach was later extended by Beyerlin and Tome [82] and applied in the self-consistent simulations of the texture evolution during ECAP.

2. The theoretical predictions of the PDZ shape and size during the ECAP deformation, as well as the induced shear-strain have been validated experimentally on partially-deformed specimens. The analysis of the scribed samples allowed the mapping of the plastic strain in partially-deformed billets. The resulted shear-strain values (at the locations for the XRD profiles and texture

measurements) have been used when mapping the profiles and the textures of the studied Mg alloys, AZ31 and ZK60. Although the mapping of the induced plastic strain cannot be continued in the multipass ECAP, the one-pass data can be used as a base for predicting the deformation through different straining paths.

3. The main effect of the ECAP on microstructures is the grain-size refinement, and the resulting UFG materials have the grain size ranging from 100 to 1,000 nm. Unless the grain-size distribution is inhomogeneous or bimodal, the hardness, the yield stress, and the strength of the materials with the same composition but different grain sizes will be inversely proportional to the square root of the grain size, according to the Hall-Petch relationship. It was found that the Mg alloys follow this behavior at a mesoscopic level. However, the mechanical behavior of these hexagonal-closed packed (HCP) structures is mainly determined by the crystallographic textures, due to their remarkable plastic anisotropy.

4. The mechanical behavior of the Mg alloys under compression at room and high temperatures up to 0.6 T_m (T_m is the melting temperature) was correlated with the texture evolution. Therefore, both the mechanical properties and the textures can be understood as an indicator for the twinning mechanism of deformation, which is highly dependent on the grain orientation. Different types of textures, characteristic of rolling and extrusion, were used in conjunction with different loading directions, along and perpendicular to the working directions. The presence or absence of twinning in the early stage of the deformation can explain

the results. However, the temperature dependence of the deformation texture is significantly influenced by the alloy type, AZ31 or ZK60.

5. The fatigue properties of the studied Mg alloys are also texture dependent, as shown by our experimental results on AZ31 and ZK60. This behavior is related to the contribution of the twinning-untwinning mechanism during the cyclic loading. After ECAP, the fatigue life was shown to improve, due to the grain-refinement effect, as well as the texture change.

6. The study of the texture evolution after the multipass ECAP revealed a distinct trend for different routes and materials. Generally, the texture is enhanced by ECAP in Mg alloys, in contrast with the previously accepted view that the ECAP has a diminishing effect on the texture. The texture components developed in ZK60 and AZ31 are quite different, and their dependence on the ECAP straining level (number of passes) is characteristic of each alloy. For example, the route B maintains in the ZK60 alloy two basal fibers, mainly oriented along the ND and TD, whereas the AZ31 alloy shows a unique basal fiber oriented out of the deformation plane. This out-of plane texture component was found to evolve with the number of ECAP passes. This trend is an indication that the plastic deformation includes material-dependent weighting factors for the deformation modes by dislocation slip.

7. The texture-mapping results demonstrated that in ECAP of the studied HCP structures, the competing deformation modes resulted in a complex behavior. The

resulting lattice-rotation data during ECAP of Mg alloys can be further applied to identify the contributions of the deformation modes for a specific grain orientation, and develop an anisotropic yield function. It was also found that the twinning may be present in the early stage of the ECAP deformation, and it is believed that the twinning-deformation mode may depend on the die design and friction conditions, i.e., on the ECAP deformation constrained to occur inside the die walls. By combining the initial preferential orientations of the grains with a specific cut of the billet, it was possible to dissociate the effect of the ECAP deformation on three different basic orientations.

8. The coherent-domain size, elastic microstrain, and the dislocation density, including the dislocations debris, <a>, <c + a>, and <c> were determined from the XRD peak-broadening analyses of the Mg alloys samples deformed in the uniaxial compression and ECAP. The results lead to the conclusion that in a late stage of the ECAP deformation, a recrystallization process competes with the deformation, changing the texture and relaxing the elastic microstrain.

7. FUTURE WORK

The ECAP technology is of great interest for the metal-forming industry, aiming at the structural applications. Being able to process bulk large billets, it is important to ensure a homogeneous deformation throughout the material, and the die design and processing conditions are the leading factors. The previously designed symmetric ECAP die, expected to be built in the near future, will be able to process two billets at once (square profiles varying from 9.5 mm up to 25 mm, and 102 mm in length), and this symmetry of processing is assuring a uniform distribution of the load during the deformation. The sharp-corner configuration, the die flexibility in changing the billet size, the angle between the channels, and the minimal friction conditions of the two billets moving together with the billet holder, are a few reasons for a successful processing using the symmetric ECAP die. An additional horizontal frame for the back-pressure will increase greatly the chances of obtaining uniform strained materials, with equiaxed and uniform distributed ultrafine grains of 1 μm or less.

The research of the ECAP macromechanics needs to be extended by refining the ECAP models. The first steps to be followed will be to build a slip-line field, with a more complex PDZ, and to develop the large-deformation approach to estimate the rigid-body spin. The goals of the modeling efforts will be: (1) to eliminate the discontinuities of the induced strain inside PDZ, (2) to generate a PDZ, whose shape and size will match better the real conditions of the deformation, where the hardening/softening properties, which are manifesting at the outer-corner of the ECAP die, the friction, or the shear localization, which are manifesting at the inner corner of the ECAP die are taken into account, (3) to

include the yield anisotropy of the hexagonal-closed packed (HCP) structures in the definition of the equivalent strain, and (4) to find an analytical flow-line model to predict the experimental data obtained for the shear-strain mapping.

The results obtained on the deformation textures of the studied Mg alloys are a valuable database for conducting the in-detail visco-plastic self-consistent simulations, and to apply the plastic spin theory to ECAP deformation. The texture-mapping procedure, which was successful in determining experimentally the lattice rotation during one pass of ECAP, by visualizing the texture components rotation, has to be further used to analyze the effect of the PDZ inhomogeneities on the texture evolution. The extension and refinement of the mapping procedure for the multipass ECAP will provide the means to identify the deformation modes in ECAP, i.e., the dislocation slip and twinning mechanisms activities, as well as the role of the recovery/recrystallization processes in defining the novel structural and mechanical properties of the HCP materials. A further advance in understanding these issues can be reached by planning in-situ diffraction studies of a simple-shear deformation, in conjunction with TEM characterizations, to link more closely the deformation-induced dislocation grain substructure and the precipitation/dissolution kinetics, with the texture evolution and the grain refinement.

REFERENCES

REFERENCES

[1] V. M. Segal, V. I. Reznikov, A. E. Drobyshevskiy, V. I. Kopilov, *Russ. Metall.* 1 (1981) 99.

[2] V. M. Segal, *Materials Science and Engineering a-Structural Materials Properties Microstructure and Processing* 197 (1995) 157-164.

[3] V. M. Segal, R. E. Ramon, K. T. Hartwig, Apparatus and Method for Deformation Processing of Metals, Ceramics, and Other Materials, in: *Patent No. 5400633*, US, 1995.

[4] V. M. Segal, K. T. Hartwig, R. E. Goforth, *Materials Science and Engineering a-Structural Materials Properties Microstructure and Processing* 224 (1997) 107-115.

[5] V. M. Segal, *Materials Science and Engineering a-Structural Materials Properties Microstructure and Processing* 271 (1999) 322-333.

[6] V. M. Segal, *Materials Science and Engineering a-Structural Materials Properties Microstructure and Processing* 345 (2003) 36-46.

[7] P. W. Bridgeman, *Studies in Large Plastic Flow and Fracture*, McGraw-Hill, NY, 1952.

[8] R. Z. Valiev, A. V. Korznikov, R. R. Mulyukov, *Materials Science and Engineering a-Structural Materials Properties Microstructure and Processing* 168 (1993) 141-148.

[9] S. Ferrasse, V. M. Segal, K. T. Hartwig, R. E. Goforth, *Journal of Materials Research* 12 (1997) 1253-1261.

[10] M. Furukawa, Z. Horita, M. Nemoto, T. G. Langdon, *Materials Science and Engineering a-Structural Materials Properties Microstructure and Processing* 324 (2002) 82-89.

[11] I. V. Alexandrov, G. I. Raab, V. U. Kazyhanov, L. O. Shestakova, R. Z. Valiev, R. J. Dowling, Ultrafine-Grained Tungsten Produced by SPD Techniques, in: Y. T. Zhu, T. G. Langdon, R. S. Mishra, S. L. Semiatin, M. J. Saran, T. C. Lowe (Eds.), Ultrafine Grained Materials II, TMS Publ., Seattle, WA, 2002, pp. 199-208.

[12] S. R. Agnew, J. R. Weertman, *Materials Science and Engineering a-Structural Materials Properties Microstructure and Processing* 242 (1998) 174-180.

[13] S. R. Agnew, J. R. Weertman, *Materials Science and Engineering a-Structural Materials Properties Microstructure and Processing* 244 (1998) 145-153.

[14] R. Z. Valiev, I. V. Alexandrov, Y. T. Zhu, T. C. Lowe, *Journal of Materials Research* 17 (2002) 5-8.

[15] R. Z. Valiev, Recent Developments of SPD Processing for Fabrication of Bulk Nanostructured Materials, in: Y. T. Zhu, T. G. Langdon, R. S. Mishra, S. L. Semiatin, M. J. Saran, T. C. Lowe (Eds.), *Ultrafine Grained Materials II*, TMS Publ., Seattle, WA, 2002, pp. 313-322.

[16] E. V. Kozlov, A. N. Zhdanov, L. N. Ignatenko, N. A. Popova, Y. F. Ivanov, N. A. Koneva, Structural Evolution of Ultrafine-Grained Copper and Copper- Based alloy During Plastic Deformation, in: Y. T. Zhu, T. G. Langdon, R. S. Mishra, S. L. Semiatin, M. J. Saran, T. C. Lowe (Eds.), *Ultrafine Grained Materials II,* TMS Publ., Seattle, WA, 2002, pp. 419-428.

[17] Z. Horita, T. Fujinami, M. Nemoto, T. G. Langdon, *Metallurgical and Materials Transactions a-Physical Metallurgy and Materials Science* 31 (2000) 691-701.

[18] V. V. Stolyarov, Y. T. Zhu, T. C. Lowe, R. K. Islamgaliev, R. Z. Valiev, *Nanostructured Materials* 11 (1999) 947-954.

[19] V. S. Zhernakov, I. N. Budilov, G. I. Raab, I. V. Alexandrov, R. Z. Valiev, *Scripta Materialia* 44 (2001) 1765-1769.

[20] A. Vinogradov, S. Nagasaki, V. Patlan, K. Kitagawa, M. Kawazoe, *Nanostructured Materials* 11 (1999) 925-934.

[21] M. Mabuchi, H. Iwasaki, K. Higashi, *Nanostructured Materials* 8 (1997) 1105-1111.

[22] T. Mukai, M. Kawazoe, K. Higashi, *Nanostructured Materials* 10 (1998) 755-765.

[23] M. V. Markushev, M. Y. Murashkin, Strength of Submicrocrystalline Severely Deformed Commercial Aluminum Alloys, in: Y. T. Zhu, T. G. Langdon, R. S. Mishra, S. L. Semiatin, M. J.

Saran, T. C. Lowe (Eds.), *Ultrafine Grained Materials II*, TMS Publ., Seattle, WA, 2002, pp. 371-380.

[24] P. L. Sun, P. W. Kao, C. P. Chang, The Effect of Strain Per Pass on the Microstructure Developed in Aluminum Processed by Equal Channel Angular Extrusion, in: Y. T. Zhu, T. G. Langdon, R. S. Mishra, S. L. Semiatin, M. J. Saran, T. C. Lowe (Eds.), *Ultrafine Grained Materials II*, TMS Publ., Seattle, WA, 2002, pp. 35-42.

[25] K. Matsuki, T. Aida, T. Takeuchi, J. Kusui, K. Yokoe, *Acta Materialia* 48 (2000) 2625-2632.

[26] Z. Horita, M. Furukawa, M. Nemoto, A. J. Barnes, T. G. Langdon, *Acta Materialia* 48 (2000) 3633-3640.

[27] J. K. Kim, H. G. Jeong, S. I. Hong, Y. S. Kim, W. J. Kim, *Scripta Materialia* 45 (2001) 901-907.

[28] R. Z. Valiev, R. K. Islamgaliev, N. F. Kuzmina, Y. Li, T. G. Langdon, *Scripta Materialia* 40 (1998) 117-122.

[29] **G. M. Stoica**, L. J. Chen, E. A. Payzant, S. R. Agnew, Y. L. Lu, B. Q. Han, T. G. Langdon, P. K. Liaw, Deformation Characteristics of Al and Mg Alloys Subjected to Equal-Channel-Angular Processing, in: D. R. Lesuer, T. S. Srivatsan (Eds.), *Performance of Engineering Structural Materials II*, TMS Publ., Indianopolis, IN, 2001, pp. 295-306.

[30] J. Wang, Y. Iwahashi, Z. Horita, M. Furukawa, M. Nemoto, R. Z. Valiev, T. G. Langdon, *Acta Materialia* 44 (1996) 2973-2982.

[31] Y. Huang, C. Xu, S. Lee, M. Furukawa, Z. Horita, T. G. Langdon, Processing of an Aluminum-6061 Metal Matrix Composite by Equal-Channel Angular Pressing, in: Y. T. Zhu, T. G. Langdon, R. S. Mishra, S. L. Semiatin, M. J. Saran, T. C. Lowe (Eds.), *Ultrafine Grained Materials II*, TMS Publ., Seattle, WA, 2002, pp. 173-182.

[32] R. Z. Valiev, D. A. Salimonenko, N. K. Tsenev, P. B. Berbon, T. G. Langdon, *Scripta Materialia* 37 (1997) 1945-1950.

[33] M. Furukawa, Z. Horita, T. G. Langdon, Developing Superplasticity at High Strain Rates through ECAP Processing, in: Y. T. Zhu, T. G. Langdon, R. S. Mishra, S. L. Semiatin, M. J. Saran, T. C. Lowe (Eds.), *Ultrafine Grained Materials II,* TMS Publ., Seattle, WA, 2002, pp. 459-468.

[34] A. Washikita, K. Kitakawa, V. I. Kopylov, A. Vinogradov, Tensile and Fatigue Properties of Al-Mg-Sc-Zr Alloy Fine-Grained by Equal-Channel Angular Pressing, in: Y. T. Zhu, T. G. Langdon, R. S. Mishra, S. L. Semiatin, M. J. Saran, T. C. Lowe (Eds.), *Ultrafine Grained Materials II*, TMS Publ., Seattle, WA, 2002, pp. 341-350.

[35] T. Mukai, H. Watanabe, T. G. Nieh, K. Higashi, *Mat. Res. Soc. Symp. Proc.* 601 (2000) 291-301.

[36] A. Yamashita, Z. Horita, T. G. Langdon, *Materials Science and Engineering a-Structural Materials Properties Microstructure and Processing* 300 (2001) 142-147.

[37] S. R. Agnew, T. M. Lillo, J. Macheret, **G. M. Stoica**, L. Chen, Y. Lu, D. Fielden, P. K. Liaw, Assessment of Equal Channel Angular Extrusion Processing of Magnesium Alloys, in: J. Hryn (Ed.) *Magnesium Technology 2001*, TMS Publ., Warrendale, PA, 2001, pp. 243-247.

[38] S. R. Agnew, **G. M. Stoica**, L. J. Chen, T. M. Lillo, L. Macheret, P. K. Liaw, Equal Channel Angular Processing of Magnesium Alloys, in: Y. T. Zhu, T. G. Langdon, S. L. Semiatin, M. J. Saran, T. C. Lowe (Eds.), *Ultrafine Grained Materials II*, TMS Publ., Seattle, WA, 2002, pp. 643-652.

[39] A. Bussiba, A. Ben Artzy, A. Shtechman, S. Ifergan, M. Kupiec, *Materials Science and Engineering a-Structural Materials Properties Microstructure and Processing* 302 (2001) 56-62.

[40] H. Watanabe, T. Mukai, M. Kohzu, S. Tanabe, K. Higashi, *Acta Materialia* 47 (1999) 3753-3758.

[41] A. Galiyev, R. Kaibyshev, G. Gottstein, *Acta Materialia* 49 (2001) 1199-1207.

[42] Z. Horita, K. Neishi, T. G. Langdon, Grain Refinement of Copper Based Alloys Using ECAP, in: Y. T. Zhu, T. G. Langdon, S. L. Semiatin, M. J. Saran, T. C. Lowe (Eds.), *Ultrafine Grained Materials II,* TMS Publ., Seattle, WA, 2002, pp. 449-458.

[43] A. Vinogradov, Y. Suzuki, V. Patlan, K. Kitakawa, V. I. Kopylov, Structure, Properties, and Thermal Stability of Ultra-Fine Grained Cu-Cr-Zr Alloy, in: Y. T. Zhu, T. G. Langdon, S. L. Semiatin, M. J. Saran, T. C. Lowe (Eds.), *Ultrafine Grained Materials II,* TMS Publ., Seattle, WA, 2002, pp. 351-360.

[44] R. Z. Valiev, *Materials Science Forum* 207 (1997) 243-245.

[45] K. T. Park, Y. S. Kim, J. G. Lee, D. H. Shin, *Materials Science and Engineering a-Structural Materials Properties Microstructure and Processing* 293 (2000) 165-172.

[46] W. J. Kim, J. K. Kim, W. Y. Choo, S. I. Hong, J. D. Lee, *Materials Letters* 51 (2001) 177-182.

[47] R. S. Mishra, V. V. Stolyarov, C. Echer, R. Z. Valiev, A. K. Mukherjee, *Materials Science and Engineering a-Structural Materials Properties Microstructure and Processing* 298 (2001) 44-50.

[48] V. Stolyarov, R. Z. Valiev, Metastable Nanostructured Alloys Processed by Severe Plastic Deformation, in: Y. T. Zhu, T. G. Langdon, S. L. Semiatin, M. J. Saran, T. C. Lowe (Eds.), Ultrafine Grained Materials II, TMS Publ., Seattle, WA, 2002, pp. 209-218.

[49] L. Wu, **G. M. Stoica**, H. H. Liao, S. R. Agnew, E. A. Payzant, G. Wang, D. E. Fielden, L. J. Chen, P. K. Liaw, "Fatigue-Property Enhancements of Magnesium Alloy, AZ31B, through Equal-Channel-Angular Pressing," *Metallurgical Transactions a-Physical Metallurgy and Materials Science*, 2007 (accepted for publication).

[50] **G. M. Stoica**, S. R. Agnew, E. A. Payzant, D. A. Carpenter, L. J. Chen, P. K. Liaw, ″Microstructure and Ductility of Mg Alloy ZK60, after Equal Channel Angular Processing,″ in: Y.

T. Zhu, T. G. Langdon, R. Z. Valiev, S. L. Semiatin, D. H. Shin, and T. C. Lowe (Eds.) The TMS Annual Meeting, TMS Publ., Charlotte, North Carolina, 2004, pp. 427-432.

[51] R. Lapovok, R. Cottam, P. Thomson, Y. Estrin, *Journal of Materials Research* 20 (2005) 1375-1378.

[52] J. Y. Chang, G. H. Kim, I. G. Moon, *Scripta Mater*. 44 (2001) 331-339.

[53] S. R. Agnew, Proc. of the 12th Int. Conf. on Textures of Materials, ICOTOM-12, Eds. J. A. Szpunar, NRC Research Press, Ottawa, Canada (1999) 575-580.

[54] M. A. Gibbs, K. T. Hartwig, L. R. Cornwell, R. E. Goforth, E. A. Payzant, *Scripta Mater*. 39 (1998) 1699-1708.

[55] H. Conrad, *Materials Science and Engineering a-Structural Materials Properties Microstructure and Processing* 341 (2003) 216.

[56] H. Conrad, J. Narayan, *Acta Materialia* 50 (2002) 5067-5078.

[57] H. V. Swygenhoven, P. M. Derlet, *Physics Review B* 64 (2001) 224.

[58] S. R. Kalidindi, A. Bhattacharyya, R. D. Doherty, *Advanced Materials* 15 (2003) 1345-1348.

[59] M. E. Merchant, *Trans. ASME*, 66 (1944) A168-A175.

[60] E. H. Lee, B. W. Shaffer, *Journal of Applied Mechanics-Transactions of the ASME* 18 (1951) 405-413.

[61] R. Hill, *Journal of the Mechanics and Physics of Solids* 3 (1954) 47-53.

[62] P. Dewhurst, *Proceedings of the Royal Society of London Series a-Mathematical Physical and Engineering Sciences* 360 (1978) 587-610.

[63] N. Fang, I. S. Jawahir, *International Journal of Mechanical Sciences* 43 (2001) 557-580.

[64] N. Fang, P. Dewhurst, *International Journal of Mechanical Sciences* 47 (2005) 1079-1098.

[65] **G. M. Stoica**, D. E. Fielden, R. McDaniels, Y. Liu, B. Huang, P. K. Liaw, C. Xu, T. G. Langdon, "An Analysis of the Shear Zone for Metals Deformed by Equal-Channel-Angular

Processing," *Materials Science and Engineering a-Structural Materials Properties Microstructure and Processing* 410 (2005) 239-242.

[66] R. N. Roth, P. L. B. Oxley, *Journal of Mechanical Engineering Science* 14 (1972) 85-95.

[67] L. E. Farmer, S. W. Conning, *International Journal of Mechanical Sciences* 21 (1979) 577-597.

[68] S. J. Oh, S. B. Kang, *Materials Science and Engineering a-Structural Materials Properties Microstructure and Processing* 343 (2003) 107-115.

[69] H. P. Stuwe, *Advanced Engineering Materials* 5 (2003) 291-295.

[70] U. F. Kocks, C. N. Tome, H. R. Wenk, *Texture and Anisotropy*, Cambridge University Press, 1998.

[71] Y. Liu, B. Y. Huang, in: *Collaborative work with P. R. China,* State Key Laboratory for Powder Metallurgy, Central South University, Changsha, Hunan, 2004.

[72] W. Johnson, P. B. Mellor, W. Johnson, *Engineering plasticity*, Van Nostrand Reinhold Co., London, New York,, 1973, p. xviii, 646.

[73] H. S. Kim, M. H. Seo, S. I. Hong, *Materials Science and Engineering a-Structural Materials Properties Microstructure and Processing* 291 (2000) 86-90.

[74] P. B. Prangnell, C. Harris, S. M. Roberts, *Scripta Materialia* 37 (1997) 983-989.

[75] J. R. Bowen, S. M. Roberts, P. B. Prangnell, *Materials Science and Engineering a-Structural Materials Properties Microstructure and Processing* A287 (2000) 87-99.

[76] S. J. Yun, An Analysis by the Finite Element Method of Material Deformation in Equal Channnel Angular Extrusion, in: vol. *Ph. D.*, Texas A & M University, 1996.

[77] **G. M. Stoica,** P. K. Liaw, L. J. Chen, C. Xu, T. G. Langdon, D. E. Fielden, Z. Buczko, and R. A. Buchanan**,** "Plastic Flow and Properties of Mg- and Al-Alloys Deformed by Equal-Channel-Angular Pressing," in: Y. T. Zhu, T. G. Langdon, R. Z. Valiev, S. L. Semiatin, D. H. Shin, and T.

C. Lowe (Eds.), Ultrafine Grained Materials III, The Minerals, Metals, and Materials Society Publ., Warrendale, PA, 2004, pp. 503-510.

[78] **G. M. Stoica**, P. K. Liaw, *Jom-Journal of the Minerals Metals & Materials Society* 53 (2001) 36-40.

[79] **G. M. Stoica**, P. K. Liaw, Evaluating the Induced Strain During Equal Channel Angular Processing, in: P. K. Liaw, R. A. Buchanan, D. L. Klarstrom, R. P. Wei, D. G. Harlow, P. F. Tortorelli (Eds.), *Materials Lifetime, Sci. & Eng.* (Proc. Symp. Struct. Mat. Division of TMS), San Diego, 2003, pp. 119-133.

[80] A. D. Shan, I. G. Moon, H. S. Ko, J. W. Park, *Scripta Materialia* 41 (1999) 353-357.

[81] Y. Iwahashi, J. T. Wang, Z. Horita, M. Nemoto, T. G. Langdon, *Scripta Materialia* 35 (1996) 143-146.

[82] I. J. Beyerlein, C. N. Tome, *Materials Science and Engineering a-Structural Materials Properties Microstructure and Processing* 380 (2004) 171-190.

[83] R. W. Ogden, *Non-linear Elastic Deformation,* Halsted Press, New York, 1997.

[84] K. Xia, J. Wang, *Metallurgical and Materials Transactions a-Physical Metallurgy and Materials Science* 32 (2001) 2639-2647.

[85] S. L. Semiatin, J. J. Jonas, Ohio: *ASM Series in Metal Processing* (1984) 22.

[86] R. E. Goforth, K. T. Hartwig, L. R. Cornwell, Investigations and Applications of Severe Plastic Deformation, Eds. T.C. Lowe, R.Z. Valiev, Kluwer, Dordrecht, The Netherlands, 2000.

[87] T. Aida, K. Matsuki, Z. Horita, T. G. Langdon, *Scripta Materialia* 44 (2001) 575-579.

[88] Y. Wu, I. Baker, *Scripta Materialia* 37 (1997) 437-442.

[89] J. W. Park, J. Y. Suh, *Metallurgical and Materials Transactions a-Physical Metallurgy and Materials Science* 32 (2001) 3007-3014.

[90] J. R. Bowen, A. Gholinia, S. M. Roberts, P. B. Prangnell, Materials Science and Engineering a-Structural Materials Properties Microstructure and Processing 287 (2000) 87-99.

[91] S. L. Semiatin, D. P. Delo, E. B. Shell, Acta Materialia 48 (2000) 1841-1851.

[92] S. L. Semiatin, D. P. DeLo, Materials & Design 21 (2000) 311-322.

[93] J. Y. Suh, H. S. Kim, J. W. Park, J. Y. Chang, Scripta Materialia 44 (2001) 677-681.

[94] R. Z. Valiev, T. C. Lowe, A. K. Mukherjee, *Jom-Journal of the Minerals Metals & Materials Society* 52 (2000) 37-40.

[95] I. J. Beyerlein, S. Li, C. T. Necker, D. J. Alexander, C. N. Tome, *Philosophical Magazine* 85 (2005) 1359-1394.

[96] S. Li, M. A. Bourke, I. J. Beyerlein, D. J. Alexander, B. Clausen, *Materials Science and Engineering a-Structural Materials Properties Microstructure and Processing* 382 (2004) 217-236.

[97] L. S. Toth, *Computational Materials Science* 32 (2005) 568-576.

[98] B. S. Altan, G. Purcek, I. Miskioglu, *Journal of Materials Processing Technology* 168 (2005) 137-146.

[99] W. F. Hosford, The Mechanics of Crystals and Textured Polycrystals, Oxford University Press, New York, 1993, pp. 248.

[100] Y. T. Zhu, T. C. Lowe, *Materials Science and Engineering a-Structural Materials Properties Microstructure and Processing* 291 (2000) 46-53.

[101] L. Dupuy, E. F. Rauch, *Materials Science and Engineering a-Structural Materials Properties Microstructure and Processing* 337 (2002) 241-247.

[102] M. Furukawa, Z. Horita, T. G. Langdon, *Materials Science and Engineering a-Structural Materials Properties Microstructure and Processing* 332 (2002) 97-109.

[103] I. J. Beyerlein, R. A. Lebensohn, C. N. Tome, *Materials Science and Engineering a-Structural Materials Properties Microstructure and Processing* 345 (2003) 122-138.

[104] D. A. Hughes, N. Hansen, *Acta Materialia* 48 (2000) 2985-3004.

[105] K. J. Kurzydlowski, Size and Shape of Nano-Grains in Polycrystals Subjected to SPD, in: Y. T. Zhu, T. G. Langdon, R. S. Mishra, S. L. Semiatin, M. J. Saran, T. C. Lowe (Eds.), *Ultrafine Grained Materials II*, TMS Publ., Seattle, WA, 2002, pp. 615-622.

[106] *ASTM, E112-96*, Standard Test Methods for Determining Average Grain Size, 229-251, 1999.

[107] P. L. Sun, P. W. Kao, C. P. Chang, *Materials Science and Engineering a-Structural Materials Properties Microstructure and Processing* 283 (2000) 82-85.

[108] G. Holzer, M. Fritsch, M. Deutsch, D. Rollett, H. R. Wenk, *Materials Science and Engineering a-Structural Materials Properties Microstructure and Processing* 132 (1991) 1-11.

[109] P. Thompson, D. E. Cox, J. B. Hastings, *Journal of Applied Crystallography* 20 (1987) 79-83.

[110] G. K. Williamson, W. H. Hall, ″X-Ray Line Broadening from Filed Aluminium and Wolfram,″ *Acta Metallurgica* 1 (1953) 22-31.

[111] B. E. Warren, B. L. Averbach, ″The Effect of Cold Work Distortions on X-Ray Pattern,″ *J. Appl. Phys*. 21 (1950) 595-610.

[112] **G. M. Stoica**, E. A. Payzant, L. Wu, H. H. Liao, J. E. Spruiell, P. K. Liaw, *Adv. X-ray Analysis* 39 (2006) 116-121.

[113] N. C. Popa, D. Balzar, *Journal of Applied Crystallography* 35 (2002) 338-346.

[114] P. R. Dawson, D. E. Boyce, R. B. Rogge, *Materials Science and Engineering a-Structural Materials Properties Microstructure and Processing* 399 (2005) 13-25.

[115] M. Wilkens, *Fundamental Aspects of Dislocation Theory* Vol. II, Natl. Bur. Stand. (US) Spec. Pub. No. 317, Washington, DC, 1970, p. 1195-1221.

[116] A. Borbely, J. H. Driver, T. Ungar, *Acta Materialia* 48 (2000) 2005-2016.

[117] T. Ungar, A. Borbely, *Applied Physics Letters* 69 (1996) 3173-3175.

[118] T. Ungar, I. Dragomir, A. Revesz, A. Borbely, *Journal of Applied Crystallography* 32 (1999) 992-1002.

[119] I. C. Dragomir, T. Ungar, *Journal of Applied Crystallography* 35 (2002) 556-564.

[120] J. S. Kallend, U. F. Kocks, A. D. Rollett, H. R. Wenk, *Materials Science and Engineering a-Structural Materials Properties Microstructure and Processing* 132 (1991) 1-11.

[121] H. R. Wenk, S. Matthies, J. Donovan, D. Chateigner, *Journal of Applied Crystallography* 31 (1998) 262-269.

[122] A. P. Hammersley, *Fit 2D*, v.12.077, ESRF, BP220, 38043, Grenoble, France (1997).

[123] H. R. Wenk, L. Lutterotti, S. C. Vogel, *Nucl. Instr. & Meth. in Phys. Res*. A 515 (2003) 575-588.

[124] A. C. Larsen, R. B. Von Dreele, *General Structure Analysis System, GSAS*, LAUR 86-748, LANL (2004).

[125] Y. Iwahashi, Z. Horita, M. Nemoto, T. G. Langdon, *Acta Materialia* 46 (1998) 3317-3331.

[126] A. Gholinia, P. B. Prangnell, M. V. Markushev, *Acta Materialia* 48 (2000) 1115-1130.

[127] U. Chakkingal, A. B. Suriadi, P. F. Thomson, *Materials Science and Engineering a-Structural Materials Properties Microstructure and Processing* 266 (1999) 241-249.

[128] J. Y. Chang, J. S. Yoon, G. H. Kim, *Scripta Materialia* 45 (2001) 347-354.

[129] C. P. Chang, P. L. Sun, P. W. Kao, *Acta Materialia* 48 (2000) 3377-3385.

[130] S. Komura, M. Furukawa, Z. Horita, M. Nemoto, T. G. Langdon, *Materials Science and Engineering a-Structural Materials Properties Microstructure and Processing* 297 (2001) 111-118.

[131] S. R. Agnew, D. W. Brown, S. C. Vogel, T. M. Holden, *Materials Science Forum* 404-407 (2002) 747-752.

[132] S. R. Agnew, C. N. Tome, D. W. Brown, T. M. Holden, S. C. Vogel, *Scripta Materialia* 48 (2003) 1003-1008.

[133] R. Gehrmann, G. Gottstein, in: J. A. Szpunar (Ed.) Proc. of the 12th Int. Conf. on Textures of Materials, *ICOTOM-12*, NRC Research Press, Ottawa, Canada, 1999, pp. 665-670.

[134] M. A. Gharghouri, C. N. Tome, J. Root, in: J. A. Szpunar (Ed.) Proc. of the 12th Int. Conf. on Textures of Materials, *ICOTOM-12,* NRC Research Press, Ottawa, Canada, 1999, pp. 677-682.

[135] D. W. Brown, A. Jain, S. R. Agnew, B. Clausen, Twinning and Detwinning During Cyclic Loading of Mg Alloy, AZ31B *(private communication)*.

[136] M. A. Gharghouri, G. C. Weatherly, J. D. Embury, J. Root, *Philosophical Magazine a-Physics of Condensed Matter Structure Defects and Mechanical Properties* 79 (1999) 1671-1695.

[137] E. C. Oliver, M. R. Daymond, P. J. Withers, *Materials Science Forum* 490-491 (2005) 257-262.

[138] X. Y. Lou, M. Li, R. K. Boger, S. R. Agnew, R. H. Wagoner, *International Journal of Plasticity* 23 (2007) 44-86.

[139] C. N. Tome, G. C. Kaschner, *ICOTOM 14: Textures of Materials-Mat. Sci. Forum*, 495-497 (2005) 1001-1006.

[140] R. A. Lebensohn, C. N. Tome, *Acta Metallurgica et Materialia* 41 (1993) 2611-2624.

[141] R. W. Hertzberg, *Deformation and Fracture Mechanics of Engineering Materials,* 4th Ed., John Wiley & Sons, New York, 1996.

[142] H. J. Cui, R. E. Goforth, K. T. Hartwig, JOM-e 50 (1998) 8.

[143] M. N. Rittner, J. R. Weertman, J. A. Eastman, K. B. Yoder, D. S. Stone, *Materials Science and Engineering a-Structural Materials Properties Microstructure and Processing* 237 (1997) 185-190.

[144] R. S. Mishra, T. R. Bieler, A. K. Mukherjee, *Acta Mater.*, 45 (1997) 561-568.

[145] T. Mukai, H. Watanabe, T. G. Nieh, K. Higashi, Mat. Res. Soc. Symp. Proc. 601 (2000) 291-301.

[146] ASM Metals Reference Book, Third Edition, Ed. M. Bauccio, p. 495, 1993.

[147] K. Xia, J. T. Wang, X. Wu, G. Chen, M. Gurvan, *Materials Science and Engineering a-Structural Materials Properties Microstructure and Processing* 410 (2005) 324-327.

[148] S. R. Agnew, P. Mehrotra, T. M. Lillo, **G. M. Stoica**, P. K. Liaw, "Texture Evolution of Five Wrought Magnesium Alloys during Route A Equal Channel Angular Extrusion: Experiments and Simulations," *Acta Materialia*, vol. 53, no. 11 (2005) 3135-3146 .

[149] S. B. Yi, H. G. Donemeier, J. Bohlen, D. Letzig, K. U. Kainer, *Physica*, B350 (2004) 507-509.

[150] S. R. Agnew, Ö. Duygulu, *Intl. J. of Plasticity*, 21 (2005) 1161-1193.

[151] **G. M. Stoica**, L. Wu, P. K. Liaw, E. A. Payzant, A. D. Stoica, Y. Ren, J. E. Spruiell, S. R. Agnew, and D. E. Fielden, ″Grain Preferential-Orientation and Plastic Behavior of Mg Alloys: Part I: Texture Evolution after Uniaxial Compression″ (to be submitted); **G. M. Stoica**, L. Wu, J.

E. Spruiell, P. K. Liaw, E. A. Payzant, A. D. Stoica, Y. Ren, and D. E. Fielden, ″Grain Preferential-Orientation and Plastic Behavior of Mg Alloys: Part II: Elastic Microstrain and Dislocations Configuration″ (to be submitted).

[152] W. H. Huang, L. Chang, P. W. Kao, and C. P. Chang, *Materials Science and Engineering a-Structural Materials Properties Microstructure and Processing 307 (2001)* 113-119.

[153] R. Gehrmann, M. M. Frommert, G. Gottstein, *Materials Science and Engineering a-Structural Materials Properties Microstructure and Processing* 395 (2005) 338-349.

[154] S. R. Agnew, P. Mehrotra, T. M. Lillo, **G. M. Stoica**, and P. K. Liaw, "Crystallographic Texture Evolution of Three Wrought Magnesium Alloys during Equal Channel Angular Extrusion," *Materials Science and Engineering a-Structural Materials Properties Microstructure and Processing 408 (2005)* 72-78.

[155] L. S. Toth, P. Gilormini, and J. J. Jonas, *Acta Met.* **36**, 12, (1988) 3077-3091

[156] M. Cohen, *Thesis*, Ecole de Mines de Paris, France, 1983.

[157] F. Montheillet, M. Cohen, J. J. Jonas, *Acta Met.* **32** (1984) 2077.

APPENDIX: Tables and Figures

Table 1 - ECAP parameters used to obtain UFG materials.

Material	Reference	Billet size (mm)	2Φ (deg)	2Ψ (deg)	Speed (mm/s)	Route	No. passes	ECAP temperature
Al	[148]	10Φ[*1] × 150	90	90	19	B	3 - 4	RT[*2]
Al	[129]	10 × 10 × 150	90 - 157.5	10-30	-	B	1 - 21	RT
Al; Al-1Mg	[30]	5Φ × 45	90	90	0.008 - 8	B_c	8	RT
Al-3Mg	[15]	14 × 14 × 60	90	-	-	-	4	RT
Al-3Mg-0.2Sc	[94]	10Φ × 60	90	45	-	B_c	8	RT
Al-3Mg-.2Zr Al-0.3Mn	[92]	15Φ × 90	120	-	-	A, B, C	16 - 25	RT 200^0C
1050Al	[25]	12 × 12 × 80	90	20	0.1	B_c	8	RT
101 Cu; 3003Al	[20]	25 × 25 × 152	-	-	0.5	-	2 - 8	RT
5056Al	[19]	20Φ	90	-	-	C	8	100^0C - 250^0C
5056 Al	[25]	55Φ × 100	90	-	1	C	4	150^0C
6061 Al	[28]	24 × 24 × 130	90	-	0.5	B	4	110^0C
6061Al **6061Al/Al_2O_3**	[13,14]	Rod Φ = 100 20Φ[*] × 20	90	-	-	B	8 8 + 4	400^0C 400^0C + 200^0C
Cu	[4]	Cylinder	90	-	-	C	11 - 14	RT
Cu-25Ag; Cu-18Nb	[27]	25 × 25 × 125	90	0	0.5	-	1 - 24	RT
Mg-alloys: AZ31B ZK60	[37,38]	22 × 22 × 100	90	-	1/6	A, B, C	1 - 8	300^0C 260^0C
Low C steel	[147]	18Φ × 130	90	20	-	C	4	350^0C
Ti	[21]	20Φ × 100	-	-	-	B	7	500^0C ; 450^0C
Ti-45.5Al-2Cr-2Nb	[36]	17 × 7 × 137	90	-	25	-	1 - 2	1,150^0C; 1,250^0C
Ti-6Al-4V	[47]	23 × 3 × 127	90	-			1 - 2	900^0C ; 1,005^0C

*[1]Φ - diameter; *[2]RT - room temperature, A, B, B_C, and C - ECAP routes.

Table 2 - Microstructures and mechanical properties obtained on pure metals, Cu, Al, Ti, and W using the ECAP technology.

Material	Reference	Grain size (μm)	Microstructure	Properties
Cu	[9-11]	0.25	LAGBs Fine cell structure	H_V = 135 (40)*; RA = 42% Softening under low-cycle fatigue testing; m = 0.013 after 4A for the strain-rate range of 10^{-6} - 10^{-2}/s; Q (creep) = 119 kJ/mol
Cu	[12,13]	0.2	Equiaxed grains with HAGBs	Increased both strength and ductility: YS = 450 MPa (250 MPa) ε = 850%, 200^0C, 1.4×10^{-3}/s.
Cu	[14]	0.1 0.1 - 0.25 0.23 - 0.6	Dislocation free grains Dislocation network within grains Cell and subgrain dislocation structure	Density of dislocations: $1.3 \times 10^{11}/cm^2$ YS = 390 MPa UTS = 500 MPa
1100-Al (99.9%Al)	[15]	1 (RT, $6B_C$)	Uniform equiaxed	ε = 25% (5 - 15%); YS = 190 MPa (152 MPa)
Ti (HPT)	[12,13]	0.1	Equiaxed (B_C)	RA = 43% (5 HPT revolutions)
Ti	[16]	0.3	Uniform equiaxed ($4B_c$); HAGBs	ε = 14%, and better hardness and strength
Ti	[17]	0.2 - 0.3 (10) Route B_C Route C	homogeneous, HAGBs nonhomogeneous, LAGBs & HAGBs	B_C: Fatigue limit increased by 60%; N = 3.45×10^4 (4.2×10^3) C: Fatigue limit increased by 40%; N = 1.75×10^4 (4.2×10^3)
W (hot-rolled)	[18]	1 (60 - 80) (8C, 110^0)	As-received: Polygonized dislocations ECAP, 4C: serrated GBs, elongated ECAP, 8C: equiaxed, dislocation free	H_V = 6.1 GPa (5.6 GPa)

* The values in parentheses are for the coarse-grained material; RT - room temperature; A, B_c, or C - ECAP route; GBs - grain boundaries; LAGB, HAGB - low and high-angle grain boundaries, respectively; YS - yield strength; UTS – ultimate-tensile stress; ε - elongation; RA - reduction of area; m - strain-rate sensitivity; Q - activation energy; H_V - Vickers hardness; LCF - low-cycle fatigue; HCF - high-cycle fatigue; HPT - high-pressure torsion.

Table 3 - Microstructures and mechanical properties obtained on Al alloys using the ECAP technology.

Material	Ref.	Grain size (μm)	Microstructure	Properties
5056 Al-H38 (Al-4.8Mg-0.06Cr)	[19]	0.3 at 4C, 150^{0}C	Lamellar with LAGBs	Fatigue testing: N = 10^7 (σ_a = 120 MPa)* Increased strength by 3 times
5056-Al-H38	[21]	0.22 at 140^{0}C 10 - 35 at 200^{0}C	LAGB After annealing: HAGBs	YS is 3 times greater;
1560 Al- H14 (Al-6Mg-0.6Mn)	[22]	0.4	Post-ECAP annealing: recovery elim. non-eq. GBs	YS = 375 MPa (320 MPa); ECAP + rolling: YS = 540 MPa ; ε = 9 % (10 %)
2024Al (Al-3Fe-5Ni)	[24]	0.6	Route A: elongated Route B: isotropic, spherical	Increased hardness by 2 times
6061Al (Al-1Mg-0.6Si-0.3Cu-0.2Cr)	[25]	0.2-0.4 at 110^{0}C; 8B_A	Elongated, misoriented grains	Hardness = 97 HB; UTS = 400 MPa (310 MPa); ε = 11 % (12 %)
6061Al-T6	[28]	0.3-0.4 at 125^{0}C, 4B_c	Equiaxed grains, forming GBs ⊥ to bands direction; Mg_2Si	Increased hardness by 40% when post-ECAP aged
6061 Al/Al_2O_3	[28]	0.6	Random irregular grains, with extrinsic dislocations	Increased YS by 2 times; ε = 150%, 200^{0}C at 10^{-3}/s; H_V ~ 1,200 MPa (650 MPa);
6061Al/Al_2O_3	[29]	1 (80)	Equiaxed (8B_c)	YS = 205 MPa (144 MPa); ε = 15% (25%)
6061Al/SiO_2	[30]	0.4 at RT, 12 passes	Random misorientation	ε = 120%, 300^{0}C, 10^{-3}; UTS = 47 MPa; ε = 220%, 590^{0}C, 10^{-1}/s; UTS = 15 MPa
Al-Cu-Zr	[32]	1.2		ε = 970% (300^{0}C, 10^{-2}/s);
Al-3 Mg-0.2 Sc	[26]	0.2 at 320^{0}C, 4B_C	Non-equilibrium GBs	ε = 2,280% at 400^{0}C, 3.3 × 10^{-2}/s
Al-3Mg-0.2 Sc	[33]	0.3 at RT, 8A, 8B, 8C	Precipitates retaining the grain size from growing at high temperatures	Route A: ε = 1,170% at 400^{0}C, 3.3 × 10^{-2}/s Route B_C: ε = 2,280% at 400^{0}C, 3.3 × 10^{-2}/s Route C: ε = 1,370% at 400^{0}C, 3.3 × 10^{-2}/s
Al-6Mg-0.2 Sc-0.15Zr	[34]	1 - 2 at 320^{0}C, 4B_C	- Elongated grains; - Dislocation slip within grains	LCF, 1Hz; fatigue life 1.5 - 2 times better; HCF, 10Hz; fatigue limit 150 MPa; ε = 29% (9%); UTS = 400 MPa (365 MPa)

* The values in parentheses are for the coarse-grained material; GBs - grain boundaries; LAGB, HAGB - low and high-angle grain boundaries; YS - yield strength; UTS - ultimate-tensile stress; ε - elongation; LCF - low-cycle fatigue; HCF – high-cycle fatigue.

Table 4 - Microstructures and mechanical properties obtained on Mg alloys using the ECAP technology.

Material	Ref.	Grain size (μm)	Microstructure	Properties
AZ 31-as-rolled sheet (Mg-3Al-1Zn-0.2Mn) **AZ61 (Mg-6Al-1Zn-0.2Mn)**	[35]	0.5 - 1 (>50)*	Homogeneous	Elongation two times better; Q = 96 kJ/mol (127 kJ/mol); n = 2, p = 3 Q = 143 kJ/mol; n = 2, p = 2
Mg alloy, Mg-0.9Al	[36]	17 (200^0C)	Homogeneous, equiaxed	15% increased both strength and ductility
AZ 31 (Mg-2.5Al-0.92Zn-0.39Mn) **ZK60 (Mg-4.9Zn-0.49Zr)**	[29, 37]	17 2.5 and 10	- Equiaxed - Bimodal, elongated and grain substructures	ε and YS not changed ε = 371% (4A), 350^0C, 5×10^{-3}/s;
AZ31 **ZK60**	[39]	15 (350^0C, 10^{-2}/s)	Grain growth Dynamic recrystallization	Extrusion: ε = 220%, 177^0C, 10^{-5}/s; m = 0.2
AZ61	[40]	1 (375^0C)	- Equiaxed grains; HAGBs	ε ~ 400%
AZ91	[20]	0.5 (175^0C)	- Equiaxed grains, HAGBs; - Non equilibrium GBs	ε = 661% (200^0C , 6×10^{-5}/s)
ZK60	[41]	1	Two secondary phases: $Zn_2 Zr_3$ (globular) β-Mg_2Zn_3 phase (lamellar)	ε = 400%
ZK60	[51]	1 and 12 (200^0C)	Bimodal uniform distributed in samples with backpressure	ε = 1,400% , 220^0C, 3×10^{-3}/s, (cast + ECAP) ε = 480% (rolling before ECAP)

* The values in parentheses are for the coarse-grained material; Q - activation energy; ε - elongation; YS - yield strength; GBs - grain boundaries; LAGB, HAGB - low and high-angle grain boundaries; YS - yield strength; n - stress exponent; p - grain-size exponent from the constitutive relationship [144]: $\dot{\varepsilon} = A\frac{D_g Gb}{kT}\left(\frac{b}{d}\right)^p\left(\frac{\sigma}{G}\right)^n$.

Table 5 - Microstructures and mechanical properties obtained on Cu, Zn, Fe, and Ti Alloys using the ECAP technology.

Material	Ref.	Grain size (μm)	Microstructure	Properties
Cu alloy (Cu-40Zn)	[42]	1 (1 mm)	Equiaxed and elongated grains	ε = 640% (400^0C, 10^{-2}/s)
Cu alloy (Cu-Cr-Zr)	[43]	0.16	Uniform UFG	LCF: softening
Cu-0.18Zr **Cu-30Zn** **Cu-30Zn-0.13Zr** **Cu-40Zn**	[42]	0.4 at 90^0, $4B_c$, RT 0.1 0.1	Single phase without phase transf.; Elongated grains Single phase without phase transf.; Two phases with phase transf.	 ε = 360%, 400^0C, 10^{-3}/s ε = 640%, 400^0C, 10^{-2}/s
Zn alloy (Zn-22Al)	[44]	0.6	Unstable; non-equilibrium GBs	ε = 1,900% (3.3×10^{-2}/s)
Low C steel	[45]	0.2 at 350^0C, 4C	Elongated grains; high density of dislocations near GBs	UTS = 805 MPa (310 MPa) ε = 12% (30%)
Low carbon steel (Fe-0.06V)	[46]	0.2	- Ferrite grain refinement - Cementite precipitations	Higher strength
Low carbon steel (Ti-V)	[46]	0.2 $4B_C$		UTS = 940 MPa (450 MPa) $\frac{Y}{UTS} = 0.63$ (0.97 for plain steel)
Ti alloy (Ti-6Al-4V)	[47]	0.03 – 0.05 0.1 - 0.13	Non-eq. GBs with significant internal stress (elastic microstress)	ε = 220 %, 625^0C, 10^{-3}/s; ε = 145 %, 625^0C, 10^{-3}/s;
Al-2%Fe (Immiscible 2 phases) **TiNi**	[48]	0.6 (80) 1 (80) at 400^0C and 110^0C		YS = 185 MPa (52 MPa) UTS = 235 MPa (58 MPa); ε = 13.7% (6.8%) YS = 910 MPa (600 MPa); UTS = 1,460 MPa (1,100 MPa)

* The values in parentheses are for the coarse-grained material; RT - room temperature; GBs - grain boundaries; LAGB, HAGB - low and high-angle grain boundaries; YS - yield strength; UTS - ultimate-tensile stress; ε - elongation; LCF - low-cycle fatigue.

Table 6 - The compositions and mechanical properties of the as-received Mg-alloys [146]; ρ - density, E -Young modulus, ν - Poisson ratio, $\sigma_{0.2}$ and Y - tensile and yield strengths, ε - elongation, H - hardness, G - shear modulus, σ_f - fatigue strength.

Starting materials	Composition (weight percent)	Mechanical Properties
Mg alloy, AZ31-H24 (hot rolled) (H24: strain hardened and partially annealed at 330^0C, 1 hr)	96Mg-3Al-1Zn $T_m = 650^0$C ECAP: T = 0.55 T_m	ρ = 1.77 - 1.83 g/cm^3 E = 44.8 GPa; ν = 0.35 $\sigma_{0.2}$ = 290 MPa; Y = 220 MPa (180)* ε = 15%; H = 73 HB; G = 160 MPa
Mg alloy, ZK60-T5 (hot extruded) (T5: solution treatment at 525^0C, 2 hrs, and aging at 182^0C, 8 hrs)	94Mg-5.5Zn-0.45Zr	ρ = 1.83 g/cm^3 E = 44.8 GPa; ν = 0.35 $\sigma_{0.2}$ = 365 MPa; Y = 305 MPa (250)* ε = 11%; H = 88 HB; G = 180 MPa

* The value of the corresponding strength in compression.

Table 7 - The apparent-shear strain, γ_T, and equivalent strain, ε_{eq}, as derived from the models predicting the plastic-deformation zone (PDZ) in ECAP (from Ref. 65).

ECAP Models	γ_T	ε_{eq}	
		Engineering	**True**
Sharp Corner (SP-PDZ)*	[Eq. 1] from Ref. 2 $2\cot\Phi$	[Eq. 4] from Ref. 2 $\frac{2}{\sqrt{3}}\cot\Phi$	[Eq. 7] from Ref. 147 $\frac{2}{\sqrt{3}}\ln\left(\frac{1+\cos\Phi}{\sin\Phi}\right)$
Round Corner (ψ-PDZ)	[Eq. 2] from Ref. 79 $2\cot(\Phi+\Psi)+\frac{2\Psi}{\sin^2(\Phi+\Psi)}$	[Eq. 5] from Ref. 142 $\frac{2}{\sqrt{3}}\left[\cot(\Phi+\Psi)+\Psi\right]$	[Eq. 8] from Ref. 79 $\frac{2}{\sqrt{3}}\left[\ln\left(\frac{1+\cos(\Phi+\Psi)}{\sin(\Phi+\Psi)}\right)+\ln\left(\sqrt{1+\Psi^2}+\Psi\right)\right]$
Round Free-Surface (PS-PDZ)**	[Eq. 3] from Ref. 79 $2\left[\cot(\Phi+\chi)+\tan(\chi-\delta)\right]$	[Eq. 6] from Ref. 77 $\frac{\gamma_T}{\sqrt{3}}$	[Eq. 9] from Ref. 77 $\frac{2}{\sqrt{3}}\ln\left(\frac{\gamma_T}{2}+\sqrt{1+\left(\frac{\gamma_T}{2}\right)^2}\right)$

*SP-PDZ (single-plane plastic-deformation zone); **PS-PDZ (partial split-PDZ); Φ - the angle between the die channels; Ψ - angular span of the round outer-corner; χ and δ - variable angles when moving on the curved rigid-plastic boundary.

Table 8 - The apparent-equivalent strain, P_r, describing the degree of redundancy for the routes, A, B_A, B_C, and C, in multipass ECAP; n - integer, N - number of passes.

N	P_r values for the ECAP routes			
	A	**B_A**	**B_C**	**C**
4 n	N	$N/\sqrt{2}$	0	0
4 n + 2	N	$N/\sqrt{2}$	$\sqrt{2}$	0
2 n + 1	N	$\sqrt{(N^2+1)/2}$	1	1

Table 9 - The four emission lines, λ_1, λ_2, λ_3, and λ_4 and their widths and weights used to determine the instrumental resolution [108].

λ (Å)	$\Delta\lambda/\lambda$	**Weights**
0.154059	0.000284	0.579
0.154106	0.000417	0.08
0.154440	0.000332	0.236
0.15469	0.000445	0.105

Table 10 - The slip systems, dislocations types, and contrast parameters for Mg [119].

Type	Slip system	Sub-slip system	Slip plane	b	b-type	C_{hk0}	q_1	q_2
Edge	Basal	BE	{0001}	$\langle 2\bar{1}\bar{1}0 \rangle$	*a*	0.19483	0.067864	-0.19759
	Prismatic	PrE	$\{0\bar{1}10\}$	$\langle \bar{2}110 \rangle$	*a*	0.33713	-1.14306	0.326649
		PrE2	$\{0\bar{1}10\}$	$\langle 0001 \rangle$	*c*	0.03967	4.880886	1.079577
		PrE3	$\{0\bar{1}10\}$	$\langle \bar{2}113 \rangle$	*c*+*a*	0.08297	3.055985	-1.01943
	Pyramidal	PyE	$\{0\bar{1}\bar{1}1\}$	$\langle \bar{1}2\bar{1}0 \rangle$	*a*	0.2986	-0.86223	0.170791
		PyE2	$\{2\bar{1}\bar{1}2\}$	$\langle \bar{2}113 \rangle$	*c*+*a*	0.08233	1.75516	0.248391
		PyE3	$\{1\bar{1}2\bar{1}\}$	$\langle \bar{2}113 \rangle$	*c*+*a*	0.0817	3.501807	-0.66875
		PyE4	$\{0\bar{1}\bar{1}1\}$	$\langle \bar{2}113 \rangle$	*c*+*a*	0.0816	2.081515	-0.03236
Screw		S1		$\langle 2\bar{1}\bar{1}0 \rangle$	*a*	0.12366	1.191931	-1.008
		S2		$\langle \bar{2}113 \rangle$	*c*+*a*	0.38948	1.321473	-0.91879
		S3		$\langle 0001 \rangle$	*c*	0.00023	-2471.84	1412.024

b - Burgers vector

Table 11 - The fatigue-strength exponent, b, and the fatigue-strength coefficient, σ_f', determined from the low-cycle fatigue of the Mg alloys, AZ31 (hot rolled) and ZK60 (hot extruded), and tested in the CC - and TT - loading directions.

Sample	b	σ_f'/E
AZ-CC	-0.094 ± 0.005	0.009 ± 0.001
AZ-TT	-0.238 ± 0.003	0.020 ± 0.001
ZK-CC	-0.16 ± 0.002	0.025 ± 0.003
ZK-TT	-0.09 ± 0.002	0.011 ± 0.002

Table 12 - The fatigue-strength exponent, b, and the fatigue-strength coefficient, σ_f', for the Mg alloy, AZ31, before and after ECAP, 1, 2, and 8 passes, routes A and B.

Sample	b		σ_f' (MPa)	
	Cross (CC)	Top (TT)	Cross (CC)	Top (TT)
As-rec.	-0.094 ± 0.005	-0.238 ± 0.003	400 ± 17	900 ± 17
1A	-0.083 ± 0.008	-0.164 ± 0.013	390 ± 27	660 ± 71
2A	-0.082 ± 0.006	-0.114 ± 0.003	400 ± 21	440 ± 12
2B	-0.071 ± 0.007	-0.197 ± 0.005	370 ± 24	900 ± 38
2B2	-0.070 ± 0.005	-0.132 ± 0.016	360 ± 15	470 ± 56
8B		-0.082 ± 0.014		330 ± 34
8BB		-0.149 ± 0.001		680 ± 3

Table 13 - The low energy X-ray diffraction results from the whole-pattern fitting of the profiles obtained for the AZ31 compressed samples for different loading directions: FF, CC, and TT (FF, CC, and TT - the loading directions normal to the flow, cross, and top planes, respectively), and at different testing temperatures; D_V - the volume-averaged coherent-domain size; <a>, <a + c>, and <c> - the percentage of the dislocation debris corresponding to the three orientations of the Burgers vectors; ρ - dislocation density.

Compression		**D_V (nm)**	**Micro-strain**	**$I_{00.2}/I_{10.0}$**	**<a> (%)**	**<a + c> (%)**	**<c> (%)**	**ρ [$10^{14}/m^2$]**
FF	As-rec	220	1.4E-03	0.1	92	3	5	0.7
	RT	100	3.4E-03	2.3	64	18	18	4.5
	150^0C	500	2.8E-03	1.3				
	250^0C	320	3.5E-03	4.9	79	6	15	4.7
	350^0C	2000	1.4E-03	10.5	98	1	1	0.7
CC	As-rec	250	2.0E-03	0.1				
	RT	290	3.9E-03	4.1	62	29	9	5.7
	150^0C	160	3.6E-03	5.2	79	6	15	5.1
	250^0C	210	3.6E-03	3.6	8	7	13	4.9
	350^0C	880	1.8E-03	7.2	92	3	5	1.2
TT	As-rec	310	1.1E-03	17.7				
	RT	200	1.5E-03	17.7				
	250^0C	170	4.0E-03	22.1	92	3	5	5.9

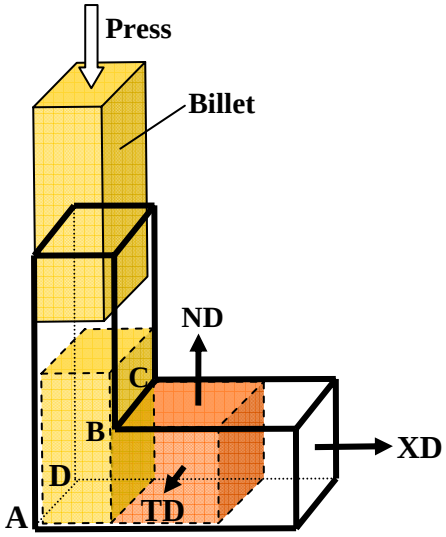

Figure 1 - In the ECAP technique, the billet is passing through the two channel die (in this case, a 90^0 die). The coarse-grained billet is plastically deformed by a simple shear at the shearing plane, ABCD, and is exiting into the second channel; XD, TD, and ND are the pressing, transverse, and normal directions.

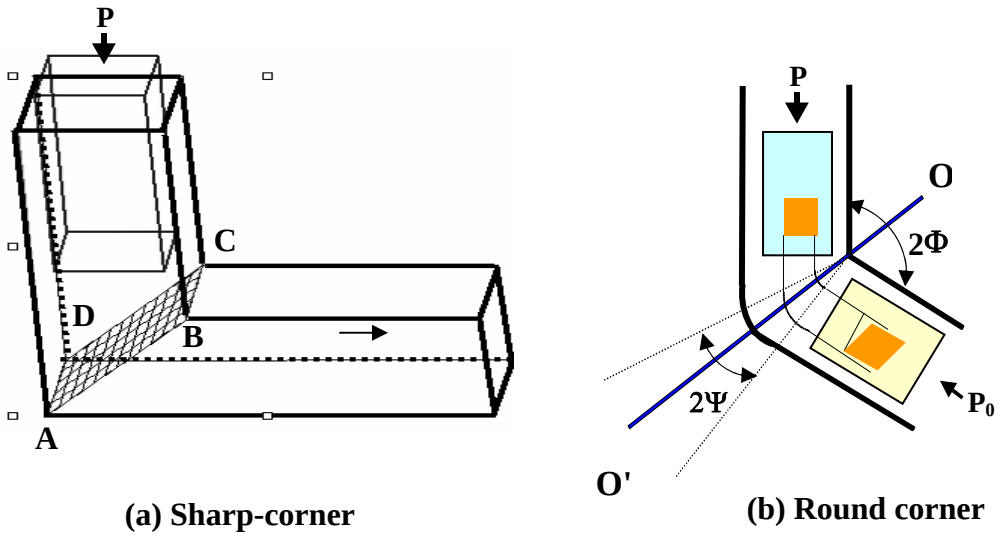

Figure 2 - The ECAP-die geometry: (a) a sharp corner between the two channels at $\Phi = 90^0$; the plastic zone confined to a single shear-plane, ABCD; (b) a round corner between the channels at 120^0, and with the angular span, 2Ψ, encompassing the roundness of the outer corner. The central plane of shearing, OO′, is at the intersection of the channels, dividing in two parts the plastic-deformation zone (PDZ).

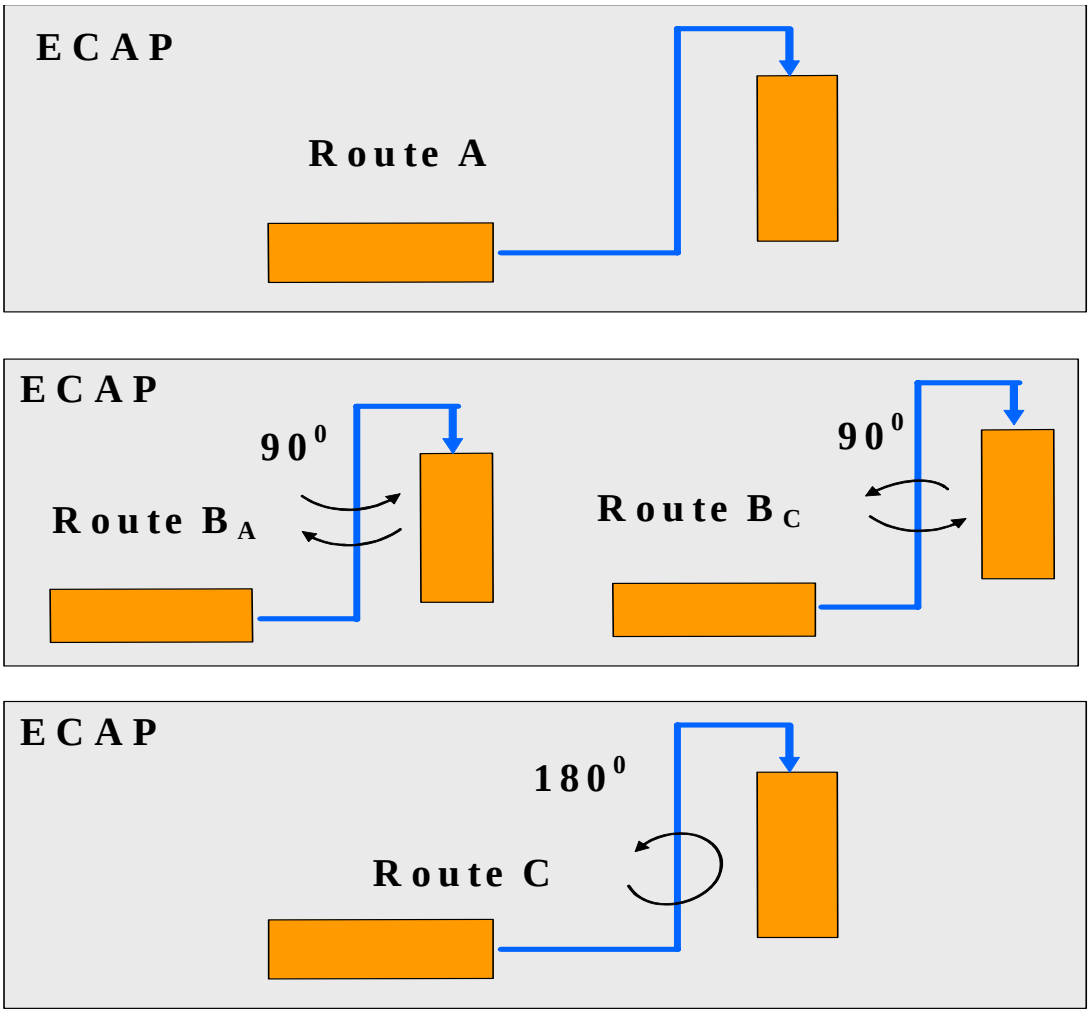

Figure 3 - The ECAP straining routes: route A with no rotation between passes, route B_A with alternate rotation of 90^0, route B_C with consecutive rotation of 90^0, and route C with a rotation of 180^0 of the billet between passes.

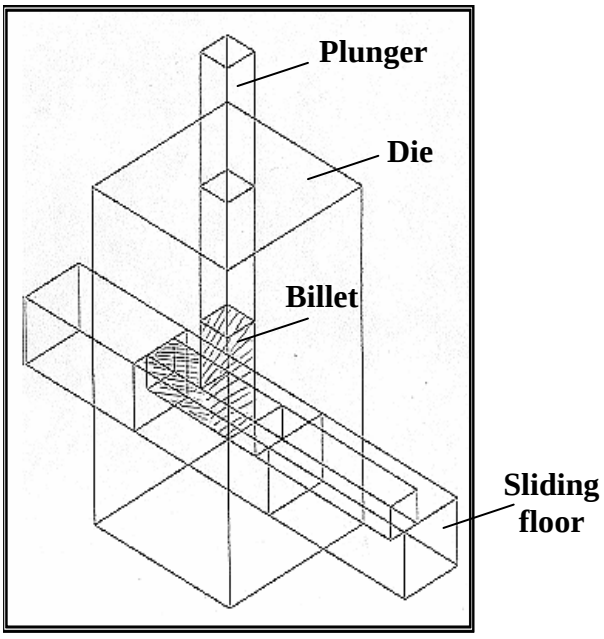

Figure 4 - A split ECAP-die with sharp-corner; the sliding floor reduces the friction billet-die, and is the second channel of the die.

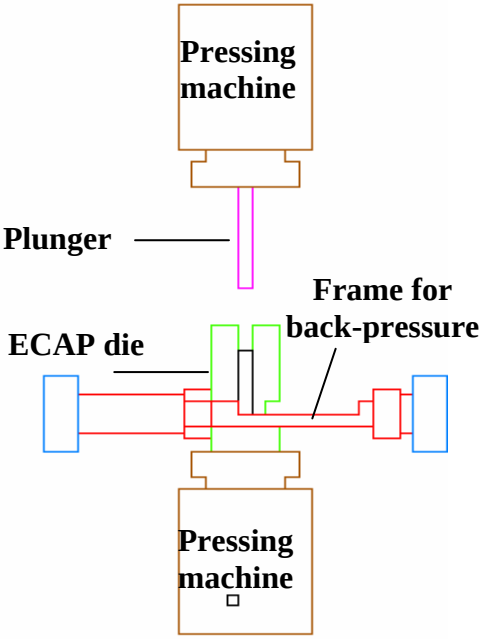

Figure 5 - Lateral view of the ECAP setup, including the pressing machine, ECAP die, and a frame for the back-pressure.

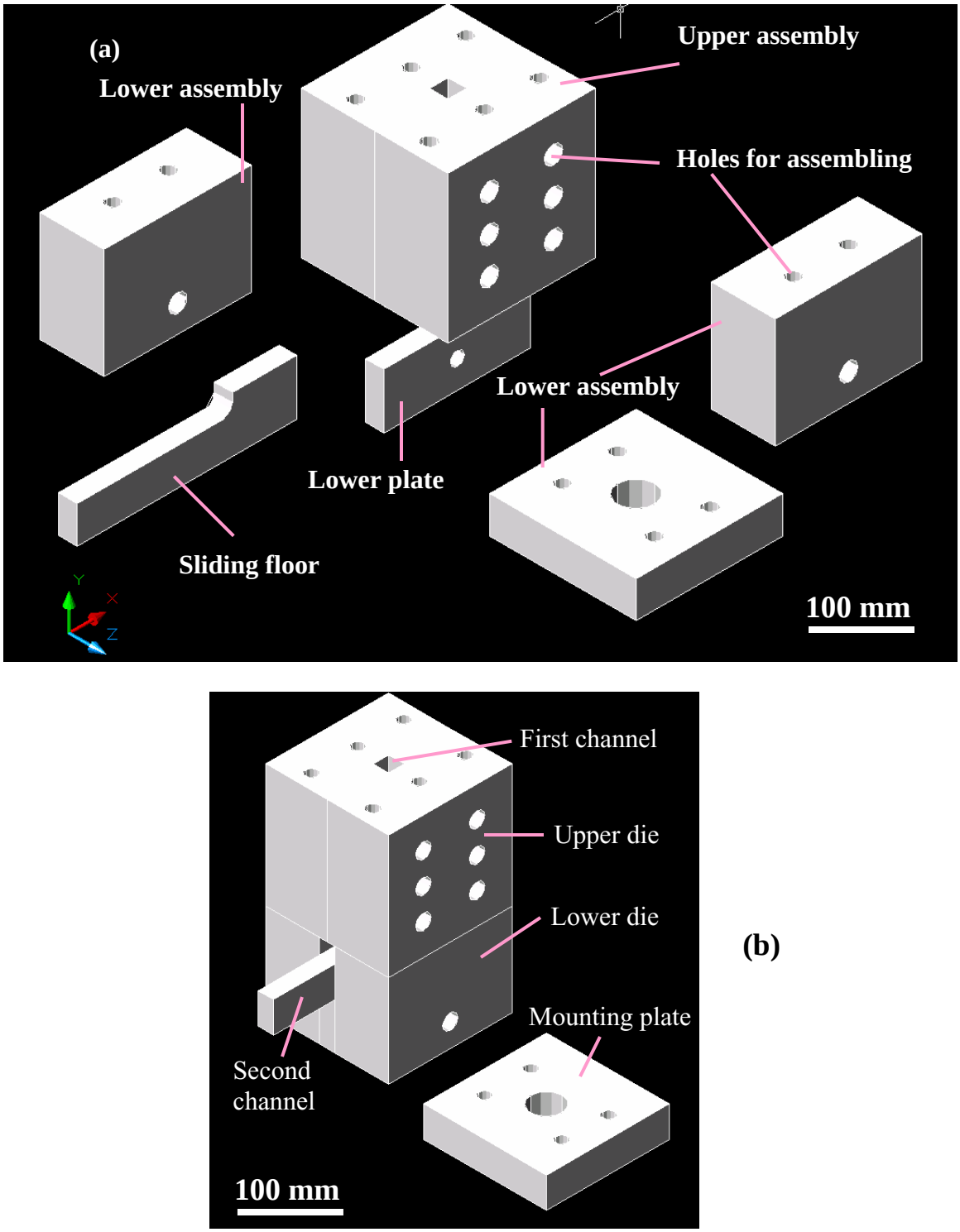

Figure 6 - (a) The components of the modified sharp-corner ECAP die: upper and lower assemblies, and the sliding floor; (b) assembled die.

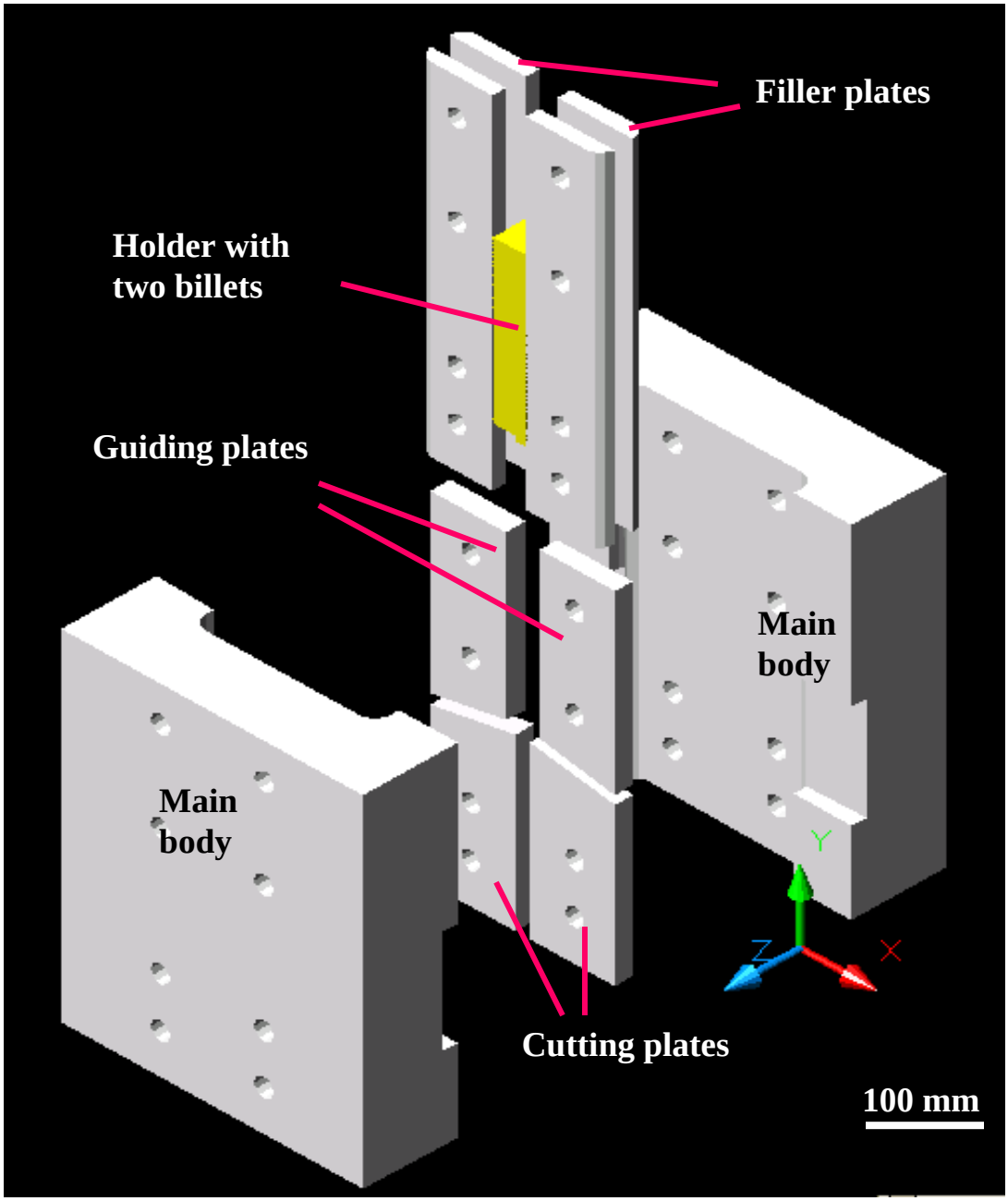

Figure 7 - The components of the symmetric ECAP die designed to process two billets at once; the billets are square-shaped, and the size can vary from 9.5 × 9.5 to 25 × 25 mm, with the length of 102 mm. The die allows for flexible angles between the two channels ranging from 90º to 120º, and the die-billet interface has a minimal friction, i.e., the two billets move together with the holder.

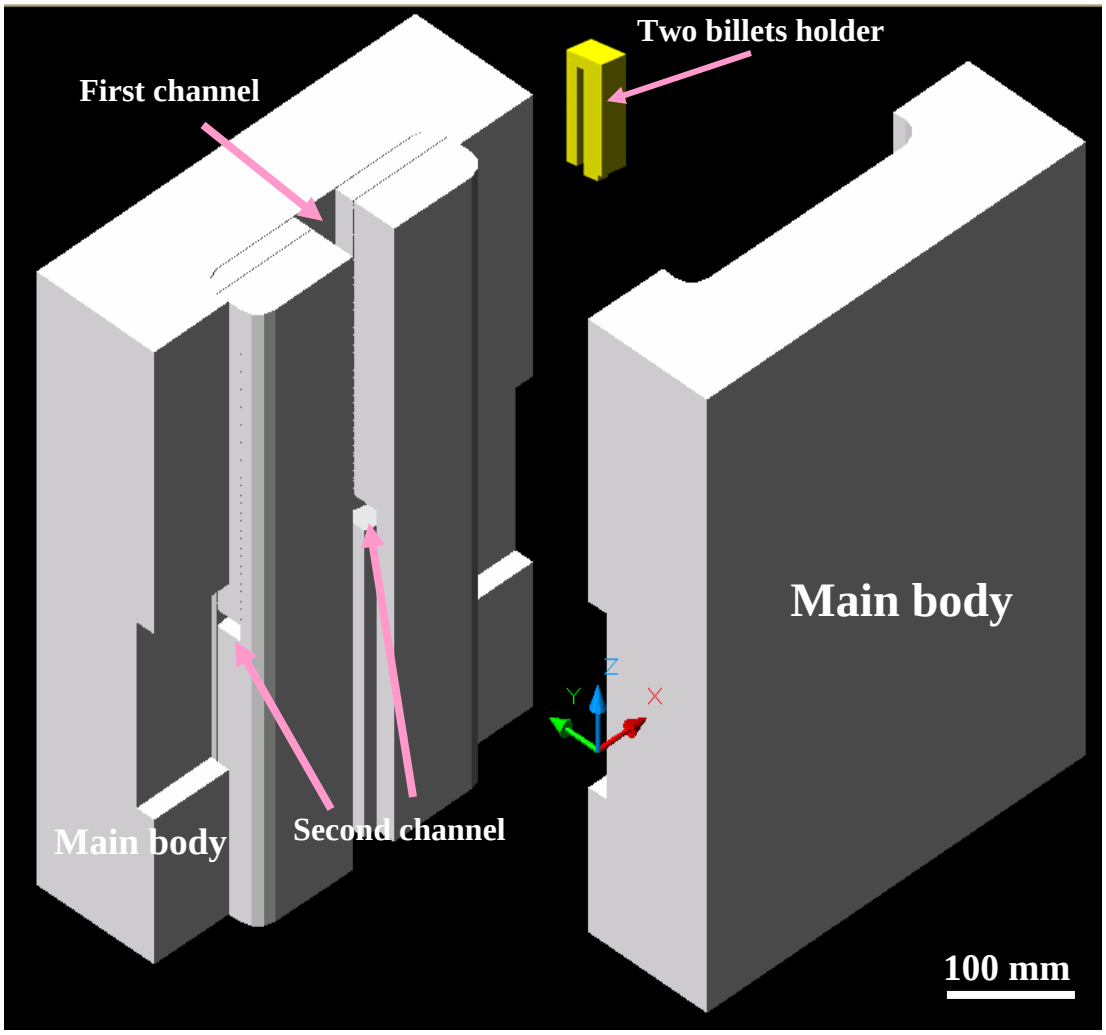

Figure 8 - Assembly of the symmetric ECAP die, including the main body with the guiding and filling plates mounted to form the first and second channel of the die, and the holder for the two billets. The billet size can vary from 9.5 × 9.5 to 25 × 25 mm, with the length of 102 mm.

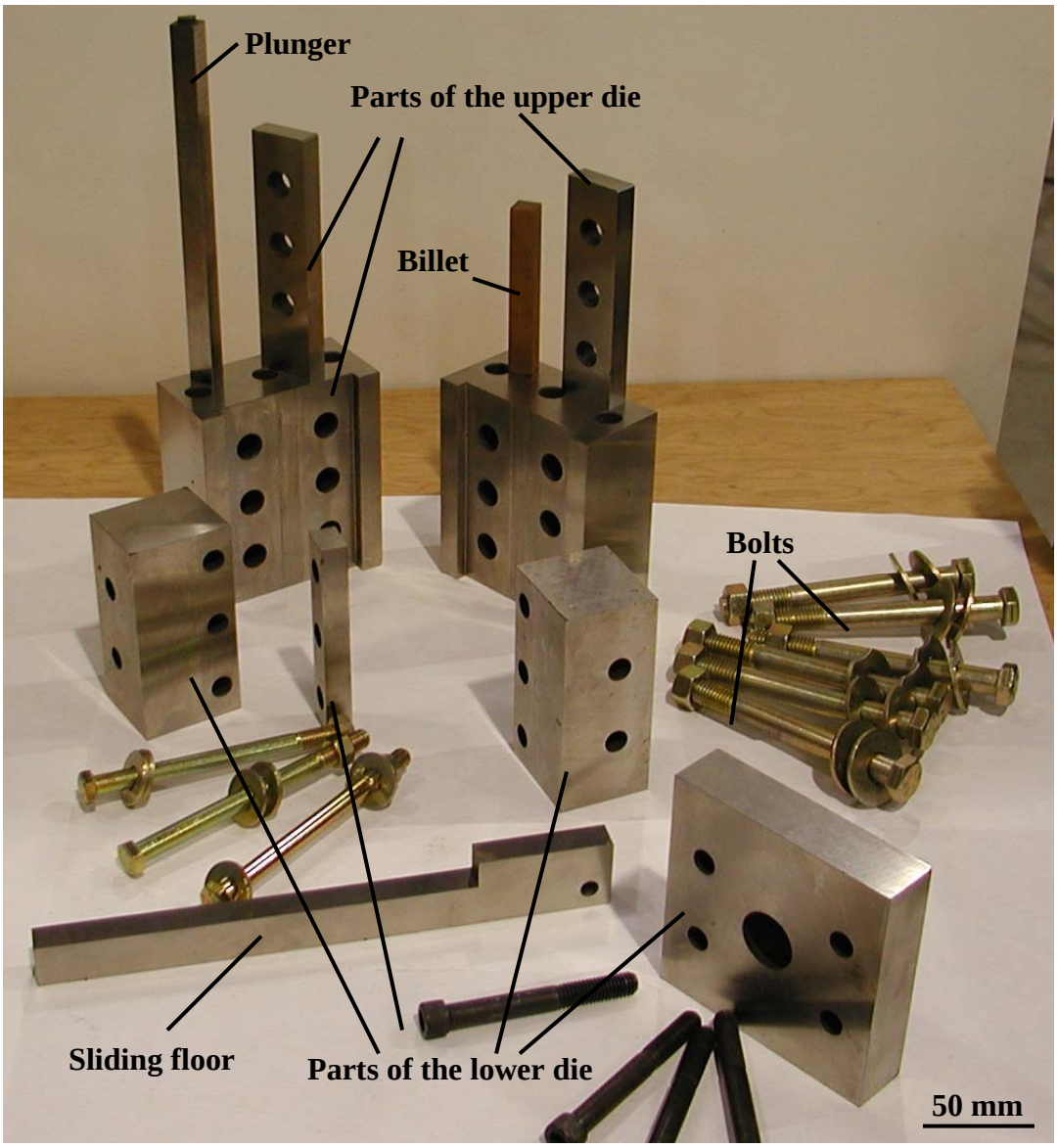

Figure 9 - The components of the sharp-corner ECAP die.

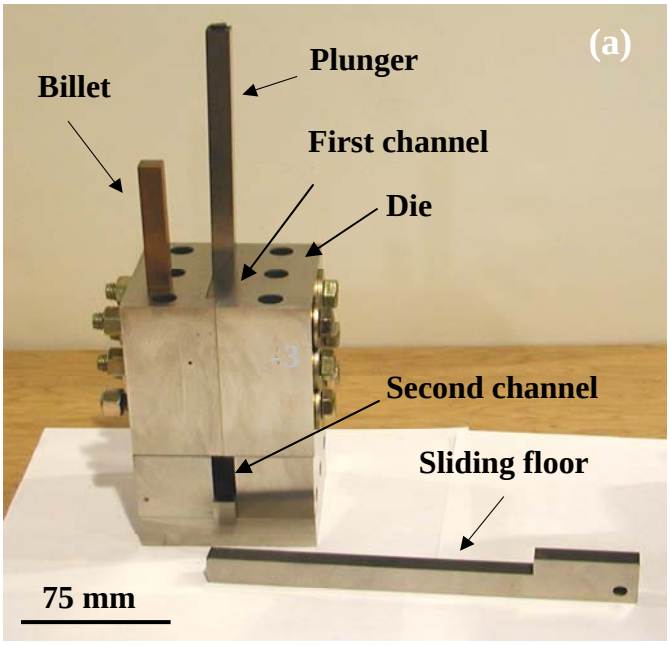

Figure 10 - A sharp-corner ECAP die with a sliding floor in the second channel, and moving together with the billet during the processing. The billet size is 12.5 × 12.5 × 102 mm.

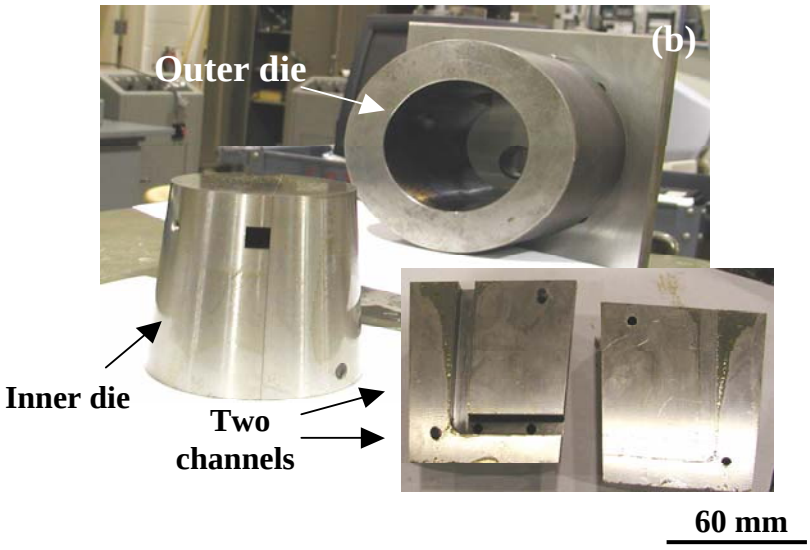

Figure 11 - A round-corner ECAP die with the angular span, $2\Psi = 60^0$, which is the roundness of the outer corner of the die.

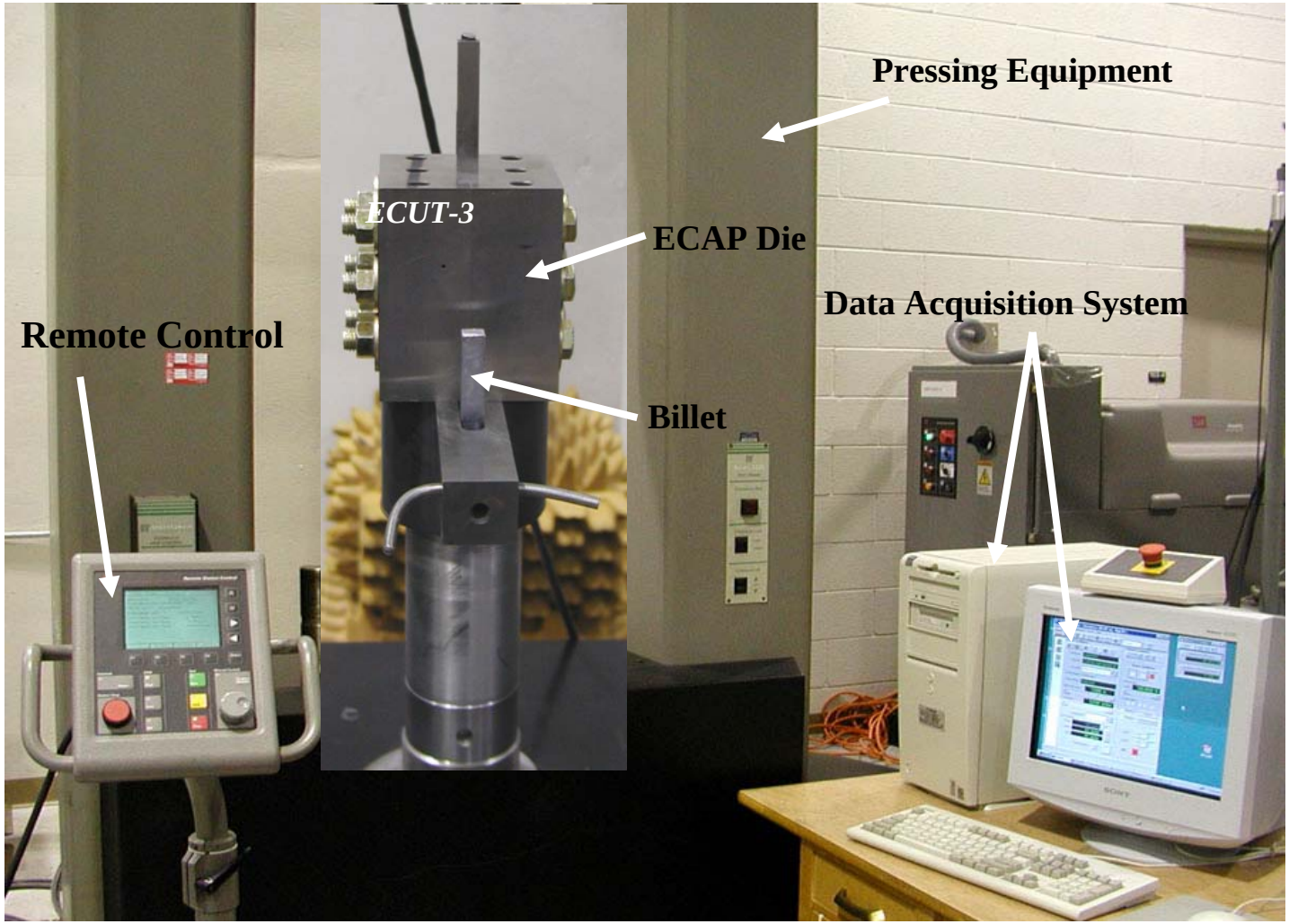

Figure 12 - The ECAP sharp-corner die mounted on the hydraulic pressing machine, Interlaken - 200 kip.

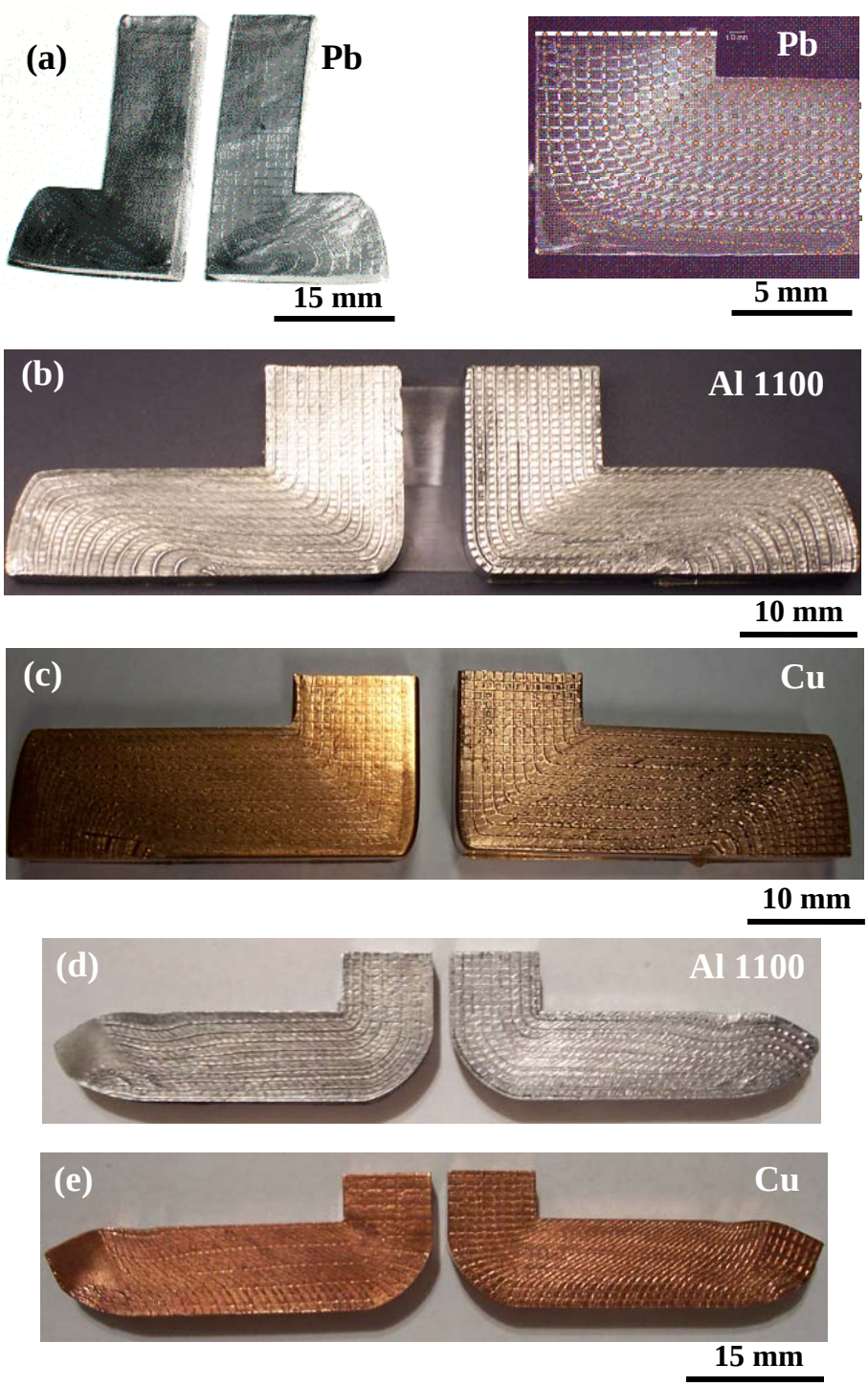

Figure 13 - Partially-deformed billets during ECAP: (a, b, and c) billets processed in a sharp-corner die, and (d and e) billets processed in a round-corner die. Prior ECAP, the billets were split in two parts, scribed with a network of 1 × 1 mm, and processed at room temperature, with a pressing speed of 0.5 mm/sec.

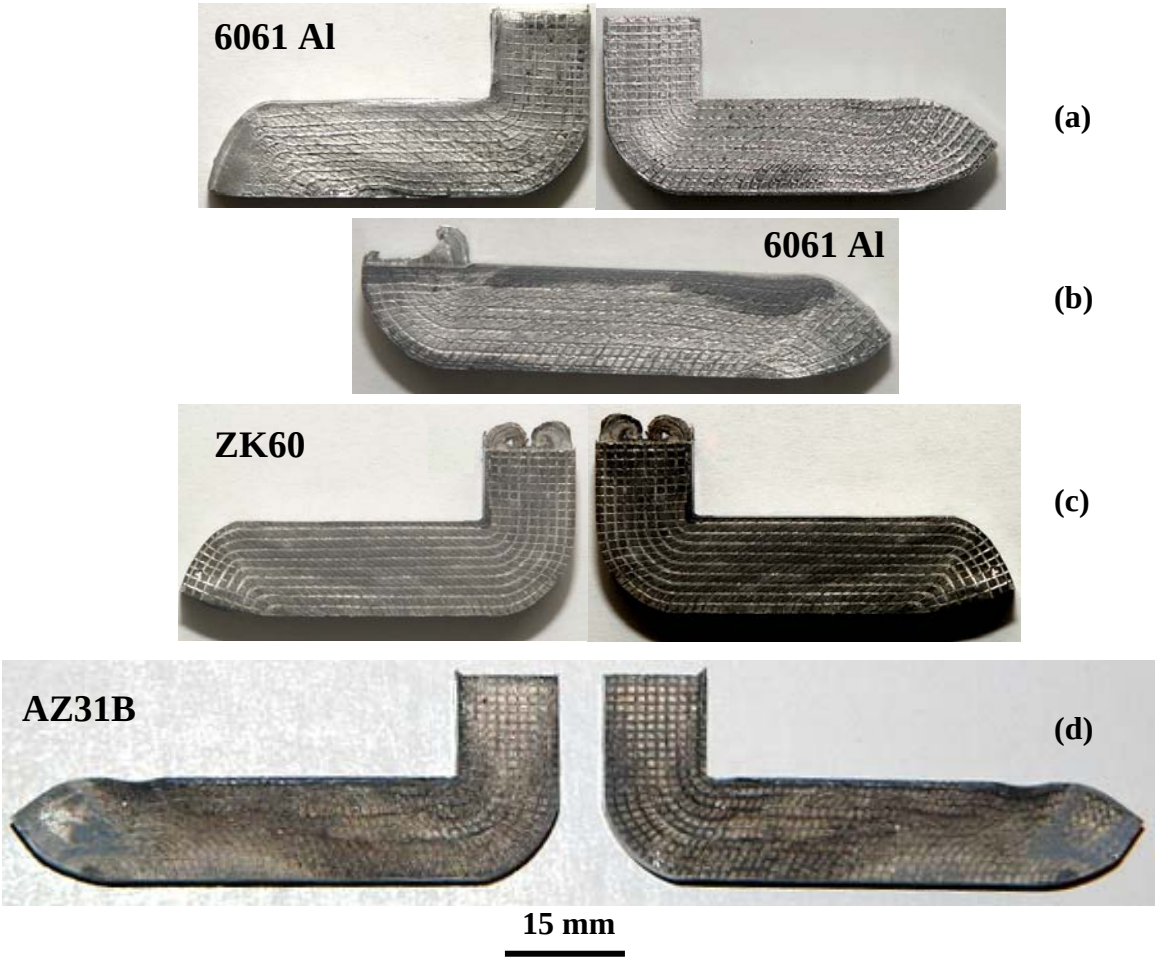

Figure 14 - Partially-deformed billets in a round-corner ECAP die at high temperature. The split billets of (a and b) the 6061 Al alloy, and Mg alloys, (c) ZK60 and (d) AZ31B, were scribed with a network of 1 × 1 mm, and were processed at temperature, T = 250^0C, with a pressing speed of 0.5 mm/sec.

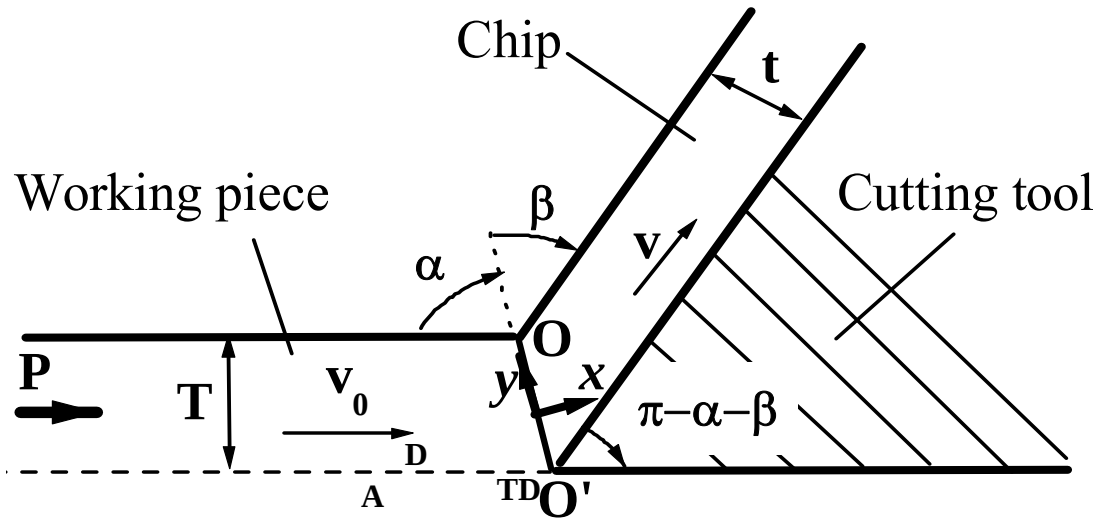

(a) Orthogonal cutting

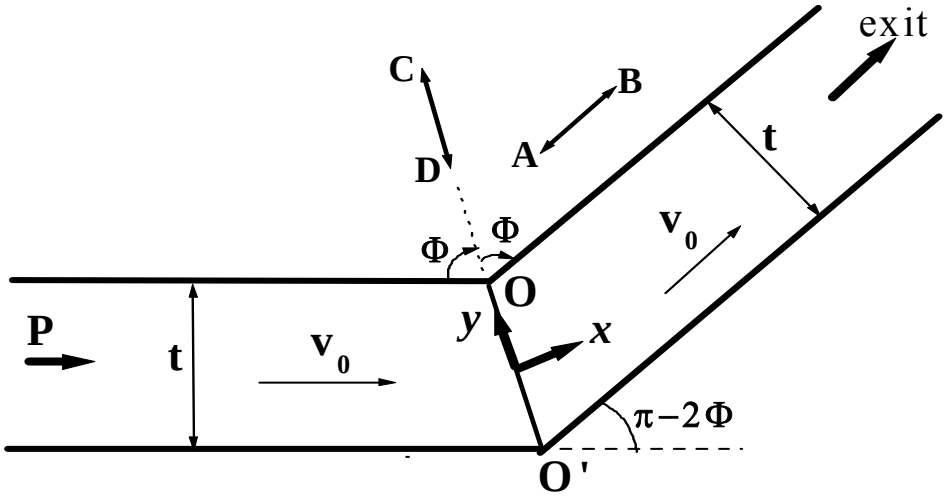

(b) ECAP with two channels at 2Φ = 120^0

Figure 15 - Geometrical parameters in the case of (a) the orthogonal-cutting deformation, and (b) the ECAP deformation; OO′ is the shear plane, T is the working piece thickness, t is the chip thickness, v_0 and v are the velocities before and after the deformation, respectively.

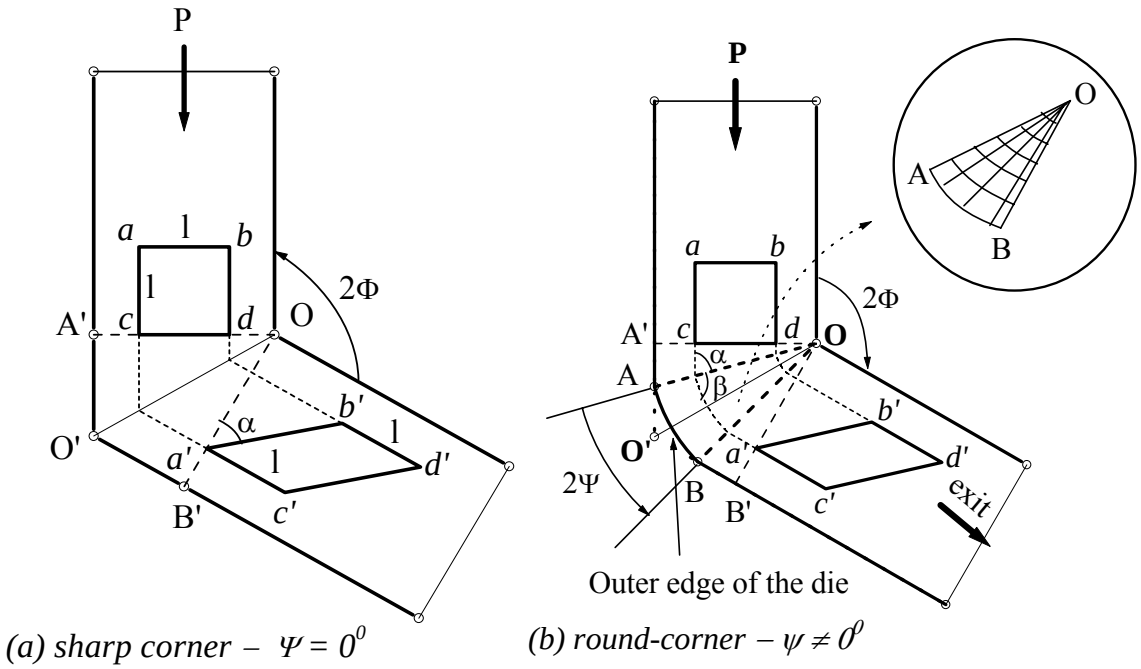

Figure 16 - The ECAP-die configurations with the two channels at the angle, $2\Phi = 120^0$, and with: (a) sharp corner, and (b) round corner. The unit element, abcd, is moving from the first into the second channel, and is transformed into a′b′c′d′ after the deformation. The PDZ extension is inside AOB, and encompasses the angular span, 2Ψ. Inside AOB (right insert), the two orthogonal slip-line families are represented, and AO and BO are the two rigid-plastic boundaries (reproduced from Ref. 78).

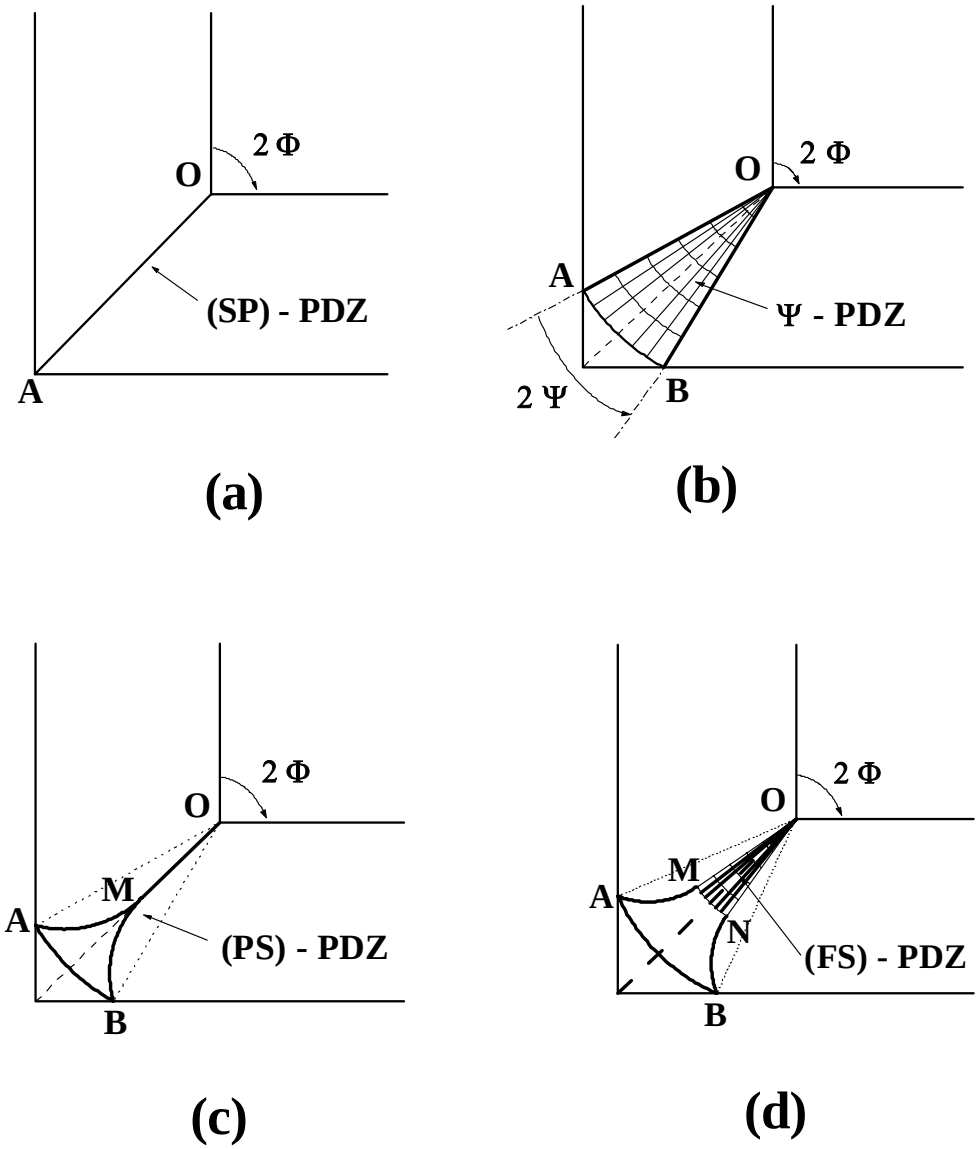

Figure 17 - Four ECAP models for the plastic-deformation zone (PDZ) shape and size: (a) single-shear plane, AO: SP-PDZ model; (b) shearing fan, AOB: Ψ-PDZ model; (c) shearing plane, MO, and splitting, MAB: partial-split, PS-PDZ model; and (d) shearing fan, MON, and splitting, AMNB: full-split, FS-PDZ model (reproduced from Ref. 65).

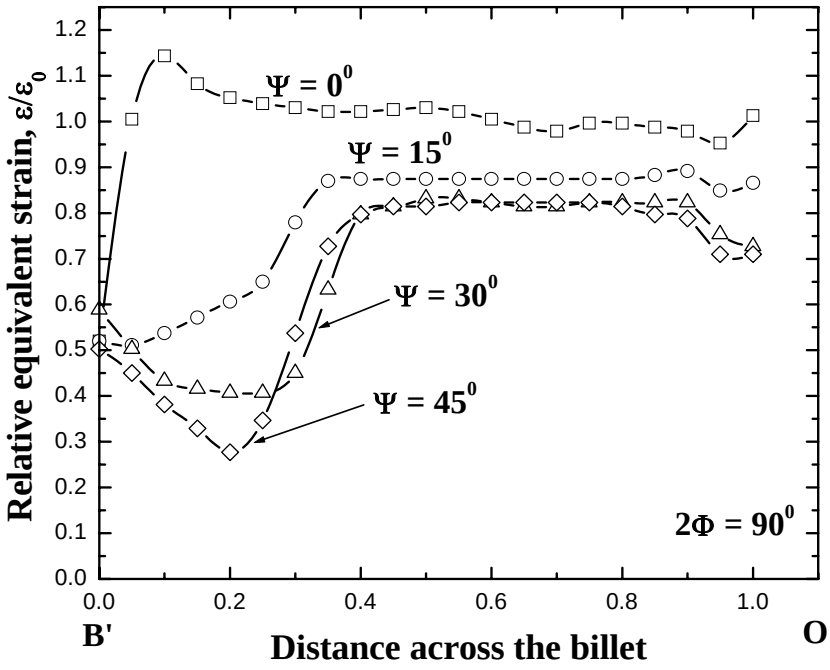

Figure 18 - The finite-element modeling (FEM) predicting the shear-strain nonuniformity across the billet (when moving from the top position, O, to the bottom position, B′) in ECAP. Different angular spans of a round-corner die, with the two channels at 90^0, are considered (reproduced from Ref. 93 and modified).

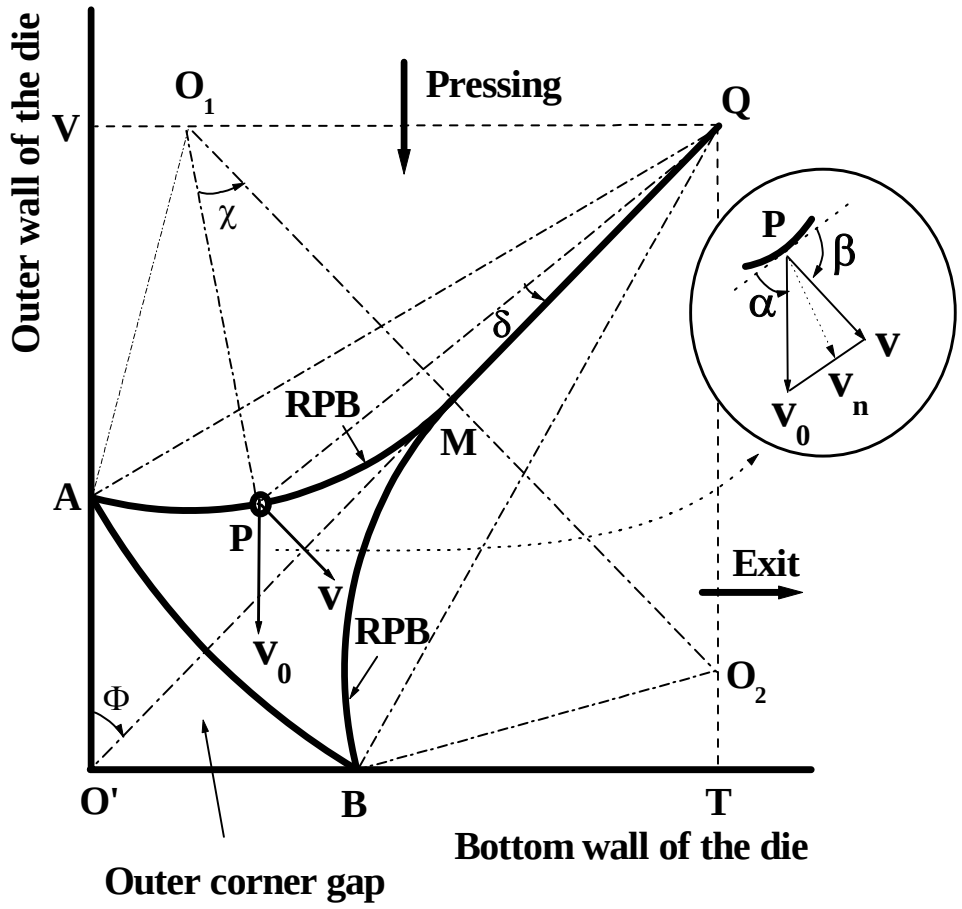

Figure 19 - Partial-split model, PS-PDZ [79], for the ECAP plastic deformation, in a 90^0 die, including the straight rigid-plastic boundary (RPB), QM, two curved RPBs, MA and MB, a free-surface, AB, and the variable angles, δ and χ, when moving the point, P, on curved RPBs. The right insertion shows the velocity components.

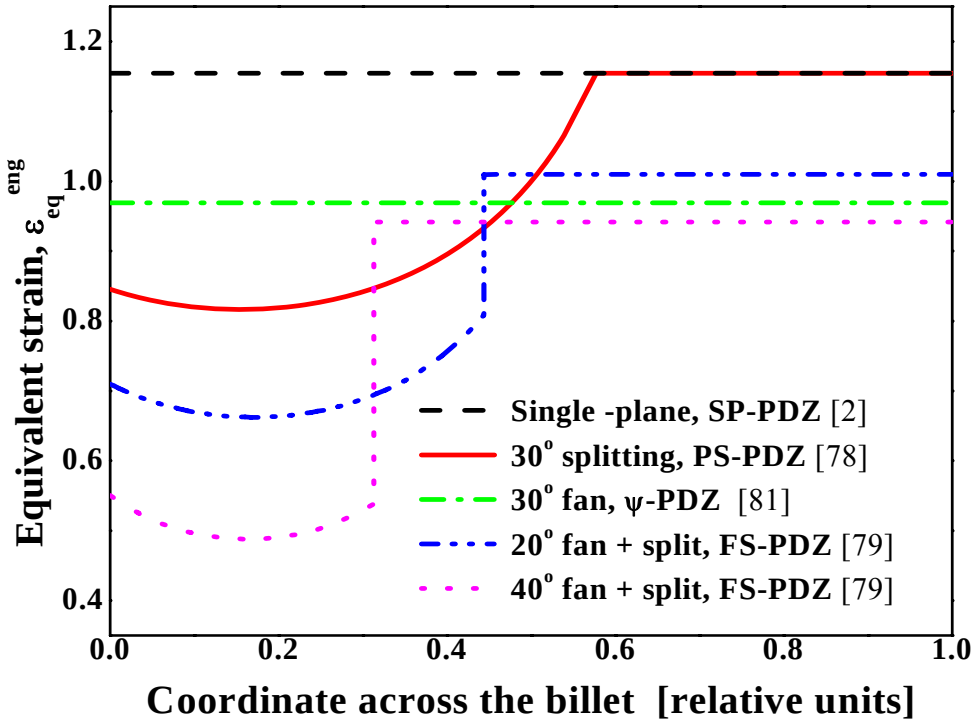

Figure 20 - Comparison of the calculated equivalent-strains as a function of the relative position across the billet (the top of the billet toward the bottom) for different PDZ models in ECAP (die with $2\Phi = 90^0$): the single-plane model (SP-PDZ), the shearing-fan model (ψ-PDZ), the partial-split model (PS-PDZ), and the full-split model (FS-PDZ), for two shearing fans of 20^0 and 40^0 (from Refs. 2, 78 , 79, and 81).

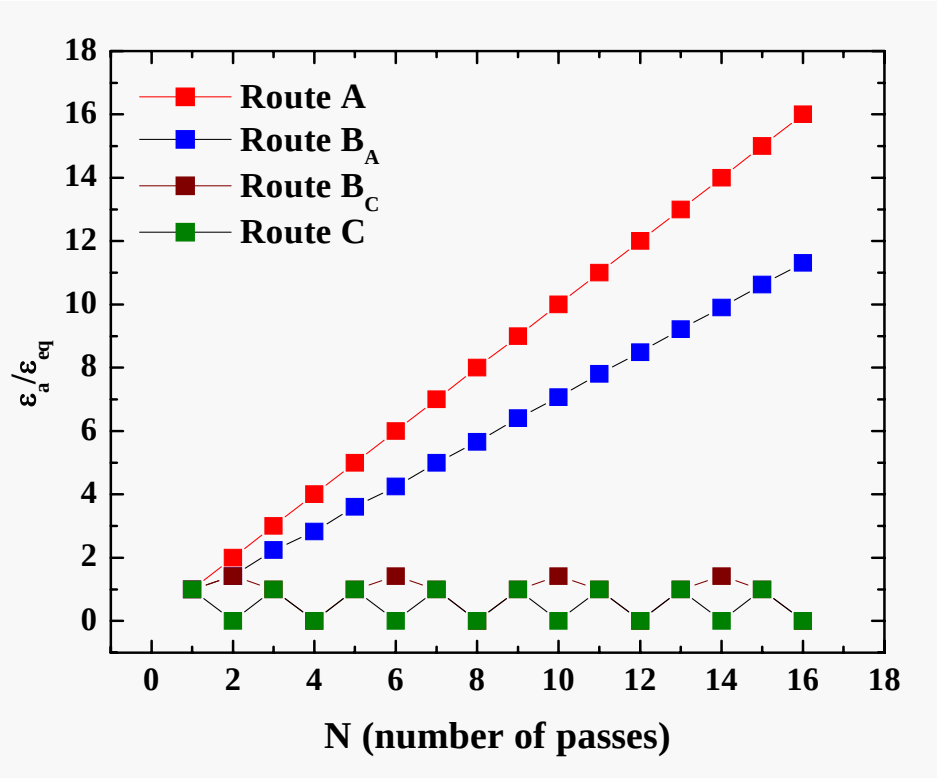

Figure 21 - The apparent equivalent strain, $\varepsilon_a = P_r \times \varepsilon_{eq}$, describing the degree of redundancy for each route in ECAP.

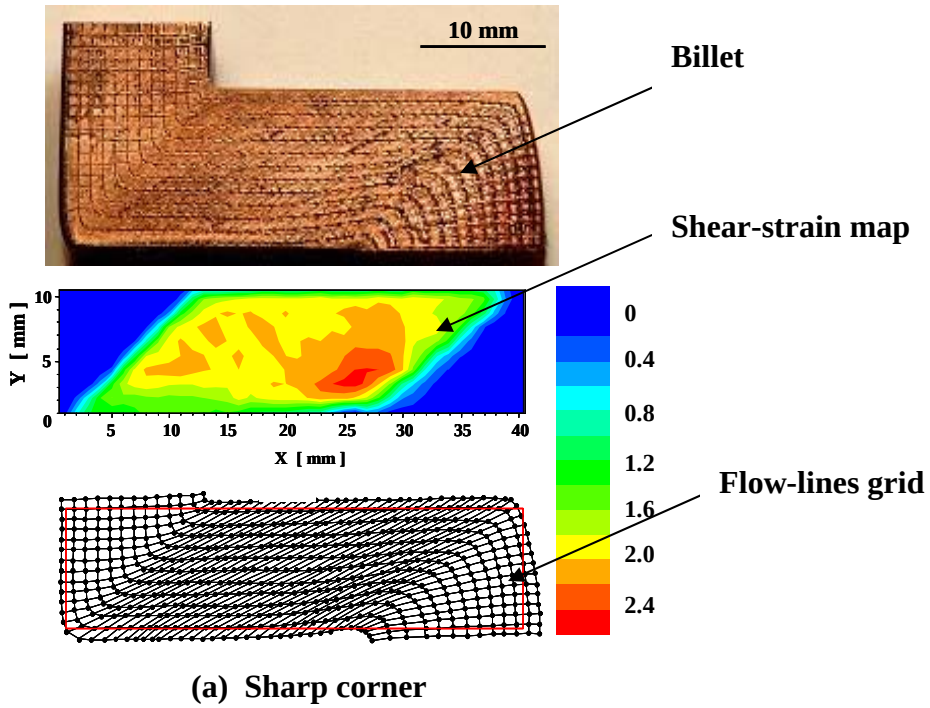

(a) Sharp corner

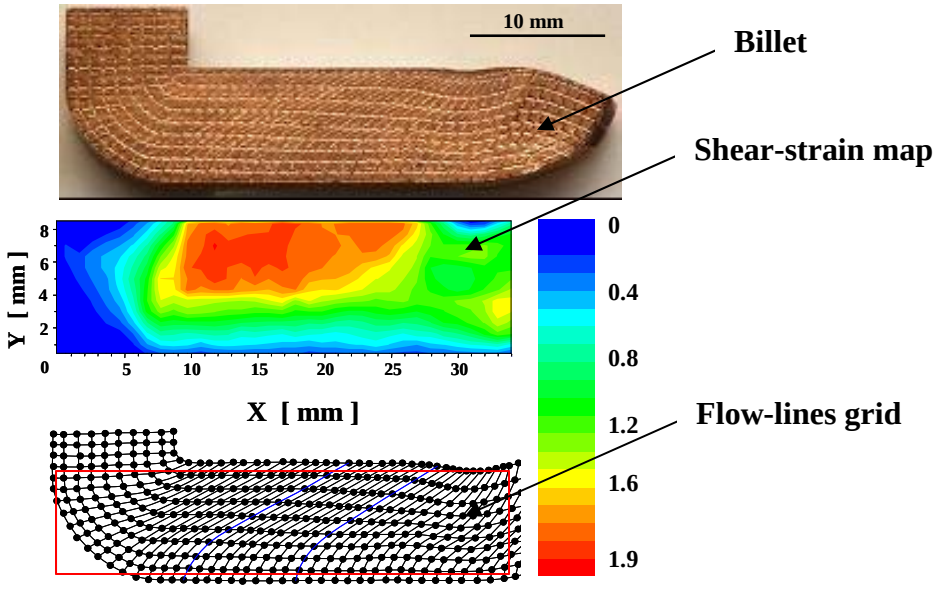

(b) Round corner

Figure 22 - The shear-strain mapping and the calculated flow-lines grids for the billet of pure Cu deformed in one pass of ECAP using (a) a sharp-corner die, and (b) a round-corner die. The ECAP-ed billets are shown above the maps.

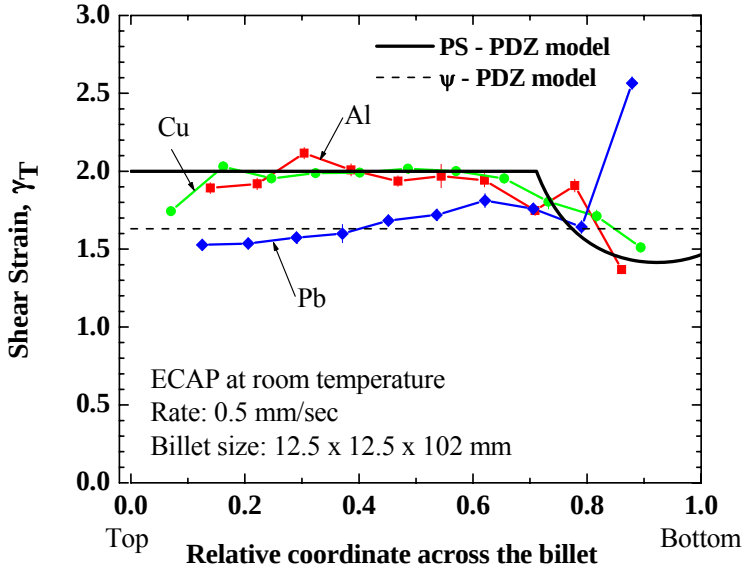

Figure 23 - The shear-strain distributions for the sharp-corner die: a comparison between the experiment and theory shows a good agreement for Al and Cu billets, but for the Pb billet there is a significant instability near the bottom of the billet.

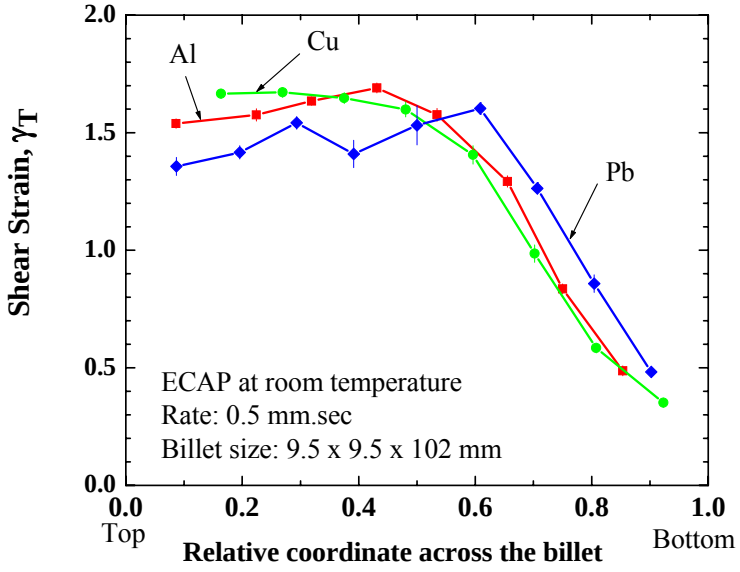

Figure 24 - The shear-strain distributions for the round-corner die**:** the apparent shear strain values, γ_T, as a function of the position across the billet for Al, Cu, and Pb billets shows a significant decrease towards the bottom of the die.

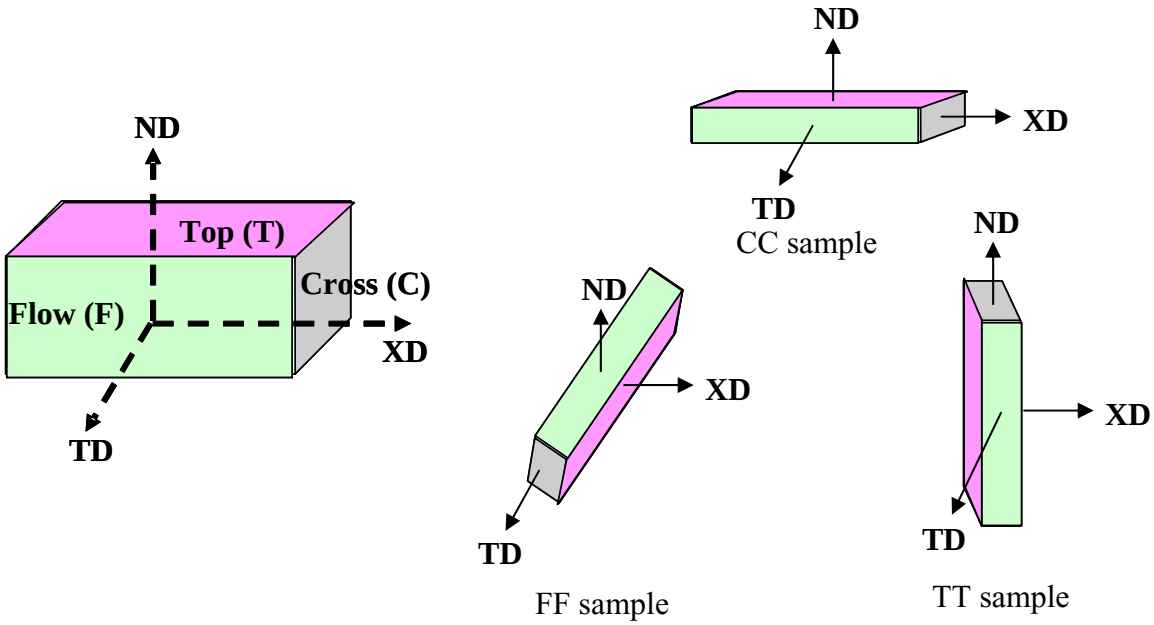

Figure 25 - Sample preparation for the microstructural characterizations. The three surfaces of observation are flow plane (F) with normal TD, top plane (T) with normal ND, and cross plane (C) with normal XD. The XD is the extrusion/rolling direction, and CC, TT, and FF are the designations of the three orientations for machining the samples.

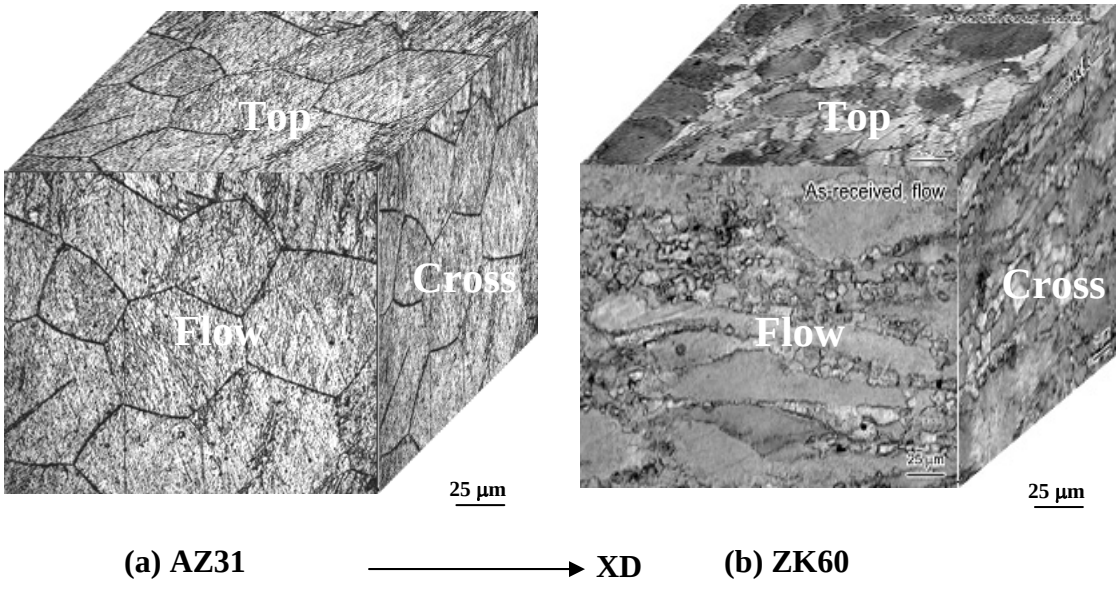

Figure 26 - Optical micrographs of the as-received alloys: (a) AZ31-H24 (hot-rolled), flow plane, and (b) ZK60-T5 (hot-extruded), flow, top, and cross planes.

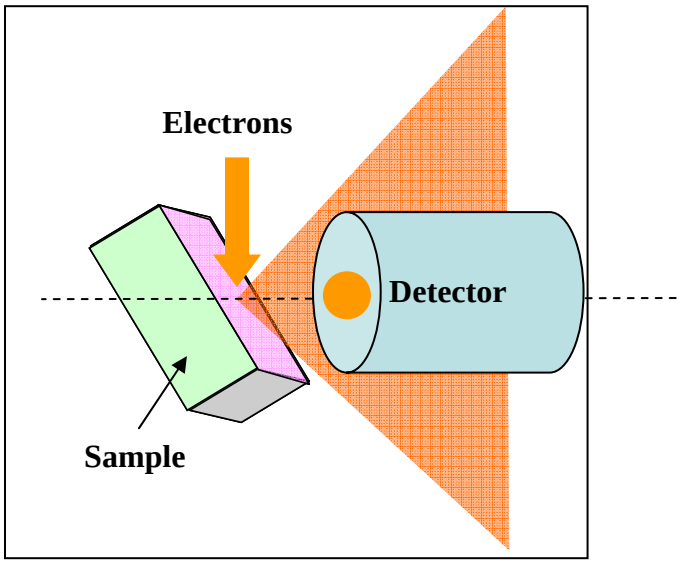

Figure 27 - Schematic of the electron-backscattered diffraction (EBSD) used in orientation-imaging microscopy (OIM).

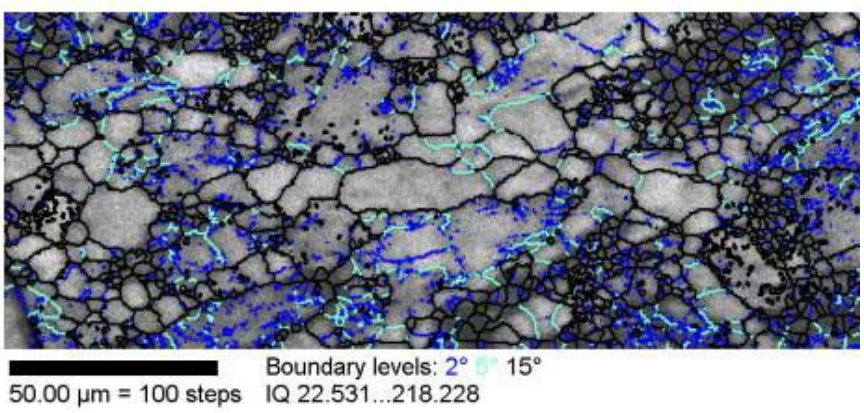

Figure 28 - The grain-boundaries distribution obtained from the orientation-imaging microscopy (OIM) measurements on the ZK60 samples in the as-received condition; the blue color shows the low-angle grain boundaries (LAGBs), and the black color, the high-angle grain boundaries (HAGBs).

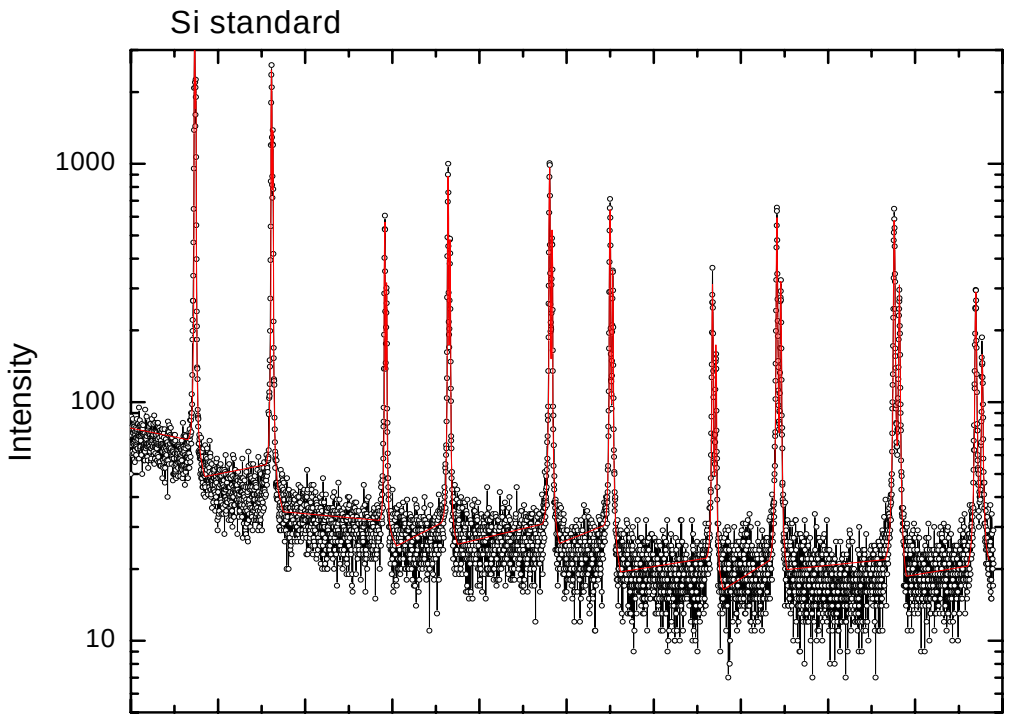

Figure 29 - The whole-pattern fitting of the θ - 2θ scan with low-energy (LE) XRD obtained for the instrumental profile using a Si standard; the theoretical prediction (the red line) is in a good agreement with the experimental data (the open dots).

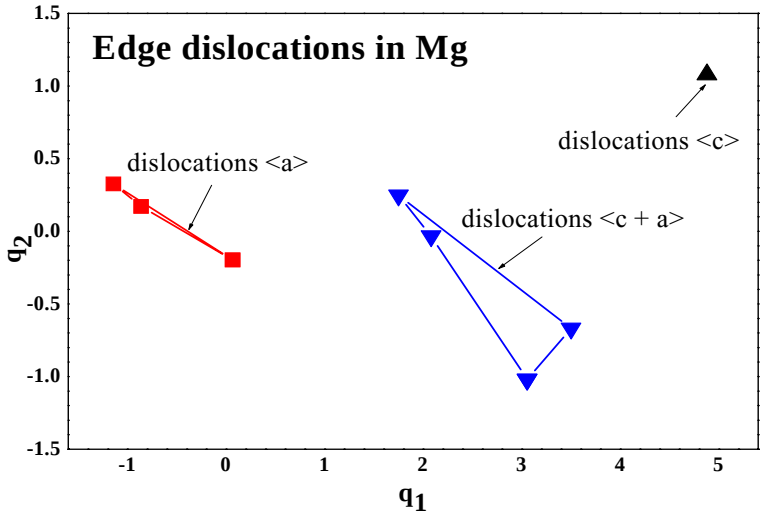

Figure 30 - The diffraction contrast parameters, q_1 and q_2, calculated for the edge dislocations in Mg using the data from the Ref. 118.

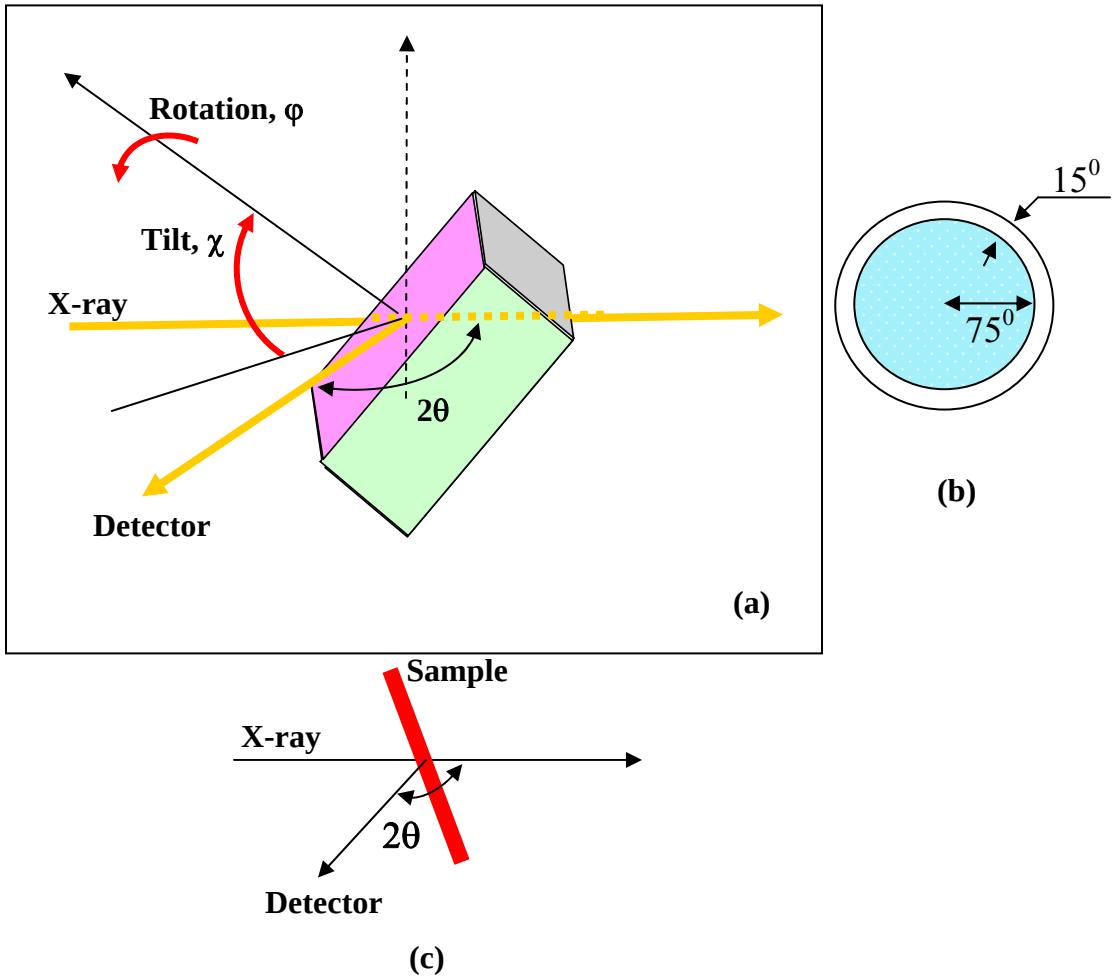

Figure 31 - In the low-energy (LE) XRD measurements for obtaining the pole figures, the sample is rotated with an angle, φ, and tilted with an angle, χ, varying from 0^0 to 75^0: (a) the 3-D arrangement; (b) the measured diffracted intensities, projected in one plane, cover 75^0, and the remaining 15^0 are calculated to obtain the full pole figure; (c) the horizontal section through the arrangement.

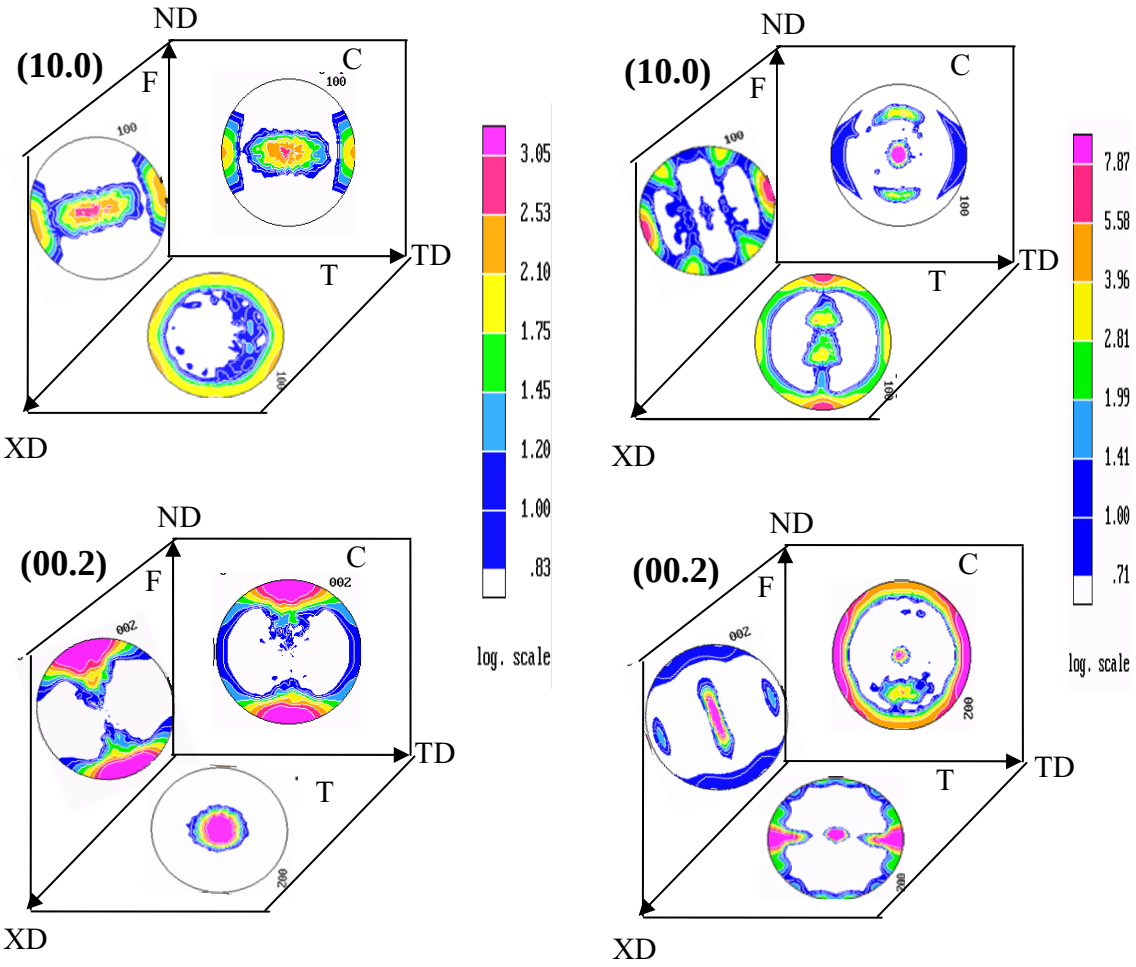

(a) Rolling (b) Extrusion

Figure 32 - The low-energy (LE) XRD pole-figures of the as-received samples: (a) AZ31-H24 (hot rolled), and (b) ZK60-T5 (hot extruded), for the three surfaces of observations, flow (F), top (T), and cross (C) planes, and for the reflection planes, (10.0) and (00.2).

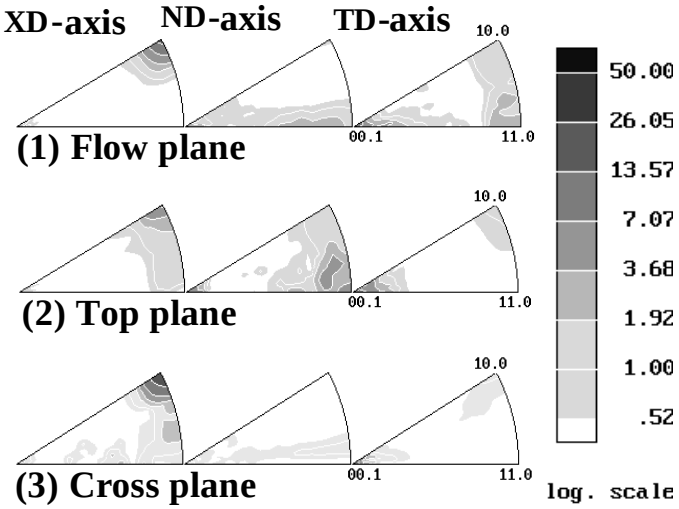

(a) ZK60, as-received

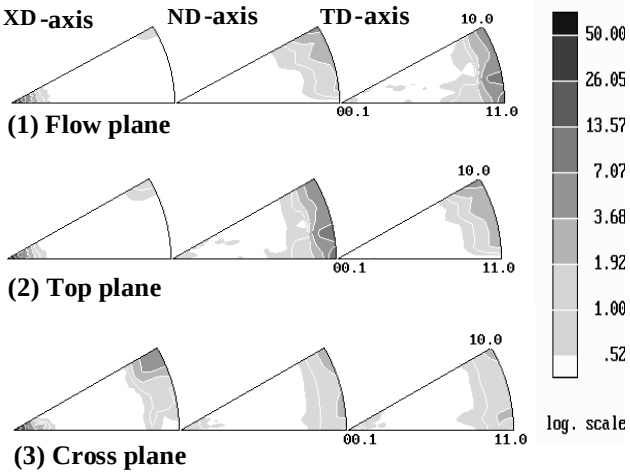

(b) ZK60, compression CC

Figure 33 - The inverse pole-figures (IPFs) calculated from the LE-XRD data obtained for the ZK 60-T5 (hot extrusion) sample observed on flow, top, and cross planes: (a) as-received, and (b) after compression CC (with the loading direction parallel to the extrusion direction). The XD, ND, and TD are the directions normal to the cross, top, and flow planes, respectively.

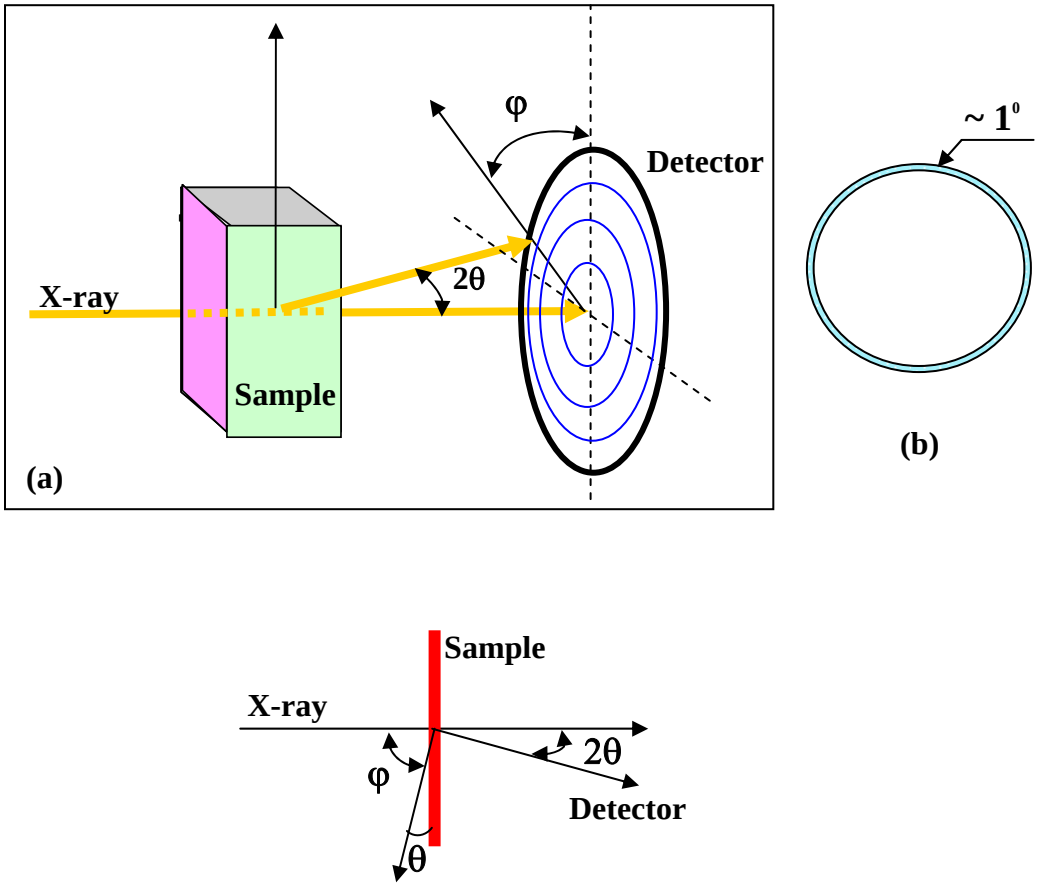

Figure 34 - (a) In the high-energy (HE) XRD (synchrotron radiation with the wavelength, $\lambda = 0.108004$ Å) measurements in transmission geometry, the scattered radiation is detected by an image-plate (detector) as a diffraction-ring pattern; the diffraction angle is 2θ, and the rotation angle, φ; (b) The in-plane pole distribution (IPPD) covers a section of ~ 1^0, with the orientations almost perpendicular to the beam direction (equivalent to a tilting angle, $\chi \sim 90^0$).

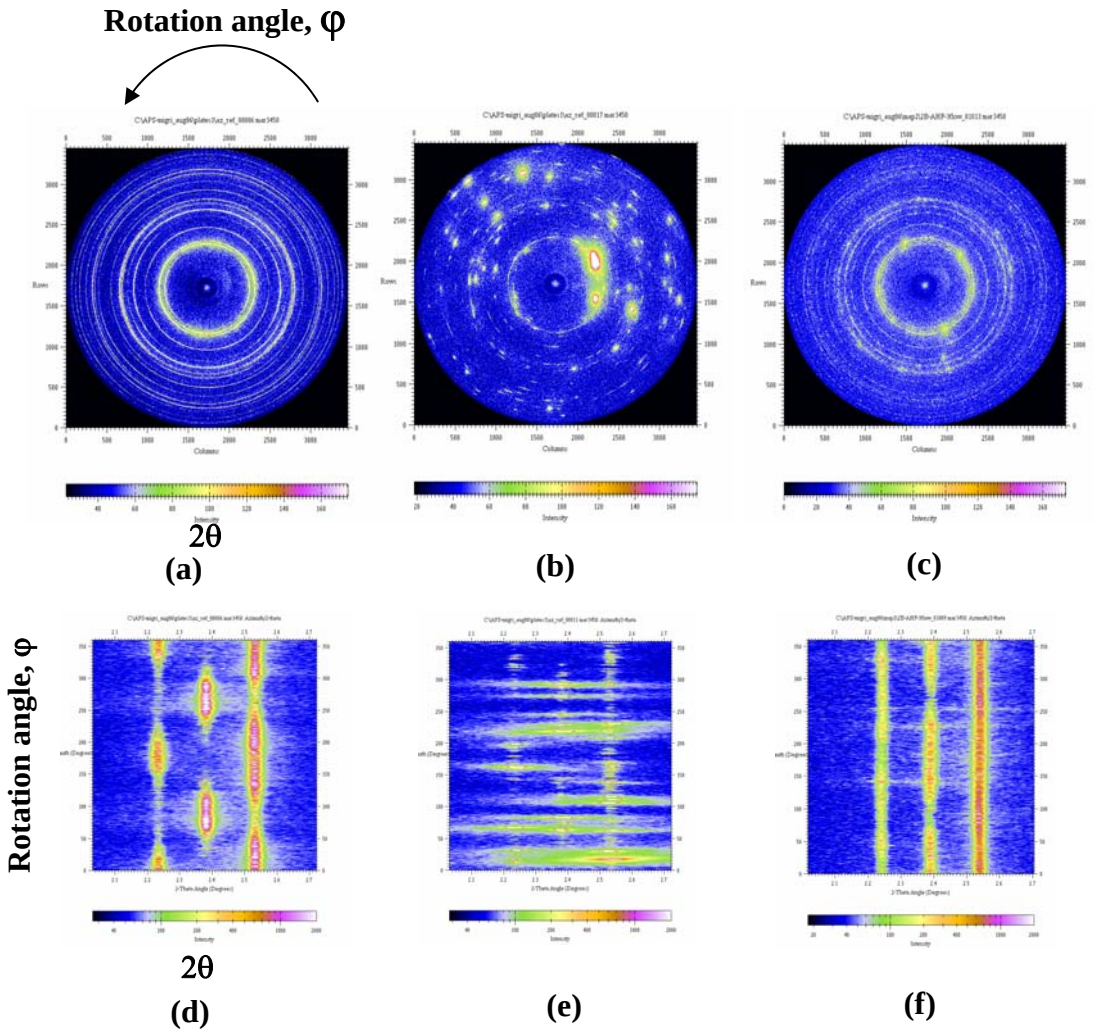

Figure 35 - The diffraction-rings pattern recorded in the high-energy (HE) XRD experiment for the Mg alloy, AZ31-H24 (rolled): (a) as-received, (b) annealed at 350^0C for 1h, and (c) ECAP at 250^0C, 2 passes, route B_C. On the lower row, d, e, and f, are shown the 2-D rectangular maps of the three unfolded diffraction rings (from a total of 22 rings shown in a, b, and c), corresponding to the reflection planes (10.0), (00.2), and (10.1).

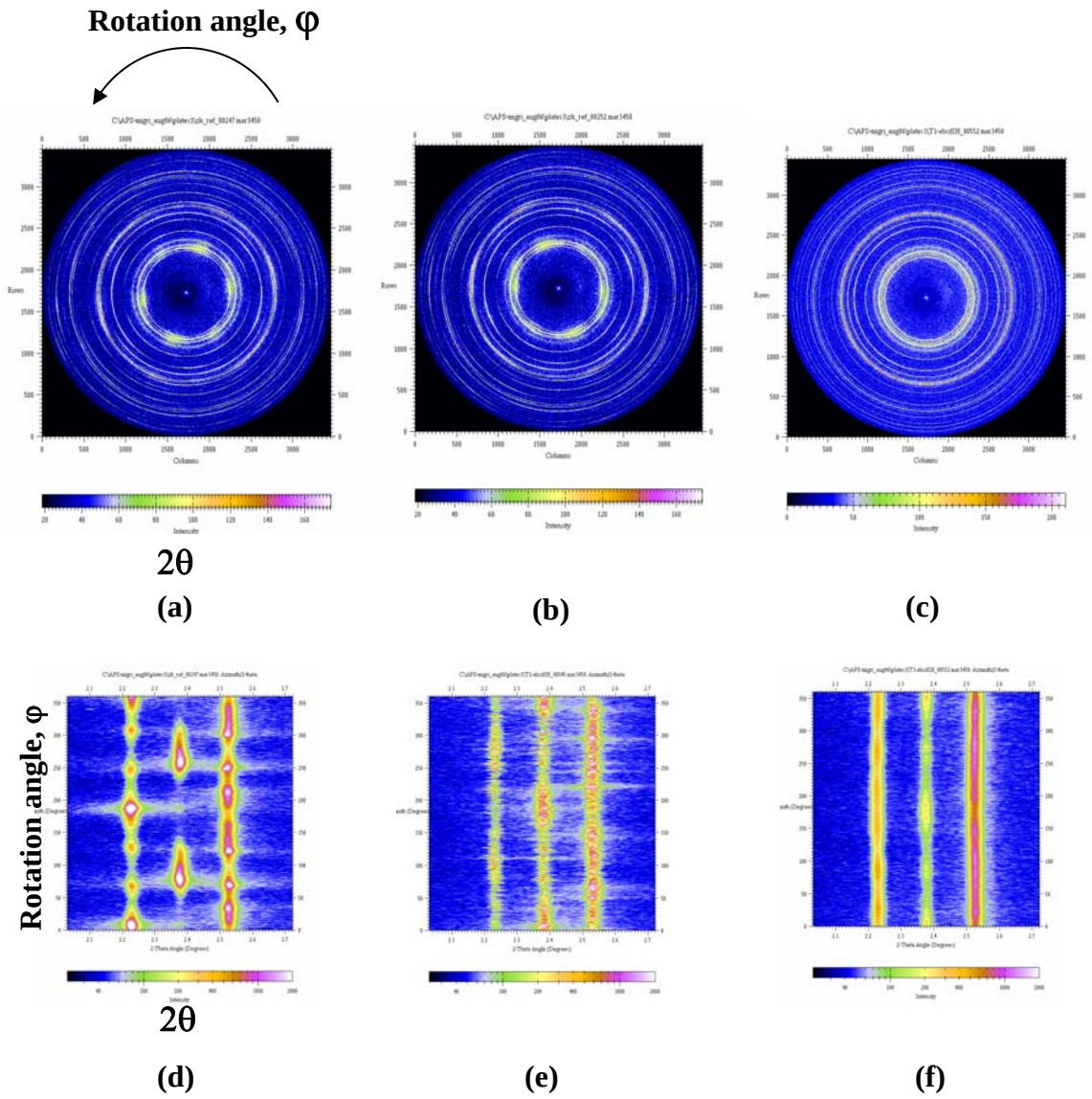

Figure 36 - The diffraction-rings pattern recorded in the high-energy (HE) XRD experiment for the Mg alloy, ZK60-T5 (hot extruded): (a) as-received, (b) annealed at 350^0C for 1h, and (c) ECAP-ed at 260^0C, 2 passes, route A. On the lower row, d, e, and f, are shown the 2-D rectangular maps of the three unfolded diffraction rings (from a total of 22 rings shown in a, b, and c), corresponding to the reflection planes (10.0), (00.2), and (10.1).

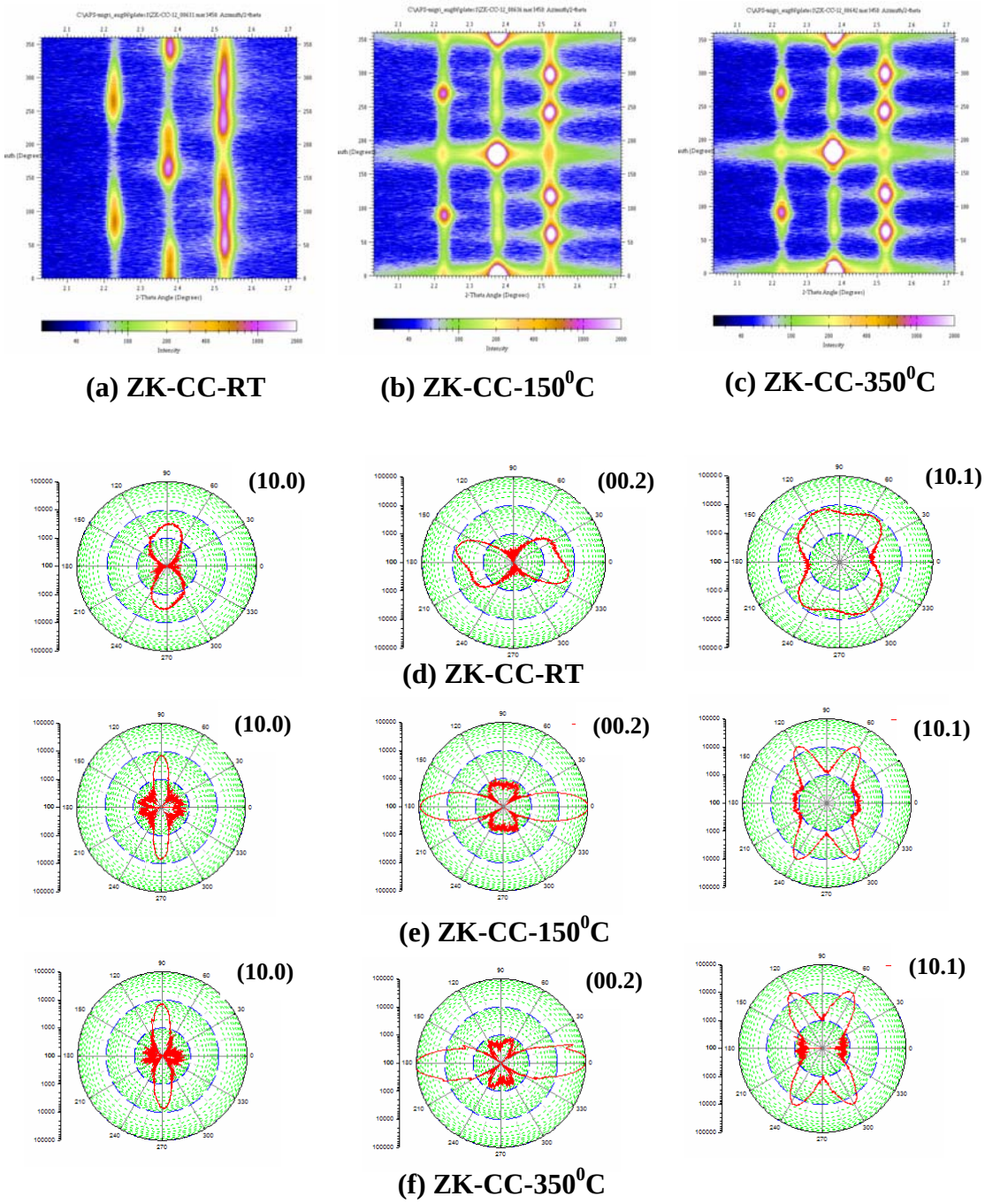

Figure 37 - The diffraction-ring patterns for three peaks recorded in the HE-XRD experiment for the ZK60 samples compressed along the extrusion direction (ZK-CC) at (a) room temperature (RT), (b) 150^{0}C, and (c) 350^{0}C. The corresponding representation of the in-plane pole distributions (IPPDs) is shown for the reflection planes (10.0), (00.2), and (10.1), for (d) RT, (e) 150^{0}C, and (f) 350^{0}C.

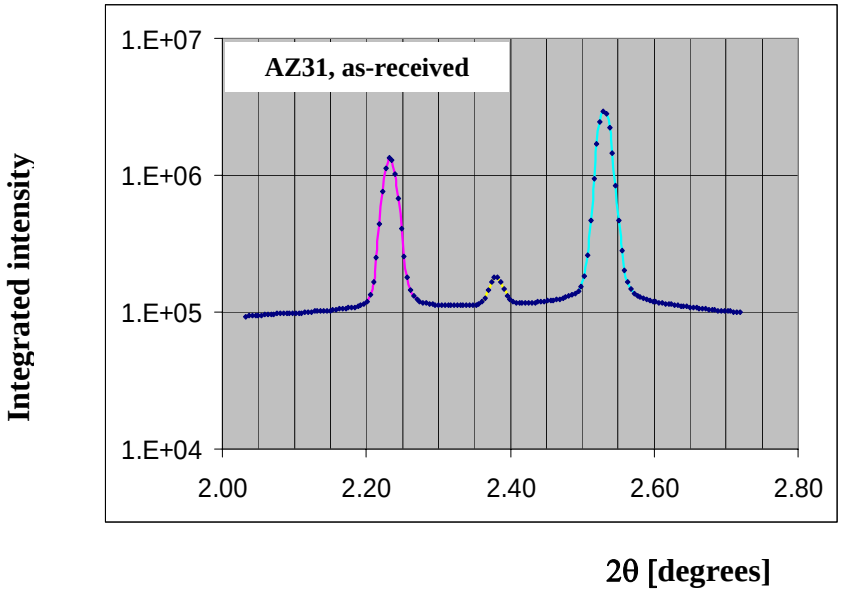

(a) as-received, top

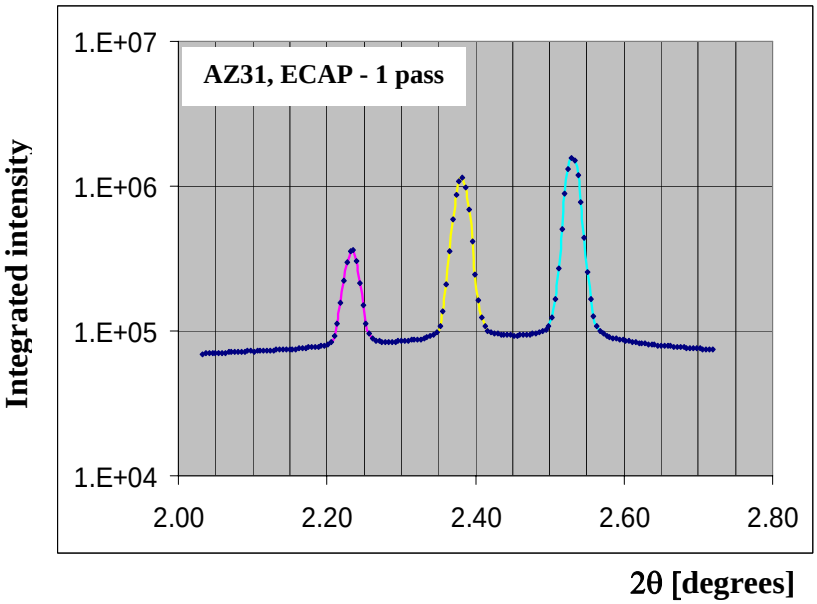

(b) ECAP, 1 pass, top

Figure 38 - The high-energy (HE) XRD intensities, integrated over the rotation angle, φ, and represented versus 2θ for the reflections (10.0), (00.2), and (10.1) obtained for the Mg alloy, AZ31, observed on the top surface: (a) as-received (hot-rolled), and (b) after ECAP, 1 pass.

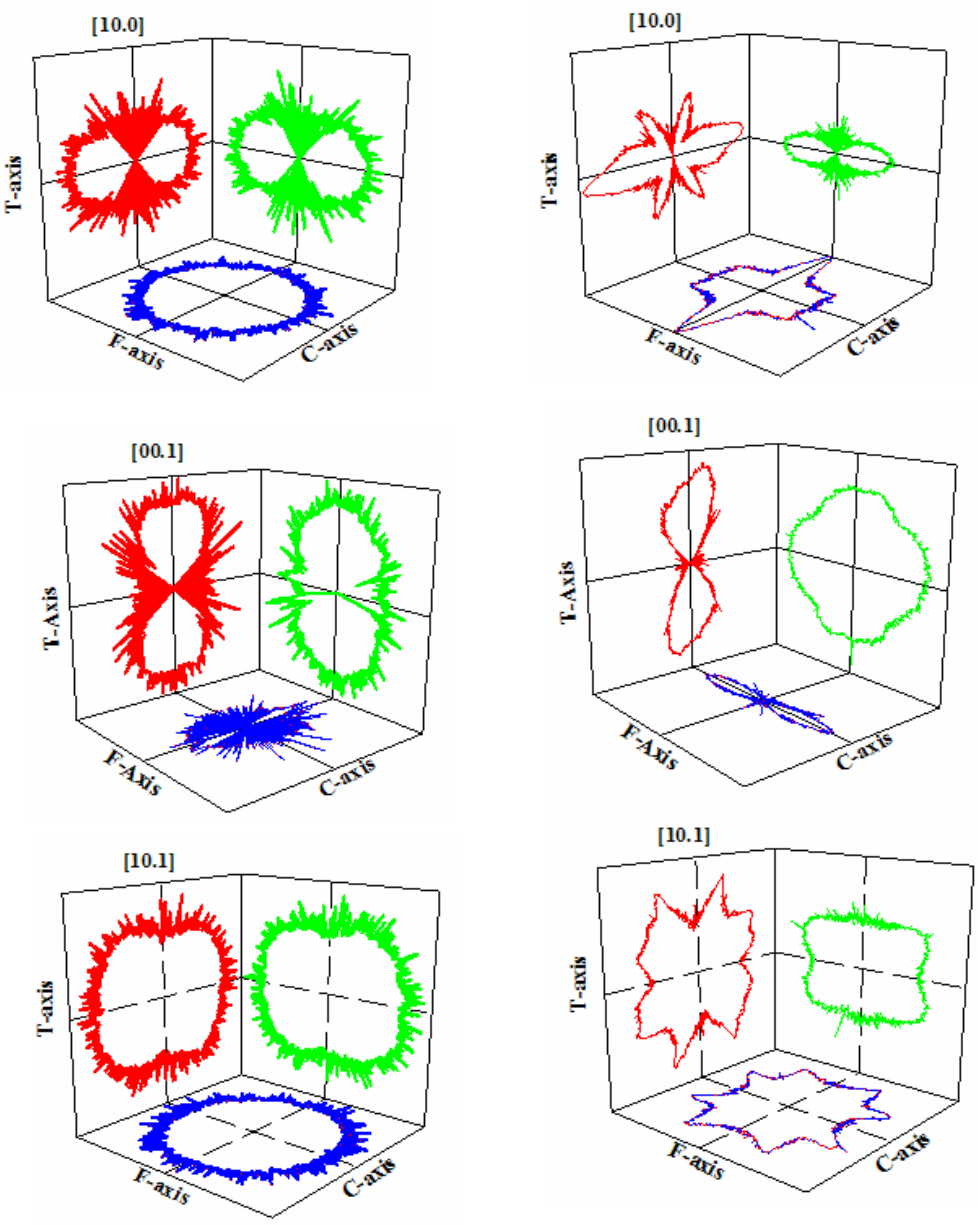

(a) AZ31, as-received **(b) ZK60, as-received**

Figure 39 - The 3D representation (for three planes of observations) of the in-plane pole distributions (IPPDs) in polar plots of the two Mg alloys characterized using the high-energy (HE) XRD technique: (a) AZ31-H24 (hot rolled), as-received, and (b) ZK60-T5 (hot extruded), as-received.

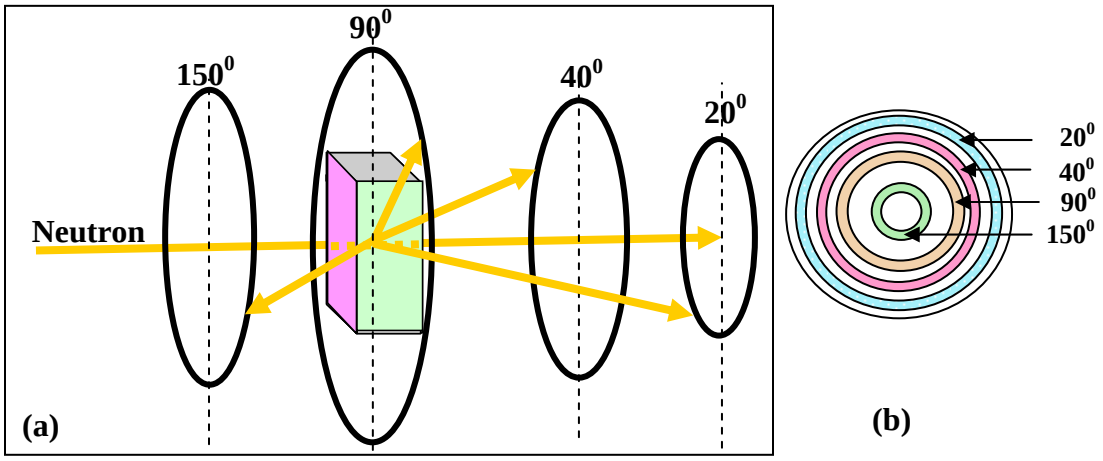

Figure 40 - In neutron diffraction measurements (HIPPO, Los Alamos), the detectors are placed at 20^0, 40^0, 90^0, and 150^0 to record the intensities; (b) The coverage of the projected in one plane intensities are discs, corresponding to the four detector positions.

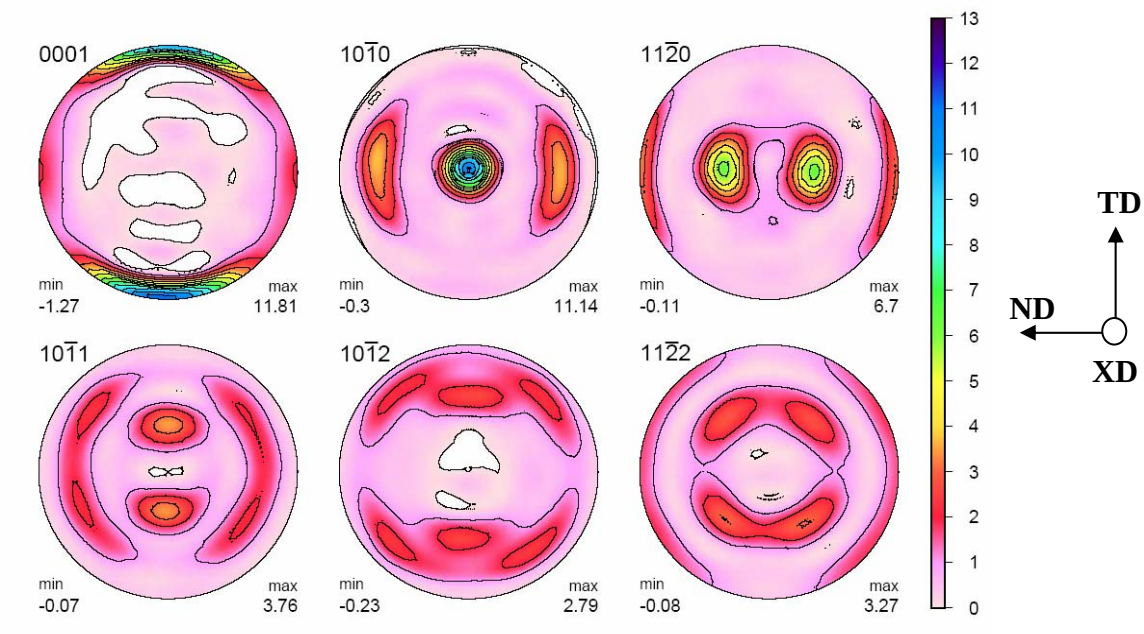

Figure 41 - The PFs for six reflection planes obtained from the neutron diffraction on the ZK60 sample in the as-received condition (hot extruded).

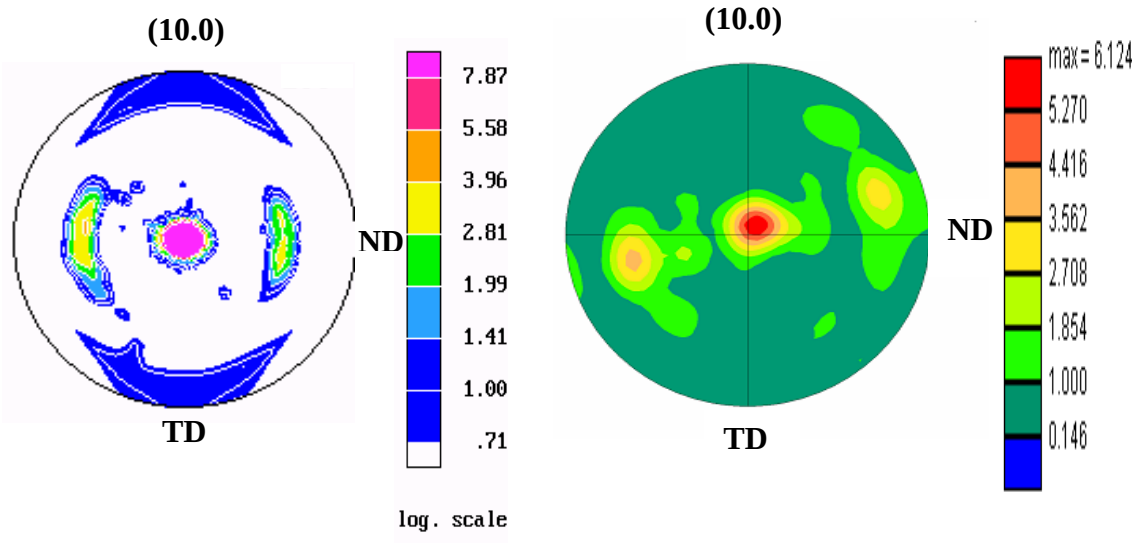

(a) LE-XRD **(b) OIM**

Figure 42 - Comparison of the prismatic PFs obtained on an as-received ZK60 sample, cross plane: (a) from the low-energy (LE) XRD, and (b) from the orientation-imaging microscopy (OIM) measurements.

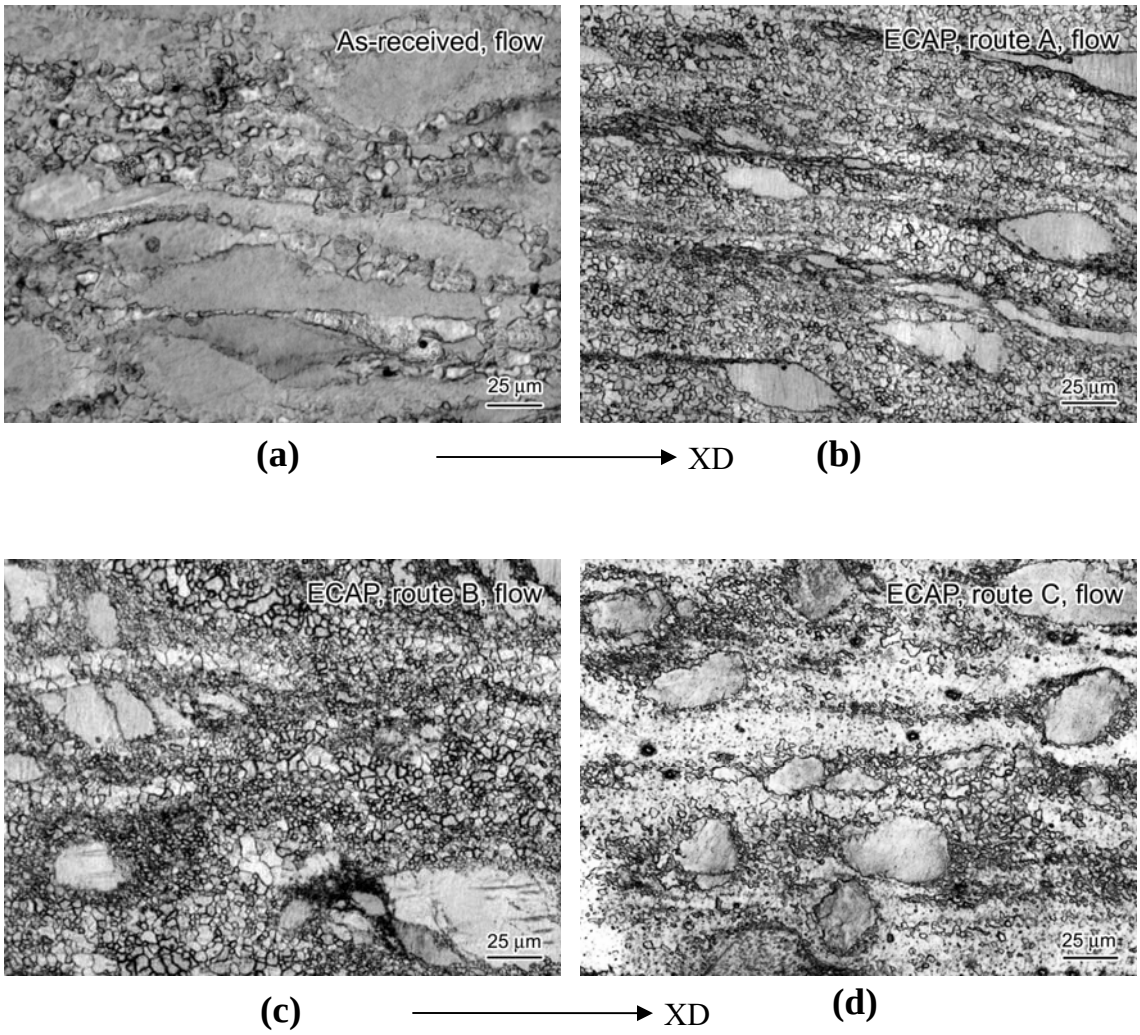

Figure 43 - The grain-size refinement (flow plane) for the ZK60 alloy before and after the ECAP deformation: (a) as-received, (b) ECAP, 4 passes, route A (4A), (c) ECAP - 4B, and (d) ECAP - 4C.

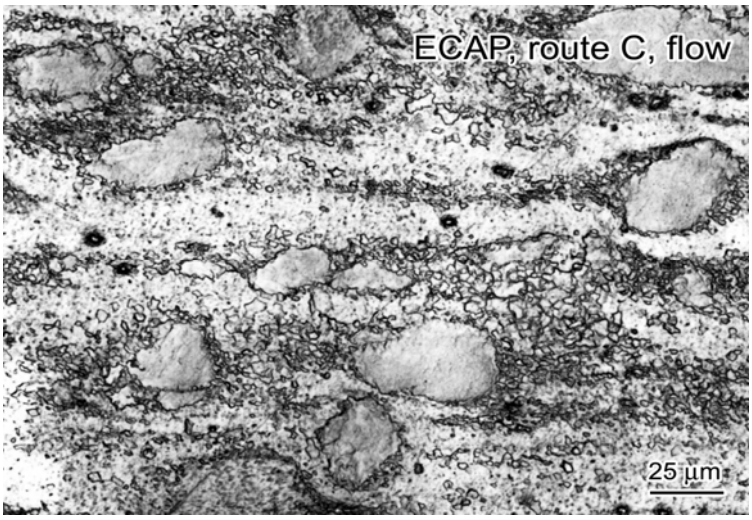

(a) ZK60, ECAP-4C

XD

(b) ZK60, ECAP-8C

Figure 44 - Optical micrographs of the ZK60-T5 alloy after the ECAP deformation for (a) 4 passes, route C, and (b) ECAP, 8 passes, route C; XD - pressing direction.

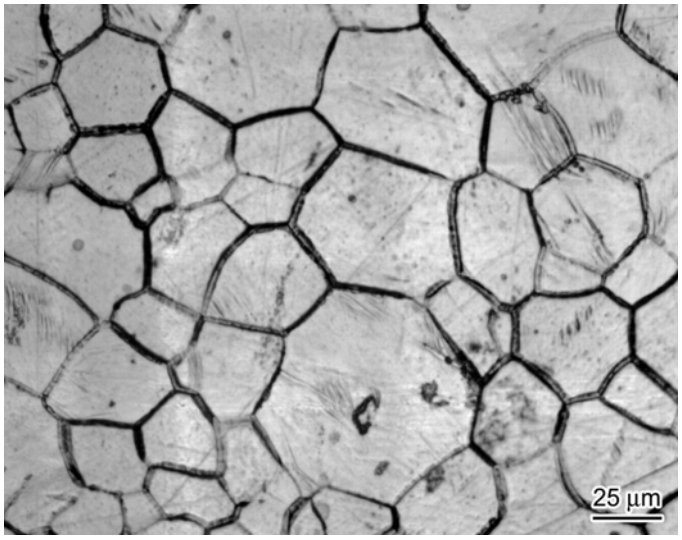

(a) AZ31, ECAP, 1 pass at 300^{0}C

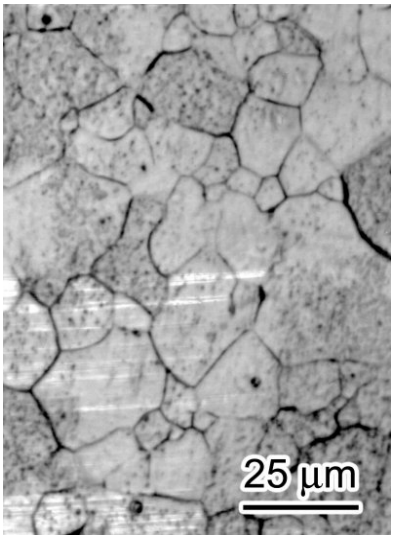

(b) AZ31, ECAP-8A at 300^{0}C

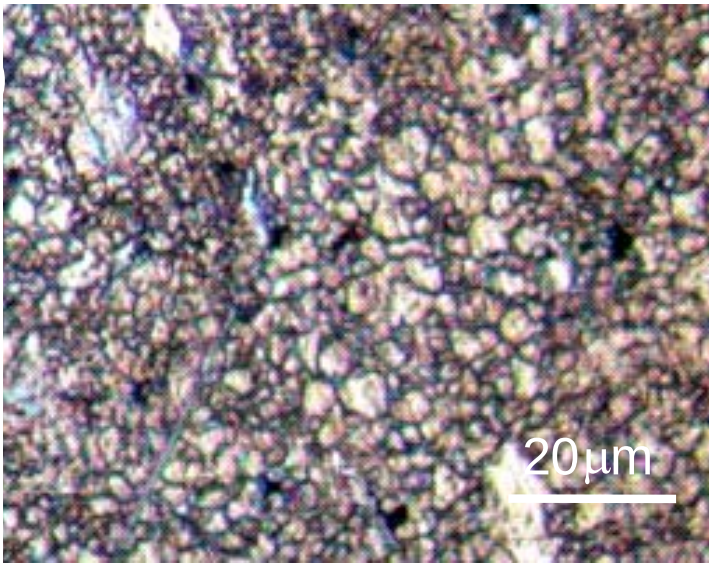

(c) AZ31, ECAP-2A at 200^{0}C

Figure 45 - The effect of the ECAP temperature on grain refinement in the Mg alloy, AZ31B, after ECAP: (a) at 300^{0}C, 1 pass, (b) at 300^{0}C, 8 passes, route A, and (c) at 200^{0}C, 2 passes, route B_C.

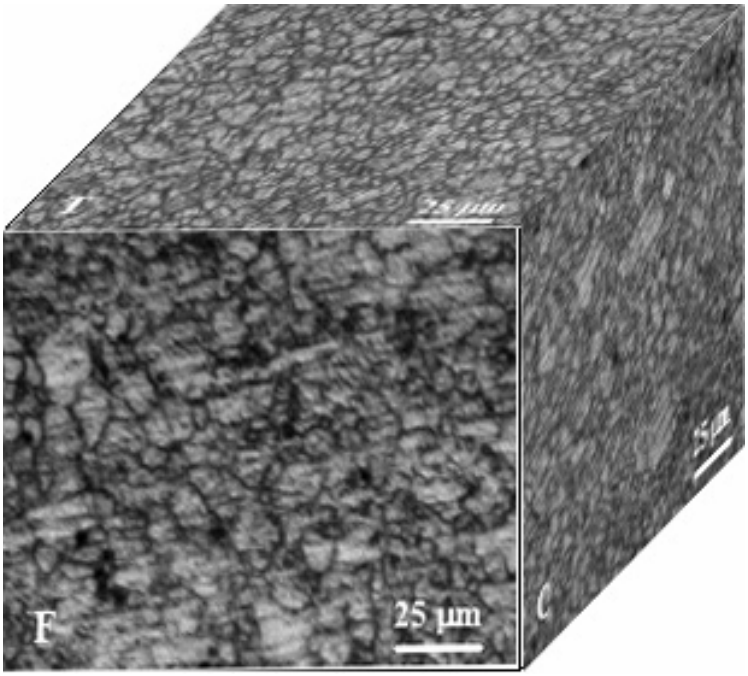

Figure 46 - The ECAP deformation homogeneity observed on the micrographs on flow (F), top (T), and cross (C) planes of the AZ31B, after ECAP at 200^{0}C, 2 passes, route B_C.

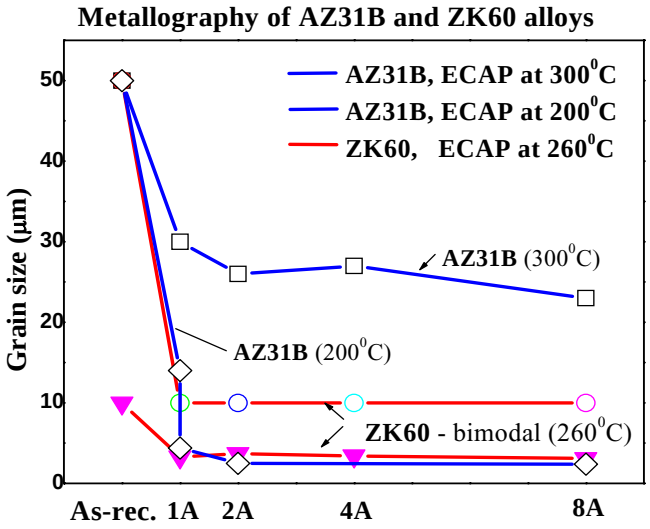

Figure 47 - Grain refinement after the ECAP deformation of Mg alloys, AZ31 and ZK60. The AZ31 alloy was ECAP-deformed at two different temperatures.

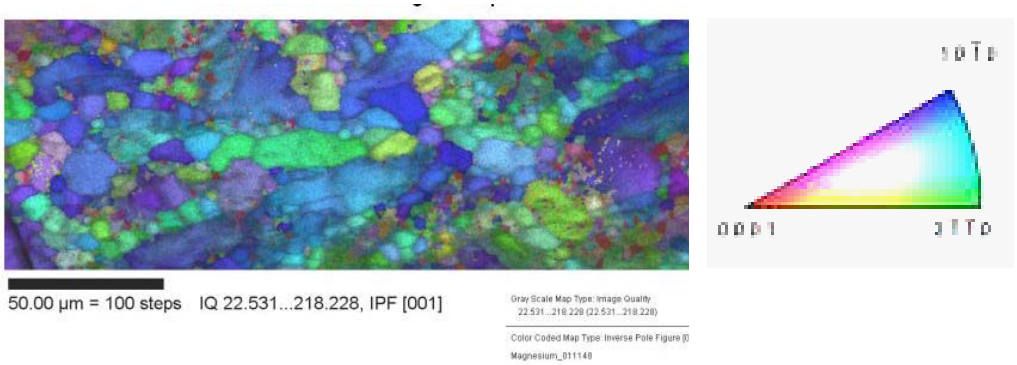

(a) ZK60, as-received, C plane

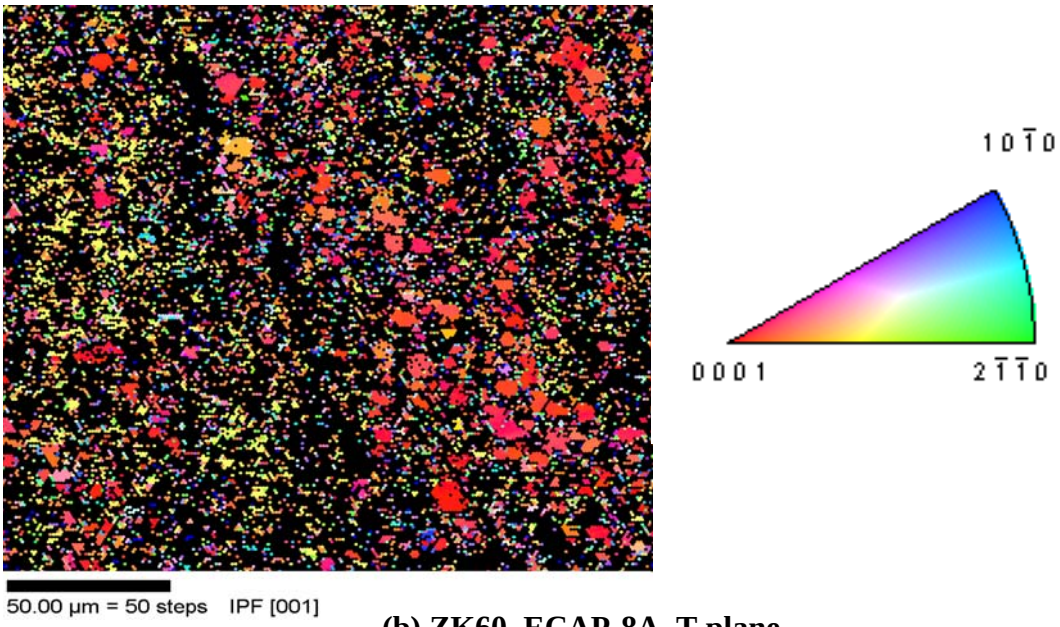

(b) ZK60, ECAP-8A, T plane

Figure 48 - The grain size and the grain-boundary distributions obtained from the OIM measurements for the ZK60-T5 alloy: (a) as-received, and (b) ECAP, 8 passes, route A. At the right, the basic stereographic triangles show the color code representing the lattice orientation of the observation planes, before (C plane) and after ECAP (T plane), respectively.

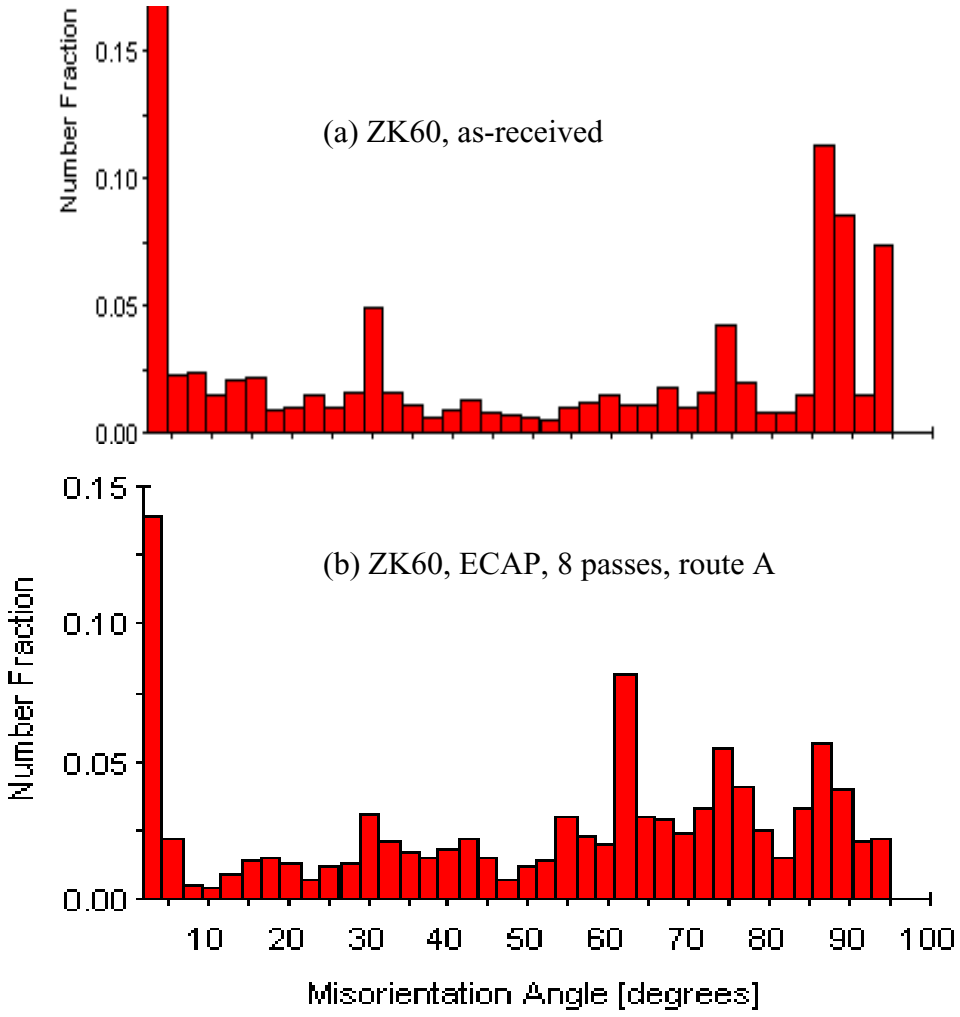

Figure 49 - The grain-boundary-misorientation distributions obtained from the OIM data for the ZK60-T5: (a) as–received and (b) ECAP, 8 passes, route A.

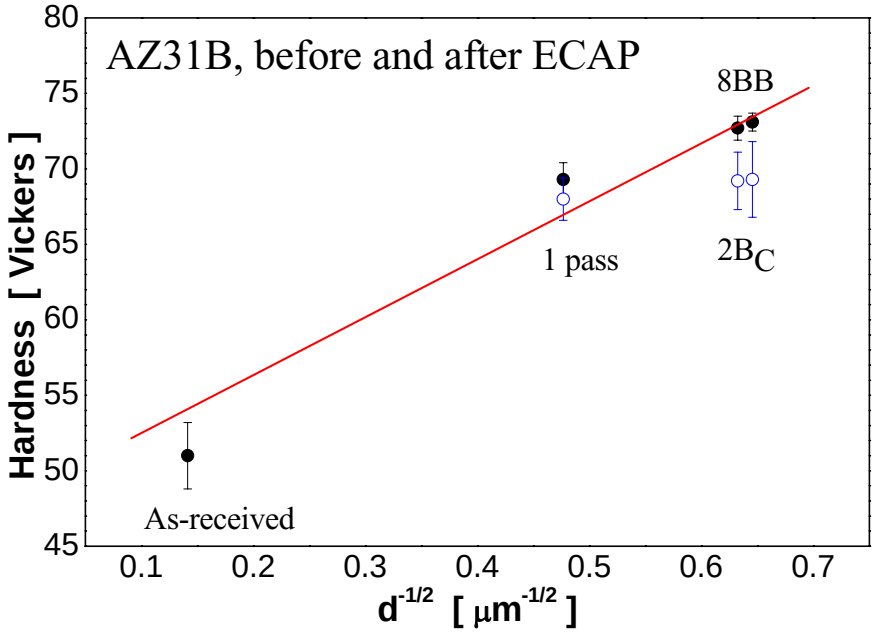

Figure 50 - Experimental results of the hardness versus the grain size for the AZ31B alloy in the as-received condition and ECAP-deformed in 1, 2, and 8 passes with backpressure (8BB); the comparison with the Hall-Petch relationship (red line) shows the grain-refinement efficiency during ECAP. The two sets of data (in black and blue) represent the values measured on the cross and top planes, respectively.

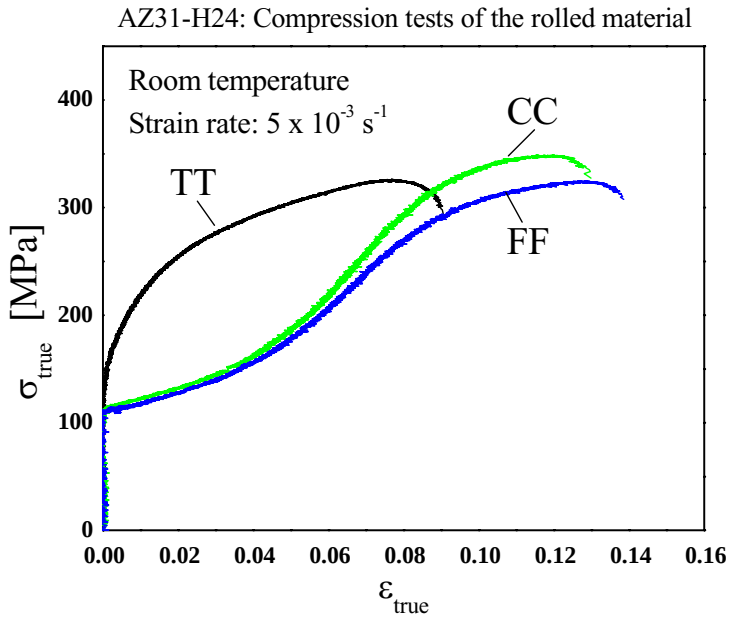

(a) Uniaxial compression of the AZ31B alloy

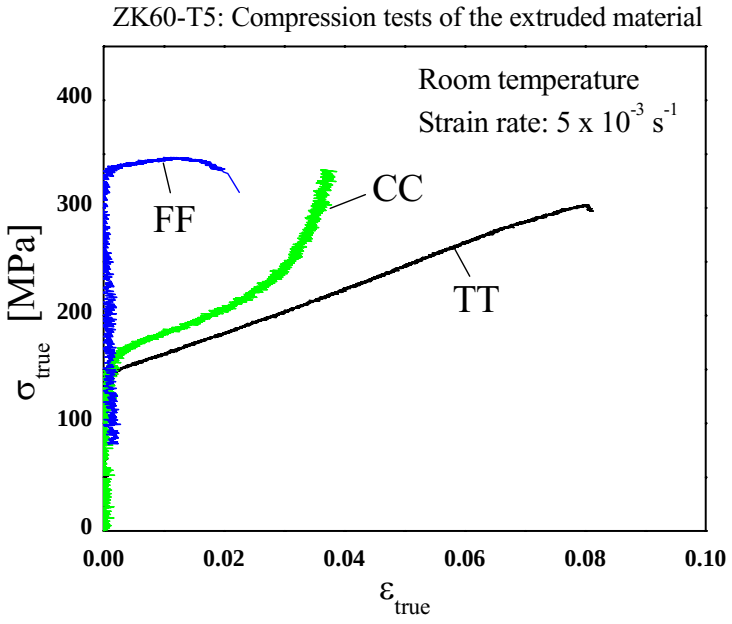

(b) Uniaxial compression of the ZK60 alloy

Figure 51 - The orientation dependence of the stress-strain curves for the (a) AZ31B samples, and (b) ZK60 samples tested in compression at room temperature for three orthogonal loading directions: FF, TT, and CC.

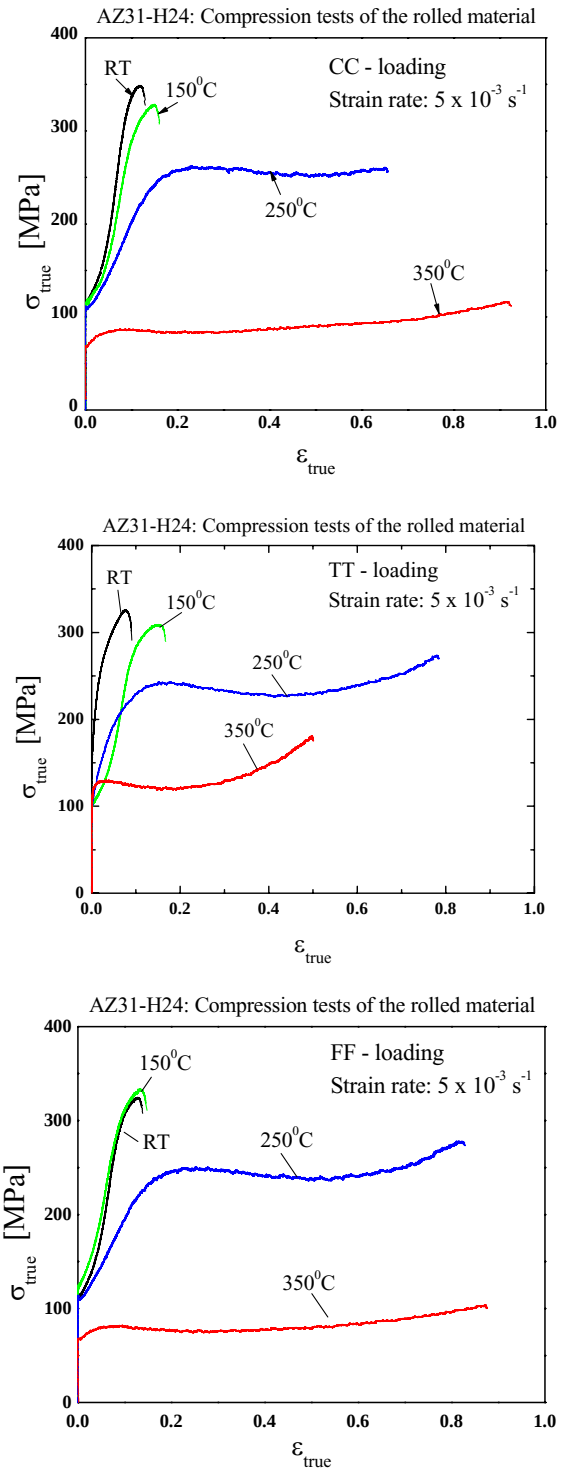

Figure 52 - The true stress-strain curves obtained from the compressive testing at different temperatures of the AZ31B-H24 rolled alloy for the CC-, TT-, and FF-loadings, respectively.

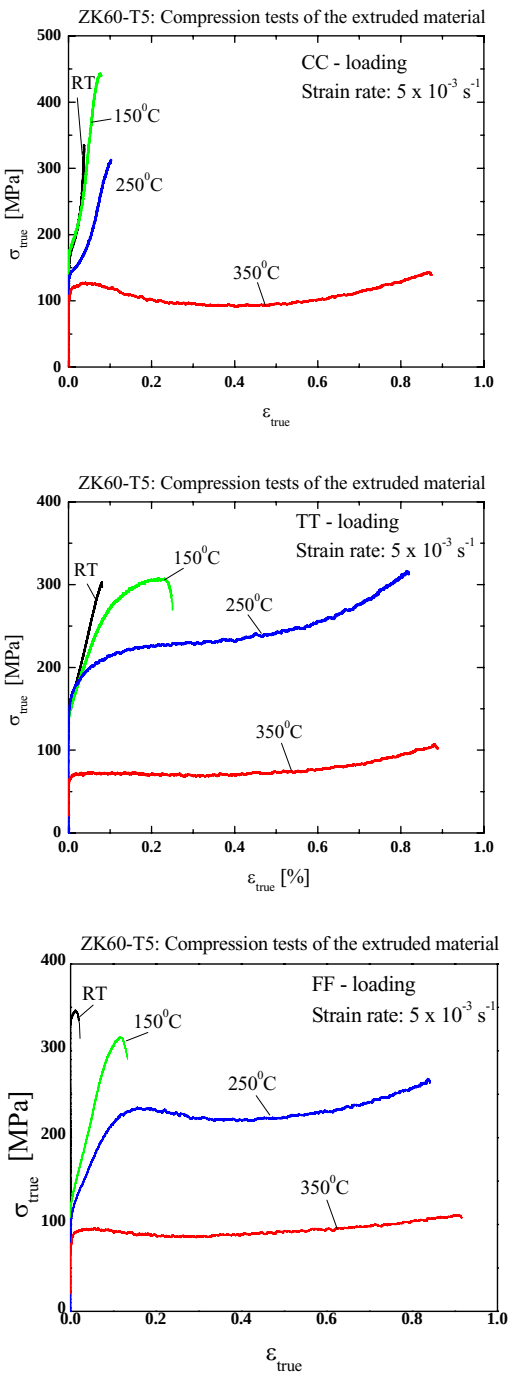

Figure 53 - The true stress-strain curves obtained from the compressive testing at different temperatures of the ZK60-T5 extruded alloy for the CC-, TT-, and FF-loadings, respectively.

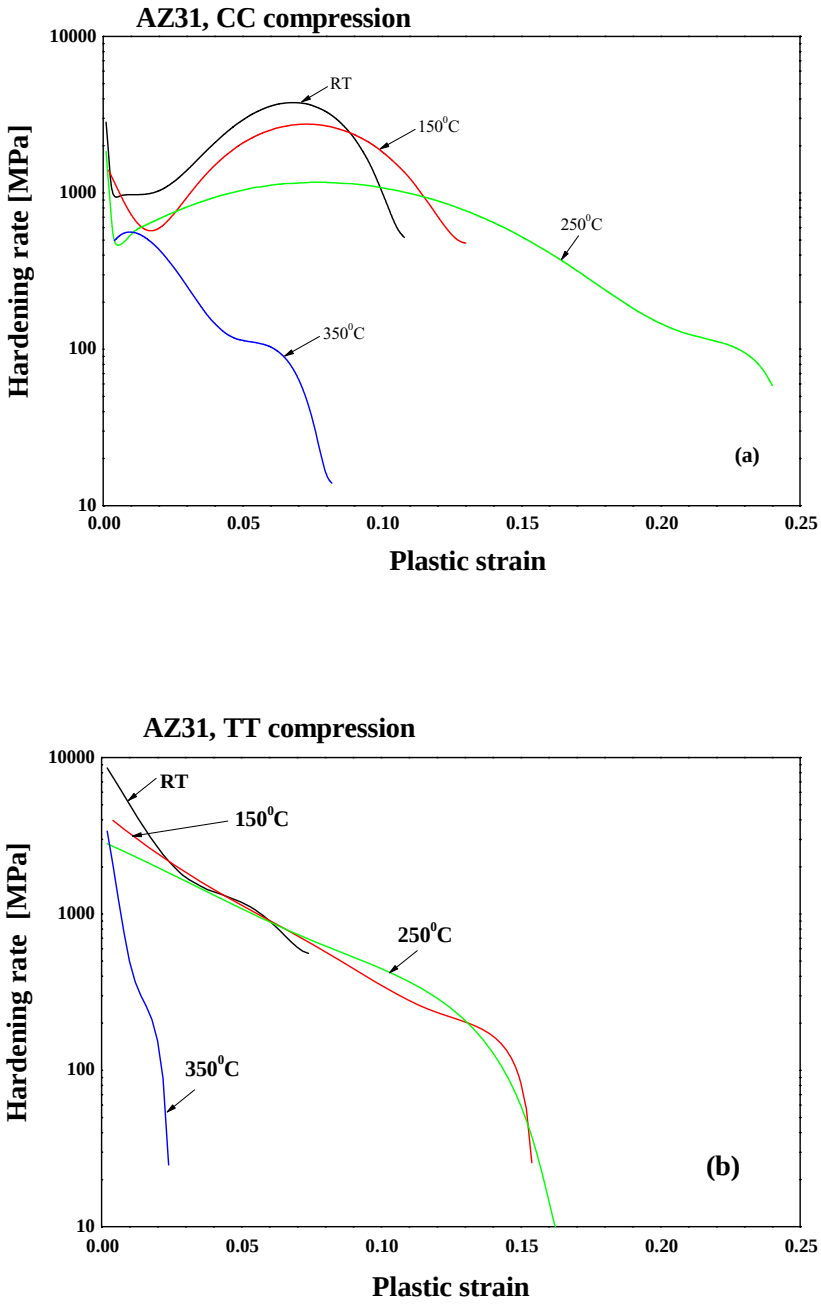

Figure 54 - The hardening rate versus the plastic strain resulted from the compression at different temperatures of the AZ31 alloy (a) for the CC loading, and (b) for the TT loading.

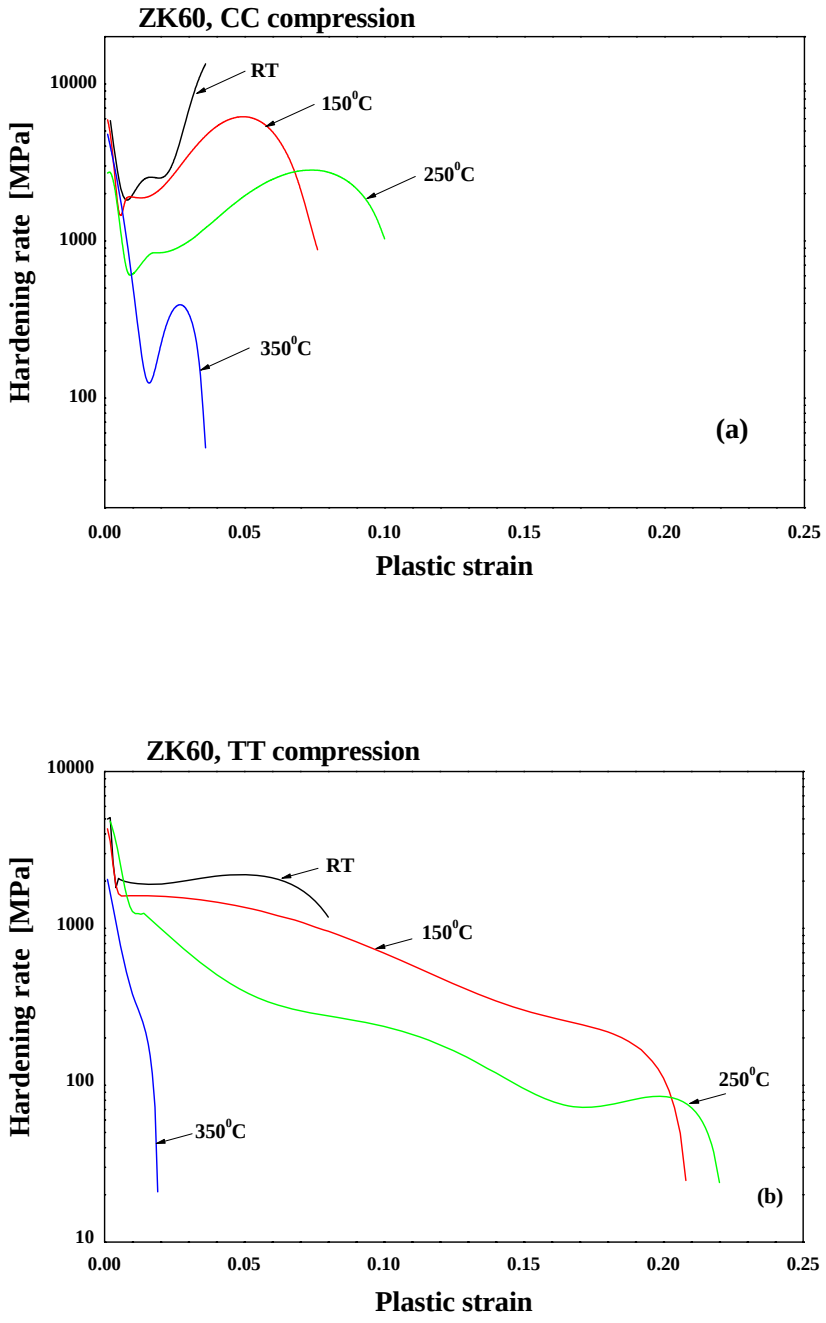

Figure 55 - The hardening rate versus the plastic strain resulted from the compression at different temperatures of the ZK60 alloy (a) for the CC loading, and (b) for the TT loading.

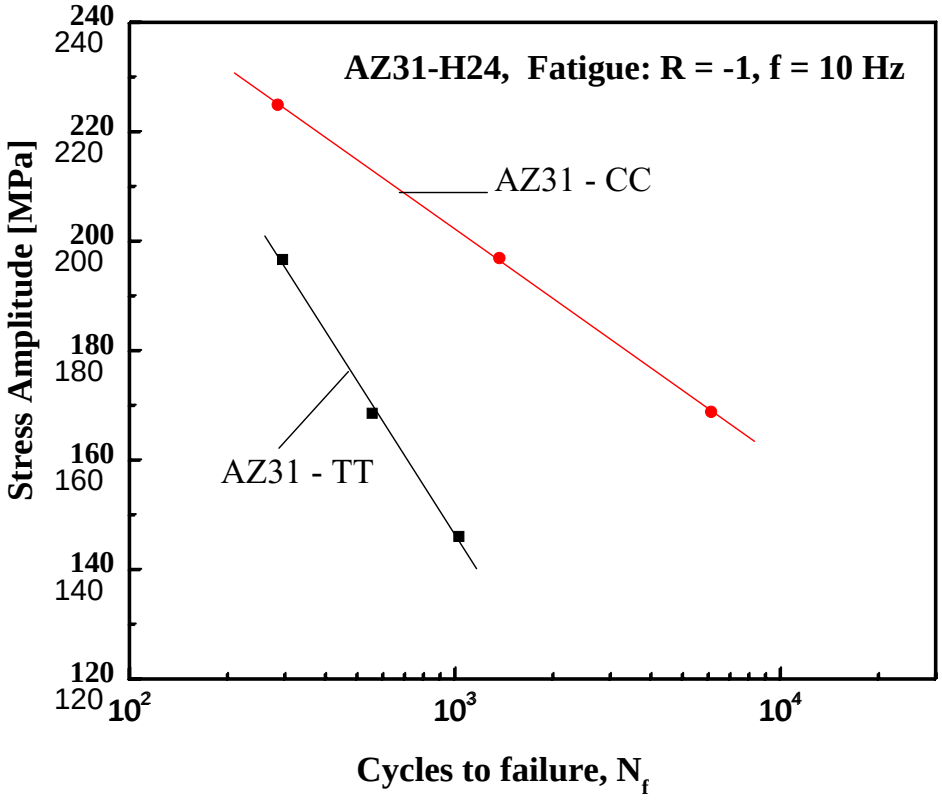

Figure 56 - Stress amplitude versus cycles to failure of the AZ31B alloy samples for the CC-loading (along the rolling direction) and for the TT-loading (perpendicular to the rolling direction).

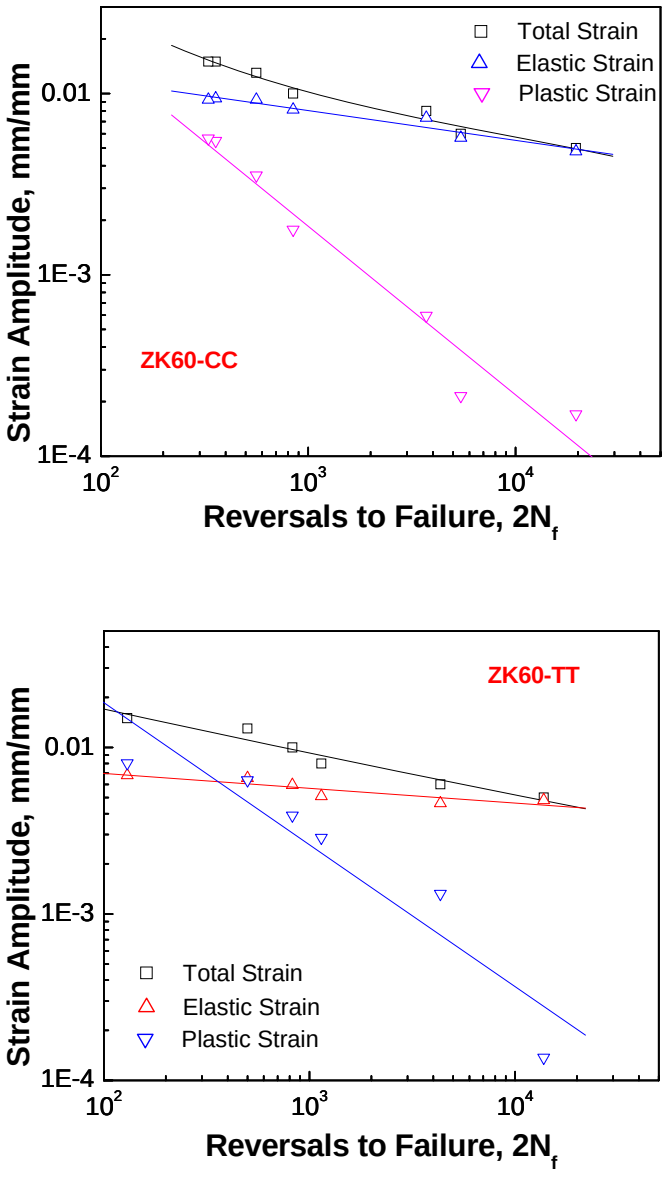

Figure 57 - Total strain versus reversals to failure for two loading directions applied to the ZK60-T5 alloy samples during low-cycle fatigue: CC-loading, along the extrusion direction, and TT-loading, perpendicular to the extrusion direction.

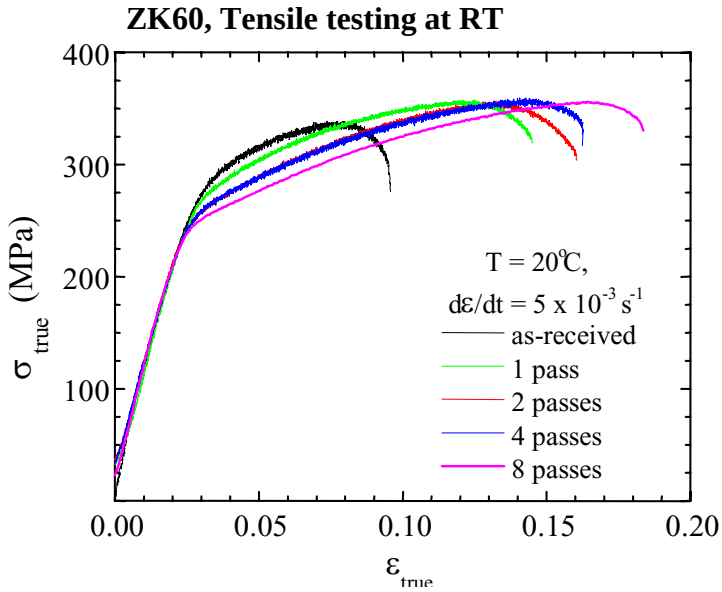

(a) Tensile testing at room temperature

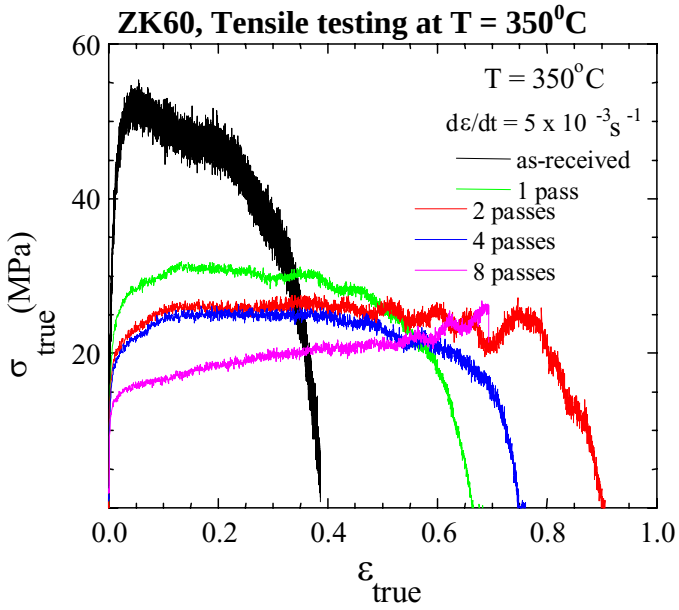

(b) Tensile testing at T = 350^{0}C

Figure 58 - True stress-strain curves of the ZK60 samples, deformed by ECAP for 1, 2, 4, and 8 passes, route A, and tested in tension with the strain rate of 5×10^{-3} s^{-1} at (a) room temperature (RT), and (b) 350^{0}C.

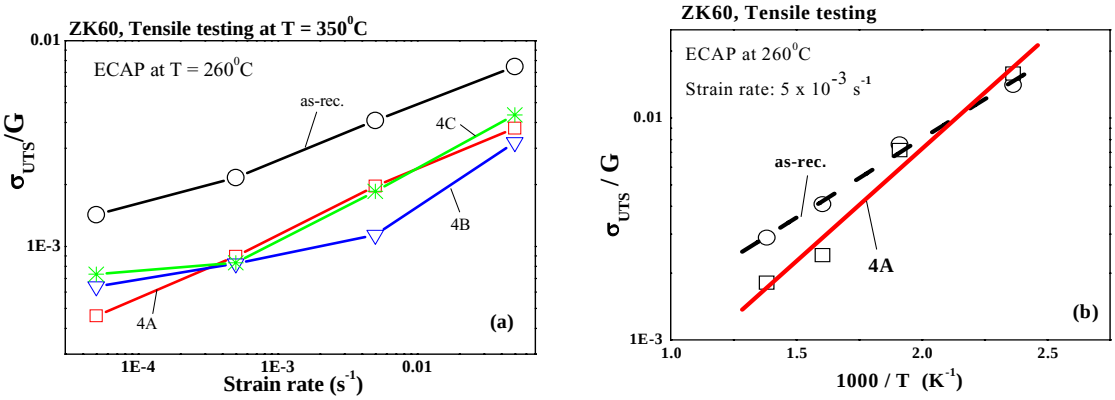

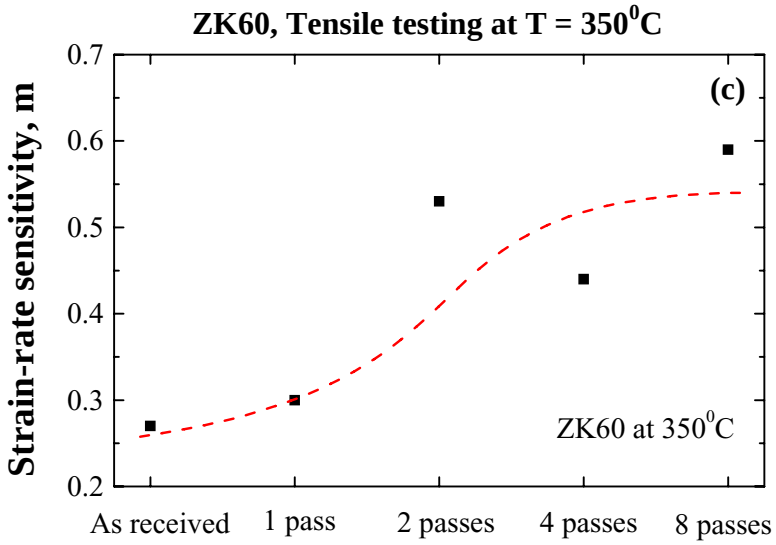

Figure 59 - The normalized stress of ZK60, tested in tensile, (a) versus strain rate, at testing temperature, T = 350^{0}C, and (b) versus test temperatures for the samples before and after ECAP, 4 passes, route A; (c) the strain-rate sensitivity versus number of ECAP passes of the ZK60 alloy tested in tension at 350^{0}C.

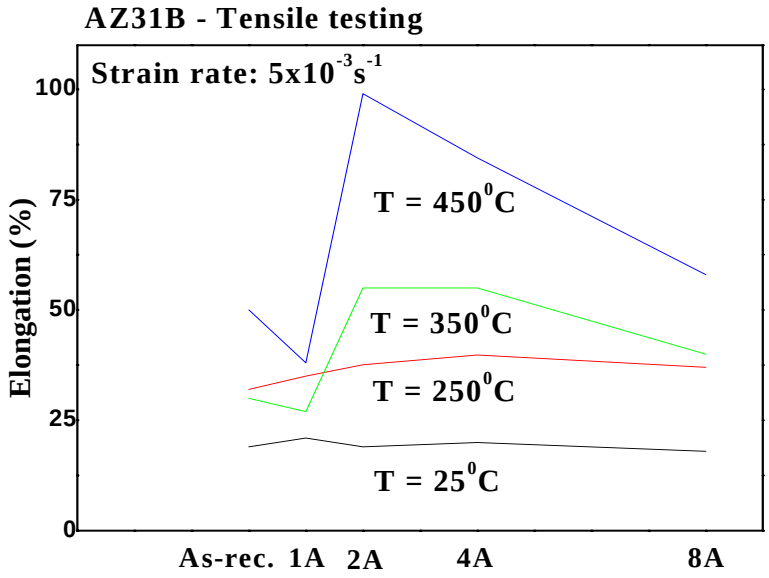

(a) AZ31B

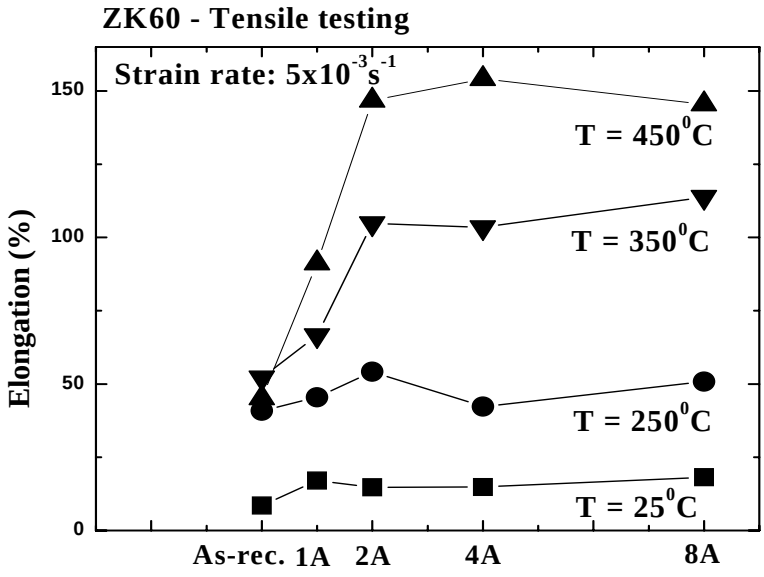

(b) ZK60

Figure 60 - The elongations obtained from the tensile testing of AZ31B and ZK60 alloys at different temperatures, before and after ECAP for 1, 2, 4, and 8 passes, route A: (a) AZ31 and (b) ZK60.

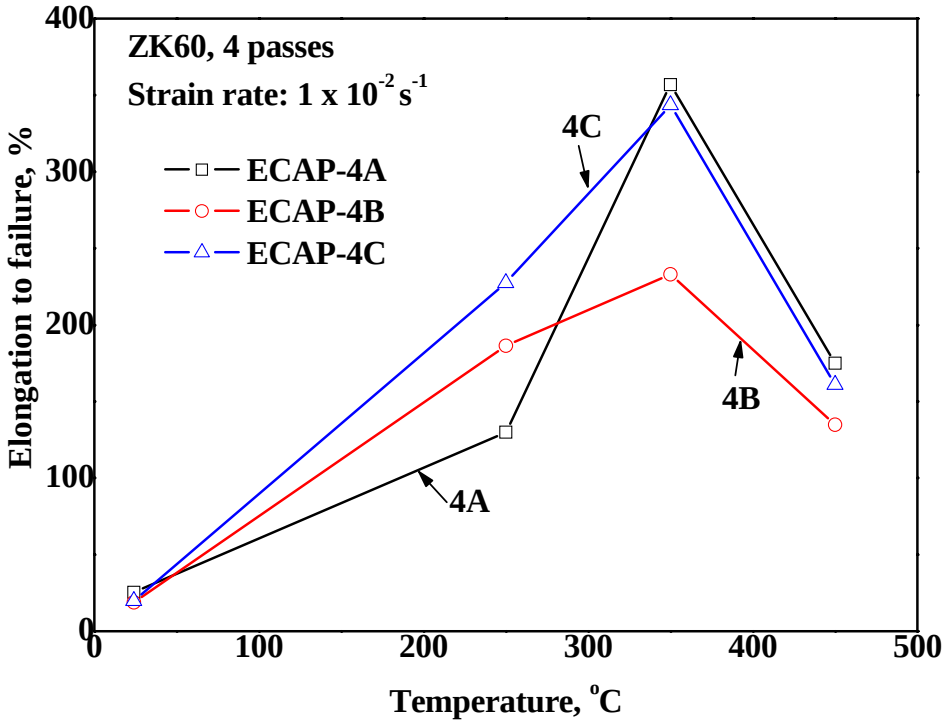

Figure 61 - Superplastic behavior of the ZK60 deformed in ECAP for 4 passes, and tested in tension at different temperatures, and for different ECAP routes (A, B, and C).

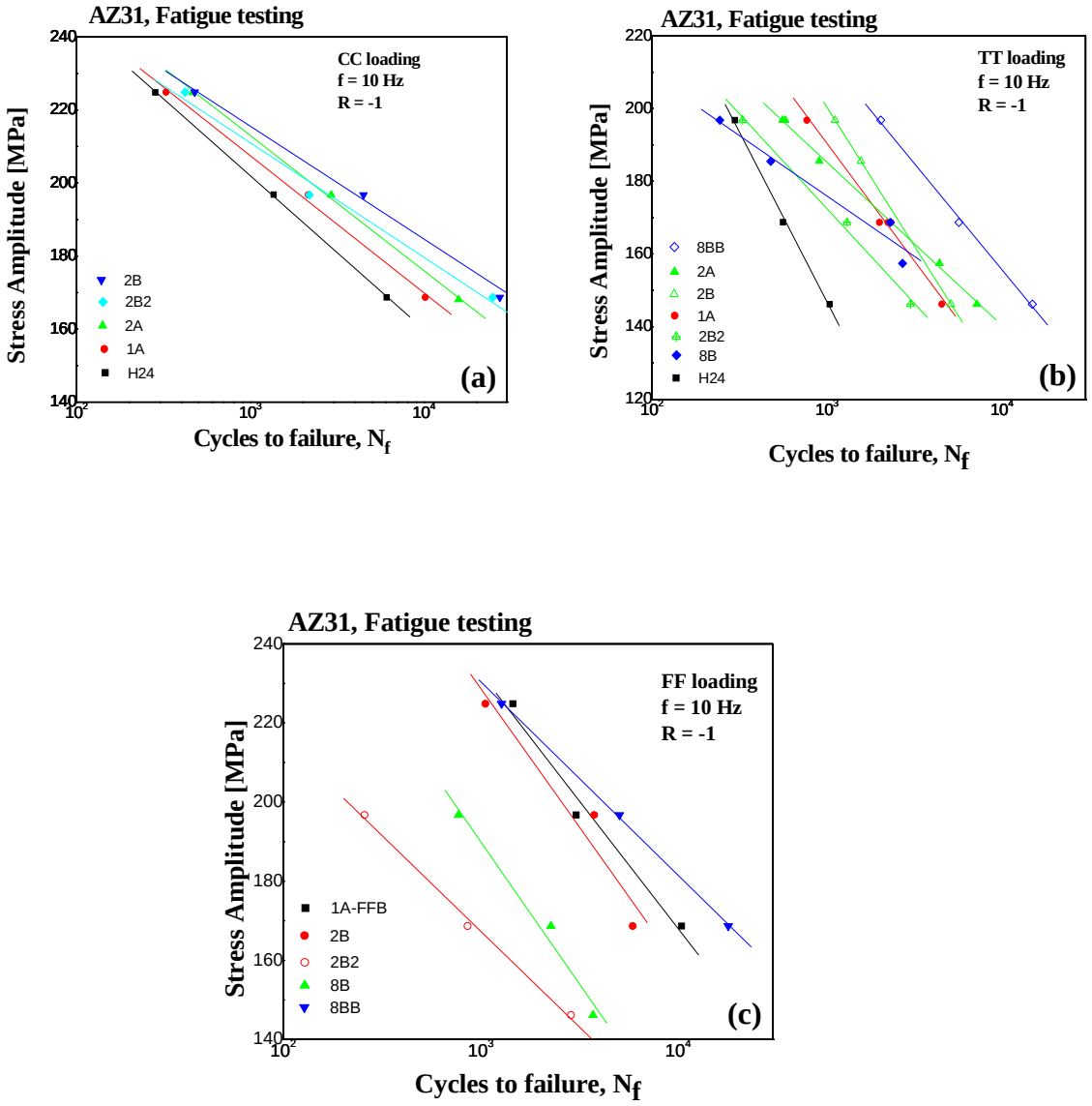

Figure 62 - The stress amplitude versus cycles-to-failure resulted from the fatigue testing of ECAP-ed AZ31 (routes A and B_C) for 1 pass, 2 passes, 8 passes without back-pressure (8B), and 8 passes with back-pressure (8BB). During fatigue, three loading directions were used: (a) CC loading, along the pressing direction, and (b and c) TT and FF loadings, perpendicular to the pressing direction.

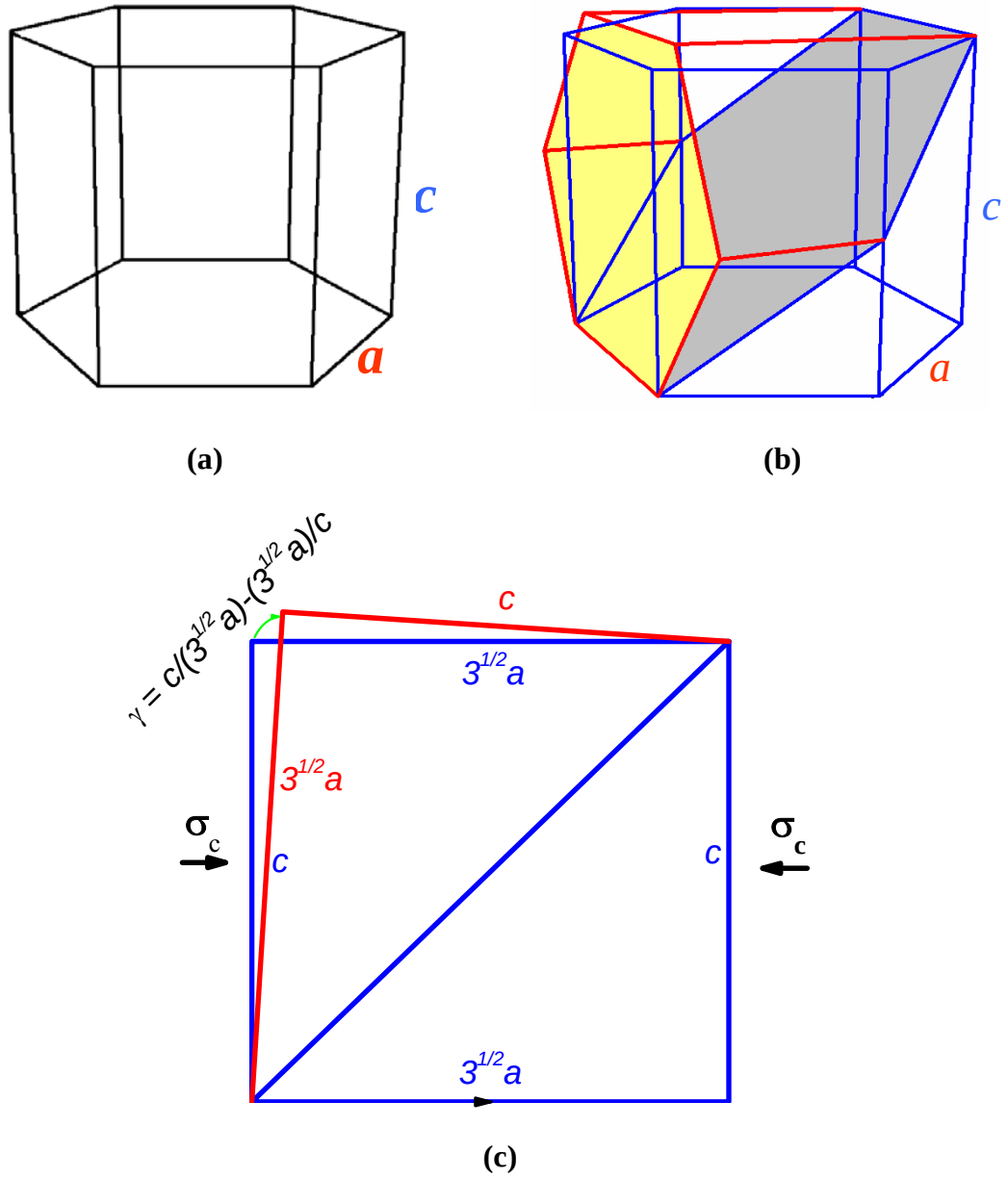

Figure 63 - The twin formation in the hexagonal-closed packed (HCP) structure of Mg: (a) the HCP structure of Mg before twinning, with the lattice constants a = b, and c, where $\frac{c}{a} = 1.624 < \sqrt{3}$; (b) the HCP structure after twinning (the twin is represented with red lines); (c) the tensile twin formation after a compressive loading perpendicular to the c-axis. The shear strain, γ, due to twinning is $\gamma = \frac{c}{a\sqrt{3}} - \frac{a\sqrt{3}}{c}$.

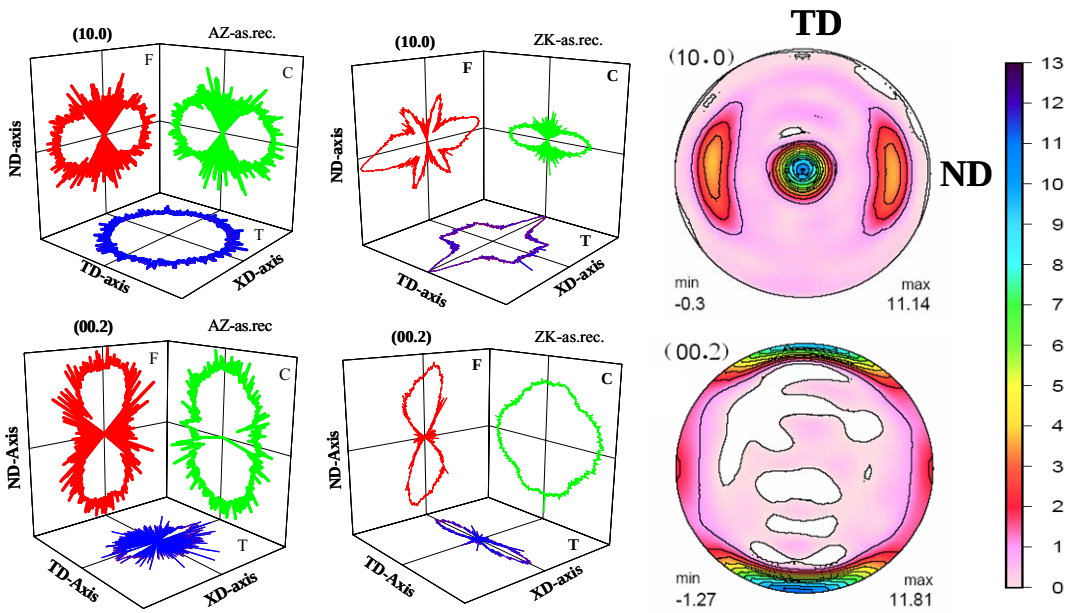

(a) AZ31 **(b) ZK60** **(c) ZK60**

Figure 64 - The characterizations of the two Mg alloys in the as-received condition, for three surfaces of observations, F - flow, T - top, and C - cross planes, and for two reflections planes, (10.0) and (00.2): (a) the high-energy (HE) XRD in-plane pole distributions (IPPDs) of the hot-rolled AZ31 alloy, (b) the HE-XRD IPPDs of the hot-extruded ZK60 alloy; (c) the neutron-diffraction pole figures of the ZK60 alloy, cross plane.

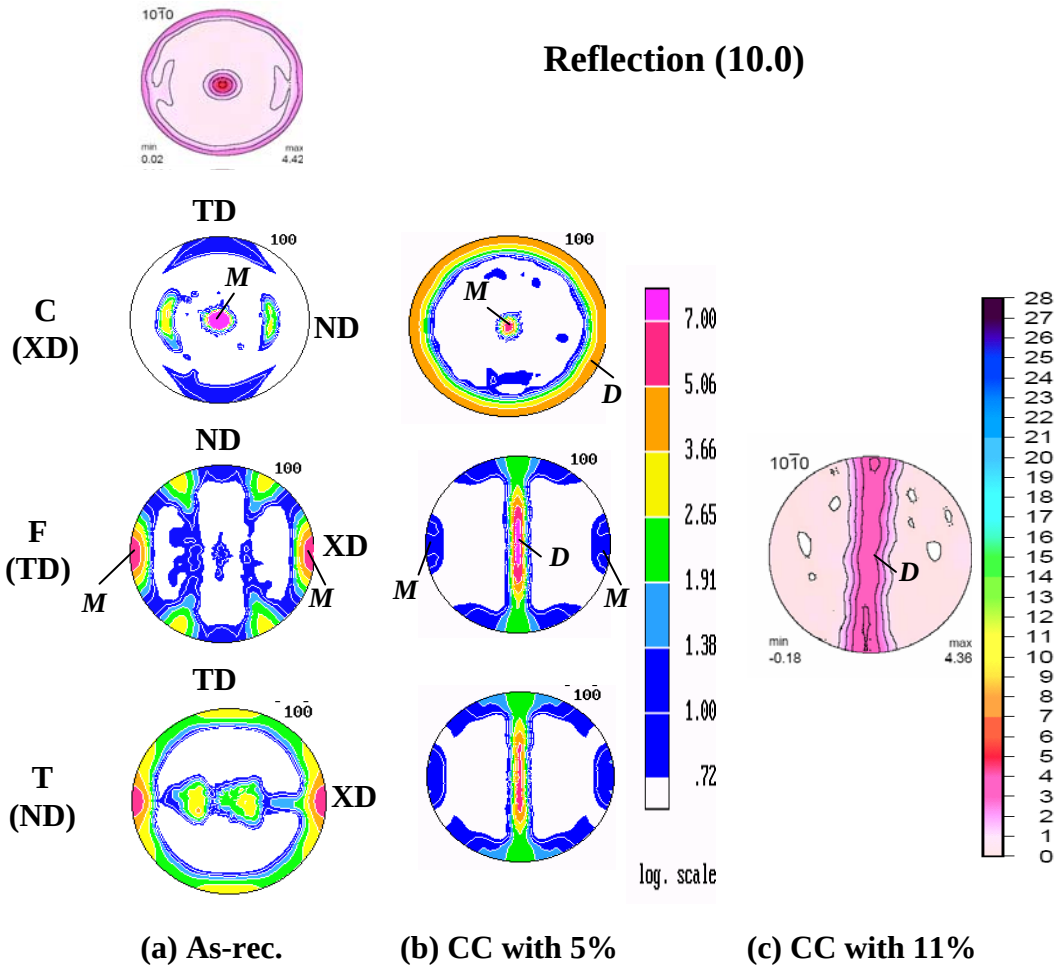

Figure 65 - The low-energy (LE) XRD pole-figures of the ZK60-T5 samples after uniaxial compression at room temperature along the CC axis. The (10.0) reflection is shown for the three planes of observations (F - flow, T - top, and C - cross), where XD, ND, and TD are the pressing, normal, and transverse directions, respectively. The mother grains are designed with *M*, and the daughter grains with *D*.

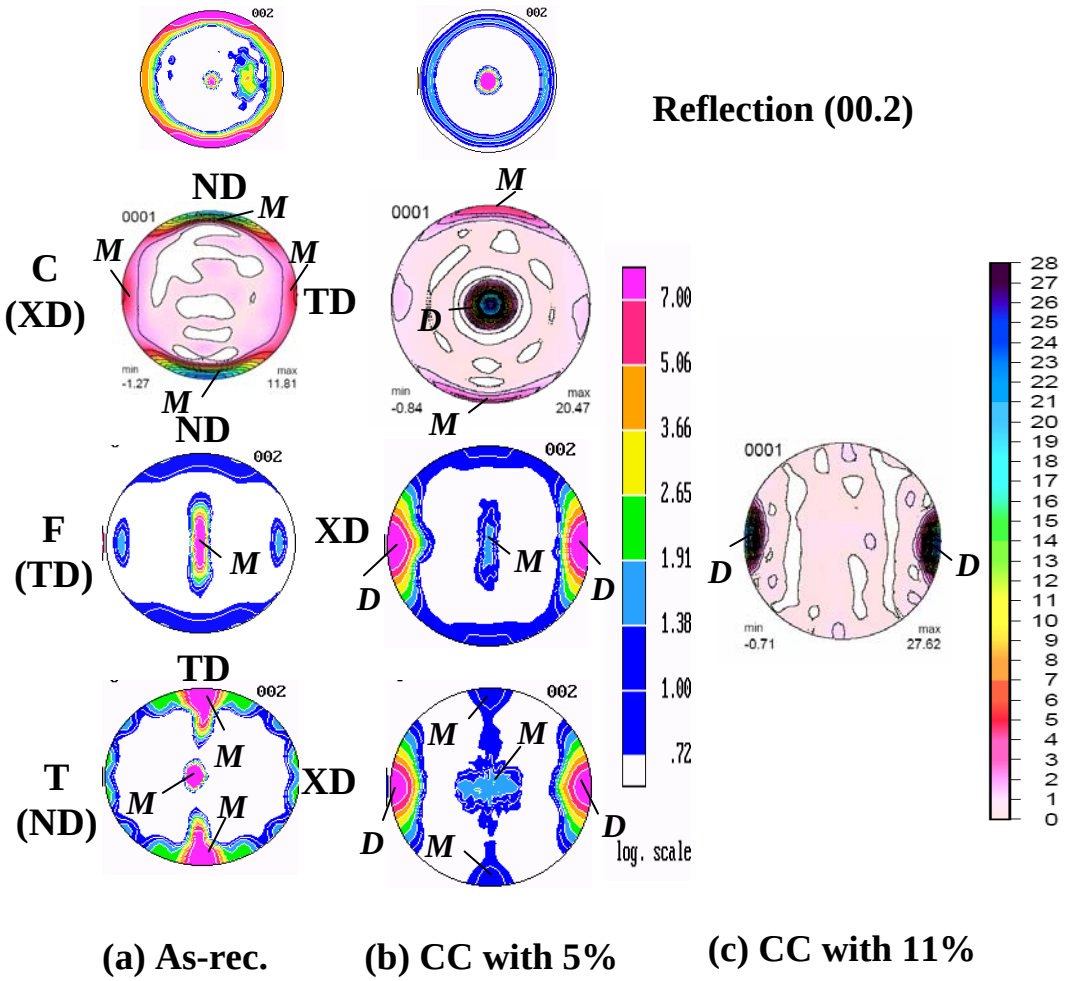

Figure 66 - The low-energy (LE) XRD pole-figures of the ZK60-T5 samples after uniaxial compression at room temperature along the CC axis. The (00.2) reflection is shown for the three planes of observations (F - flow, T - top, and C - cross), where XD, ND, and TD are the pressing, normal, and transverse directions, respectively. The mother grains are designed with *M*, and the daughter grains with *D*.

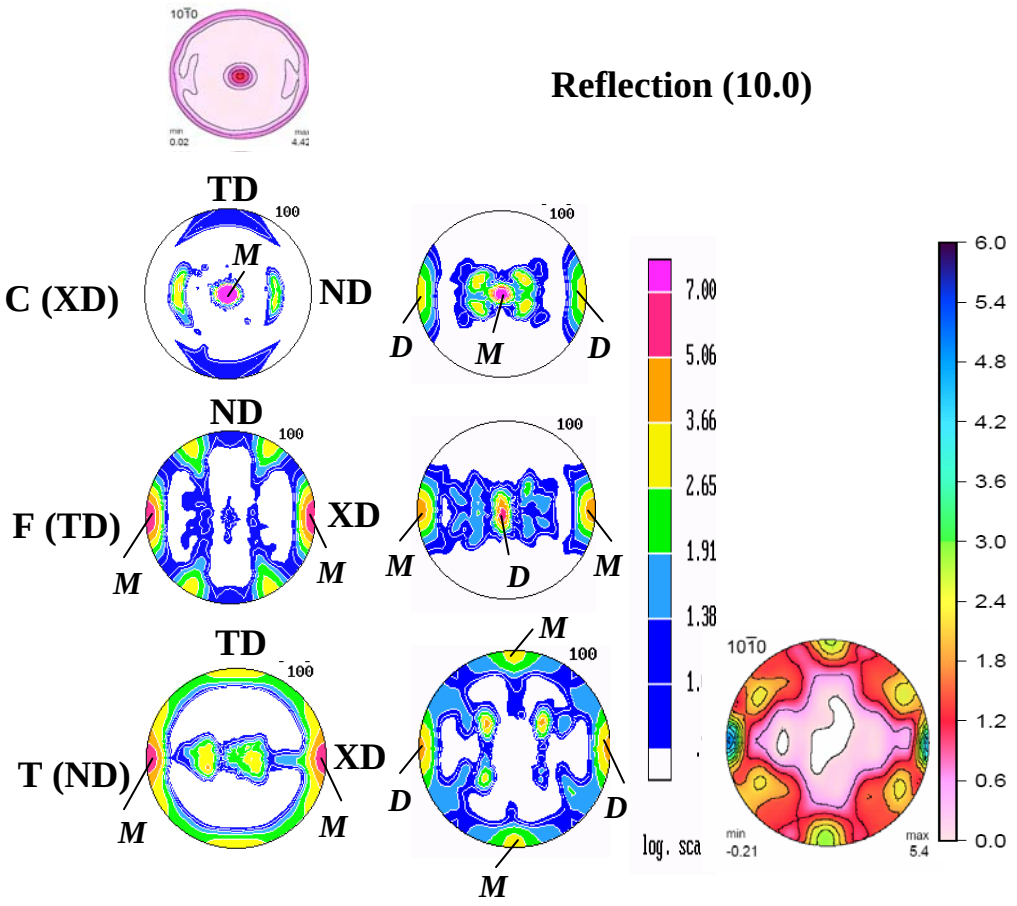

Figure 67 - The low-energy (LE) XRD pole-figures of the ZK60-T5 samples after uniaxial compression at room temperature along the TT axis. The (10.0) reflection is shown for the three planes of observations (F - flow, T - top, and C - cross), where XD, ND, and TD are the pressing, normal, and transverse directions, respectively. The mother grains are designed with *M*, and the daughter grains with *D*.

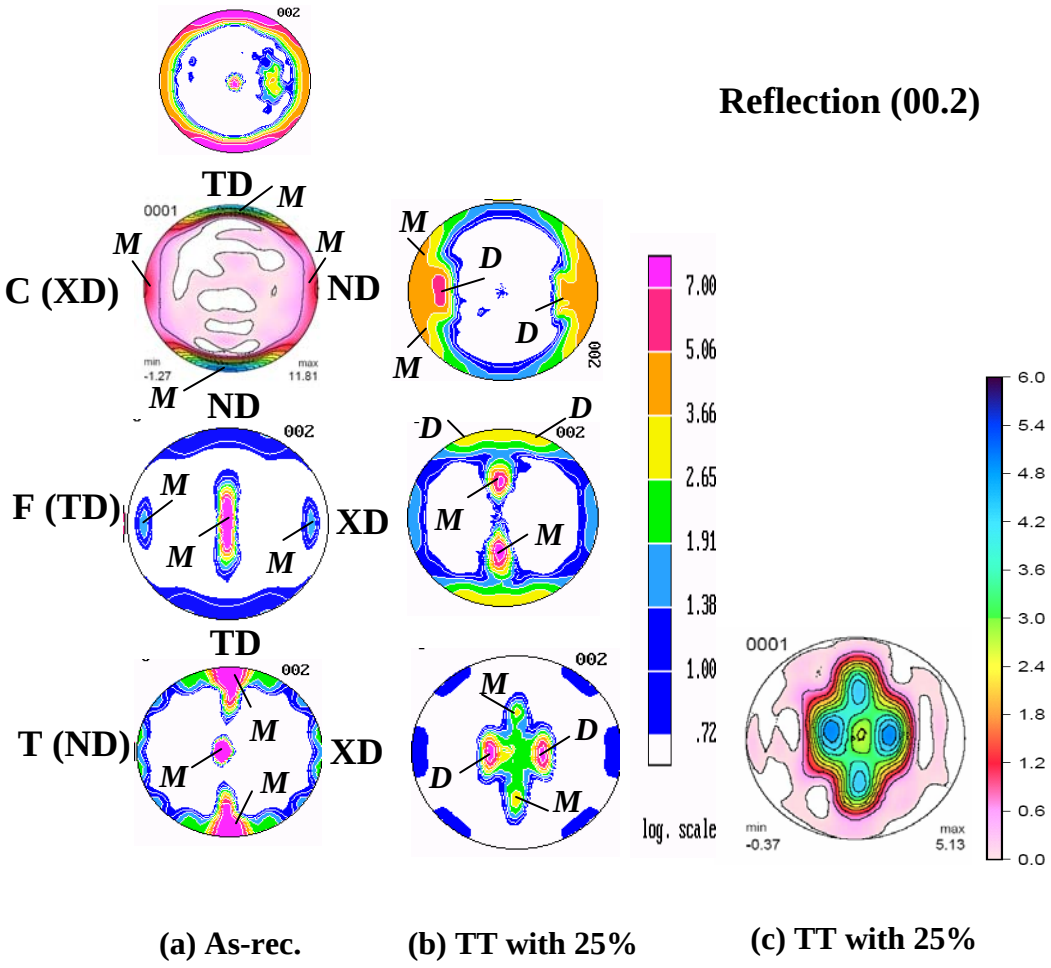

Figure 68 - The low-energy (LE) XRD pole-figures of the ZK60-T5 samples after uniaxial compression at room temperature along the TT axis. The (00.2) reflection is shown for the three planes of observations (F - flow, T - top, and C - cross), where XD, ND, and TD are the pressing, normal, and transverse directions, respectively. The mother grains are designed with *M*, and the daughter grains with *D*.

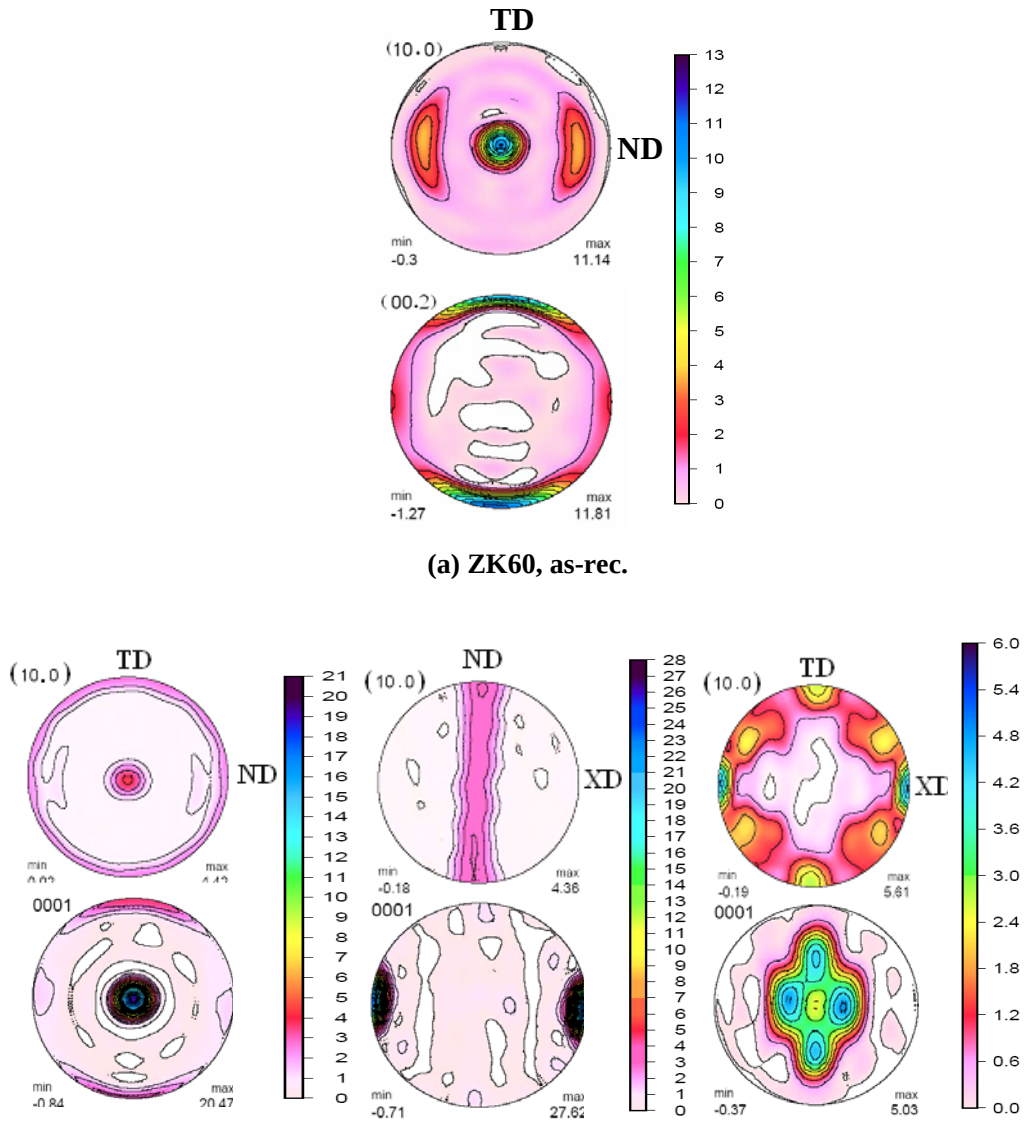

(a) ZK60, as-rec.

(b) ZK60-CC, **(c) ZK60-CC, 11%** **(d) ZK60-TT, 25%**

Figure 69 - The neutron diffraction PFs for the reflection planes, (10.0) and (00.2), of the ZK60 samples, (a) as-received, and after the compression tests at room temperature: (b) CC-loading, 5% strain, (c) CC-loading, 11% strain, and (d) TT-loading, 25% strain.

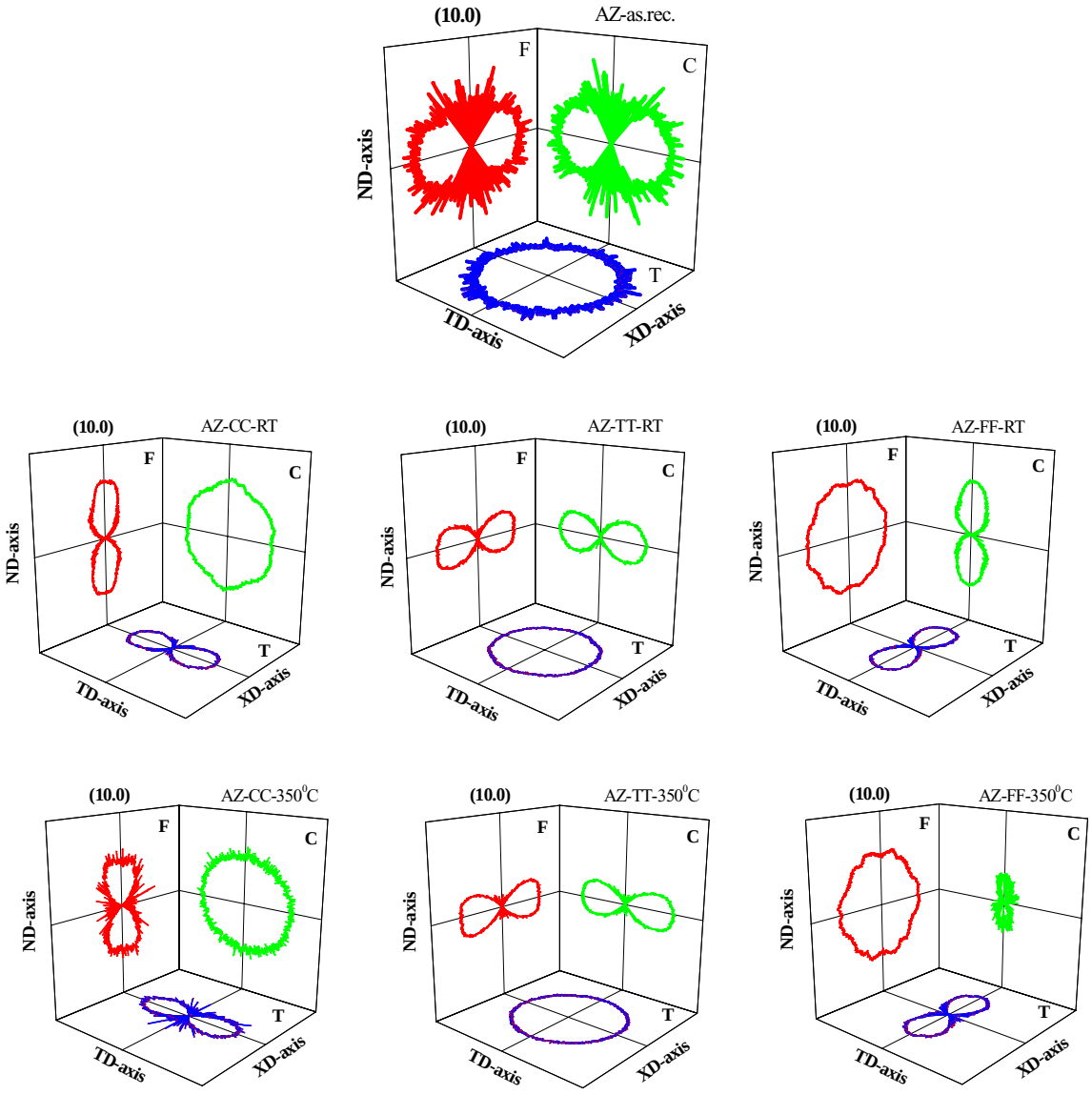

Figure 70 - The HE-XRD IPPDs of the prismatic poles, (10.0), of the AZ31 samples tested in compression, CC, TT, and FF, at different temperatures, and on three planes of observations: the flow plane (F), with the normal, TD, the top plane (T), with the normal, ND, and the cross plane (C), with the normal, XD.

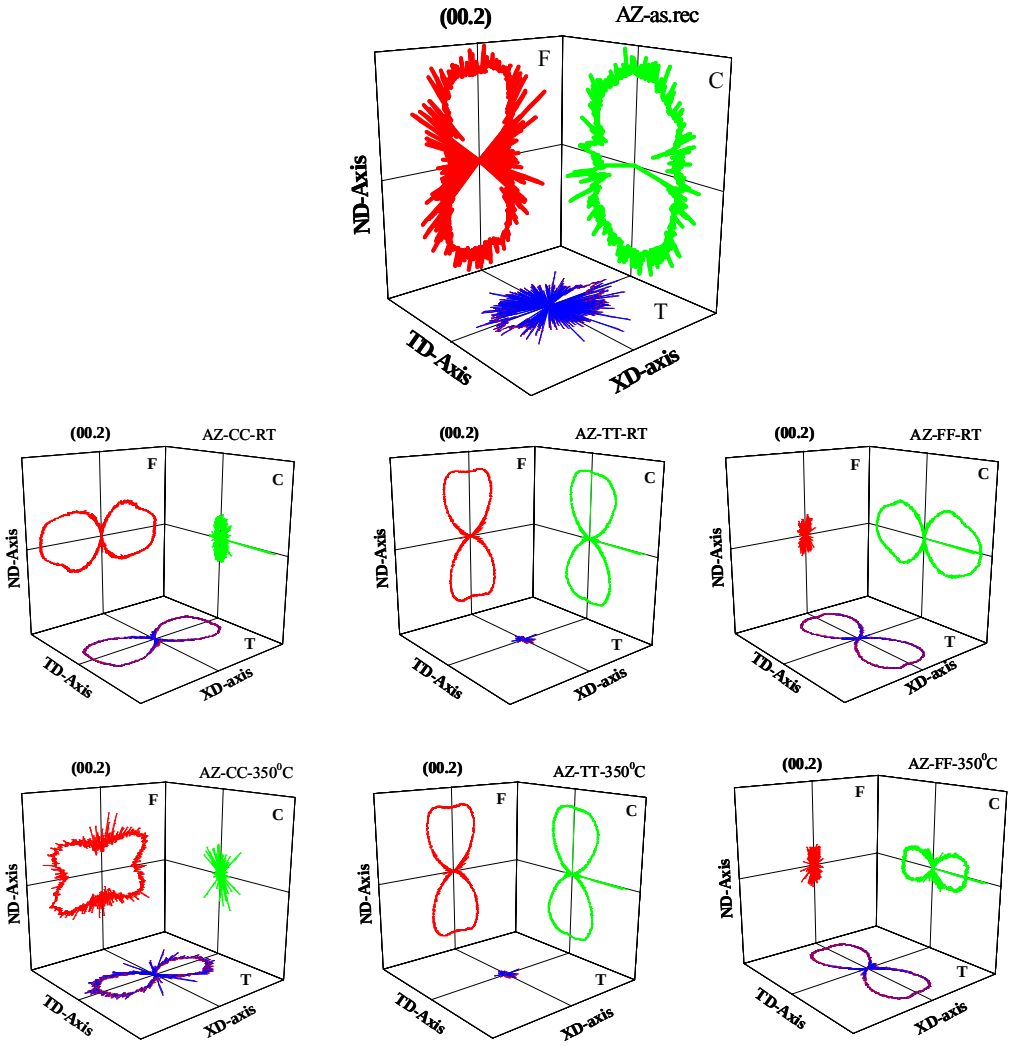

Figure 71 - The HE-XRD IPPDs of the basal poles, (00.2), of the AZ31 samples tested in compression, CC, TT, and FF, at different temperatures, and on three planes of observations: the flow plane (F), with the normal, TD, the top plane (T), with the normal, ND, and the cross plane (C), with the normal, XD.

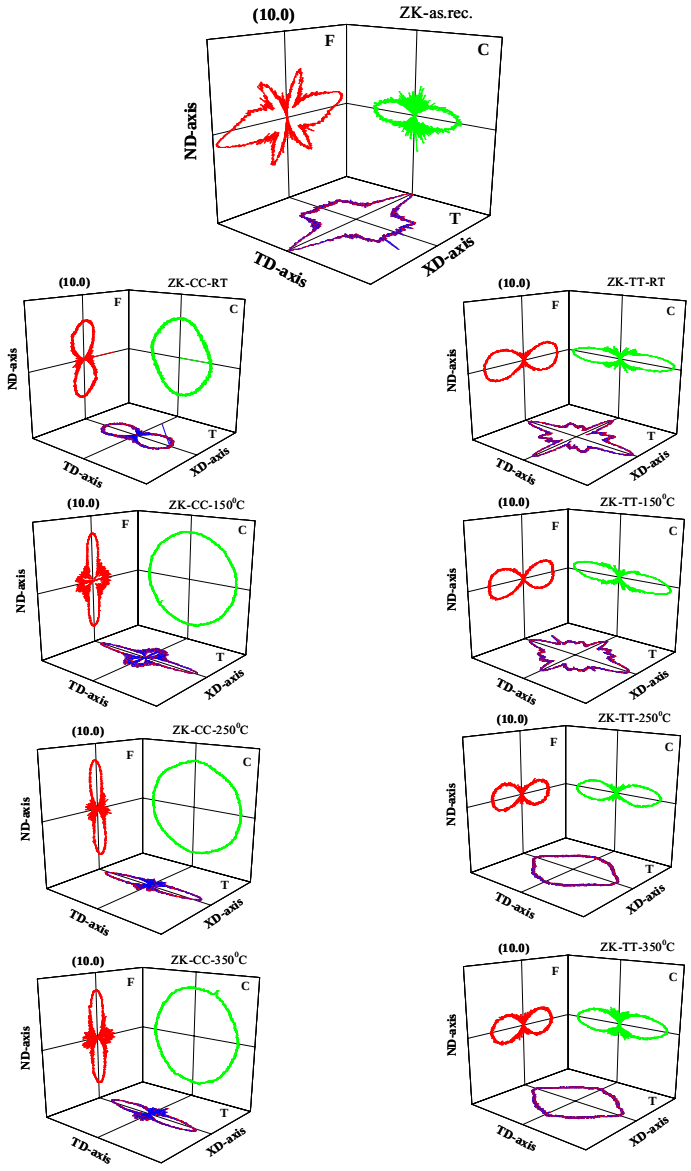

Figure 72 - The HE-XRD IPPDs of the prismatic poles, (10.0), of the ZK60 samples tested in compression, CC and TT, at different temperatures, and on three planes of observations: the flow plane (F), with the normal, TD, the top plane (T), with the normal, ND, and the cross plane (C), with the normal, XD.

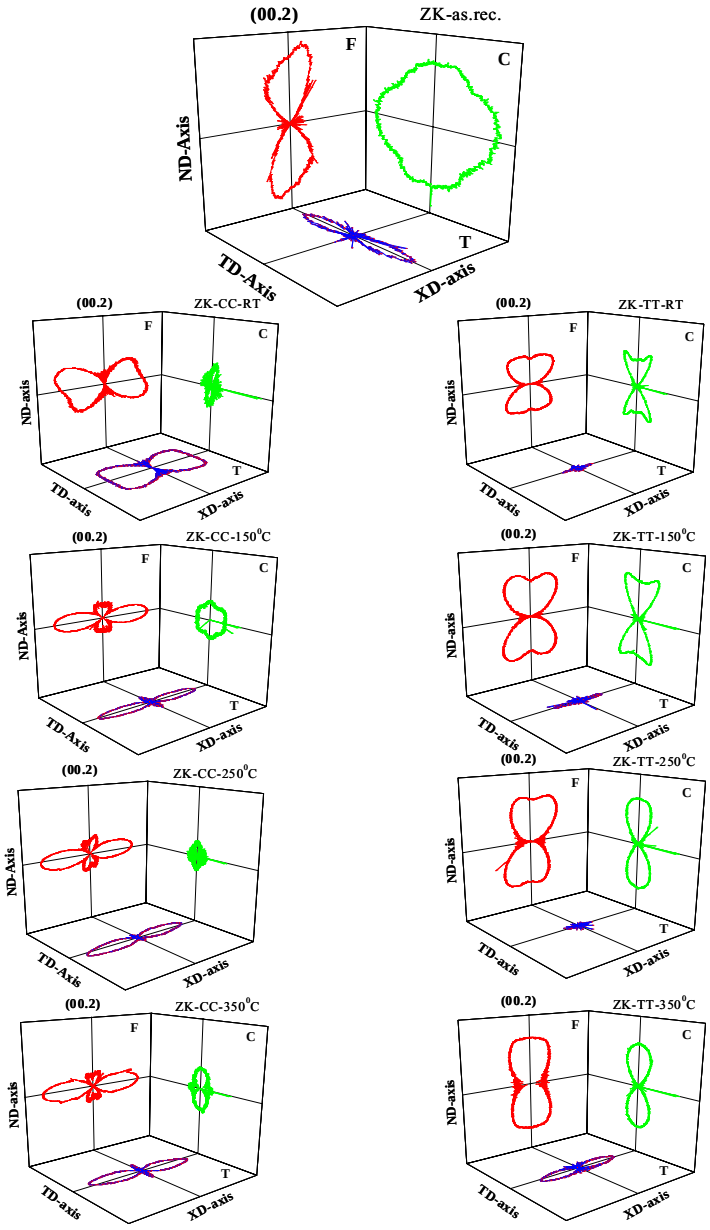

Figure 73 - The HE-XRD IPPDs of the basal poles, (00.2), of the ZK60 samples tested in compression, CC and TT, at different temperatures, and on three planes of observations: the flow plane (F), with the normal, TD, the top plane (T), with the normal, ND, and the cross plane (C), with the normal, XD.

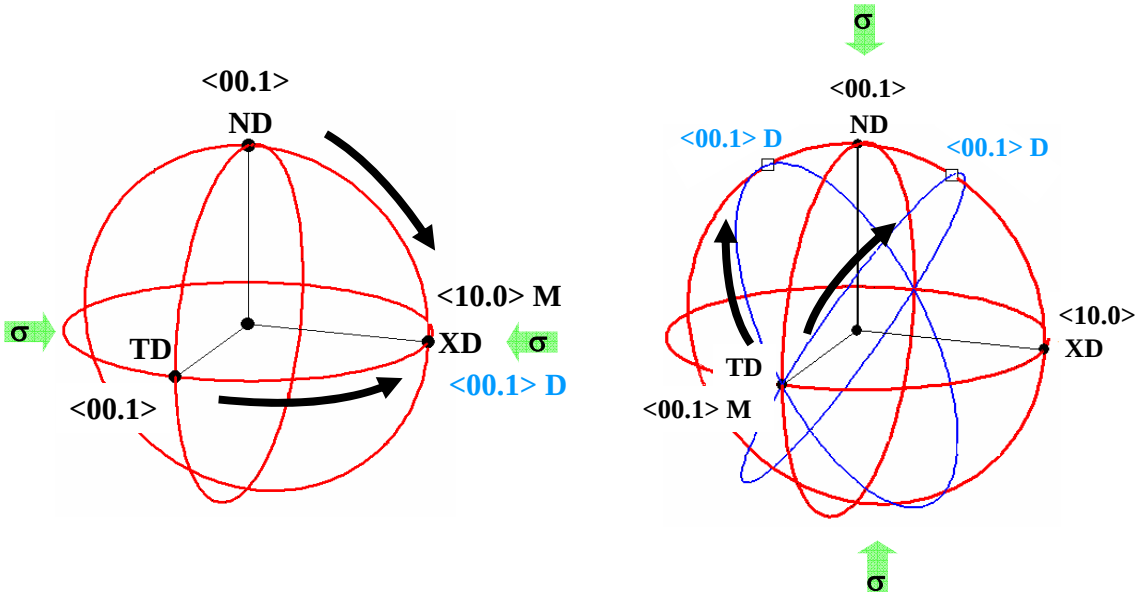

(a) ZK60, Compression CC

(b) ZK60, Compression TT

Figure 74 - The twinning mechanism during the plastic deformation in uniaxial compression of the ZK60 alloy for two loading directions: (a) compression CC, along the extrusion direction, and (b) compression TT, perpendicular to the extrusion direction. The mother texture, M, becomes daughter, D, after the compression test.

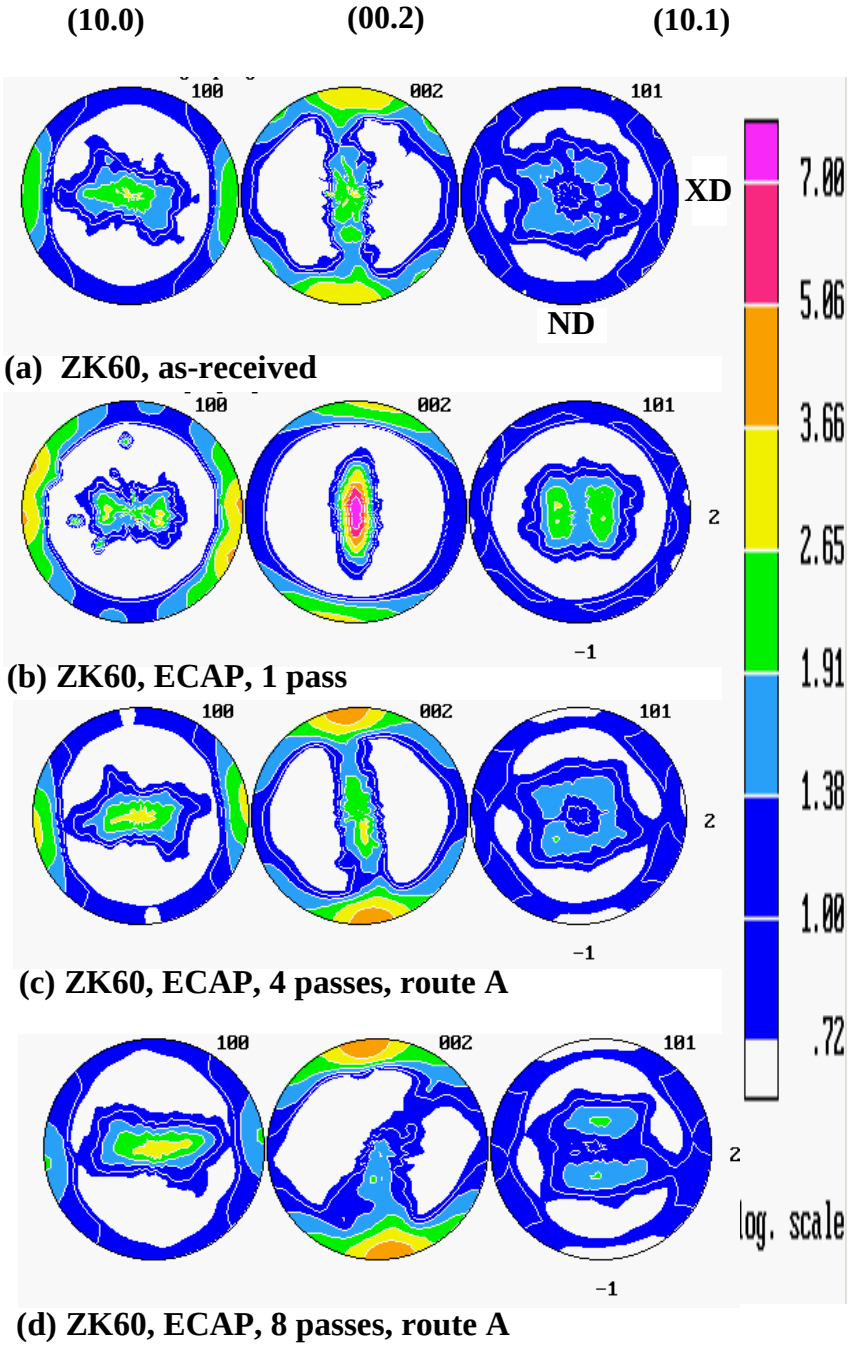

Figure 75 - Texture development with the number of ECAP passes for the ZK60 samples: (a) as-received, (b) ECAP, 1 pass, c) ECAP, 4 passes, route A, and (d) ECAP, 8 passes, route A.

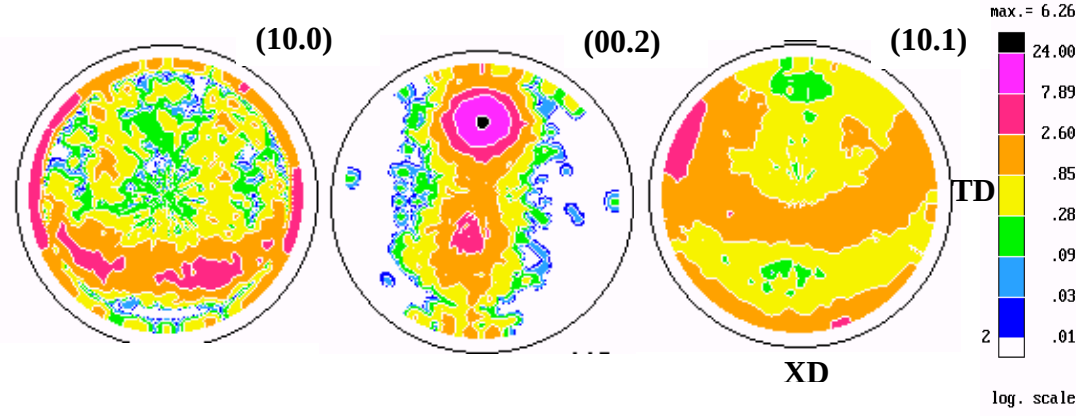

(a) ZK60 after ECAP, 8 passes, route A: PFs from LE-XRD

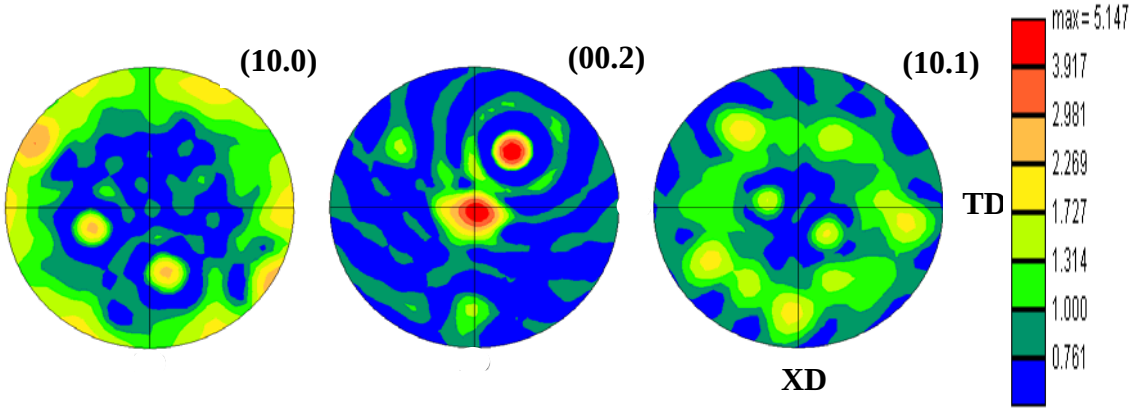

(b) ZK60 after ECAP, 8 passes, route A: PFs from OIM

Figure 76 - Comparison of the PFs for the ZK60-T5 deformed in ECAP for 8 passes, route A: (a) low-energy (LE) XRD and (b) orientation-imaging microscopy (OIM) for three reflections planes, (10.0), (00.2), and (10.1).

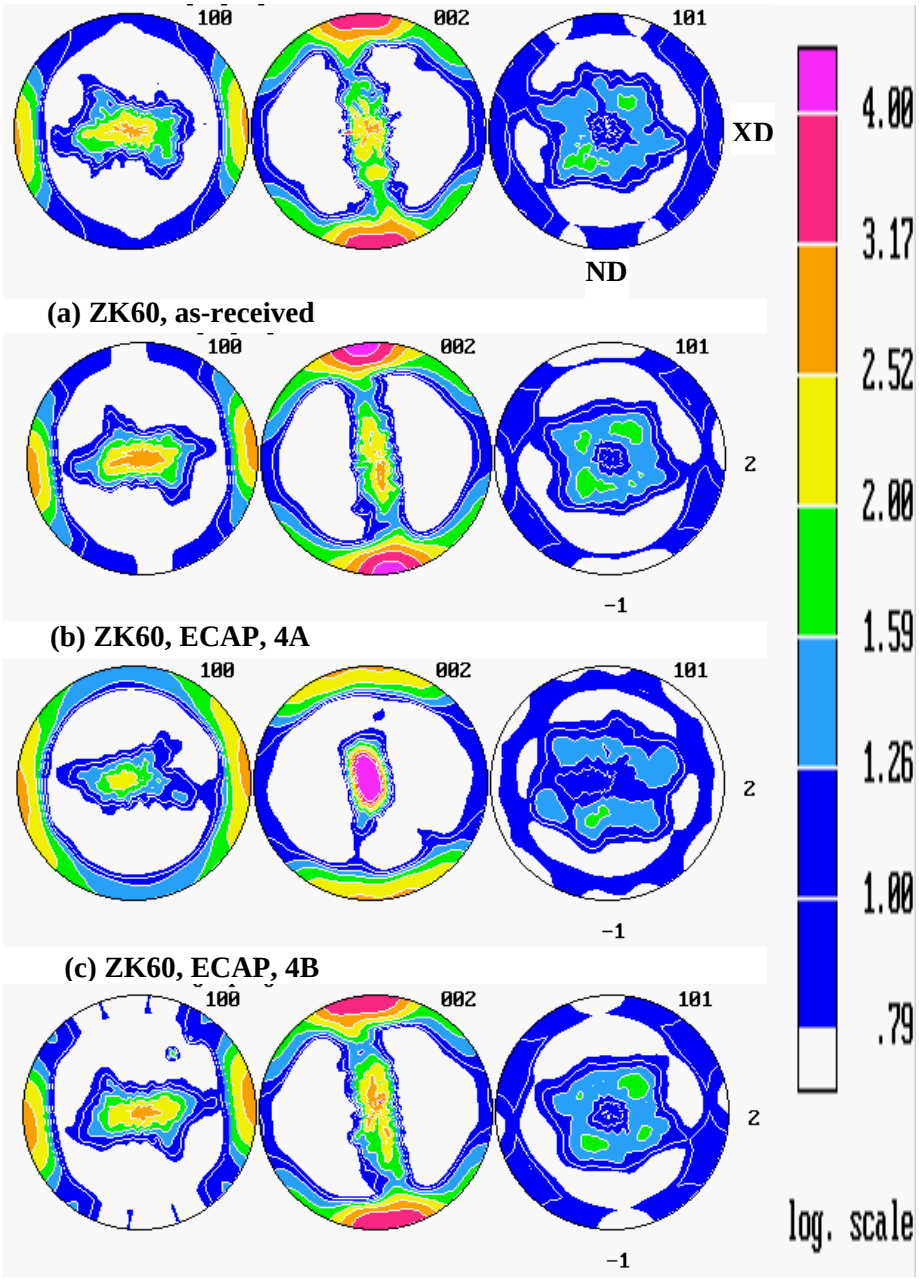

Figure 77 - The LE- XRD PFs of the ZK60-T5 (hot extrusion): (a) as-received, (b) ECAP- 4A, (c) ECAP-4B, and (d) ECAP-4C; XD, ND, and TD - pressing, normal, and transverse directions.

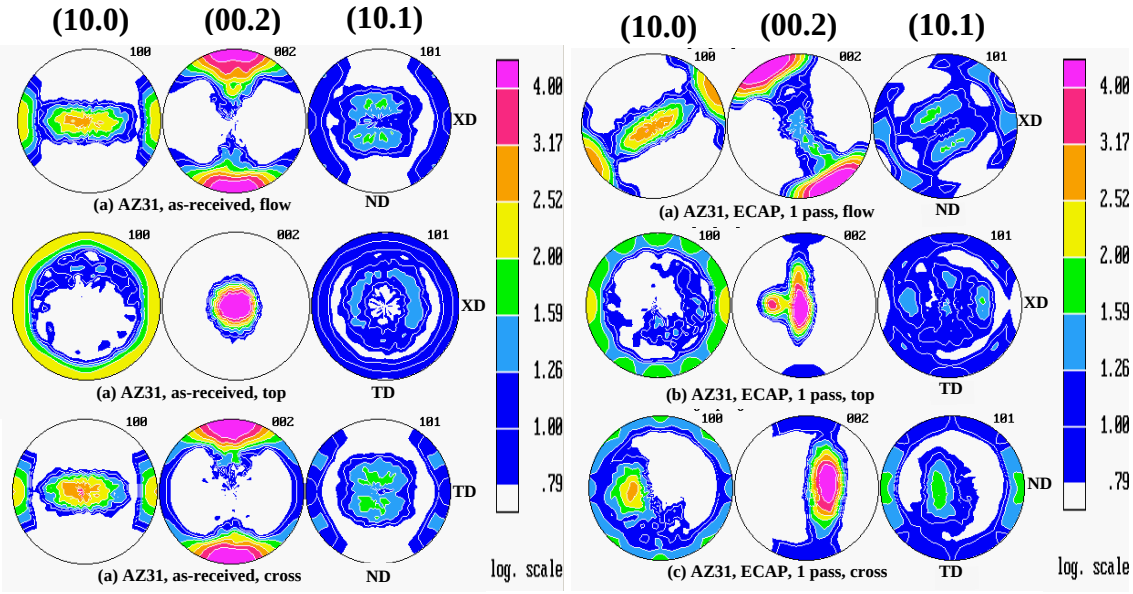

Figure 78 - The low-energy (LE) XRD PFs of the AZ31-H24 (hot rolling), before and after one pass of ECAP, observed on three surfaces, flow, top, and cross planes, for three reflection planes, (10.0), (00.2), and (10.1).

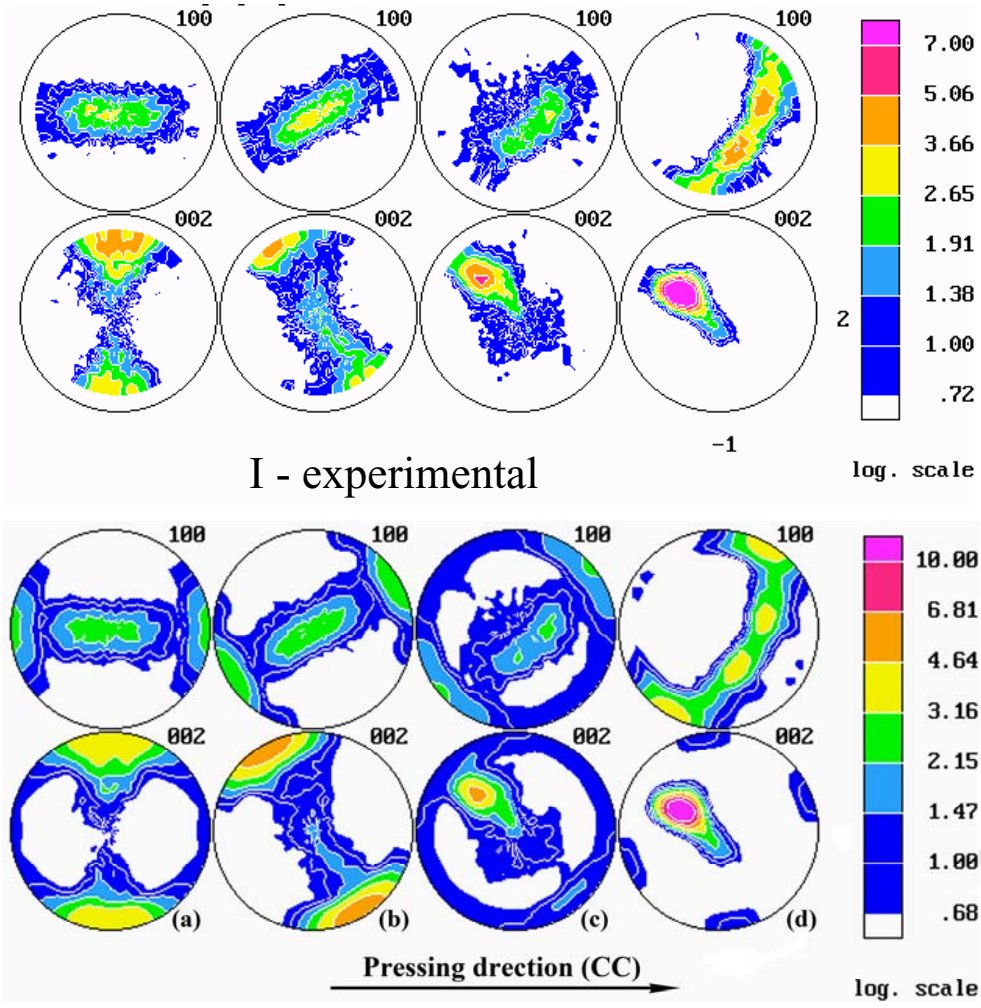

Figure 79 - The texture evolution with the strain intensity obtained from the low-energy (LE) XRD PFs for the prismatic and basal poles, for the AZ31B samples: (a) as-received, (b) 1 pass, (c) 2 passes, route B_C, and (d) 8 passes, route B_C with back-pressure. The experimental (I) and full PFs (II) are shown for each case.

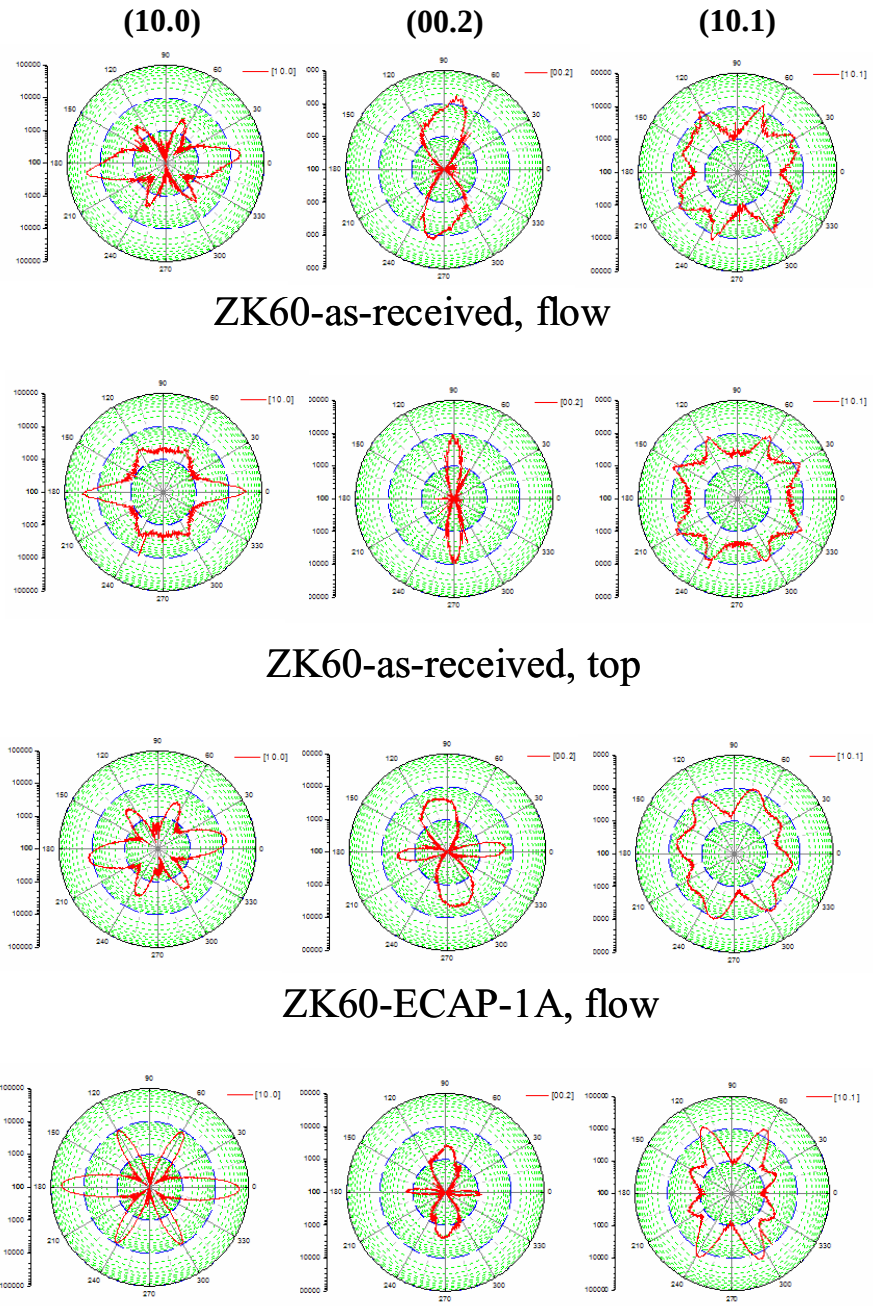

Figure 80 - The high-energy (HE) XRD in-plane pole distributions (IPPDs) for the three reflection planes (10.0), (00.2), and (10.1) of the ZK60 samples observed on flow and top planes, before and after ECAP, 1 pass.

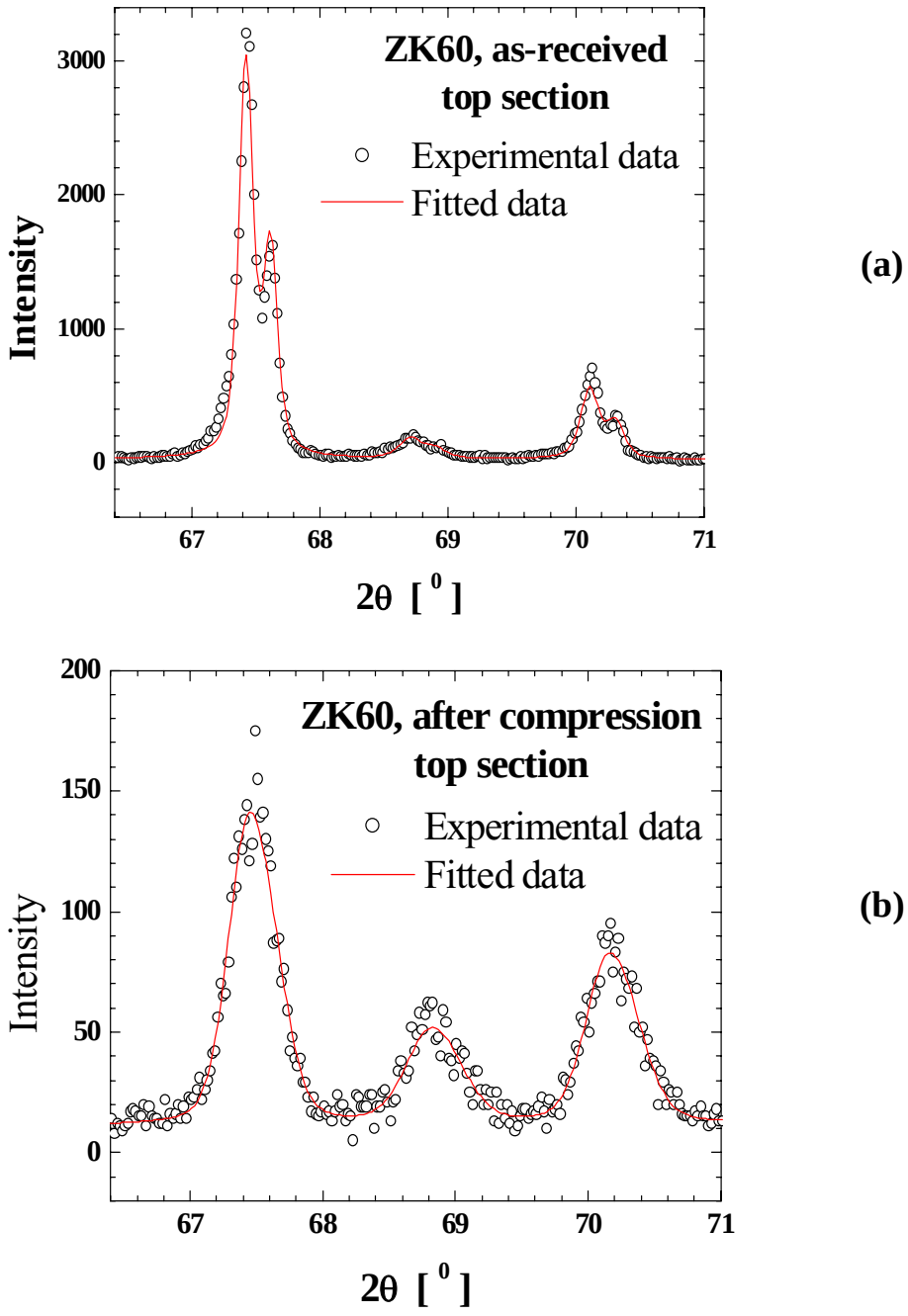

Figure 81 - The theoretical modeling (red lines) are in good agreement with the experimental (open dots) LE-XRD profiles measured for the ZK60 alloy; the partial θ - 2θ scans show the maxima at <20.0>, <11.2>, and <20.1> for the (a) ZK60, as-received, and (b) ZK60, after compression CC.

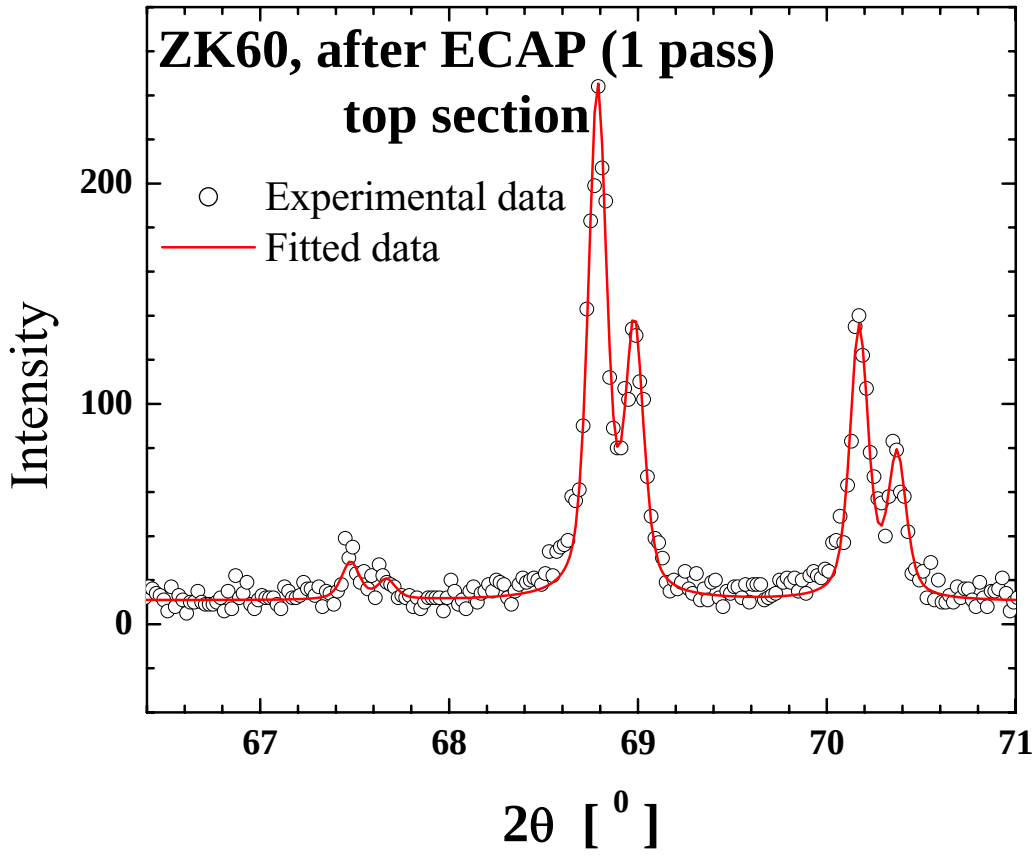

Figure 82 - The XRD profile (red lines) obtained from the whole-pattern fitting are in good agreement with the experimental (open dots) profile measured for the ZK60 alloy after one pass of ECAP at 260^0C; the partial θ - 2θ scan show the maxima at <20.0>, <11.2>, and <20.1>.

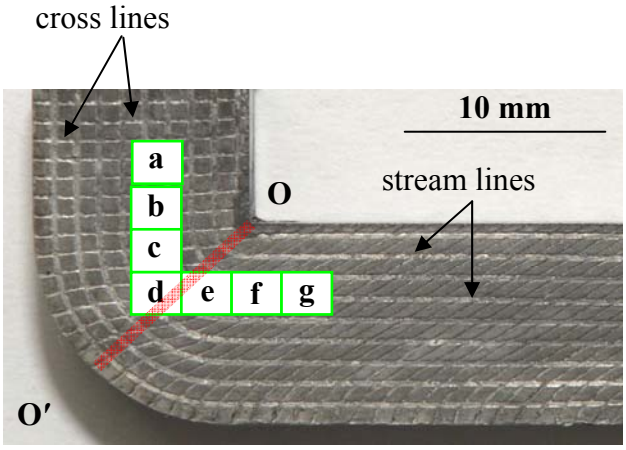

Figure 83 - The partially-ECAP-ed billet of the Mg alloy, ZK60, with the flow lines network of the stream and cross lines (1 × 1 mm), and the locations (a through g) for the pole-figure mapping. The billet was deformed in a round-corner die, with the angular span of its roundness of $2\psi = 60^0$. The intersection between the channels is OO′.

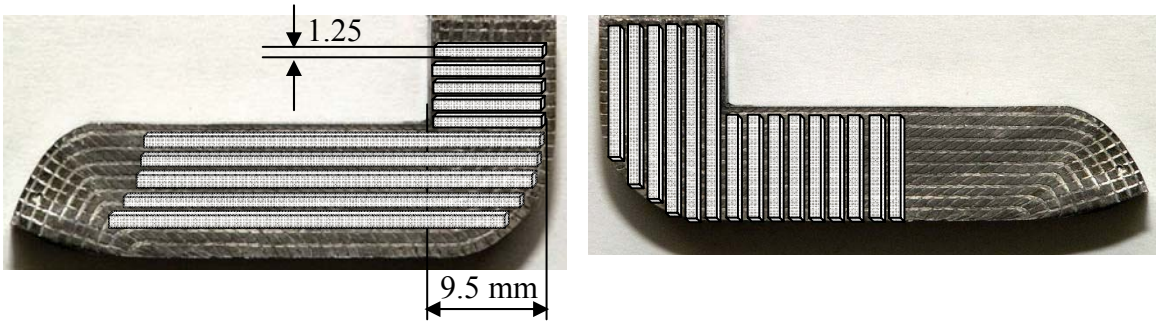

Figure 84 - The two-mirror parts of the partially ECAP-deformed ZK60 billet cut in horizontal and vertical bars (1.25 mm each) for the high-energy (HE) XRD mapping. The horizontal bars allow the measurements of the cross-undeformed and top-deformed planes, when rotated 90^0, and the vertical bars allow the measurements of the top-undeformed and cross-deformed planes, when rotated 90^0.

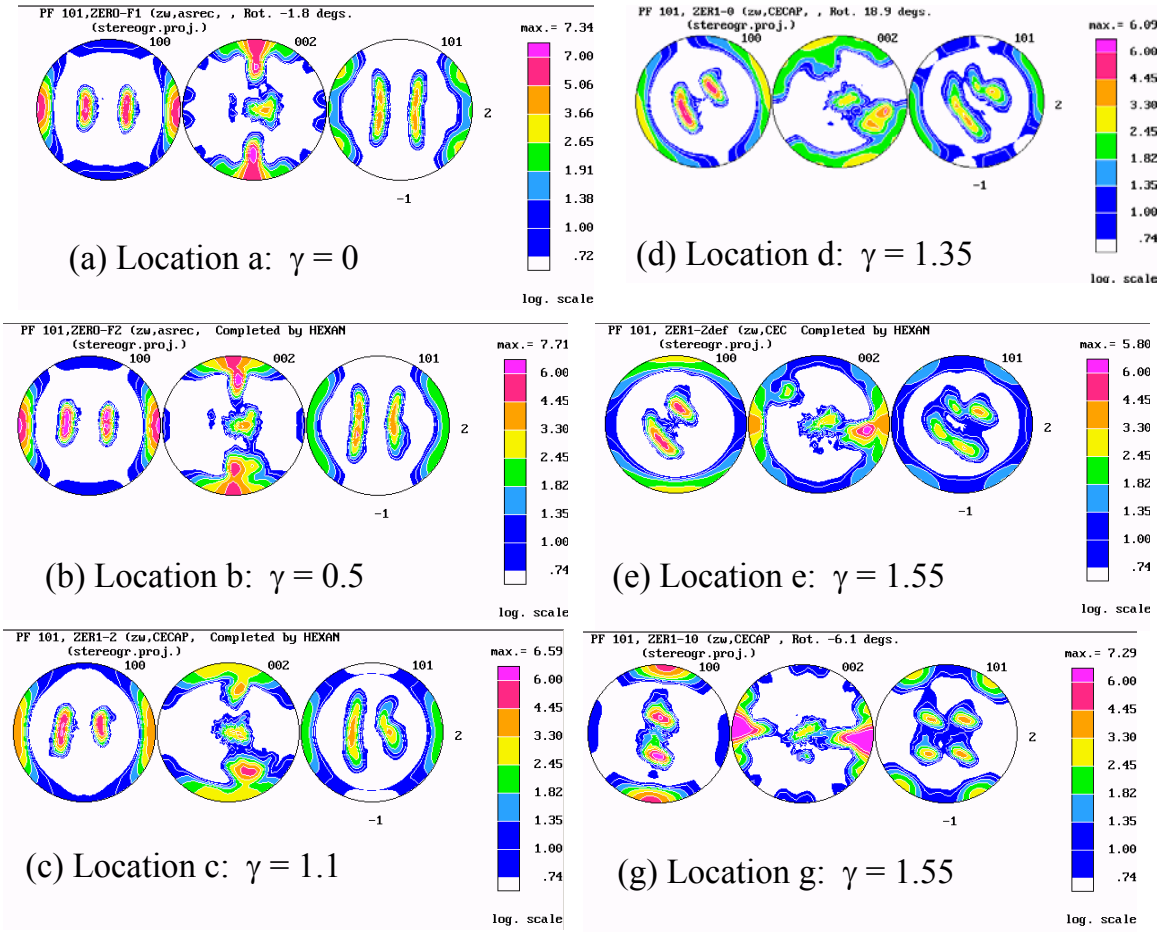

Figure 85 - The low-energy (LE) XRD texture mapping of the ZK60 partially-deformed billet, ZK-CC-T, during the ECAP in one pass, at the locations defined in Figure 83: (a, b, and c) before ECAP, (d) at the intersection between the two channels, and (e and g) after ECAP. The shear-strain values, γ, were determined experimentally, and are taken from Ref. 65.

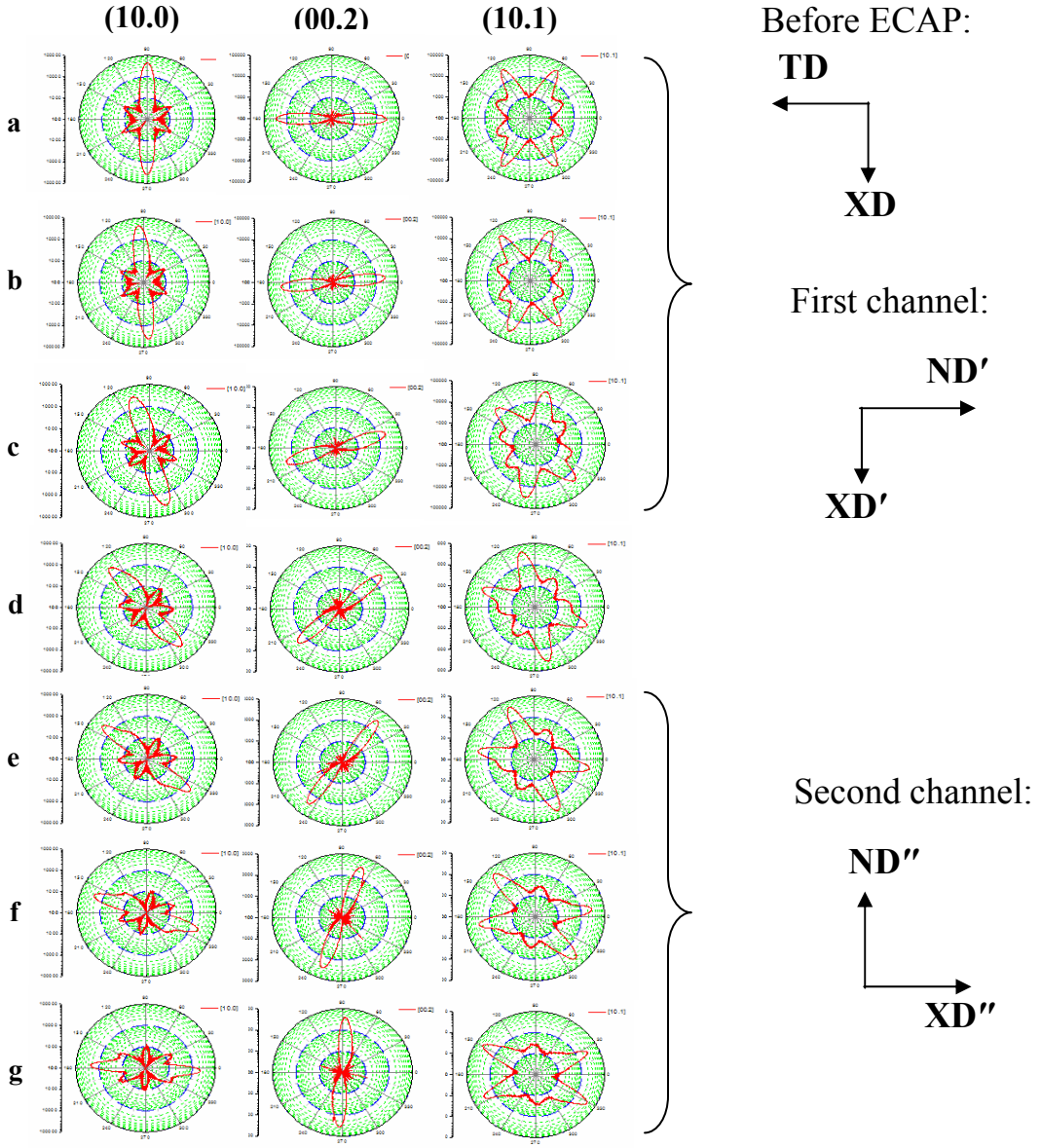

(a) ZK-CC-T-F (flow undeformed + flow deformed)

Figure 86 - (a) The HE-XRD IPPD mapping at the locations a through g (see Fig. 83) for the central stream line of the partially-deformed ZK60, ZK-CC-T, for three reflections, (10.0), (00.2), and (10.1), and on the flow plane of observation. The directions (defined in Fig. 25) before ECAP are XD, ND, and TD; the directions in the first channel are marked with ′, and in the second channel with ″.

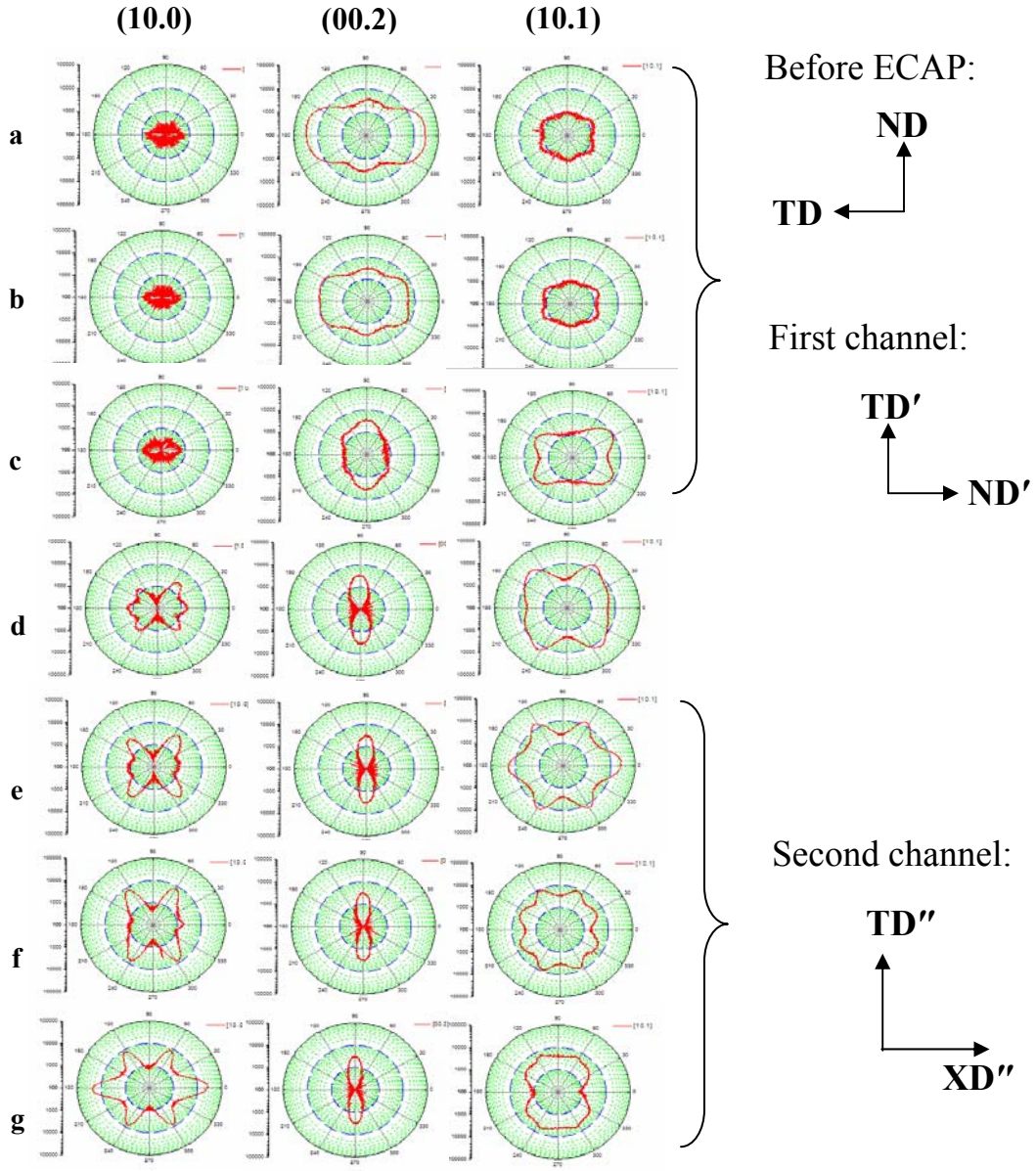

(b) ZK-CC-T-H (cross undeformed + top deformed)

Figure 86 - (b) The HE-XRD IPPD mapping at the locations a through g (see Fig. 83) for the central stream line of the partially-deformed ZK60, ZK-CC-T, for three reflections, (10.0), (00.2), and (10.1), and on the cross undeformed (a, b, and c) and top deformed (e, f, and g) planes of observations. The directions (defined in Fig. 25) before ECAP are XD, ND, and TD; the directions in the first channel are marked with ′, and in the second channel with ″.

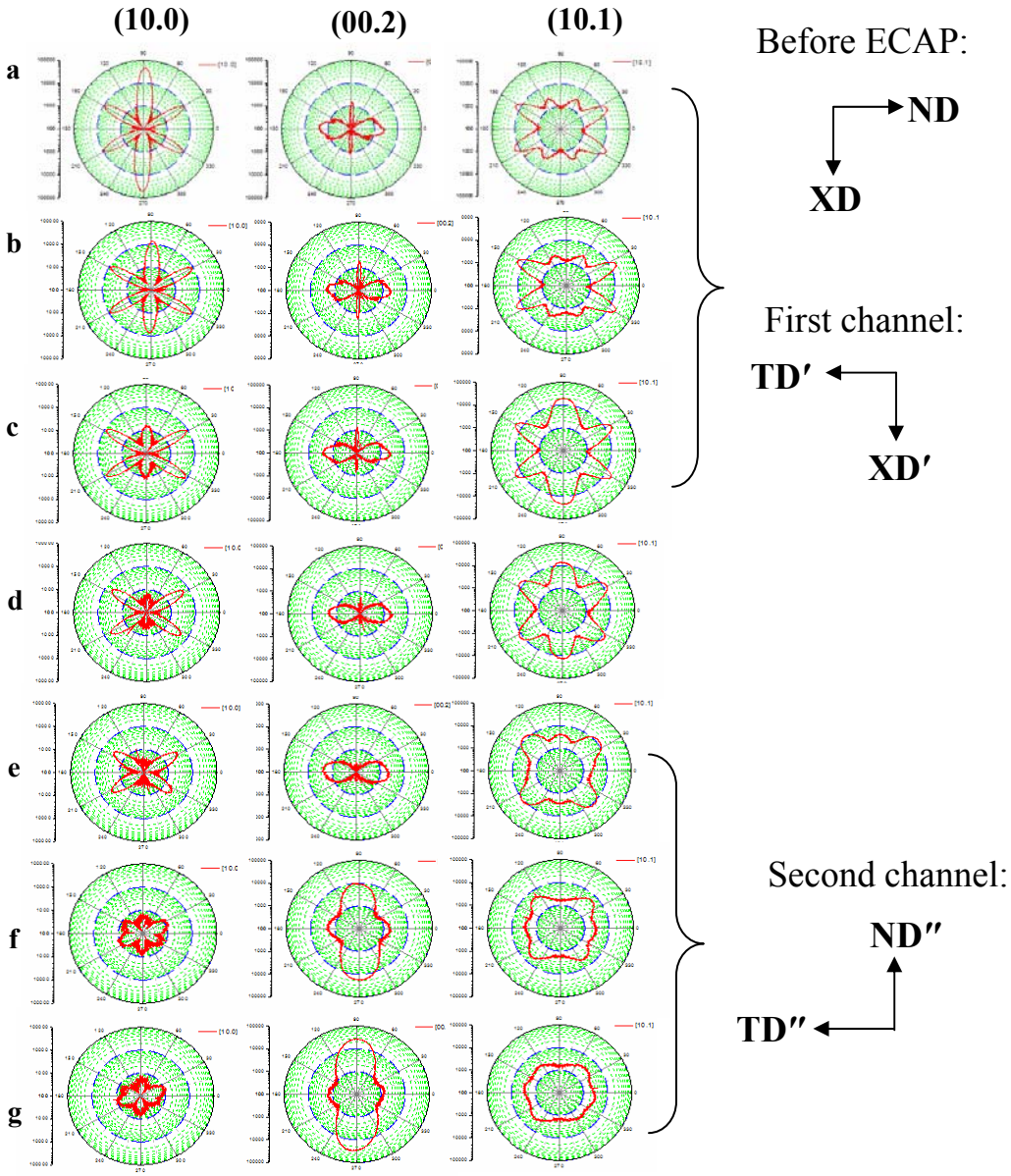

(c) ZK-CC-T-V (top undeformed + cross deformed)

Figure 86 - (c) The HE-XRD IPPD mapping at the locations a through g (see Fig. 83) for the central stream line of the partially-deformed ZK60, ZK-CC-T, for three reflections, (10.0), (00.2), and (10.1), and on the top undeformed (a, b, and c) and cross deformed (e, f, and g) planes of observations. The directions (defined in Fig. 25) before ECAP are XD, ND, and TD; the directions in the first channel are marked with ′, and in the second channel with ″.

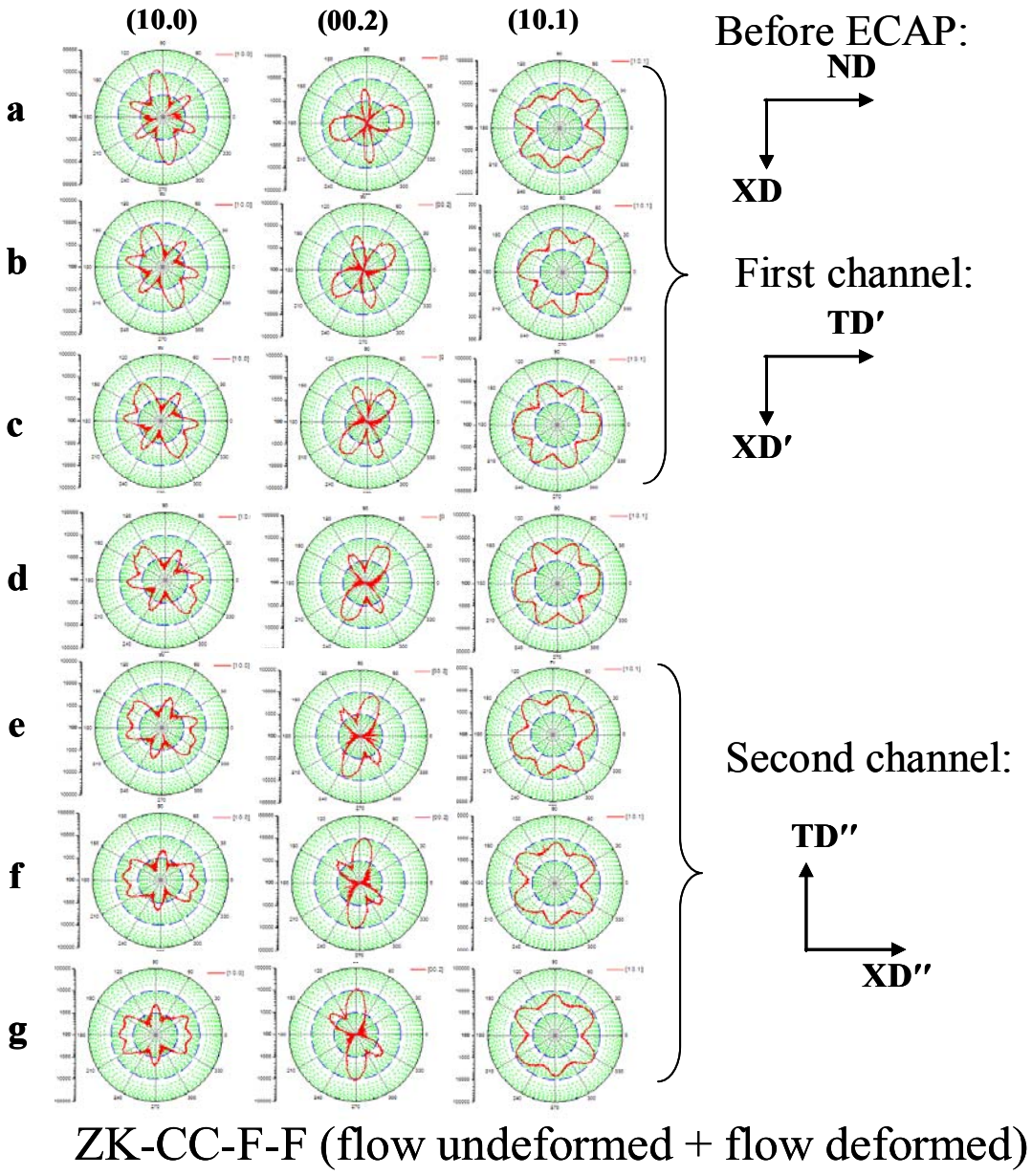

Figure 87 - (a) The HE-XRD IPPD mapping at the locations a through g (see Fig. 83) for the central stream line of the partially-deformed ZK60, ZK-CC-F-F, for three reflections, (10.0), (00.2), and (10.1), and on the flow (undeformed and deformed) plane of observations. The directions (defined in Fig. 25) are XD, ND, and TD before ECAP; the directions in the first channel are marked with ′, and in the second channel with ″.

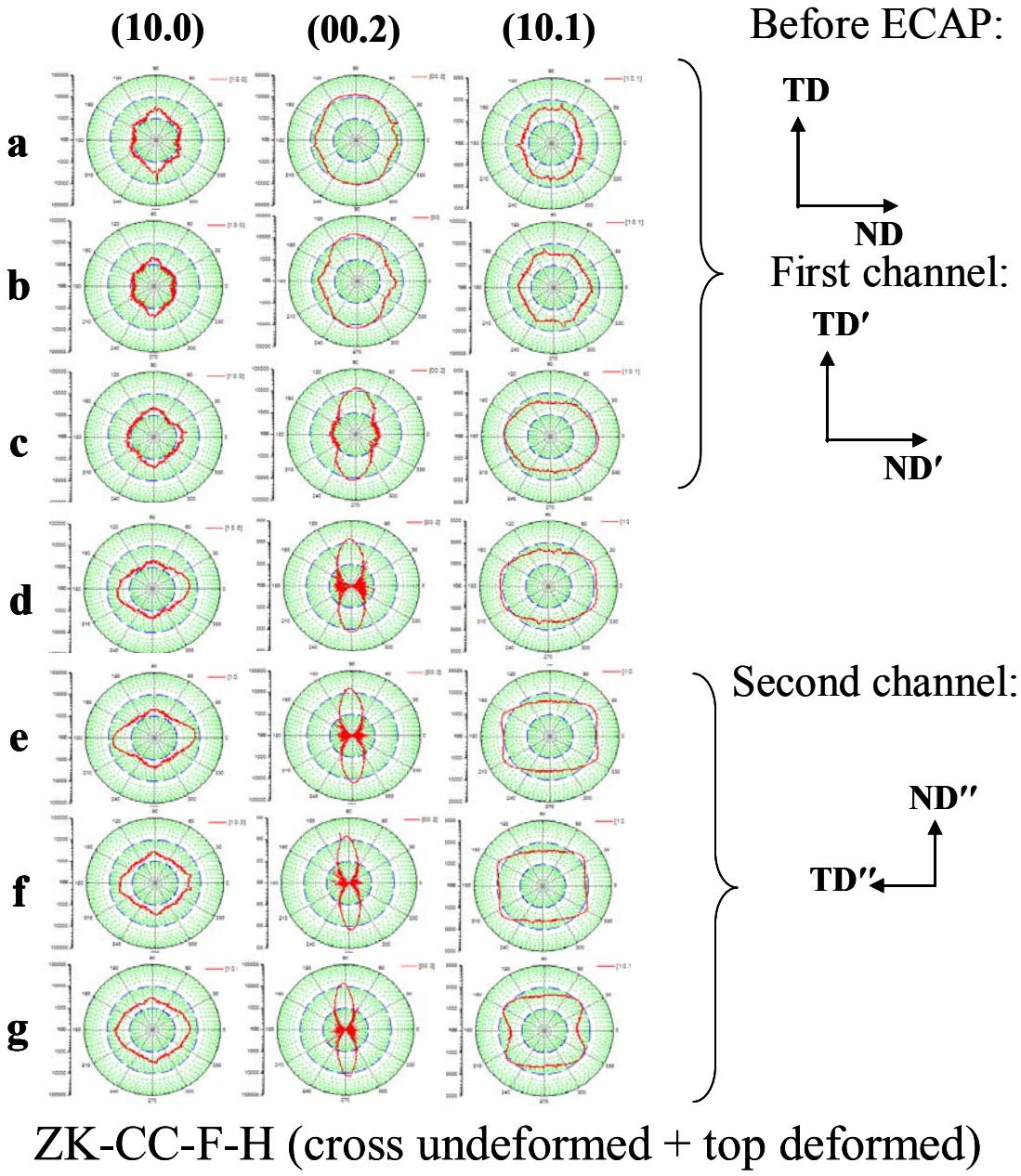

Figure 87 - (b) The HE-XRD IPPD mapping at the locations a through g (see Fig. 83) for the central stream line of the partially-deformed ZK60, ZK-CC-F-H (H - the horizontal bars), for three reflections, (10.0), (00.2), and (10.1), recorded on the cross undeformed (a, b, and c) and top deformed (e, f, and g) planes of observations. The directions (defined in Fig. 25) are XD, ND, and TD before ECAP; the directions in the first channel are marked with ′, and in the second channel with ″.

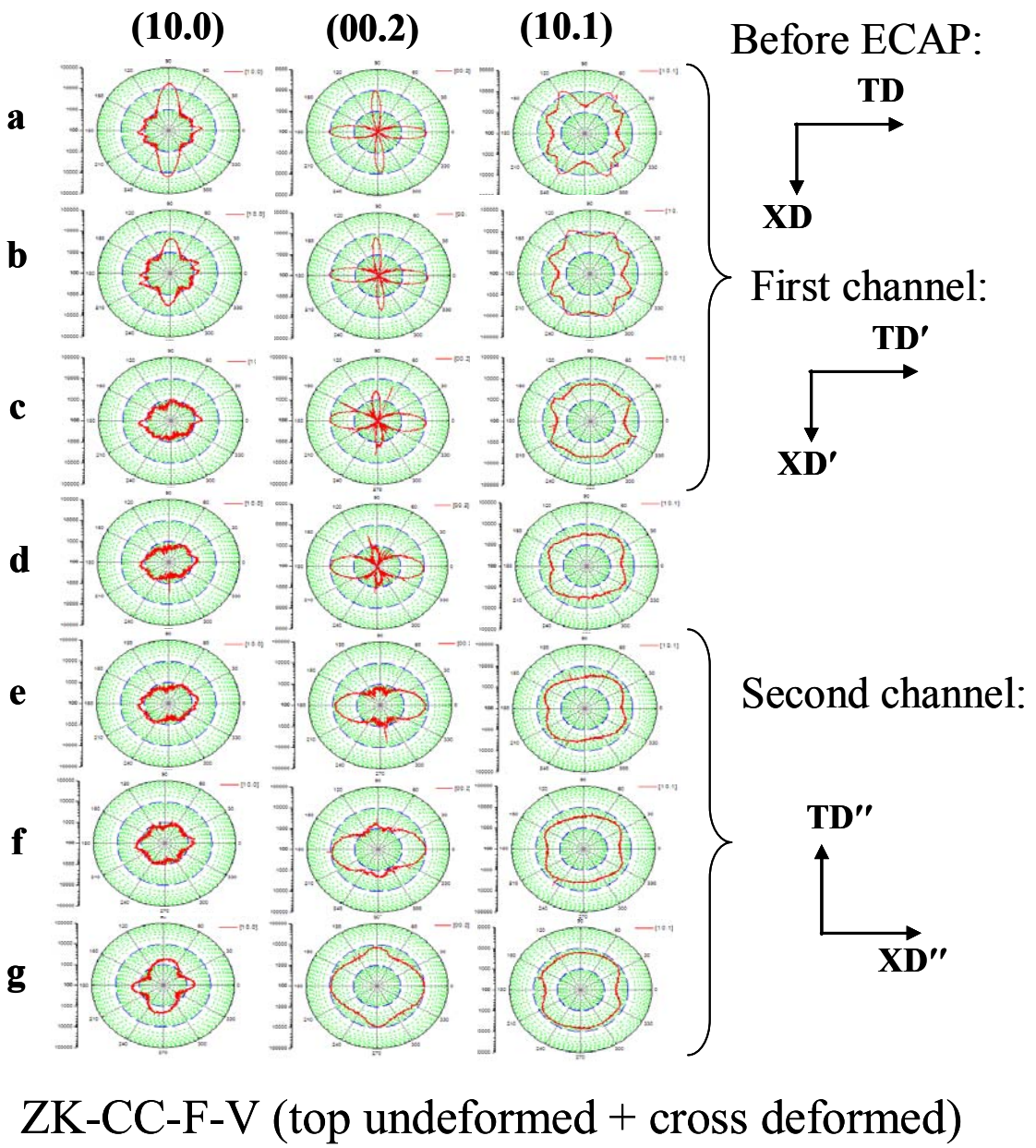

Figure 87 - (c) The HE-XRD IPPD mapping at the locations a through g (see Fig. 83) for the central stream line of the partially-deformed ZK60, ZK-CC-F-V (V - the vertical bars), for three reflections, (10.0), (00.2), and (10.1), and on the top undeformed (a, b, and c) and cross deformed (e, f, and g) planes of observations. The directions (defined in Fig. 25) are XD, ND, and TD before ECAP; the directions in the first channel are marked with ′, and in the second channel with ″.

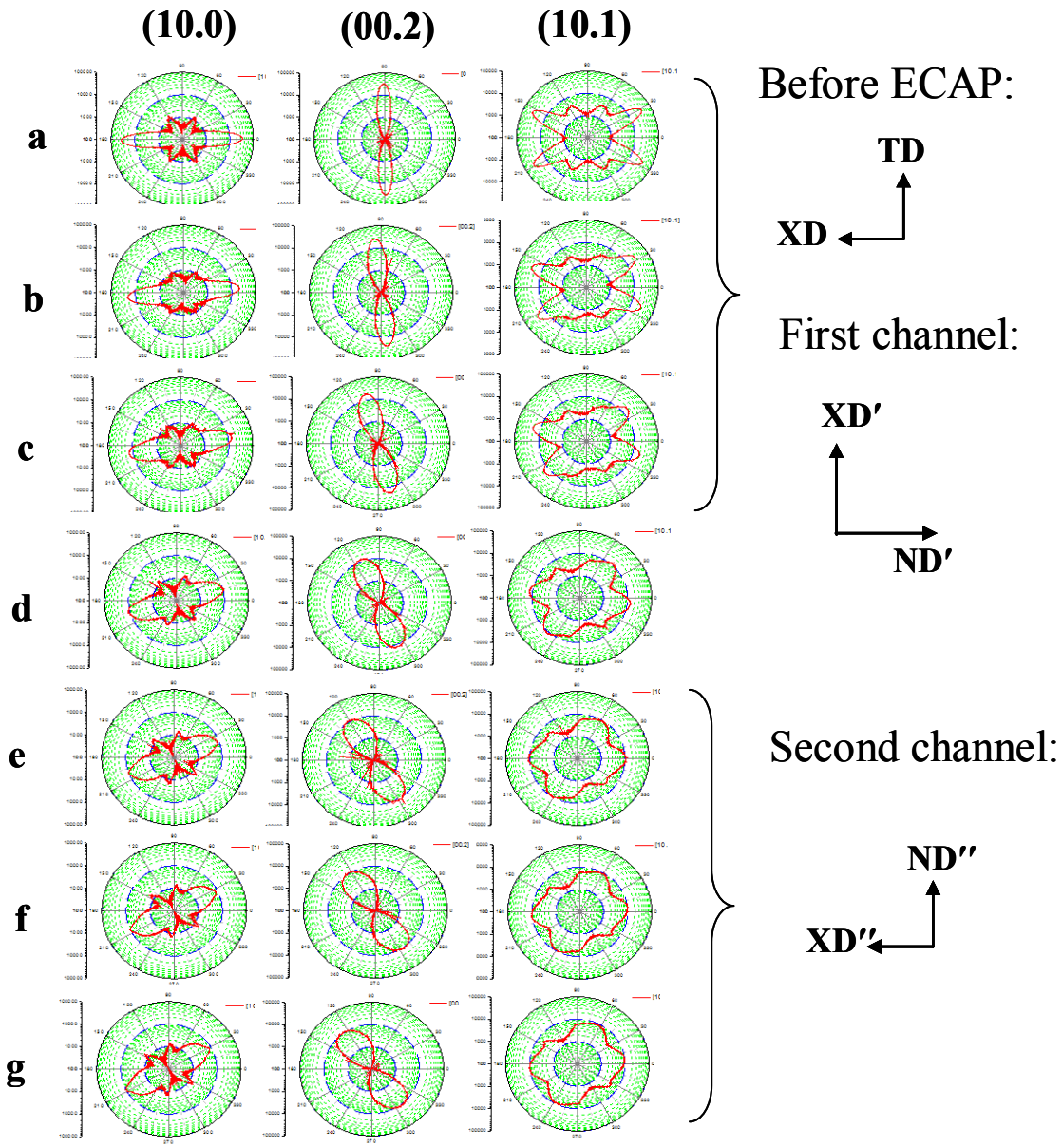

Figure 88 - (a) The HE-XRD IPPD mapping at the locations a through g (see Fig. 83) for the central stream line of the partially-deformed ZK60, ZK-FF-T-F, for three reflections, (10.0), (00.2), and (10.1), and flow (undeformed and deformed) plane of observations. The directions (defined in Fig. 25) are XD, ND, and TD before ECAP; the directions in the first channel are marked with ′, and in the second channel with ″.

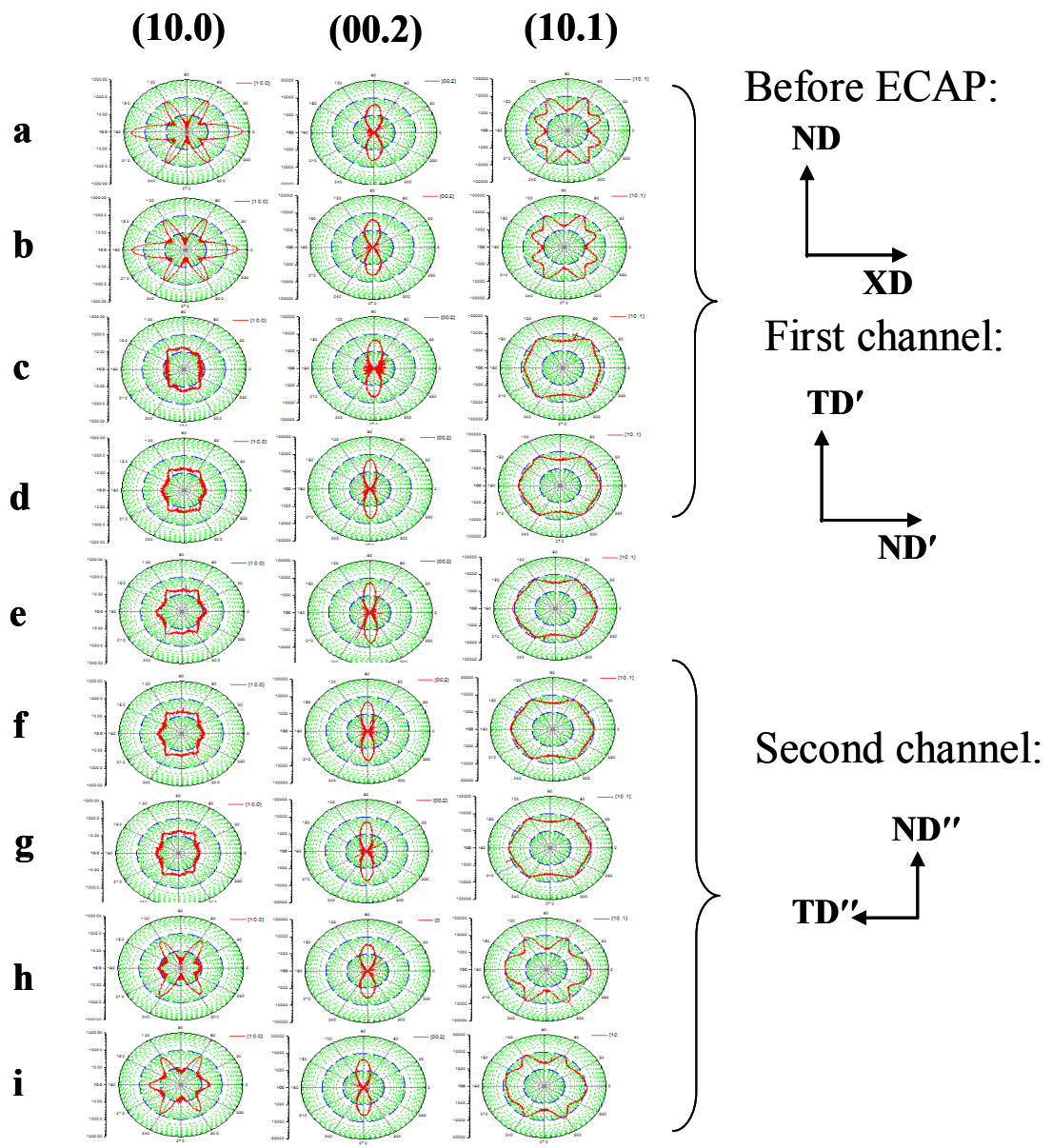

(b) ZK-FF-T-H (cross undeformed + top deformed)

Figure 88 - (b) The HE-XRD IPPD mapping at the locations a through g (see Fig. 83) for the central stream line of the partially-deformed ZK60, ZK-FF-T-H (H - horizontal bars), for three reflections, (10.0), (00.2), and (10.1), and on the cross undeformed (a, b, and c) and top deformed (e, f, and g) planes of observations. The directions (defined in Fig. 25) are XD, ND, and TD before ECAP; the directions in the first channel are marked with ′, and in the second channel with ″.

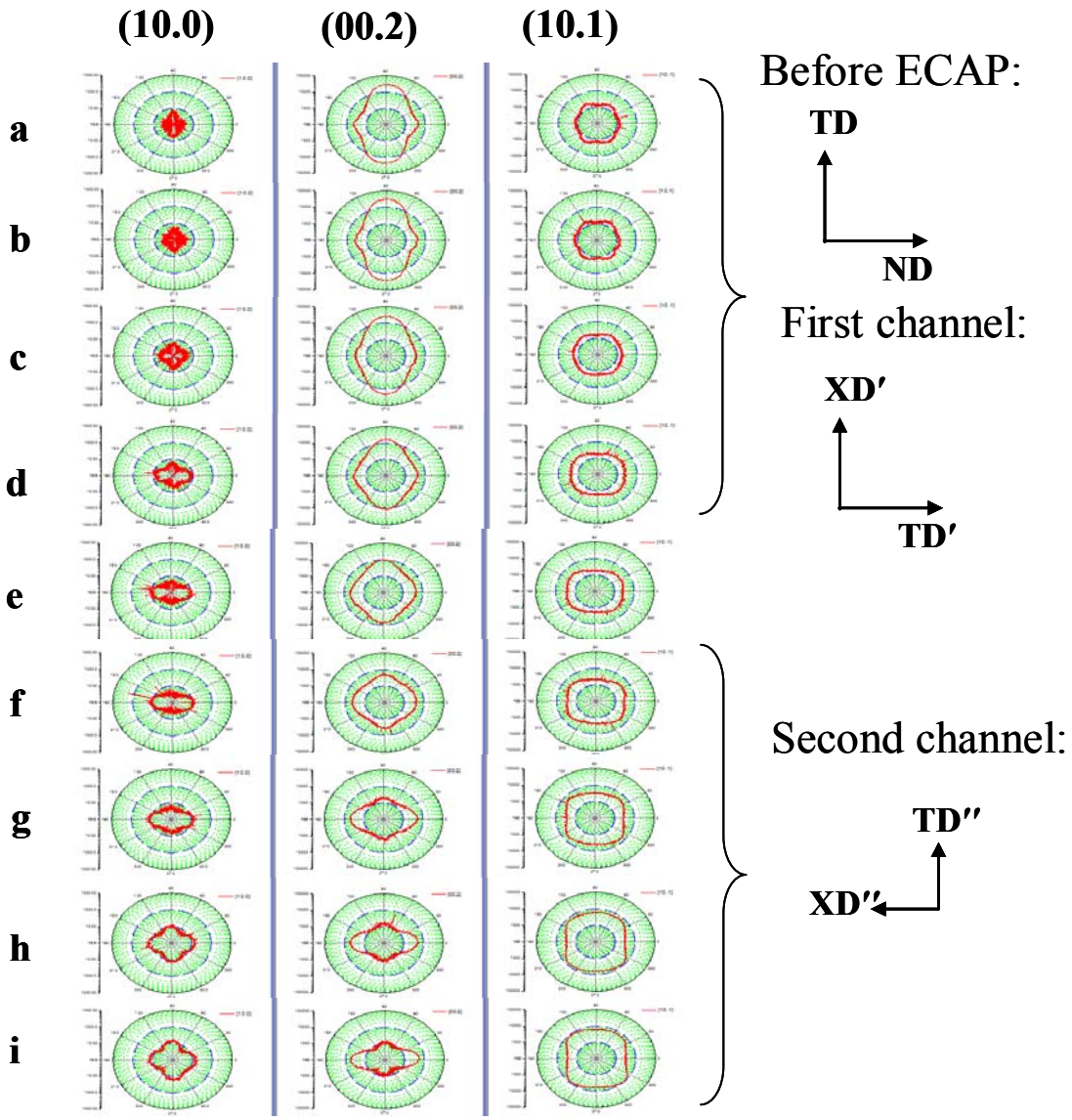

Figure 88 - (c) The HE-XRD IPPD mapping at the locations a through g (see Fig. 83) for the central stream line of the partially-deformed ZK60, ZK-CC-F, for three reflections, (10.0), (00.1), and (10.1), and on the top undeformed (a, b, and c) and cross deformed (e, f, and g) planes of observations. The directions (defined in Fig. 25) before ECAP are XD, ND, and TD; the directions in the first channel are marked with ′, and in the second channel with ″.

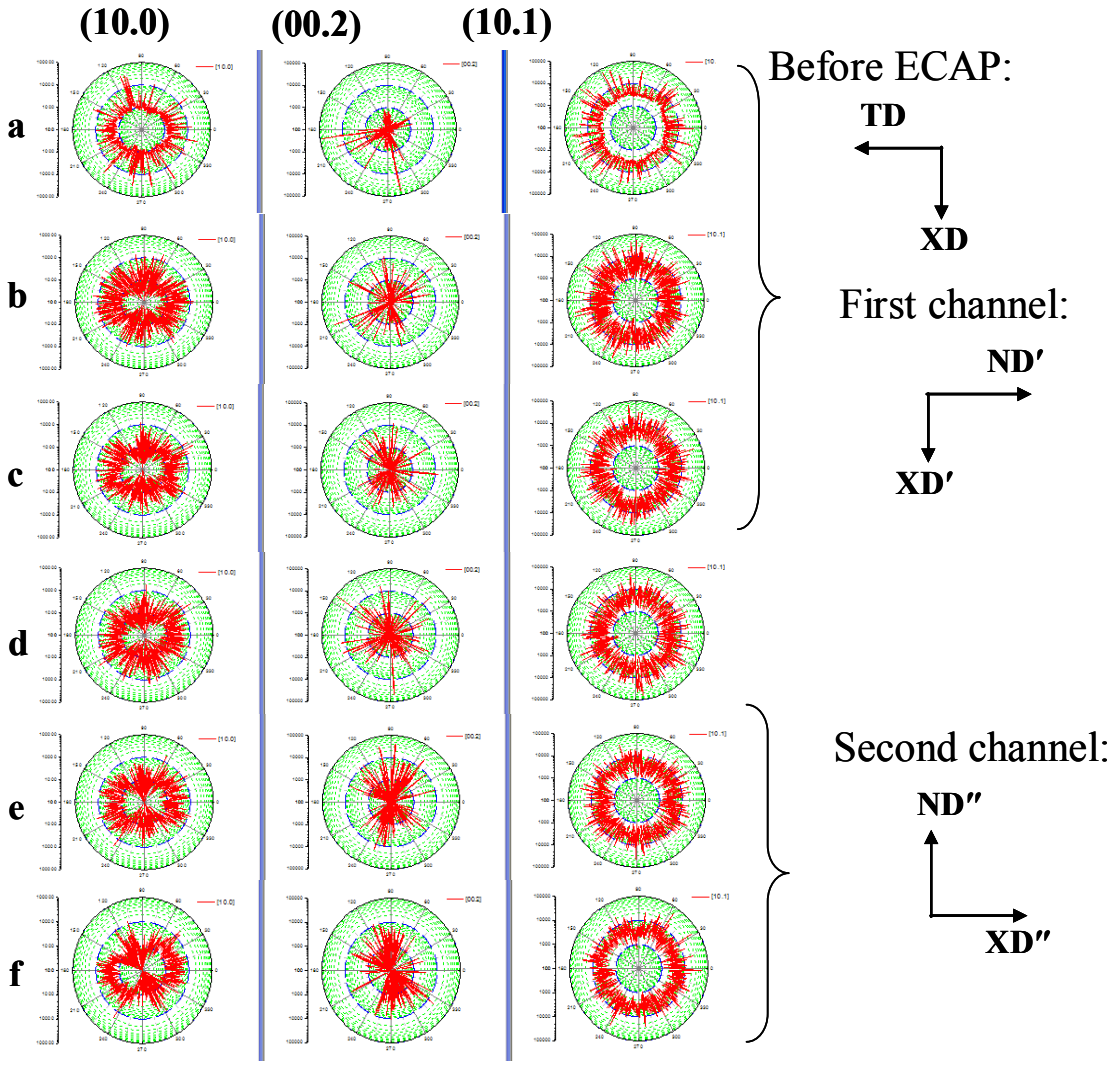

(a) AZ-CC-T-F (flow undeformed + flow deformed)

Figure 89 - The HE-XRD IPPD mapping at the locations a through f (see Fig. 83) for the central stream line of the partially-deformed AZ31, AZ-CC-T-F, for three reflections, (10.0), (00.2), and (10.1), recorded on the flow (undeformed and deformed) plane of observations. The directions (defined in Fig. 25) are XD, ND, and TD before ECAP; the directions in the first channel are marked with ′, and in the second channel with ″.

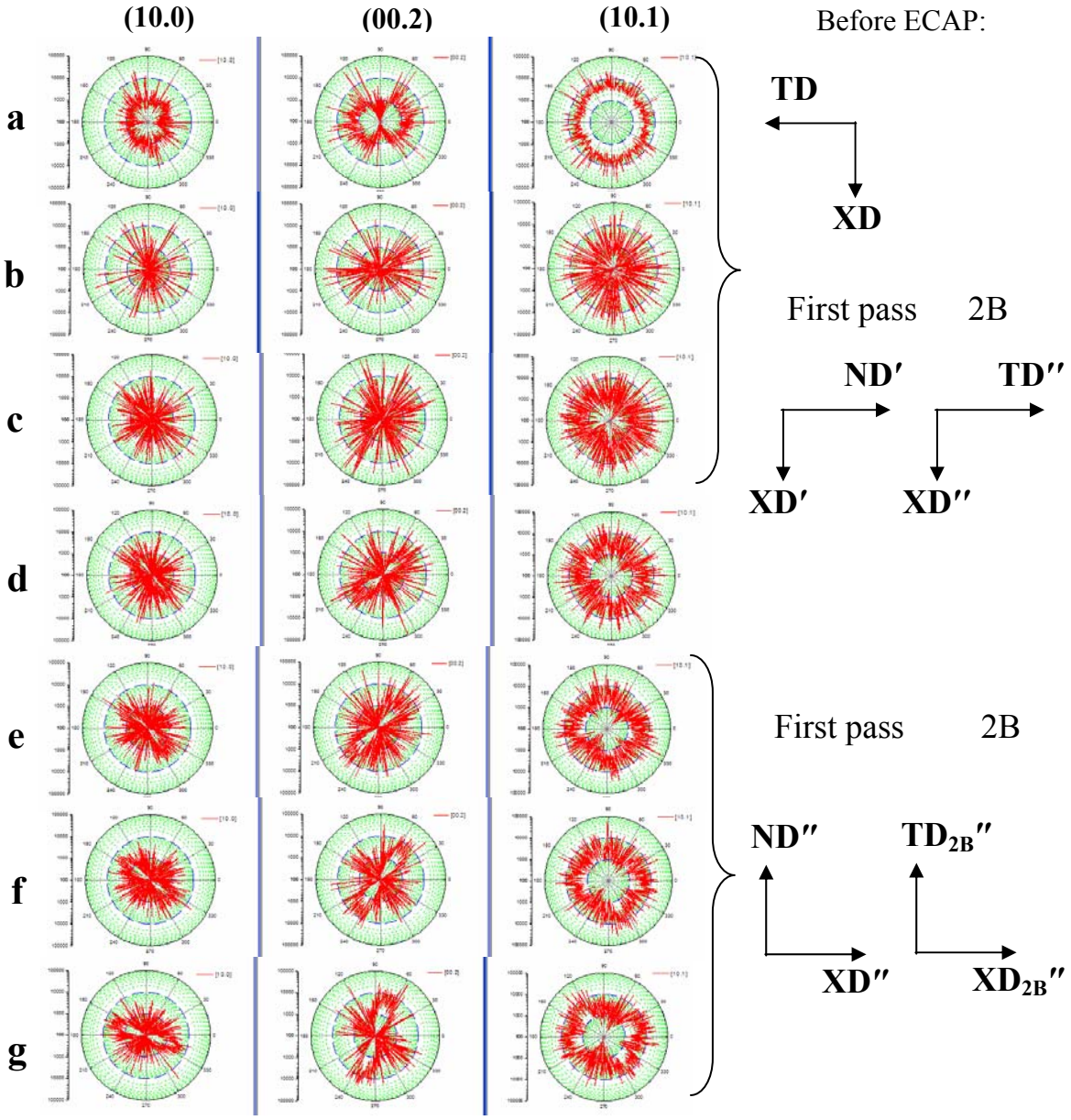

Figure 90 - The HE-XRD IPPD mapping, following the central stream line (the locations a through g in Fig. 83) of the partially-deformed billet of AZ31, AZ-CC-T, on the flow plane, for three reflections, (10.0), (00.2), and (10.1). The billet was deformed in ECAP at 250^0, 2 passes, route B_C. The directions (defined in Fig. 25) are XD, ND, and TD before ECAP; the directions in the first channel are marked with ′, and in the second channel with ″.

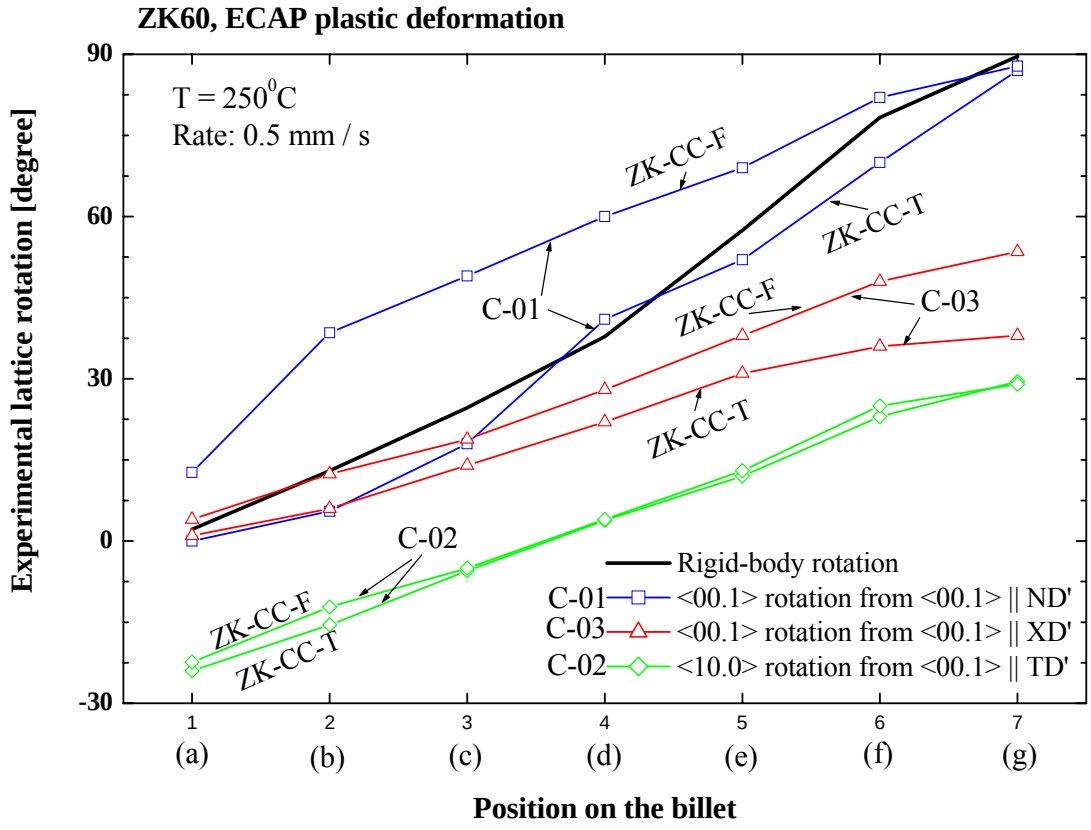

Figure 91 - The experimental lattice rotation as a function of the position on the billet (the locations a through g in Fig. 83) resulted from the HE-XRD IPPD data on the partially-ECAP-deformed ZK60 billets, ZK-CC-T and ZK-CC-F. The three texture components, C-01, C-02, and C-03 are shown for both billets, and the rigid-body rotation is given for comparison. The lattice rotations versus time are shown for the three cases: the c-axis parallel to the pressing direction, XD′, and perpendicular to the pressing directions, TD′ and ND′.

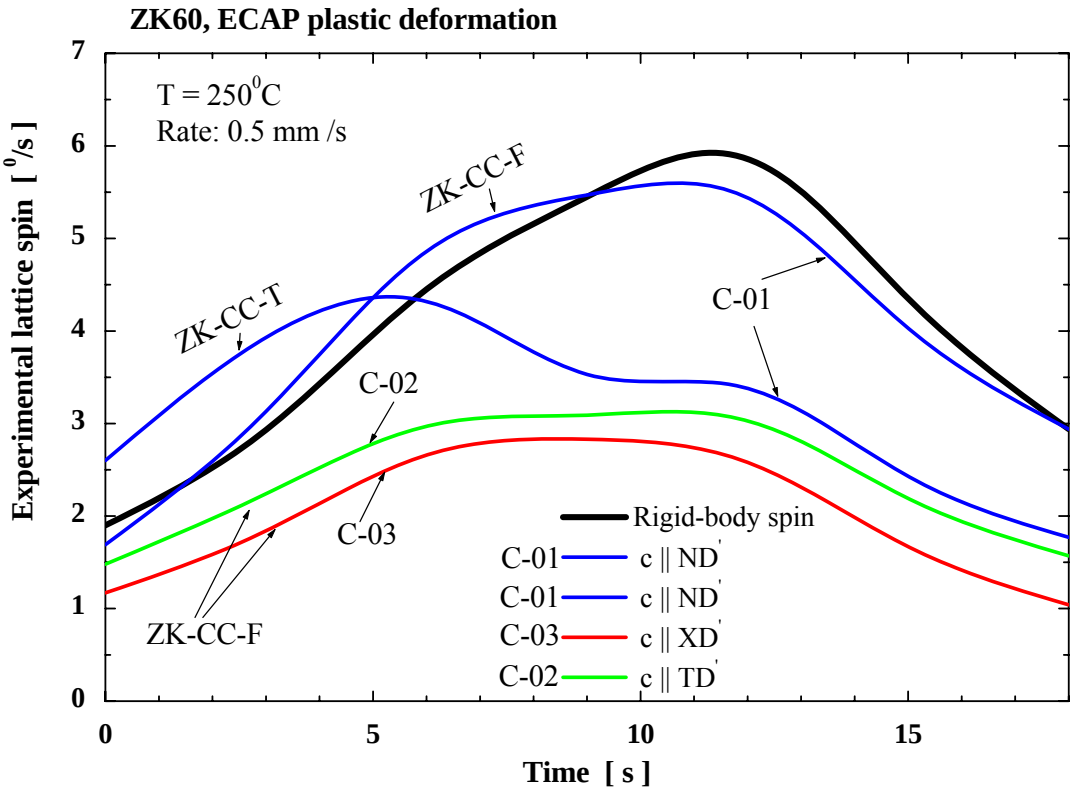

Figure 92 - The temporal evolution of the lattice spin resulted from the HE-XRD measurements on the partially-ECAP-deformed ZK60 billets, ZK-CC-T and ZK-CC-F. The three texture components, C-01, C-02, and C-03, are produced during the ECAP deformation of the Mg alloy, ZK60, and the rigid-body spin is shown for comparison. The lattice spin versus time is shown for the three cases: the c-axis parallel to the pressing direction, XD′, and perpendicular to the pressing directions, TD′ and ND′.

VITA

Grigoreta Mihaela Stoica was born in Romania, Codlea of Brashov, a little city surrounded by the Carpathian Mountains, not far away from Dracula's place. She attended the high-school in Brashov, and at the age of 18 she left her hometown for Bucharest, where she graduated the University of Bucharest, Faculty of Physics. Her major was Solid-State Physics, and the MS dissertation was "The Excess Current in GaAs Tunnel Diodes." After the graduation and until October 1997 she did research in the semiconductor technology field, mainly at the Institute for Electronic Components, Bucharest, Romania. The research topics were related to the technology of Si electronic devices, structural and electrical characterizations, as well as, failure analysis. In 1999 she came with her husband to TN. After a short period of working as a research associate at the University of Tennessee, Materials Science and Engineering Department, she started in 2000 a doctoral program. She received the Doctor of Philosophy degree in May 2007, majoring in Materials Science and Engineering.